University of Southampton Research Repository

UNIVERSITY OF SOUTHAMPTON

FACULTY OF ENGINEERING AND THE ENVIRONMENT

Civil, Maritime and Environmental Engineering and Sciences

and

Institute of Sound and Vibration Research

Enhanced performance monitoring of a ballasted high-speed railway

by

David Robert Michael Milne

Thesis for the degree of Engineering Doctorate in Transport and the Environment

October 2017

UNIVERSITY OF SOUTHAMPTON

ABSTRACT

FACULTY OF ENGINEERING AND THE ENVIRONMENT

Infrastructure Engineering

Thesis for the degree of Engineering Doctorate

Enhanced performance monitoring of a ballasted high-speed railway

David Robert Michael Milne

Maintenance of railway track is required to ensure regular track geometry, adequate support conditions and good performance. Understanding the long and the short term performance and how track features and interventions affect the behaviour is important for maintenance. Lineside monitoring techniques are an effective means of assessing performance and are often used to characterise typical track movements and to determine the track stiffness. However, to study long term performance, lengths of deployment and the frequency of measurement need to increase, with implications for the measurement systems and analysis methods. This research develops lineside monitoring techniques and applies them to railway track over extended periods, for condition monitoring, investigating deterioration and evaluating maintenance on High Speed One, a ballasted high-speed railway in the United Kingdom.

Laboratory and field tests show that inexpensive Micro Electro Mechanical Systems accelerometers can provide data of sufficient quality for quantifying track deflection under high speed conditions, enabling long term condition monitoring. This generates large volumes of data, which need to be processed and analysed automatically. Train geometries mean that track vibration signals have properties which facilitate new analysis techniques for characterising deflection and determining stiffness. Characterising the range of total and downward deflection is non-trivial due to variability and signal processing artefacts. The cumulative distribution function for track deflection is used to overcome these issues. This enables the typical downward deflection, the at-rest position and uplift to be identified, while implicitly averaging over vehicles. The frequency and magnitude of the dominant peaks in the spectrum for low frequency track vibration depends on the train (or vehicle) geometry, wheel loads and track stiffness. This property has been used to determine the track stiffness in the frequency domain. Monitoring based on this approach has been applied at defect sites on High Speed One to investigate performance and inform and evaluate maintenance. Records of deflection and stiffness highlighted problems and helped improve maintenance. Using long-term monitoring to understand the condition of the track and then specify remediation work was more effective than standard practice. Results show sustained reductions in deflection and restored support conditions after an intervention, giving the infrastructure managers confidence in using monitoring to innovate maintenance.

Table of Contents

Table of Contents ..... **i**

List of Tables ..... **vii**

List of Figures ..... **ix**

Declaration of Authorship ..... **xxiii**

Acknowledgements ..... **xxv**

Definitions, Abbreviations, Symbols and Conventions ..... **xxvii**

Definitions xxvii
Abbreviations xxix
Symbols xxx
Conventions xxxiii
Photographs xxxiii

Chapter 1: Introduction **1**

1.1 Motivation 1
1.2 Aims and objectives 3
1.3 Outline 3
1.4 Industrial support 5
1.5 Original contributions 6

Chapter 2: Literature review **7**

2.1 Track behaviour 7

2.1.1 Track vibration 8
2.1.2 Train loads 10
2.1.3 Track stiffness 11
2.1.4 Plastic track behaviour 12
2.1.5 Voiding and nonlinearity 14

2.2 Quantifying track performance 15

2.2.1 Track geometry measurements 15
2.2.2 Dedicated measurements 16
2.2.3 Train borne measurements 17

2.3 Stiffness measurements 17
2.4 Lineside measurements 18

2.4.1 Velocity and acceleration 18
2.4.2 Direct measurement of displacement 22
2.4.3 Comparison of lineside monitoring approaches 24
2.4.4 Interpretation of track vibration measurements 25

2.5 Geometry defects and performance issues 27
2.6 Maintenance practice 29
2.7 Conclusion 31

2.7.1 Summary 31
2.7.2 Requirements of a lineside monitoring system 32

Chapter 3: Lineside monitoring on HS1 35

3.1 Introduction 35
3.2 Background to High Speed One 35

3.2.1 Route 35
3.2.2 Trackform 36
3.2.3 Train types 37
3.2.4 Train loads 39

3.3 Crissmill plain line site 42
3.4 Fault sites: track 43

3.4.1 Crissmill defect site 43
3.4.2 North Downs Tunnel country end portal 44
3.4.3 Crissmill points motor 45

3.5 Fault sites: bridges 46

3.5.1 Rainham Viaduct 47
3.5.2 A20 overbridge 49

3.6 Summary 50

Chapter 4: Low cost transducers for lineside monitoring 51

4.1 Introduction 51
4.2 MEMS accelerometers 51
4.3 Testing 53

4.3.1 Laboratory testing 53
4.3.2 Field trials 59

4.4 Digital sensors 63
4.5 Conclusions 66

Chapter 5: Lineside monitoring: Low frequency track vibration 69

5.1 Introduction 69
5.2 Low frequency track vibration 69
5.3 Role of the track 75
5.4 Role of the train geometry 76
  5.4.1 Infinite train 77
  5.4.2 Single vehicle 79
  5.4.3 Periodic train 81
  5.4.4 Effect of coupled of trainsets 85
  5.4.5 Effects of multiple vehicle lengths and coupling 86
  5.4.6 Implications 88
  5.4.7 Effects of variation in wheel load 90
5.5 Determination of train speed 92
5.6 Conclusion 92

Chapter 6: Interpreting track deflections 93

6.1 Introduction 93
6.2 Identifying train types 93
6.3 Truncating to stationary region 96
6.4 Characterising deflection: peak-finding 98
6.5 Characterising deflection: statistical method 100
  6.5.1 Theory 101
  6.5.2 Accounting for train geometry 103
  6.5.3 Examples 107
  6.5.4 Characterising the range of movement 109
  6.5.5 Further testing 113
6.6 Comparison of turning point and CDF analyses 117
6.7 Deflected track bed geometry 118
6.8 Rail deflection 120
6.9 Interaction between wheels 121
6.10 Conclusion 124

Chapter 7: Analysing track stiffness **127**

7.1 Introduction 127
7.2 Time domain methods 127
7.3 Frequency domain methods 129

7.3.1 By analysis of the magnitudes of a pair of dominant trainload frequencies 129
7.3.2 Numerically by regression 133

7.4 Comparison of methods 135

7.4.1 Frequency domain implementations 135
7.4.2 Frequency and time domain implementations 136

7.5 Conclusion 138

Chapter 8: Application of continuous monitoring **139**

8.1 Introduction 139
8.2 Testing of continuous monitoring 140

8.2.1 Typical results 140
8.2.2 Variation 142
8.2.3 Influence of transducer choice 145
8.2.4 Conclusion 146

8.3 Crissmill defect site 147
8.4 North Downs Tunnel 154
8.5 Rainham Viaduct 160
8.6 Trends and forecasting 165
8.7 Conclusions 166

Chapter 9: Lessons from lineside monitoring **169**

9.1 Introduction 169

9.1.1 Diagnosing the cause of track defects 169
9.1.2 Behaviour within defect zones 170
9.1.3 Evaluating maintenance 170

9.2 Track geometry and stiffness: stiff spots 171
9.3 Structural movement: bridge and ballast interaction 172

9.3.1 Rainham Viaduct: lineside measurements 172

9.3.2 A20 Bridge 184

9.4 Excitation of track-mounted equipment.. 189

9.5 Defect zones.. 191

9.5.1 Track bed condition within defect zones.. 191

9.5.2 Uplift phenomena 193

9.5.3 Defect geometry 195

9.5.4 Accelerated deterioration.. 198

9.6 Evaluating maintenance 200

9.6.1 Localised Tamping 200

9.6.2 Shimming 202

9.6.3 Targeted packing 204

9.6.4 Under-sleeper pads 206

9.7 Conclusions.. 208

Chapter 10: Conclusions 211

10.1 Improvements to lineside monitoring 211

10.2 Investigations, diagnosis and evaluation of remediation 212

10.3 Recommendations for future research 213

References 215

Appendix A Software.. 225

Appendix B Fault finding from track geometry measurement 227

Appendix C Study of ballast vibration.. 231

C.1 Instrumented grains.. 231

C.2 Study sites 232

C.2.1 Ballast vibration.. 233

C.3 Peak acceleration and velocity.. 238

C.4 Ballast lift.. 240

Appendix D Requirements for a model to study progressive deterioration of railway track 247

List of Tables

Table 2.1 Track geometry parameters.. 16

Table 2.2 Proposed use of different monitoring systems in this research....................... 33

Table 3.1 Table of train and vehicle geometries for passenger trains operated on HS1. 39

Table 6.1 Notional trainset lengths for a 20 m vehicle. 96

Table 6.2 Possible ordinates for truncating displacement signals into stationary regions containing single or multiple vehicle types... 98

Table 6.3 Typical characteristic downwards and upwards track deflections identified using different probability values from displacement data for track with well-performing sleepers and track with voided sleepers from Figure 6.14.. 112

Table 6.4 Characteristic range of total and downward displacement found from measured Javelin displacement data from Figure 6.15. 114

Table 6.5 Characteristic range of total and downward displacement found from measured Eurostar displacement data from Figure 6.16. 115

Table 6.6 Characteristic range of total and downward displacement found from measured Velaro displacement data from Figure 6.17....................... 116

Table 6.7 Comparison of the characteristic range of total and downward displacement found using turning point analysis and the CDF method, with $P(w \leq 0) = 0.7$ for measured track displacements. 117

Table 7.1 Track system support moduli obtained from ratio of the magnitudes at two dominant train load frequencies from the track vibration spectra for three different train types given in Figure 5.7. 132

Table 8.1 Timing of maintenance interventions 147

Table 9.1 Typical range of total deflection obtained for each train type at each measurement location along the A20 bridge. 187

List of Figures

Figure 1.1(a) Visible track defect; (b) ballast abrasion; (c) damage to sleepers and ballast. 2

Figure 2.1 Sketch of typical ballasted trackform for a ballasted high-speed railway, such as HS1. 7

Figure 2.2 Example of bi/non-linear load deflection behaviour expected from a sleeper with a void gap. After Sussman et al. (2001). 14

Figure 2.3 Examples of void meters installed on the track. 17

Figure 2.4 Photograph of a geophone on a sleeper end (Watson, 2016). 19

Figure 2.5 The ratio of magnitude of the filtered signal and the original signal at a particular frequency relative to the cut-off frequency of a digital high pass Butterworth filter. 21

Figure 2.6 Photographs of (a) a high-speed camera and (b) calibration targets for digital image correlation, (Watson, 2016). 23

Figure 2.7 Example track displacement data obtained from geophone measurements, showing start up transients, the shift in the at-rest position for the stationary region and variability between wheels. Estimates of the rest position and typical downwards deflection are indicated. 26

Figure 2.8 Photograph of tamping machine (a) tines above ballast (b) in operation. 30

Figure 2.9 Manual packing operation using Kango or Cobra packers (Network Rail, 2016). 30

Figure 3.1 Map of study sites used for this research (Ordnance Survey, 2015). 36

Figure 3.2 Photographs of (a) Javelin, (b) Eurostar, (c) Velaro trains. 38

Figure 3.3 Typical vehicle geometry: (a) twin bogie vehicle, (b) articulated vehicle. L_v is the vehicle length, L_b is the bogie spacing and L_w is axle spacing within a bogie. 38

Figure 3.4 Histogram of quasi-static wheel loads for (a) Eurostar and (b) Javelin, obtained from weighing-in-motion systems on HS1. 40

Figure 3.5 (a) Histogram of mean wheel load for each train, (b) Histogram of wheel loads normalised by the mean wheel load of each train from 99 Javelin trains. 41

Figure 3.6 Mean normalised wheel load at each axle position for a Javelin train. The dashed vertical lines separate individual vehicles. 41

Figure 3.7 Photograph of the Crissmill plain line site instrumented during combined track vibration and aerodynamic measurements (Watson, 2016). 42

Figure 3.8 Primary instrumentation positions used for track vibration measurements at the Crissmill plain line site 43

Figure 3.9 Photographs of Crissmill defect site, (a) before and (b) after remediation (Watson, 2016). 44

Figure 3.10 Photographs of defects near the North Downs Tunnel portal (Watson, 2016). 45

Figure 3.11 (a) surface view of UTX and inspection chambers next to the ballast shoulder, (b) view inside UTX inspection chamber. 45

Figure 3.12 Photograph of points motor at Crissmill crossovers. 46

Figure 3.13 Photograph of expansion joint plate at Rainham. 46

Figure 3.14 Simple spanning plate supporting continuous ballast, structural joint detail used on HS1 (a) between two adjacent bridge decks, (b) between a bridge deck and an abutment. 47

Figure 3.15 Example arrangement of bridge decks at Rainham Viaduct. 47

Figure 3.16 Photograph of track defect on Rainham Viaduct, (a) from the cess and (b) from the cab of a train on the Up line looking towards London. 48

Figure 3.17 Layout of A20 bridge deck. 49

Figure 3.18 Photographs of track defects either end of the A20 overbridge (Watson, 2016). 49

Figure 4.1 Photographs of (a) ADXL326 breakout board and (b) sensor package recovered from track. 53

Figure 4.2 Photographs of hydraulic actuator and electrodynamic shakers used for low and high frequency testing. 54

Figure 4.3 Displacement time histories for fixed frequency sinusoidal excitation at (a) 2 Hz, (b) 3 Hz, (c) 4 Hz, (d) 5 Hz, measured using a geophone and ±3 g and ±16 g accelerometers. 55

Figure 4.4 Transfer function magnitude between ±3 g and ±16 g accelerometers and a geophone (a) at each test frequency, (b) at the harmonics of each test frequency and for a frequency sweep between 5 and 45 Hz, expressed in 1/3 octave bands, and the frequency response of the antialiasing filter. 56

Figure 4.5 Instron electropuls E1000 servo-controlled actuator used to apply a simulated track deflection waveform. 57

Figure 4.6 (a) Displacements obtained using actuator LVDT and MEMS accelerometer, (b) displacement spectra for a waveform representative of typical sleeper deflections on HS1 for Javelin vehicles travelling at 60 m/s. 58

Figure 4.7 Comparison of displacement data obtained using actuator LVDT and MEMS accelerometer for waveform representative of (a) 0.5 mm deflections from Javelin vehicles travelling at 25 m/s and (b) 3 mm deflections for the same speed. 59

Figure 4.8 Photographs of geophones, MEMS accelerometers and targets for DIC mounted on a sleeper end (Watson, 2016). 59

Figure 4.9 Comparison of displacement data obtained using a geophone and MEMS accelerometer on the same sleeper end in (a) the time domain and (b) frequency domain. Data were sampled at 500 Hz and filtered with 2 and 40 Hz high- and low-pass cut-off frequencies, before integration. 60

Figure 4.10 Signal-to-noise ratio between train passage and background signal data for accelerometer and geophone data from Figure 4.9 in 1/3 octave bands. 61

Figure 4.11 Comparison of displacement data obtained using a geophone and MEMS accelerometer on the same sleeper end in (a) the time domain and (b) displacement spectra where the MEMS accelerometer has been affected some low frequency phenomenon. Data were sampled at 500 Hz and filtered with 2 and 40 Hz high- and low-pass cut-off frequencies before integration. 62

Figure 4.12 Comparison of sleeper deflection data obtained using a geophone and a MEMS accelerometer position on the same sleeper, though to be affected by voiding. Data were sampled at 500 Hz and filtered with 2 and 40 Hz high- and low-pass cut-off frequencies before integration.. 63

Figure 4.13 Photographs of (a) AX3 and (b) X16 accelerometers deployed on track.... 64

Figure 4.14 Track displacement data obtained using an X16 self-contained MEMS accelerometer and data aquistion system for (a) a Javelin and (b) a Eurostar, sampled at 400 Hz and filtered with 2 and 40 Hz high- and low-pass cutoffs beofre integration.. 65

Figure 4.15 Instrumented ballast grain. 66

Figure 5.1 Example track deflections for each train type operating on HS1. Obtained using geophones sampled at 500 Hz. Filtered for integration using 2 Hz and 40 Hz cut-off frequencies. (a) Six-vehicle Javelin, (b) two six-vehicle Javelin coupled together, (c) 20-vehicle Eurostar, (d) 16-vehicle Velaro.. 70

Figure 5.2 Beam on and elastic foundation subject to a point load. 70

Figure 5.3 Beam-on-elastic-foundation subject to a train of moving loads.................. 71

Figure 5.4 Rail deflections obtained using Eq.(5.5) for a train comprising six 20 m vehicles with wheel loads of 65 kN, moving at 60 m/s along a track with a UIC 60 rail and a track system support modulus of 40 MN/m^2. 72

Figure 5.5(a) Static deflection of a UIC 60 rail on elastic foundation with a range of plausible track system support moduli subject to a 50 kN point load, (b) normalised deflection for the same track, (c) normalised deflection for the same track due to wheels on the bogies from adjacent vehicle ends. 73

Figure 5.6 Fourier transform for example rail deflections from Figure 5.4 obtained using Eq.(5.8).. 74

Figure 5.7 Spectra of sleeper velocity measurements plotted against non-dimensional frequency N=f/f_1 for (a) six vehicle Javelin, (b) two six-vehicle Javelin coupled together, (c) 20-vehicle Eurostar, (d) 16-vehicle Velaro......... 75

Figure 5.8 (a) Track deflection due to a 50 kN moving load at 50 m/s for a range of track support moduli, (b) Normalised magnitude of the Fourier transform for track deflection for non-dimensional frequency for a range of track support moduli. 76

Figure 5.9 A single repeated vehicle, a=(L_b+L_w)/2v, b=(L_b–L_w)/2v. 78

Figure 5.10 Discrete load frequencies for an infinite train consisting of 20 m long Javelin vehicles and weighting function due to vehicle geometry from Eq.(5.13).. 79

Figure 5.11 Components of the single vehicle spectrum (a) contribution of axle spacing (b) contribution of bogie (c) single vehicle spectrum for a 20 m Javelin vehicle from Eq.(5.15). 81

Figure 5.12 Effect of increasing the number of vehicles in a train on the series in Eq.(5.17) series length of: (a) 1 vehicle; (b) 2 vehicles; (c) 3 vehicles; (d) 5 vehicles; (e) 8 vehicles; (f) 13 vehicles. 83

Figure 5.13 Normalised train load spectrum for a train of 20 m Javelin vehicles comprising: (a) 1 vehicle; (b) 2 vehicles; (c) 3 vehicles; (d) 5 vehicles; (e) 8 vehicles; (f) 13 vehicles. Single vehicle spectrum ‘- - -’, from Eq.(5.17).. 84

Figure 5.14 Normalised train load spectrum ‘—’ and weighting ‘- - -’ from a single vehicle for (a) Javelin and (b) Velaro. 85

Figure 5.15 Relative magnitude of the Fourier transform for the train loads from a six vehicle Javelin trainset and two six vehicle trainsets with an additional coupling length of 1.4 m. 86

Figure 5.16 Relative magnitude of the Fourier transform for the train loads of: (a) the passenger saloons in a Class 373 Eurostar trainset; (b) drive car and passenger saloons in a single Eurostar trainset; (c) two coupled Eurostar trainsets; (d) two coupled trainsets with correct wheel loads. 87

Figure 5.17 Relative differences between (a) actual and nominal frequency and (b) actual and nominal magnitude of spectral peaks in the train load spectrum for a Javelin train with different numbers of vehicles. 89

Figure 5.18 Variation of the expected magnitude at each spectral peak for a train consisting of increasing numbers of Javelin vehicles; each wheel load was modelled as a normally distributed random variable with a standard deviation of 4% of the mean load. 91

Figure 6.1 Example of (a) using a threshold on the native signal and (b) using peak finding to find the first and last wheel to determine the passing time for the train. 94

Figure 6.2 Paired half-vehicle period. 97

Figure 6.3 Boundaries for truncating displacement signals into stationary regions for (a) Javelin and (b) Eurostar. 98

Figure 6.4 Turning point analysis using data from the BOEF model Javelin vehicle geometry. 99

Figure 6.5 Turning point analysis using measured displacement data for (a) Javelin (b) Eurostar (c) Velaro. 100

Figure 6.6a) Non-dimensionalised displacement 2kw/Q at a position of x/L on a BOEF. The boundaries between monotonic regions have been highlighted using dashed lines. (b) CDF for the region [0, 2π] (hence [-2π, 2π]) evaluated analytically and numerically. 103

Figure 6.7 (a) Displacements for two half Javelin vehicles, (b) corresponding CDF for the Javelin, (c) displacements for two half Eurostar vehicles, (d) corresponding CDF for the Eurostar, (e) displacements for two half Velaro vehicles, (f) corresponding CDF for the Velaro, evaluated for a nominal 50 kN wheel loads for a range of plausible track support moduli. 104

Figure 6.8 Probability corresponding to the at-rest position P(w= 0) expressed as a function of track support moduli for Javelin, Eurostar and Velaro vehicle types. 105

Figure 6.9(a) Change in probability value associated with a over- or under-estimate of the at-rest position by 1% of the downward deflection for a Javelin trainset on track with a system support modulus of 25 MN/m^2. (b) Probability values for P(w=±0.01), for a Javelin on a track with a range of plausible track system support moduli... 106

Figure 6.10 Probability values for P(w = 0±0.01) of normalised displacement for(a) Eurostar and (b) Velaro on a track with a range of plausible track system support moduli. 107

Figure 6.11 Displacement data for a well-performing sleeper, (a) obtained from measured geophone data, sampled at 500 Hz, filtered with 2 and 40 Hz high- and low-pass cut-offs, (b) obtained using the beam-on-elastic-foundation model, (c) the CDFs for the measured and modelled data. 108

Figure 6.12(a) Displacement data for a voided sleeper obtained using a MEMS accelerometer, sampled at 333 Hz and filtered with 2 and 40 Hz high- and low-pass cut-offs. (b) CDF for that displacement data. 109

Figure 6.13 Difference between exact and approximate deflection determined using confidence intervals, (a) for the downward deflection and (b) for the uplift. 111

Figure 6.14 Identification of typical characteristic upward and downward deflection and at-rest position for(a) track with well-performing and(b) track with voided sleepers. 112

Figure 6.15 (a), (b) and (c) Three-vehicle-length windows of displacement time histories obtained at either end of three different sleepers at Crissmill plain line site. (d) The empirical CDF for each of these displacement time histories for the passage of a Javelin.. 114

Figure 6.16 (a), (b) and (c) Three-vehicle-length windows of displacement time histories obtained at either end of three different sleepers at Crissmill plain line site. (d) The empirical CDF for each of these displacement time histories for the passage of a Eurostar. 115

Figure 6.17 (a), (b) and (c) Three-vehicle-length windows of displacement time histories obtained at either end of three different sleepers at Crissmill plain line site. (d) The empirical CDF for each of these displacement time histories for the passage of a Velaro. 116

Figure 6.18 Visualisation of the deflected shape of the track under load found by interpolating between transducers aligned to a common datum using the CDF for the track deflection at each location. 119

Figure 6.19 Reliability of visualising a deflection bowl simulated using the BOEF model with a UIC60 rail and a track system support modulus of 40 MN/m^2 using a 'cubic spline' for interpolation for two positions relative to the wheels of a Javelin for (a) 0.6 m transducer spancing and (b) 1.2 m transducer spacing. 120

Figure 6.20 Wheel positions relative to a wheel closest to (a) the vehicle centre and (b) the vehicle end. 122

Figure 6.21 Ratio of downward rail deflection due to a vehicle and that from a single wheel for a track with a UIC60 rail and a range of plausible track system support moduli. 123

Figure 6.22 Comparison of maximum track deflection under a nominal wheel load of 50 kN moving at 50 m/s and from a Javelin vehicle with the same loads and speed (a) on softer track with a track system support modulus of 10 MN/m^2 and (b) on stiffer track with a track system support modulus of 40 MN/m^2. Both use a UIC 60 rail. 124

Figure 7.1 Displacement magnitude ratios between different pairs of dominant frequencies for a Javelin as a function of the track system support modulus. The plausible range of support modulus is also indicated. . 131

Figure 7.2 Expected displacement magnitude ratio for different track system support moduli for the Javelin and Velaro using the ratio between the 7th and 3rd dominant frequencies and the Eurostar using the ratio between the 6th and 2nd. 132

Figure 7.3 Velocity shape function obtained for Javelin data used to estimate the track system support modulus of 33 MN/m^2 by fitting the BOEF model in the frequency domain using regression. 135

Figure 7.4 Comparison between track system support modulus obtained using numerical regression and ratio analysis for (a) May 2015 and (b) May 2016. 136

Figure 7.5 Comparison between track system support modulus obtained directly using a range of assumed loads with measured deflections, corrected for a pad stiffness of 84 MN/m with (a) numerical regression and (b) ratio analysis of the 7th/3rd dominant frequencies for 49 Javelins in May 2015 and (c) numerical regression and (d) ratio analysis of the 7th/3rd dominant frequencies for 65 Javelins in May 2016. 137

Figure 8.1 12 hours of (a) characteristic total and downwards track displacement and (b) track system support modulus data from May 2015 and (d) characteristic total and downwards track deflection and (d) track system support modulus data from May 2016 for Javelin trains from sleeper 3.6_O at the Crissmill plain line site. 141

Figure 8.2 (a) Mean and 99.7% confidence intervals of the characteristic downward deflection, (b) mean and 99.7% confidence intervals of the track system support modulus, (c) mean equivalent applied wheel load, for the cess side of the Crissmill plain line site from one day of measurements taken in May 2015 and May 2016 from Javelin passage data. 142

Figure 8.3 (a) Characteristic downward deflection, (b) track system support modulus either end of sleeper 4.2 at Crissmill plain line plotted against train weight from a weighing-in-motion system. 143

Figure 8.4 (a) Characteristic downward deflection (adjusted for the weight of the train), (b) track system support modulus either end of sleeper 3.6 at Crissmill plain line plotted against train speed. 144

Figure 8.5 (a) Characteristic downward deflection adjusted for train weight, (b) track system support modulus either end of sleeper 3.6 at Crissmill plain line plotted against air temperature from a local weather station. 144

Figure 8.6 (a) Characteristic downward displacement data and (b) track system support modulus obtained from a geophone and a MEMS accelerometer co-located on a sleeper end. 146

Figure 8.7 Vertical track geometry for 100 m of track (66.67-66.77 km) surrounding the Crissmill defect site. Before any interventions (January 2015), after tamping (March and April 2015) and after instaltion of USPs (May and June 2015). 148

Figure 8.8 Trandsucer locations used for continuous monitoring as the Crissmill defect site. 149

Figure 8.9 Characteristic total (P=0.025-0.975) and downward (P=0.025-0.7) track deflection due to passing Eurostar at the Crissmill defect site. 150

Figure 8.10 Characteristic total (P=0.025-0.975) and downward (P=0.025-0.7) track deflection due to passing Javelin at the Crissmill defect site. 150

Figure 8.11 Track system support modulus calculated using the ratio of the magnitudes of 7th to the 3rd dominant frequencies in the acceleration spectrum for Javelin and Velaro trains at the Crissmill defect site. 151

Figure 8.12 Equivalent applied wheel load from the characteristic downward deflection and track system support modulus for Javelin and Velaro at the Crissmill defect site, assuming a rail pad stiffness of 84 MN/m. 153

Figure 8.13 (a) Characteristic downward deflection (b)track sytem support modulus (c) equivalent wheel load at location 4.2_O after monitoring was resumed in May 2017 for Javelin trains. 154

Figure 8.15 Vertical track geometry from the North Downs Tunnel defect site (a) and (c) above the UTX and (b) and (d) along the site, before and after maintenance. 155

Figure 8.16 Transducer locations and UTX positons for the North Downs Tunnel defect zone. 156

Figure 8.17 Characteristic total (P=0.025-0.975) and downward (P=0.025-0.7) track deflections due to passing Eurostars at the North Downs Tunnel defect site. 156

Figure 8.18 Characteristic total (P=0.025-0.975) and downward (P=0.025-0.7) track deflectionds due to passing Javelins at the North Downs Tunnel defect site. 157

Figure 8.19 Track system support modulus calculated using the ratio of the 7th to the 3rd dominant frequency using the acceleration spectrum for the Javelin at the North Downs Tunnel defect site........ 158

Figure 8.20 Equivalent applied wheel load corresponding to the measured characteristic downward deflection and track system support modulus data for the Javelin, assuming a rail pad stiffness of 84 MN/m, at the North Downs Tunnel defect site. 159

Figure 8.21 Transducer positions on Rainham Viaduct fault site used for continuous monitoring. 160

Figure 8.22 Vertical track geometry from the TRC across Rainham Viaduct before and after shimming of the cess side rail. 161

Figure 8.23 Characteristic total and downwards track displacement at Rainham Viaduct due to passing Javelins (Sleepers 2.4 and 3.6 have been corrected for bridge deflection). 162

Figure 8.24 Characteristic total and downwards track deflections at Rainham Viaduct due to passing Eurostars (Sleepers 2.4 and 3.6 have been corrected for bridge deflection). 162

Figure 8.25 Characteristic total and downwards track deflections at Rainham Viaduct due to passing Velaros (Sleepers 2.4 and 3.6 have been corrected for bridge deflection). 163

Figure 8.26 Amplitude of bridge movement 3.6 m from expansion joint for all train types. 165

Figure 9.1 Transducer locations used for conventional montioring at Rainham. 172

Figure 9.2 Trackbed deflecion found on the six-foot side (a) ahead of the defect zone 173

Figure 9.3 Track bed displacements found at Rainham on the cess side (a) directly above the joint 0.0_{O} and (b) towards the centre of the defect zone 1.8_{O}.

Obtained using high speed video at 200 Hz (fps), low-pass filtered with a 40 Hz cut-off freqeuncy. 174

Figure 9.4 Bridge deflections at Rainham, filtered between 2 and 40 Hz and corresponding velocity spectrum for bridge span vibration (a) and (b) on the approach span A2 and (c) and (d) on the exit span E2 for a Javelin. 175

Figure 9.5 Bridge deflections at Rainham, filtered between 2 and 40 Hz and corresponding velocity spectrum for bridge span vibration (a) and (b) at A2 on the approach span and (c) and (d) at E2 on the exit span for a Eurostar. 175

Figure 9.6 Vibration of Rainham Viaduct at the approach (A2) and exit spans (E2) and corresponding velocity spectra after a Eurostar trainset had left the bridge. 176

Figure 9.7 Sleeper deflection at 0.0_I over the joint overlain by bridge deflection 6.7 m away from the joint on the approach span A2 and 6 m away from the joint on the exit span E2, for (a) the Javelin and (b) half a Eurostar. . 177

Figure 9.8 Effect of deck end rotations on the ballast above the joint. 178

Figure 9.9 Mechanism to identify volume change above the expansion joint due to passing trains. 178

Figure 9.10 (a) Photograph of LVDT used to measured expansion across the bridge joint, (b) results for a Eurostar supplied by NRHS. 180

Figure 9.11 Time lapse photos of the track above the bridge joint, used to visualise ballast stability, taken 30 minutes apart. 181

Figure 9.12 (a) Daily temperature record from a weather station near Rainham Viaduct for April to August 2016, (b) record of characteristic downward deflections for either end of the sleeper located above the structural expansion joint for the same period. 182

Figure 9.13 Mechanism for volume change in ballast above joint from thermal expansion/contraction. 183

Figure 9.14 Geophone positions on the A20 bridge. V – vertical and H – horizontal sensor. 184

Figure 9.15 Track deflection data obtained using high speed video for DIC for the defects zones above structural expansion joints (a) and (c) on the approach to and (b) and (d) exiting from the A20 bridge for Javelin and Eurostar trains. 185

Figure 9.16 Bridge deflections obtained using geophones, filtered between 2-40 Hz (a), (c) and (e) above an intermediate support and (b), (d) and (f) at the middle of the central span for Javelin, Eurostar and Velaro trains passing across the A20 bridge. 186

Figure 9.17 Free vibration in the middle of the central span of the A20 bridge, for a Eurostar passing on (a) the instrumented side, (b) the opposite side and (c) the corresponding velocity spectrum for these measurements. 188

Figure 9.18 transducer locations on the sleepers and points motor. 190

Figure 9.19 Track deflection for (a) cess sleeper end at location 3, (c) points motor bracket at location 9. Acceleration spectrum for forced and free vibration of (b) cess sleeper end at location 3, (d) points motor bracket at location 9 for a Javelin passing at 60 m/s. 191

Figure 9.20 (a) A defect zone, (b) ballast and sleeper end outside a defect zone and (c) inside a defect zone. 192

Figure 9.21 (a) Excavation into the ballast crib, (b) damage to sleepers, (c) track bed below sleeper level. 193

Figure 9.22 Track deflection for a voided sleeper on the A20 overbridge obtained using high speed video and DIC for (a) a Javelin and (b) and Eurostar. 194

Figure 9.23 Track deflection of a voided sleeper at 1.2 m in the Crissmill plain line site obtained using MEMS accelerometers for (a) Javelin, (b) Eurostar, (c) Velaro. 194

Figure 9.24 Uplift data from (a) either end of sleeper 3.6 from the North Downs Tunnel fault site following targeting packing and (b) cess side data from sleepers 2.4_{O} and 4.2_{O} from the Crissmill fault site following installation of USPs. Maintenance interventions are indicated by the vertical dashed line.. 195

Figure 9.25 Visualisation of deflected track geometry at the Crissmill plain line site, (a) on the cess side, (b) on the six-foot side. 196

Figure 9.26 Ratio of deflected track geometry at the Crissmill plain line site between a Javelin and a Eurostar and a Javelin and a Velaro, (a) on the cess side, (b) on the six-foot side. 197

Figure 9.27 (a) Ratio of deflected track geometry, pre-intervention, between a Javelin and a Eurostar, (b) visualisation of deflected track geometry on the six-foot side of the North Downs Tunnel defect site. 197

Figure 9.28 Deterioration of performance at sleepers within the Crissmill defect zone. 199

Figure 9.29 Track deflection data for a sleeper within the defect zone on Rainham Viaduct obtained using DIC before (left) and after tamping (right) for a Javelin (a) and (b) and for a Eurostar (c) and (d) train types. Filmed at 300 fps and low-pass filtered at 40 Hz.. 200

Figure 9.30 Photographs of track on Rainham Viaduct (a) 1-day (b) 6 days (c) 6 months after tamping. 201

Figure 9.31 data from Figure 8.10 showing the effect of shimming and tamping on the track at Crissmill, (a) at the voided end and (b) at the well-perfomrning end of the sleeper 2.4 using Javelin data... 203

Figure 9.32 Data from the North Downs Tunnel defect site from Figure 8.18 and 8.13 showing improvements in track deflection and restoration of support conditions after targeted packing at sleeper 2.4_I for Javelin train passages.. 205

Figure 9.33 Photographs of retrofitting USPs to sleepers in situ................................ 206

Figure 9.34 Photographs of installing new sleepers with USPs. 207

Figure 9.35 Vertical track geometry from the TRC the Crissmill defect site after installation of the USPs.. 208

Declaration of Authorship

I, DAVID ROBERT MICHAEL MILNE

declare that this thesis and the work presented in it are my own and has been generated by me as the result of my own original research.

ENHANCED PERFOMANCE MONITORING OF A BALLASTED HIGH-SPEED RAILWAY

I confirm that:

1. This work was done wholly or mainly while in candidature for a research degree at this University;
2. No part of this thesis has previously been submitted for a degree or any other qualification at this University or any other institution.
3. Where I have consulted the published work of others, this is always clearly attributed;
4. Where I have quoted from the work of others, the source is always given. With the exception of such quotations, this thesis is entirely my own work;
5. I have acknowledged all main sources of help;
6. Where the thesis is based on work done by myself jointly with others, I have made clear exactly what was done by others and what I have contributed myself;
7. Parts of this work have been published as:
   Journals
   Le Pen, L., Milne, D., Thompson, D. & Powrie, W. (2016) Evaluating railway track support stiffness from trackside measurements in the absence of wheel load data. *Canadian Geotechnical Journal* 53(7):1156-1166.
   Milne, D. R. M., Le Pen, L. M., Thompson, D. J. & Powrie, W. (2017) Properties of train load frequencies and their applications. *Journal of Sound and Vibration* 397:123-140.
   Milne, D., Le Pen, L., Thompson, D. J. & Powrie, W. (2016) Measurement of ballast grain acceleration at track level. *The Journal of the Permanent Way Institution* 134(4).

Soper, D., Baker, C., Jackson, A., Milne, D. R., Le Pen, L., Watson, G. & Powrie, W. (2017) Full scale measurements of train underbody flows and track forces. *Journal of Wind Engineering and Industrial Aerodynamics* 169:251-264.

Conferences

Baker, C., Soper, D., Flynn, D., Jackson, A., Powrie, W., Milne, D., Le Pen, L., Zhou, J. & Hu, Z. (2017) Ballast flight under high-speed trains – aerodynamic and geotechnical studies In *Proceedings of The Stephenson Conference 2017.* Institution of Mechanical Engineers.

Milne, D., Le Pen, L., Watson, G., Thompson, D., Powrie, W., Hayward, M. & Morley, S. (2016) Proving MEMS Technologies for Smarter Railway Infrastructure. *Procedia Engineering* 143:1077-1084.

Milne, D., Pen, L. M. L., Watson, G., Thompson, D. J., Powrie, W., Hayward, M. & Morley, S. (2016) Measuring Acceleration of Ballast Particles at Track Level. *Proceedings of The Third International Conference on Railway Technology: Research, Development and Maintenance* (Pombo, J. (ed)). Civil-Comp Press.

Milne, D., Le Pen, L. M., Watson, G. V. R., Powrie, W., Thompson, D. J., Morley, S. & Hayward, M. (2015) Bridge and ballast interaction at a viaduct structural expansion joint on a high-speed rail way. *XVI European Conference on Soil Mechanics and Geotechnical Engineering*. Edinburgh.

Signed: ....

Date: ....

Acknowledgements

I am grateful for the support, encouragement and opportunities given by my supervisors Professor William Powrie, Professor David Thompson and Dr Louis Le Pen. I appreciate the extent that I have been challenged, had freedom to be creative and direct my work, and been exposed to influential and intelligent people over the course of this research. I also appreciate their considerable efforts raising the quality of my research outputs.

I am grateful for the project support by Simon Morley, Mick Hayward and their colleagues from Network Rail High Speed. I give particular thanks to Mick, whose exceptional attitude and efforts towards this research have been of considerable benefit and key to success. It has been very rewarding to see the context and direct benefits of the research from the outset.

I acknowledge financial support from the Engineering and Physical Sciences Research Council in funding my studentship through the Industry Doctoral Training centre in Transport and the Environment and supporting other research activities I have become involved with through the project grant “Track systems for high-speed railways: getting it right” and the programme grant “Track to the future”.

I have benefitted from the collegiality of staff and students at the University of Southampton and research partners at other Institutions and in Industry. I am thankful for the direct assistance, creative thinking and new perspectives gained through these interactions. Special thanks to Geoff Watson for assisting with digital image correlation, sharing photographs, providing intelligent and insightful comments that have improved this work and Rod Anderson for giving kind help and support through out the research.

Finally, thanks to my friends and my family, particularly Georgie, Clare, Michael and Helen who have always listened encouraged and enabled me to pursue what I find interesting, such that studying for a doctorate was enjoyable and achievable.

Definitions, Abbreviations, Symbols and Conventions

This section provides definitions for technical and railway related terms (see Ellis (2014) for an exhaustive list), abbreviations, a list of symbols and conventions used for figures in this research.

Definitions

At-rest position – unloaded level of the track

Ballast – crushed rock aggregate used to support the track superstructure

Bridge deck – part of a bridge structure that acts as a single beam

Bridge span – unsupported length between two supports

Characteristic deflection – typical range of movement under a train

  Total – entire range of track movement under a train

  Downward – range of track movement below the at-rest position

  Uplift – range of track movement above the at-rest position

Cess – the area running along the side of a railway track (see Fig. a)

Deterioration – worsening of the condition or performance of the track

Defect zone- a section of track affected by a defect

Differential settlement – a consequence of settlement occurring at different rates

Down – direction of travel away from a major destination, for HS1 this means away from London.

Formation – the natural soils or rocks beneath the engineering layers that make up the track substructure

Four-foot – the area in between the two running rails of a railway track (see Fig. a)

Isolated defect – an unacceptable localised deviation in track geometry

Line and level – the mean vertical and horizontal position of the track over a given length

Track alignment – the plan position of the track

Track bed – the engineered layers below the track superstructure

Track defect/fault – a deviation in track geometry from design

Track deflection – recoverable elastic deformation of the track

Track gauge – Distance between the running rails.

Track geometry – the horizontal and vertical alignment and cross level of the track

Track geometry measurements – measurable parameters used to assess the track geometry

Track stiffness – the supporting force for a unit vertical deflection at the rail

Track substructure – the layers below the track superstructure

Track superstructure – the mechanical system consisting or rails, pads and fastenings and the sleepers.

Track system modulus – the supporting force per unit length for unit deflection at the rail

Track quality – an assessment of track quality based on track geometry measurements over a specified length

Transducer – a device that converts one type of energy to another. Sensors are transducers that convert physical signals into electrical ones

Transient – region in a track vibration signal associated with a change in state of the system. i.e. the change from track being unloaded to being loaded by a passing train

Six-foot – the area in between two tracks on a double track railway (see Fig. a)

Stationary region – region in a track vibration signal due to a passing train that has the characteristics of a stationary process.

Voided/Voiding – gaps between the bottom of the sleeper and the ballast

Under-track crossing – a structure designed to carry services (e.g. signalling cables) underneath a railway track.

Up – direction of travel towards a major destination, for HS1 means towards London.

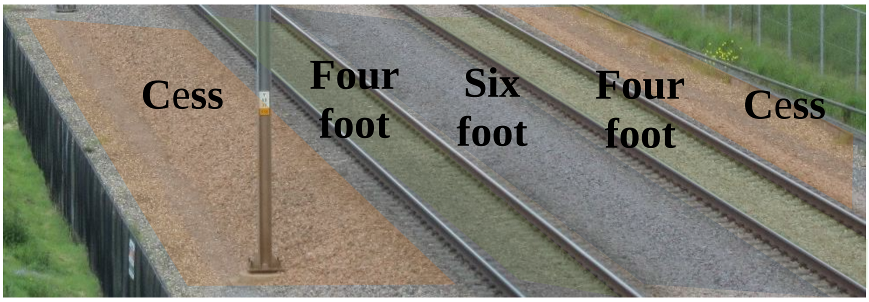

Fig. a Indication of track areas.

Abbreviations

ADC – Analogue to digital convertor

BOEF – Beam on an elastic foundation

CDF – Cumulative distribution function

DIC – Digital image correlation

HS1 – High Speed One

LGV – Lignes à Grande Vitesse (French high-speed railway line)

MEMS – Micro electrical-mechanical systems

NRHS – Network Rail High Speed

S&C – Switches and crossings

SNR – Signal-to-noise ratio

TGV – Train à Grande Vitesse (French high-speed train)

TRC – Track Recording Car

UIC - Union Internationale des Chemins de fer (International Union of Railways)

UTX – Under-track crossing

USP – Under sleeper pad

Symbols

Variables

E – Young’s modulus

I – second moment of area, current

L – characteristic Length

L_b – spacing of bogie centres within a vehicle

L_c – coupling length between trains

L_d – length of bridge deck

L_s – length of bridge span

L_t – length of train

L_{te} – equivalent train length

L_v – vehicle Length

L_{ve} – equivalent vehicle length

L_w – spacing of axle centres within a bogie

N – non-dimensionalised frequency $f/f`_1$

N_c – number of vehicles in a train

P– wheel load, probability

Q– wheel load,

R -resistance

V - voltage

d – depth of bridge deck

f – frequency

f_1 – vehicle-passing frequency

f_n – n^{th} multiple of the vehicle-passing frequency

g – gravitational acceleration

i – imaginary unit $\sqrt{-1}$

k – track system support modulus

k_p – rail pad modulus

k_t – track bed modulus

w – general elastic deflection of the track

w_m – measured deflection

w_o – downward deflection beneath a single wheel load

w_r – at-rest position

w_s – characteristic downward system deflection

w_t – characteristic downward sleeper deflection

x – position along the track

x_j – width of structural expansion joint

x_n – wheel position

s – system spring stiffness

s_p – rail pad spring stiffness

s_t – track bed stiffness

v – train speed

t – time

t_b – thickness of the ballast layer

t_t – train passing time

ΔL_d – thermal movement

ΔT – temperature change

α – coefficient of thermal expansion, coefficient of thermal resistivity

δ – differential movement

ρ – ballast settlement

θ – rotation

μ – Poisson ratio

Functions

$D(f)$ – Fourier transform for the solution of the beam-on-elastic-foundation model for a single unit moving load

$F(f)$ - Fourier transform for a sequence of wheel loads from a train

$W(f)$ – Fourier transform for track deflection

$W(N)$ – magnitude of the Fourier transform at a multiple of the vehicle-passing frequency

U_N – Fourier series coefficients

$c(w)$ – cumulative distribution function for track deflection

$d(t)$ – the solution of the beam-on-elastic-foundation for a single unit moving load

$f(t)$ – a sequence of wheel loads from a train

$w(x)$, $w(t)$, $w(x, t)$ – track deflection in space, time or both

$x(w)$ – inverse function for track deflection

$\delta(t)$ - Dirac delta function

Conventions

Instrument locations and numbering

Instrument diagrams are given so that the direction of travel is from left to right across the page. On HS1 this perspective corresponds to the layout of the site if viewed from the centre of the track in the six-foot looking towards the cess.

Instrument numbering is given using its distance from the first sensor or another significant location within the deployment (assuming a standard sleeper spacing of 0.6 m) and whether it is placed on the cess side or the six-foot side is denoted using a subscript of either O or I respectively. e.g. 1.2_O would denote a sensor 1.2 m away from the first sensor (or a significant location within the site) on the cess rail as shown in Fig. b.

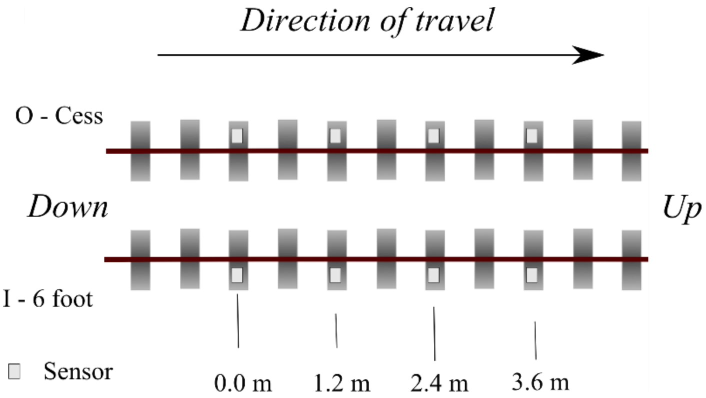

Fig. b Transducer diagram convention.

Photographs

Unless otherwise credited (generally Watson (2016)), all photographs were taken by the Author.

Chapter 1: Introduction

1.1 Motivation

The number of high-speed rail systems has been steadily increasing in recent years and this is expected to continue. There is around 41000 km of operational high-speed railway track worldwide (with a permitted speed of 200 km/h or more). About 9000 km of this is in Europe, where another 3000 km has been planned or under construction and a further 10000 km is expected, nearly all of the rest is in Asia (predominantly China) (International Union of Railways, 2017). Railway track is designed to provide a stable platform for the running of trains and to transmit the loads imparted by trains to the ground. Both slab and ballasted trackforms are used for high speed railways. This research is concerned with ballasted track, which is used for most of High Speed One (HS1) (currently the only high-speed line with a permitted speed in excess of 200 km/h in the United Kingdom) and many other existing high-speed lines, as well as being the predominant trackform for conventional railways worldwide.

All railway tracks deteriorate to some extent as they are trafficked by passing trains. On ballasted track one way that deterioration manifests itself is as settlement of the ballast and other trackbed layers. Often, rates of settlement are variable, which can lead to differential settlement and the development of irregular track geometry. This means that maintenance may be required to ensure the correct geometry for the safe running of trains. Maintenance costs make up a large proportion of railway expenditure. For example, maintenance and renewals were responsible for about 20% of Network Rail’s £6.3 billion of expenditure in both 2014-15 and 2015-16 (Office of Rail and Road, 2017) and track maintenance costs alone were expected to be about 5-6% of the £40 million annual operating and maintenance costs for HS1 between 2013 and 2018 (HS1 Ltd, 2013), even though this is a relatively new piece of infrastructure.

Certain locations can experience accelerated rates of deterioration leading to isolated faults or defects. These are defined in the rail industry as a deviation in the track geometry beyond an acceptable threshold (this is also how they are identified from track geometry measurements). Defect zones are characterised by poor geometry and support conditions; voids forming between the sleepers and the track bed; excessive deflection; damage to the track superstructure; and abrasion, attrition and breakage of the ballast. Examples of this are shown in Figure 1.1. Track defects require additional and unplanned maintenance, often at short notice. They reduce the lifespan of the affected section of track, can exacerbate adverse loading conditions and often reoccur, with common maintenance practice sometimes proving ineffective. Understanding why track defects form and how performance is affected by them can inform maintenance and design, helping to minimise the impact and occurrence of track defects.

Figure 1.1(a) Visible track defect; (b) ballast abrasion; (c) damage to sleepers and ballast.

Research into accelerated deterioration of track defects has used both modelling and field studies to investigate the causes of the defects. Many of these studies were motivated by an association between track defects and physical features on railway lines, for example, at transitions where the trackform or support conditions change. Field studies often involve lineside monitoring in which transducers are installed by the side of the track, on the track or into the track bed. These are used to make measurements of how the track behaves as trains pass, although such measurements are rarely made for extended periods.

In principle, lineside monitoring techniques could be used for extended periods enabling continuous condition and performance monitoring of railway track, particularly in maintenance-critical zones. The capability to quantify performance continuously would provide information to manage the impact of recurring defects on operations, through targeting maintenance interventions. Data generated could provide timely feedback to justify future maintenance strategies and enable a data-rich approach to analyse how the track deteriorates and how defects form.

1.2 Aims and objectives

Motivated by the need to understand and manage the impact of accelerated deterioration the aim of this research is: *to improve lineside measurement systems and apply them to investigate, diagnose and evaluate remediation associated with performance issues on a ballasted high-speed railway line*. To meet the aim of the research two sets of objectives are established.

Improve lineside measurements systems:

- understand aspects of track behaviour relevant to studying performance issues;
- review monitoring technologies, analysis techniques and applications;
- develop requirements of a monitoring system for studying performance issues;
- validate alternative transducers for lineside monitoring;
- develop analysis techniques to deliver that system.

Apply the systems to investigate, diagnose and evaluate track performance:

- identify suitable trial sites, with support from Network Rail High Speed (NRHS);
- apply monitoring system to study performance at various study sites on HS1;
- analyse and report on effectiveness of monitoring;
- evaluate maintenance interventions;
- provide insights into performance within defect zones.

1.3 Outline

The thesis has the following structure:

- Chapter 2 reviews aspects of railway track behaviour relevant to monitoring the performance of the track. It introduces the different measures and techniques used to quantify the condition, behaviour and properties of the track and discusses how these approaches have been used to study performance issues. It draws on the limitations of current technologies and previous applications identified to develop the requirements for a system to be used to study track performance issues.

- Chapter 3 describes the background to HS1, supplies relevant supplementary data sources used for the research and introduces the various test sites studied.
- Chapter 4 describes the validation of low-cost micro electro-mechanical systems (MEMS) accelerometers for lineside monitoring. The affordability and robustness of these sensors means that condition monitoring for extended periods becomes a realistic proposition.
- Chapter 5 explores and exploits the frequency domain properties of a beam on an elastic foundation model. These are used to develop methods to interpret the large volumes of track vibration data that would be generated by extended deployment of lineside monitoring systems.
- Chapter 6 develops methods for characterising the range of total and downward track deflection using the cumulative distribution function for track deflection.
- Chapter 7 develops a method for obtaining measure of the track stiffness using the properties of the spectrum for track vibration at low frequency.
- Chapter 8 tests the methods developed in Chapters 6 and 7 using data from a well-performing study site and presents results from the application of the monitoring system developed in Chapter 4, using the analysis methods from Chapters 5, 6 and 7 to study performance at the fault sites described in Chapter 3.
- Chapter 9 discusses the lessons learnt from the application of lineside monitoring to diagnose and explain performance issues, evaluate remediation and study various aspects of poor performance encountered during the research.
- Chapter 10 presents the main conclusions reflecting on the validation and usage of low-cost sensors, the effectiveness and validity of the data interpretation tools developed and applied during the research and the insights into performance and maintenance gained during the research. It also gives recommendations for future research.

Four appendices are included, three of which cover research which was outside the main scope of this thesis:

- Appendix A includes descriptions of the matlab code used for analysis that accompanying this research.
- Appendix B provides a method of identifying possible track defects from track geometry recordings.
- Appendix C details development and analysis of results from an instrumented ballast grain used for measuring acceleration of the ballast bed and investigating ballast flight.
- Appendix D lists the requirements of a model useful for studying progressive deterioration and the formation of track defects.

1.4 Industrial support

This research was supported by Network Rail High Speed (NRHS), the infrastructure manager and maintainer for the HS1 railway line in South East England, which links London to the Channel Tunnel and then on to continental Europe. They have provided the opportunity to trial new lineside monitoring techniques by studying performance issues on an operational high-speed railway. This research is useful for directly informing, evaluating and improving maintenance practices.

NRHS support to this research included sharing and supplying background data for the project including:

- track geometry data obtained using the Track Recording Car (TRC),
- details of the trackform, track components and structures,
- details about the train types operated on the railway,
- train weights from their weighing-in-motion system,

as well as direct involvement with the lineside monitoring,

- identifying and providing track access to the study sites,
- procuring, installing and collecting data from many of the monitoring systems developed and deployed during this research for near continuous monitoring,

- planning and carrying out maintenance.

1.5 Original contributions

A number of original contributions have been made during this research.

- Low-cost sensors have been validated for long-term lineside monitoring applications on a high-speed railway. The same technology has enabled innovative methods to be developed for studying ballast vibration.
- Improved understanding has been obtained of the sensitivity of the frequency and magnitude of the dominant train load frequencies to train and vehicle geometry as well as variations in the wheel load.
- New analysis techniques have been developed for characterising the typical range total and downward deflection caused by a passing train, and a method has been produced for obtaining the track system support modulus in frequency domain. The methods can be automated to allow interpretation of large volumes of track vibration data.
- The low-cost sensors and new analysis methods have enabled a long-term and data-rich approach to the field studies. This has allowed an intuitive approach to be adopted for identifying processes that may influence deterioration within a defect zone as well as planning and evaluating maintenance, which has led to improved practices on HS1.

Chapter 2: Literature review

To study the performance of railway track it is necessary to understand how the track is expected to behave, the different options available for quantifying that behaviour and how they can and have been used. This section reviews relevant aspects of track behaviour; lineside monitoring systems, analysis techniques and previous applications and approaches to studying deterioration; and maintenance practice.

2.1 Track behaviour

Ballasted railway track is a layered system, which may be thought of in terms of the track superstructure and the track bed or substructure (Selig and Waters, 1994; Esveld, 2001; Aursudkij et al., 2009). In a high-speed rail system, the superstructure will comprise a pair of running rails, fastened using rail clips and resilient pads to the sleepers (or bearers). The sleepers are usually concrete and may be a mono-block or duo-block joined by a crossbar (as used on HS1). On occasion, under sleeper pads (USP) are fitted to the bottom of the sleeper. The track bed layers are the ballast, sub-ballast and a prepared subgrade, which overlies any embankment material or the natural soil. Ballasted track is also used over bridges and inside tunnels on HS1. A typical cross-section for HS1 is given in Figure 2.1.

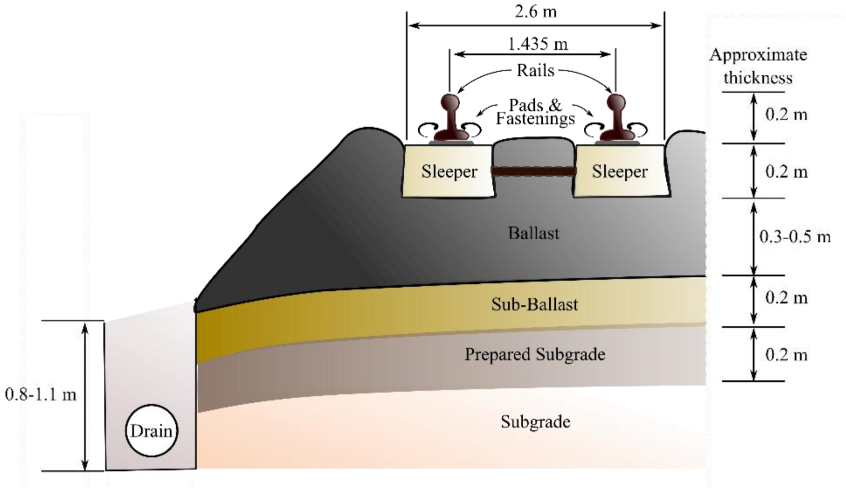

Figure 2.1 Sketch of typical ballasted trackform for a ballasted high-speed railway, such as HS1.

The performance of railway track as it is trafficked by passing trains needs to be considered on two timescales. In the short term, a single train passage, often of only a few seconds for high-speed rail, the track behaviour is predominantly elastic and depends on the current track geometry, support conditions and the train geometry and loading. The settlement or plastic deformation of the track is a very small fraction of the elastic deflection but is more significant for the long-term performance of the track (Shenton, 1984). The long and short-term behaviour are interrelated, as under most circumstances track settlement is made up of the accumulated plastic effects from the passage of many trains. This may change the track geometry and support conditions, thereby affecting the instantaneous behaviour of the track.

2.1.1 Track vibration

When a train runs along the track it will cause vibration, noise and deflections of the track. The response is governed by the properties of the track system (track geometry and support conditions) and the interaction with passing trains. Different mechanisms are responsible for the various aspects of track behaviour (Thompson, 2009). The significance of these mechanisms is frequency-dependent (Knothe and Grassie, 1993). Quasi-static loading and dynamic excitation are responsible for track vibration. The quasi-static contribution is caused by the weight of the train transferred through the suspension system to the track through each wheel, moving at a steady speed. On straight track, the axle loads are split evenly between the wheels. During curving, a train will experience a centripetal force, although super-elevation or cant allows the normal reaction at the rail to resist these forces, and there will be a difference in the load applied by each wheel at either end of an axle (Iwnicki, 2006), which depends on the cant deficiency.

The train and vehicle geometry control the pattern of deflection from the quasi-static loads, and hence the spectrum for track vibration at low frequency. This has a distinct shape in which certain peak frequencies are prominent. Several authors have identified that these peaks occur at multiples of the vehicle-passing frequency f_1,

$$f_1 = \frac{v}{L_v} \tag{2.1}$$

where L_v is the length of the vehicle. These have previously been termed ‘train load dominant frequencies’ (Auersch, 2005; Ju et al., 2009; Kouroussis et al., 2014; Bian et al., 2015; Gatti et al., 2016; Le Pen et al., 2016). Auersch (2006) showed that high and low amplitude regions of the spectra are characterised by the axle spacing of a vehicle bogie. Ju et al. (2009) showed that the dominant peaks are caused by the repeated loading from vehicles within a train.

Dynamic excitation arises from track and wheel unevenness and impact at discontinuities at the wheel/rail interface. Models and measurements by Sheng et al. (2003; 2004) showed that the steady quasi-static loading is the most significant mechanism for low frequency track vibration, whereas dynamic excitation from other mechanisms is usually more significant at higher frequencies above about 20 Hz. Studies by Lombaert et al. (2006), Auersch (2006), Triepaischajonsak et al. (2011) and Alves Costa et al. (2012) confirm the differing importance of these mechanisms with varying frequency. As the time lag between each load, for both the quasi-static and dynamic contributions, is governed by the axle spacing within the train, the modulation of the low frequency spectrum is the same for both dynamic and quasi-static loading (Ju et al., 2010; Lombaert et al., 2015).

The frequency dependence of track vibration means that certain mechanisms can be neglected when looking at particular aspects of railway track behaviour. For example if track deflections are the primary interest, a simple quasi-static model will describe the expected fundemental behaviour at low frequency. A static model of a beam-on-an-elastic-foundation (BOEF), in which inertial effects are neglected, is commonly used to represent the deflection of railway track at the rail (Timoshenko and Langer, 1932; Hetényi, 1946). More detailed beam formulations (e.g. Timoshenko beam (Weaver et al., 1990; Graff, 2012)) can be used to include shear deformation and rotational inertia for accuracy at higher frequencies for rail vibration. More complicated foundation models (e.g. Pasternak or other two parameter models (Kerr, 1964)) can be included to account for the effect of shear interaction on vertical planes in the foundation. The equation of motion can be formulated in the time domain subject to a moving load, rather than transforming from the static problem, allowing the mass and damping of the beam to be included (Frýba, 1972), and hence inertial effects to be accounted for. More detailed beam formulations or foundation models may be needed for improved accuracy at high frequency.

However, as models become more complex, determining the interaction between the track and train becomes increasingly involved. Numerical methods provide an alternative approach (Yang et al., 2009; Shih et al., 2017). Although more sophisticated models potentially allow for more physically representative behaviour, simple analytical models are vital for understanding the fundamentals of the process and provide an effective means and useful starting point for data interpretation and analysis of lineside measurements.

2.1.2 Train loads

A train moving along railway track will load and dynamically excite the track. These loads are transferred at the wheel-rail interface. Although it may be acceptable to treat the track behaviour as static, the total vertical load applied to the track has a quasi-static and a dynamic component. The dynamic component is frequency dependant. At low frequency, the reaction of the vehicle to the track geometry is most significant. The vehicle dynamics, longer wavelength track geometry irregularities and changes in alignment govern the applied loads (Iwnicki, 2006). Vehicle dynamics packages such as VAMPIRE or MSC RAIL are often used to compute these loads where rail geometry data is available. At higher frequencies, the dynamic contribution arises from impact loads and excitation of vehicle components from unevenness at the wheel/rail interface (Thompson, 2009). Above a few Hertz, vehicle suspension systems are designed to isolate the mass of the bogie and vehicle body from the track. Hence the un-sprung mass of the wheel and axle equipment is most significant for dynamic loads above 10-20 Hz (Knothe and Grassie, 1993). The dynamic excitation may be affected by unevenness of the running rail or wheel profile and the operational speed. Both low (<20 Hz) and medium frequency (20-90 Hz) loads are transferred through the track superstructure into the supporting layers and can influence deterioration (Jenkins et al., 1974). Higher frequency effects are responsible for noise from the wheel and the rail; the rail pad isolates this frequency content from the ground above about 300 Hz.

The applied load will vary along the track. This is can be seen by the variation in data from both instrumented wheelsets (Bezin et al., 2016) and weighing-in-motion systems (see Chapter 3). Given the uncertainty in the applied load, static loads are often amplified by a “dynamic amplification factor” for design purposes. Van Dyk et al. (2017) give a summary of different equations used to “amplify” the static loads. Generally, these types of equations account for track geometry/quality, line speed and some aspects of the vehicle/wheelset behaviour. If the exact applied load at a particular location is of interest, it is more appropriate to measure it or calculate it using a vehicle dynamics package.

2.1.3 Track stiffness

Different measures of track stiffness are useful for assessing the track system properties (Track Stiffness Working Group, 2016). The elastic deflection of the track, and hence how loads are distributed along the track, depends on this property. The simplest definition of track stiffness is the load required to produce a unit deflection of the rail:

$$s = \frac{F}{w} \qquad (2.2)$$

Another common measure is the track system support modulus, which is used in the BOEF model (Hetényi, 1946). This defines the supporting force per unit length of rail for a unit deflection. This is related to the track stiffness by:

$$k = \sqrt[3]{\frac{s^4}{64EI}} \qquad (2.3)$$

Where E is the young’s modulus and I is the second moment of area for the rail section.

Railway track is a layered system (Figure 2.1). Each resilient layer contributes to the track system support modulus as a spring in series. For example, assuming that the sleeper is rigid, the system modulus can be treated in terms of the moduli of the rail pad k_t and of the track bed k_p:

$$\frac{1}{k} = \frac{1}{k_p} + \frac{1}{k_t} \qquad (2.4)$$

The track system support modulus is an important parameter for the behaviour of the track system. It controls how the loads are spread along the track, the peak deflection and the width of the “deflection bowl” beneath each load. Stiffer track deflects less and concentrates the load over a shorter length of track, whereas softer track deflects more and will spread the load over a longer length of track. For nearby wheels (e.g. on a train bogie) the increasing width of the deflection bowl on softer track leads to more interaction and reduced recovery between adjacent wheels (Track Stiffness Working Group, 2016).

2.1.4 Plastic track behaviour

Settlement is a consequence of accumulated plastic strain. Under most circumstances it is caused by passing trains. However, track behaviour caused by a single train is predominantly elastic and under a single cycle plastic effects are almost imperceptible (Abadi et al., 2016). This can make it challenging to reconcile, and provide evidence for, these two aspects of track performance.

In the absence of maintenance, differential settlement leads to changes in the track geometry and support conditions. This changes the interaction between track and train, hence the applied loads on the track. Rates of settlement depend on the plastic behaviour of the trackbed, the applied loads (which depend on the vehicle), the track geometry (including unevenness of and faults in the rail), the support conditions and any external processes that affect the track.

Many authors have developed settlement equations that model the rate of settlement of the track. A comprehensive review is given by Dahlberg (2001). It is generally accepted that settlement has two phases: rapid consolidation after maintenance, then slower more linear settlement. The second phase involves a variety of different mechanisms; these may include further consolidation and inelastic recovery of the ballast by rearrangement of the grains, volume reduction from grain abrasion and breakage and movement of grains away from the track either by penetrating into the subgrade or lateral spread.

Settlement equations can be used to approximate the effects of permanent deformation. Most of these equations use empirically determined parameters to relate accumulated strain or permanent settlement to the number of loading cycles. Although individual formulations rely on different parameters, there are two general forms prevalent in the literature. The first relates the permanent strain or settlement to the strain from the initial cycle using the logarithm of the number of cycles, e.g. Alva-Hurtado and Selig (1981). The second uses a power law for the initial phase of settlement and a linear relationship for the second phase, on the basis that a logarithmic relationship can significantly underestimate settlement (Shenton, 1984; Sato, 1995; Guerin, 1996). If properly calibrated, these equations may adequately forecast the average lifespan of the track between maintenance intervals. However, such equations do not account for the underlying mechanisms, the variation in track properties or applied loading along the track that are involved in causing differential settlement. Thus, to understand differential settlement it is important to obtain an understanding of how the track system properties and applied loads vary along the track and the consequences of this over time.

Although not always directly accounted for in settlement equations, differential settlement will also depend on the properties and behaviour of the track bed materials under cyclic loading, particularly of the ballast. Ballast settlement can occur due to compaction and degradation of individual particles by crushing. This can result in a more compactable and less uniform particle size distribution, as observed by Indraratna et al. (1998) and Aursudkij et al. (2009). The stress state will affect whether the volumetric behaviour is compressive or dilative, the peak strength, the dynamic response and mode of ballast degradation. Laboratory testing has demonstrated that both the volumetric behaviour and the way in which ballast particles degrade depend strongly on the degree of confinement of the ballast (Indraratna et al., 1998; Indraratna et al., 2005; Lackenby et al., 2007). Analysis of the peak angle of shearing resistance from literature and scaled ballast tests reported by Le Pen et al. (2014a) suggests this property is common to all ballast. Appropriate numerical modelling of cyclic behaviour of ballast grains is still subject to significant research (Lu and McDowell, 2010; Harkness et al., 2016; McDowell and Li, 2016). Deterioration of performance within defect zones may be influenced by other processes including ballast migration (bulk movement of material) (Priest et al., 2012).

2.1.5 Voiding and nonlinearity

The load deflection behaviour of a railway track is not necessarily linear. Non-linearity can be *geometric* or *material*, where changes in system properties arise from changes to its geometry or derive from the properties of the material.

Gaps can be present (from installation) or may develop between the ballast surface and the bottom of a sleeper, leading to a voided or partially supported sleeper (often known as a 'hanging' sleeper); this is one example of non-linear track support. Sussman et al. (2001) suggested deflection behaviour can be represented using a bi-linear relationship, (Figure 2.2), where the sleeper first seats and then the ballast deforms elastically. This means that the behaviour of a void could be considered to be geometrically non-linear. Track bed materials will also exhibit non-linear behaviour (Brown, 1996).

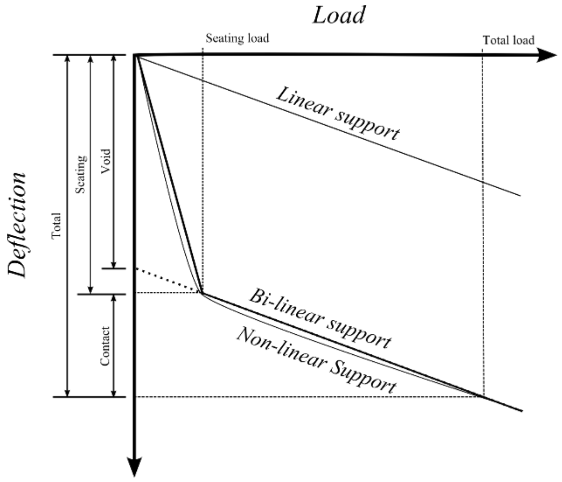

Figure 2.2 Example of bi/non-linear load deflection behaviour expected from a sleeper with a void gap. After Sussman et al. (2001).

Various authors have considered the effect of a void on track vibration and the wheel-rail contact force using numerical models (Grassie and Cox, 1985; Lundqvist and Dahlberg, 2005; Bezin et al., 2009; Yang et al., 2009; Baeza and Ouyang, 2011). These have shown that the presence of a void can increase the wheel-rail contact force and change the distribution of stresses in the region surrounding the void. This means that the presence of a voided sleeper may exacerbate loading, change the rate of deterioration, or lead to an enlarged defect zone.

Material non-linearity may lead to different behaviour for heavier and faster trains and may be important for explaining certain phenomena observed in monitoring data. Lopez-Caballero et al. (2016) found evidence for material non-linearity using buried instrumentation. Accounting for nonlinearity is also important for accurately modelling the magnitudes track deflection and stresses in the ground under passing trains (Shih et al., 2017).

2.2 Quantifying track performance

Assessing and quantifying the performance and properties of railway track is necessary for maintenance and research. There are a variety of different approaches for this. These include local geometry measurements and rolling measurements from instrumented vehicles and trackside measurements using transducers installed on the track superstructure or in the track bed. The purpose of these measurements is to obtain measurements of deviations in track geometry, track vibration and track stiffness. Together these parameters can be used to assess the condition, performance and system properties of the track.

2.2.1 Track geometry measurements

Track geometry measurements are the primary quantitative method used by maintainers to assess track quality, identify isolated defects and plan maintenance. Absolute geometry is very challenging to measure, and requires a survey which is time consuming and requires significant amounts of track access, so geometry parameters are used instead. Commonly measured track geometry parameters, from the European standard EN 13848 (British Standards Institution, 2014) are summarised in Table 2.1. These are normally measured using a vehicle or locally with specialist equipment. The parameters are based on the relative position of the two rails or the deviation from the mean line and level.

Table 2.1 Track geometry parameters.

Parameter	Description
Gauge	The distance between the inside faces of the rail.
Cross Level or Cant	The difference in height between two adjacent running rails.
Longitudinal Level	The deviation in level of the surface of a loaded running rail from the mean vertical position over a 35 m or 70 m length of track.
Horizontal Alignment	The deviation in horizontal position from the mean horizontal position over a 35 m or 70 m length of track.
Twist	The difference between two cross level measurements at a specified distance apart (often 3 m).
Curvature	The rate of turn in the horizontal plane.

Track quality is quantified in the UK as the standard deviation of a geometry measurement over a 1/8th mile length of track. Isolated defects are identified as an unacceptable level in a given geometry measurement. Both the track quality and the hazard from defects are assessed using absolute thresholds for acceptable track quality or local changes in geometry for the corresponding class of track, given in the relevant standards, e.g. GCRT5021 for Network Rail Infrastructure (Rail Safety and Standards Board, 2011). Different thresholds mandate different actions or interventions to improve track quality of remove a defect.

2.2.2 Dedicated measurements

Specialist railway equipment can be used to obtain localised track geometry and stiffness measurements. Gauge bars can be used to obtain the cross level and check the gauge. Sighting boards can be used to measure the rail level. Void meters, Figure 2.3, record the maximum difference between the deflection of the rail and the ballast bed, and thus should indicate the depth of the void and rail movement (Permanent Way Institution, 2001).

Figure 2.3 Examples of void meters installed on the track.

2.2.3 Train borne measurements

In the United Kingdom, rolling measurements are predominantly used to measure deviations in the line and level. At present, dedicated measurement trainsets are used, where track geometry measurements are made alongside a suite of other measurements needed for track inspection and other purposes.

Current dedicated track recording vehicles typically use a combination of inertial (accelerometers and gyroscopes), displacement (linear variable displacement transducers) and optical transducers to measure the vertical alignment, the horizontal alignment and the gauge (Nielsen et al., 2013; British Standards Institution, 2014). The other parameters are derived from those measurements. Dedicated track recording vehicles operate at routine intervals, typically every four weeks on High Speed One, supplemented with track inspection. Weston et al. (2007; 2015) have shown that in-service vehicles can be equipped with inertial sensors to provide more frequent but a reduced selection of measurements.

2.3 Stiffness measurements

Often there is the desire to obtain continuous measurements of stiffness along a length of track. Different approaches and techniques have been proposed and demonstrated. Generally, these are either geometric, comparing loaded and unloaded geometries (which is challenging to measure from a vehicle), or looking at the slope of deflection around a wheel (Li et al., 2002). Alternatively, the displacement and forces acting on a wheelset loaded by a known vibrating mass can be measured using dedicated equipment

(Hosseingholian et al., 2011; Berggren et al., 2014). In Sweden, the latter approach has been used to develop dedicated equipment for rolling measurements of track stiffness.

Other techniques can be used to investigate the local track system support modulus or track bed stiffness. Site investigation using the Rail Trackform Stiffness Tester (Sharpe, 2000), which is based on the falling weight deflectometer (Brough et al., 2003) can be used to determine the track bed stiffness beneath an unclipped (hence fully supported) sleeper. The lightweight deflectometer can be used to investigate the load deflection behaviour, hence stiffness, of individual sleepers clipped to the rail or the substructure. Clearly there are disparities between the support conditions, loading magnitude and loading area associated with different techniques that need to be understood.

2.4 Lineside measurements

This section discusses different techniques for measuring the behaviour of railway tracks using sensors (or targets) attached the track. A variety of systems can be used to measure track vibration caused by passing trains. It is possible to measure displacement directly using digital image correlation, laser systems or deflectometers. Geophones are used for velocity and accelerometers for acceleration. Measurements can be processed, interpreted and analysed in different ways to obtain measures of track performance and its properties.

2.4.1 Velocity and acceleration

Displacements can be obtained from velocity or acceleration, by filtering and then integrating the signal once or twice respectively (Bowness et al., 2007). To understand the benefits and limitations of obtaining displacements from velocities or accelerations it is useful to consider the signals that are being measured in comparison to the desired output. Track deflection is dominated by lower frequencies. When the same signal is considered as either velocity or acceleration the higher frequency components become more significant. Differentiation can be performed in the frequency domain by multiplying by $i2\pi f$, where f is frequency and i is the imaginary unit. This means that the higher frequencies become more important with each derivative. This has a practical significance, particularly if measuring acceleration. The lowest frequencies, which are needed to obtain displacement, will be of low amplitude in an acceleration signal. This means they are more challenging to measure accurately and more susceptible to transducer noise. Furthermore, amplification of low frequency noise will be more significant with each integration, proportional to $1/f$ for velocity and $1/f^2$ for acceleration. This means that good quality displacement data will more likely be obtained using velocity measurements than acceleration.

2.4.1.1 Geophones

Geophones are high quality velocity transducers that are suited to measuring low frequency track vibration and obtaining track deflection. The low frequency geophones from ION SENSOR used for rail research at the University of Southampton cost around £500 per sensor. Geophones use a sprung magnetic mass to induce a voltage in a coil. Above the sensor's natural frequency, that voltage is proportional to velocity. The voltage can be sampled using a data acquisition system. A velocity signal obtained using a geophone can be filtered and integrated to obtain a deflection signal. The signal must be high-pass filtered to prevent low frequency drift and may be low-pass filtered to remove high frequency content that is not of interest. Geophones have a flat frequency response above their natural frequency (0.3 Hz and 1 Hz for the newer and older generations of sensors used at the University of Southampton). A frequency domain calibration can be applied to account for the phase shift at and around the natural frequency, as well as attenuation below this frequency. This can improve the usefulness of very low frequency data (< 1 Hz).

Figure 2.4 Photograph of a geophone on a sleeper end (Watson, 2016).

The construction of a geophone physically limits the range of the sensor. Under certain conditions, e.g. when excessive deflections are caused by high speed trains, sleeper velocities may approach the operational limit of the sensor and the signal may become non-linear or clipped. This means that a sensor with a larger operation range would be needed to make measurements within a severe defect zone on a high-speed railway.

2.4.1.2 Accelerometers

Accelerometers tend to be used for higher frequency applications, but they are less well suited to measuring the low amplitude low frequency components of track vibration needed to obtain track deflection. Different types of accelerometer are available, which operate using a variety of different principles. The most relevant types for lineside monitoring are piezo-electric and low-cost capacitive micro electro-mechanical systems (MEMS) accelerometers.

Piezo-electric accelerometers are more commonly used in research for high frequency applications such as rail vibration, although they have been used to obtain track deflections by Lamas-Lopez et al. (2014). As piezo-electric sensors are of similar cost to a geophone, there is no benefit in their use for track deflections.

Capacitive MEMS sensors have a much lower cost per transducer (£2-100) than either geophones or piezo-electric accelerometers. They are small, robust and could be embedded into track components. MEMS accelerometers are common in consumer electronics for shock, motion and inclination detection. The lower capital cost of MEMS accelerometers means that the business case for a larger or longer-term deployment may be more viable as the risk of damage to a sensor is more acceptable. However, the accuracy and reliability of MEMS sensors means that these sensors are less commonly used for vibration measurements in research. In previous studies benchmarking MEMS against piezo-electric accelerometers, it was found that the accuracy of the MEMS sensors tested was insufficient for vibration measurement (Thanagasundram and Schlindwein, 2006; Albarbar et al., 2009). However, these technologies are continually improving.

Generally geophones and accelerometers are installed on the track superstructure, although they have also been shown to be effective when installed at different depths within the track bed (Priest et al., 2010; Lopez-Caballero et al., 2016).

2.4.1.3 Filter choice

The frequency content of the displacement signal obtained from velocity or acceleration measurements depends on the filters used. A low-pass filter is used to remove higher frequency content not significant for the deflection and the cut-off frequency should be chosen accordingly. The high-pass cut-off frequency should be set high enough to prevent low frequency drift. However, it must also be set low enough to ensure information relevant for displacements is not removed. Figure 2.5 shows how the ratio of magnitudes of the filtered and the original signals depends on the choice of cut-off frequency of a digital high pass Butterworth filter for 4th, 5th and 7th order of filters (Oppenheim and Schafer, 1975). This suggests that the cut-off frequency for the high pass filter should be two thirds or less of the first frequency of interest. This ratio could be increased for higher order filters.

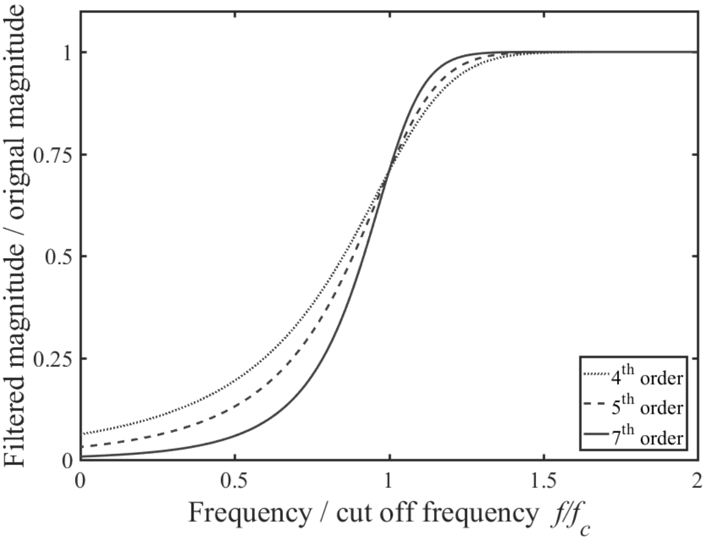

Figure 2.5 The ratio of magnitude of the filtered signal and the original signal at a particular frequency relative to the cut-off frequency of a digital high pass Butterworth filter.

2.4.2 Direct measurement of displacement

Direct measurements of displacement are desirable as there are fewer signal processing requirements, hence data will not be affected by artefacts from signal processing and filtering, unlike data from a velocity or acceleration signal. However, displacements must be measured relative to some fixed datum, which can be challenging to obtain in the lineside environment

2.4.2.1 High-speed video for digital image correlation

High-speed video recording of track-mounted targets (Figure 2.6) together with digital image correlation (DIC) is an effective method for obtaining track displacement (Bowness et al., 2007). Provided that a fixed frame of reference can be assumed, a cross correlation algorithm can be applied to compute pixel displacement between subsequent frames from the video (White et al., 2003). This approach has been refined and employed by Le Pen et al. (2014b) using a track-mounted target for calibration and more efficient processing. It may not be necessary to use a specific target (Murray et al., 2014). DIC has been shown to be effective where displacements are large and track deformations are much more significant than the effects of ground or airborne vibration on the camera, or where a correction for this can be made (Wheeler et al., 2016a). The non-contact nature of the system is attractive to infrastructure managers. However, the cost and labour requirements for the system in its present form make it more suitable for small focused investigations, e.g. for validating other measurements, or where other systems are not capable of providing suitable data. The resolution of the system is limited by the frame size, but the amount of deflection that can be measured is not restricted.

Figure 2.6 Photographs of (a) a high-speed camera and (b) calibration targets for digital image correlation, (Watson, 2016).

2.4.2.2 Laser Systems

Laser systems have been developed and used to measure track deflections (Alves Costa et al., 2012; Paixão et al., 2014; Kim, 2016). These involve directing a laser from a lineside position at position-sensitive devices installed on the track. These devices record the variation in laser beam position at high precision as a train passes. A fan of laser beams can be used to obtain data at multiple locations simultaneously. This approach still requires transducers to be placed on the track, and data transmission back from those transducers, and the stability of the laser beam may be sensitive to ground and airborne vibration.

2.4.2.3 Multi-depth deflectometers

Displacement transducers can be installed into the track to obtain track movements, accurately, relative to a fixed anchor point (Mishra et al., 2014; Stark and Wilk, 2015). Multiple transducers can be installed using a common anchor, allowing readings to be made at multiple levels. These have been used to study the deflection of different layers within the track system. Creating a fixed anchor point is invasive and will disturb the trackbed, possibly requiring time for the track to bed in. Thus, this type of instrumentation is more suited to research trials rather than monitoring to assess the current performance of existing infrastructure.

2.4.3 Comparison of lineside monitoring approaches

The objectives of a field study are likely to determine which monitoring technologies are most suitable. Each technology has its merits and limitations. For example, geophones and accelerometers can be readily installed onto the track superstructure (where track access permits this) without disturbing the trackbed. Many data acquisition systems lend themselves to larger or autonomous monitoring applications. Within this category, displacements obtained from geophones are likely to be higher quality than those obtained from accelerometer data, and are preferred as long as track movements do not exceed the operational range of the geophone. However, if suitable MEMS accelerometers become available that are significantly cheaper than geophones, they could become attractive allowing larger or long-term deployments to be used for condition monitoring.

Displacements obtained from velocity or acceleration contain artefacts from signal processing. In that respect, direct measurements of displacement are of benefit, providing more confidence in the at-rest position of the track for determining the proportion of upwards and downwards movement. However, direct measurements need a stable reference point, which can be challenging to obtain. Multi-depth deflectometers need to be anchored at depth. This means that their installation will disturb the trackbed. Although these sensors can give high precision data for settlement and deflection, their results can only give changes in performance from the state of the track left after system installation.

Optical systems need to be isolated from, or have a means of correcting for, ground and airborne vibration. Camera-based systems have the potential to be used without placing sensing elements on the track. This may eliminate the need for track access, provided that part of the track system can be used as a scale for calibration. Labour requirements and the need for transmission and storage of large image signals mean that large or long-term deployments are not yet feasible.

2.4.4 Interpretation of track vibration measurements

2.4.4.1 Track deflection

Measurements of track vibration (displacement, velocity or acceleration) provide data that describe how the track is moving. This can be used as a metric for performance and condition monitoring. More severe movements characterised by excessive deflection and large velocities or accelerations, are associated with poor performance or adverse loading conditions.

Computationally classifying the range of movement from a time-varying signal is a non-trivial problem. Artefacts arise from applying a high-pass filter to velocity and acceleration signals that lead to transients around the first and last bogies of the train and a shift in the level associated with the at-rest position. This increases the complexity of the operation and also makes it challenging to distinguish between the downward deflection into the track bed and any uplift. In most studies, this is determined by inspection. This process can be time-intensive if based on the experience of the person interpreting the data.

The regular pattern of displacement expected beneath a train makes it possible to judge the at-rest position in the result and to quantify the range of deflection. This is often called the ‘characteristic’ displacement and is intended to represent the typical range of total or downward movement. Figure 2.7 highlights the different artefacts that may affect a displacement time history obtained from velocity or acceleration measurements, and indicates an estimate of the ‘characteristic’ downward displacement. Reliable methods for interpreting track displacement data automatically using a computer would be necessary to enable long term use of these lineside monitoring techniques for condition monitoring.

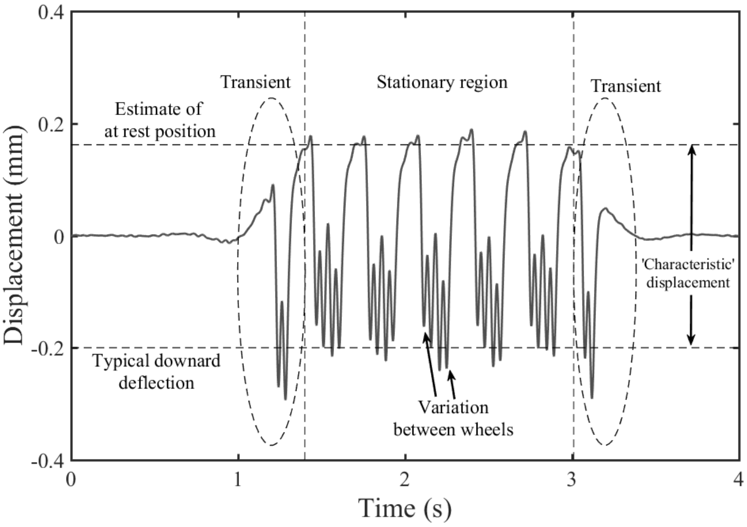

Figure 2.7 Example track displacement data obtained from geophone measurements, showing start up transients, the shift in the at-rest position for the stationary region and variability between wheels. Estimates of the rest position and typical downwards deflection are indicated.

2.4.4.2 Track stiffness

Measures of track stiffness such as the track system support modulus can be used to investigate the properties of track. This is related to the likely performance of the track. Very high, very low, highly variable or rapid changes in the support condition can all influence performance. Understanding this property, how it varies along the track and how it relates to the performance of infrastructure including the formation of track defects is an ongoing area of research.

The BOEF model can be used to determine the track system support modulus for track deflection due to a known or assumed load (Raymond, 1985). This can be done for a stationary vehicle (Kerr, 2000) or for a moving train from lineside measurements (Priest and Powrie, 2009). Vehicle geometry and whether the transducer is on a sleeper or the rail should be taken into account when implementing this method. Although nominal wheel loads can be found for many trains, the actual applied load will differ owing to variable occupancy and dynamic effects. This introduces uncertainty into the calculation. It is possible to measure the applied loads locally with appropriately calibrated strain gauges (Mishra et al., 2014), although in practice this can be difficult to achieve on an operational railway line, particularly in circumstances where the track is deteriorating and support conditions are changing. The BOEF model can be applied to determined track stiffness using different methods, commonly using the deflection beneath a wheel or the displacement basin test (Talbot, 1980; Wheeler et al., 2016b).

Simple forms of the BOEF model are linear and are based on the assumption of a homogeneous foundation. Real railway track is likely to have heterogeneous support conditions and may be affected by non-linearities from voiding.

2.5 Geometry defects and performance issues

Previous studies have used both numerical and field research to investigate the causes of track defects. Many of these have been motivated by an association between track defects and physical features on railway lines, often at transitions where the track type or support conditions change. For example, problems found near bridge abutments within transition zones are frequently reported (Hunt, 1997; Li and Davis, 2005; Stark and Wilk, 2015). As defects are often associated with physical features it should be possible to identify physical processes that can initiate or accelerate deterioration (Steenbergen, 2013). However, there is a lack of consensus regarding the relative importance of and interrelationships between the elastic support conditions, the plastic behaviour of the track, the influence of track geometry or other track-train-structure interactions as causes of accelerated deterioration.

Irregular track geometry is known to change the loading on the track and has the potential to increase the applied dynamic loads. Simple models show that changes and variations in elastic track support stiffness affect the loaded geometry, change the wheel-rail contact forces and affect how those forces are distributed along a railway line (Frohling et al., 1996; Dimitrovová and Varandas, 2009; Dahlberg, 2010; Dimitrovová, 2010).Voided or partially supported sleepers are frequently associated with track defects. Using models, it has been shown that the presence of a void can increase the wheel-rail contact force and change the distribution of stresses in the region surrounding the void (Grassie and Cox, 1985; Lundqvist and Dahlberg, 2005; Bezin et al., 2009; Yang et al., 2009). The presence of a voided sleeper may exacerbate adverse conditions and further increase the rate of deterioration.

Irregular track geometry, variations in stiffness and loss of support (voids are a geometry irregularity giving a non-linear variation in stiffness) can all potentially increase dynamic loads, and thus would be expected to increase rates of deterioration. Numerical modelling and laboratory tests have been used to study the causes of problems in transition areas (Banimahd et al., 2012; Muramoto et al., 2012). In these studies, the presence of voided sleepers is attributed as being the primary of accelerated deterioration. This conclusion was drawn by observing that, for a single train passage, the increases in wheel-rail contact forces due to presence of voids and irregular geometry were more significant than the increases due to the stiffness variation. Field studies (Stark and Wilk, 2015) have similarly concluded that the voided state of the track was affecting performance. This can explain on-going and even accelerated deterioration. However, none of these studies address why the voids form in the first place.

Evidence from site-specific field studies is useful for improving the understanding of the in-situ response of railway track and identifying likely causes of poor performance. There are a number of trackside studies reported in the literature. Priest et al. (2010) used trackside monitoring, fusing the techniques developed by Bowness et al. (2007), and finite element modelling from Yang et al. (2009), to gain a better understanding of the dynamic response of the track and substructure to the passage of trains. Coelho et al. (2011) extended these approaches combining long-term site investigation with dynamic measurements to provide physical evidence of the causes of track deterioration at the transition between plain line and a fixed structure. Priest et al. (2012) used similar methods to link observed ballast migration with enhanced curving forces on a main line railway. Le Pen et al. (2014b) investigated poorly performing track close to a level crossing using trackside monitoring integrated with novel instrumentation mounted on an in-service train set. In these studies, enhanced forces, material behaviour, local stiffness variation and discontinuities in maintenance techniques have been identified as likely causes of track defects. It is challenging to monitor a defect forming as the locations of defects are not known until they become a problem by which time it is too late.

Models that account for the effects of variations in track characteristics on both long and short term behaviour and update track geometry accordingly using a settlement equation are able to forecast plausible locations of track defects. Hunt (1997) used different deteriorated geometries as inputs to subsequent modelling steps. Ferreira and Lopez-Pita (2013) developed a model which updates its geometry once the accumulated settlement exceeds a threshold. A similar model from Varandas et al. (2014) updated the geometry every five load cycles. Settlement equations that allow for variation in the applied loads, or that relate plastic settlement to the amount of elastic deflection, have been used to model observed settlement (Grossoni and Bezin, 2015) rather than forecast geometry. These models demonstrate the importance of accounting for the long-term accumulated effects of settlement on the elastic response of the track when studying deterioration and variation in track characteristics.

2.6 Maintenance practice

Severe deterioration of track geometry into an isolated fault or defect will necessitate maintenance intervention to correct the track geometry (British Standards Institution, 2014). Local repairs within defect zones normally involve lifting the track to the specified geometry and then pushing and compacting the ballast beneath the sleepers to restore the support conditions.

This can be done automatically using a tamping machine (Figure 2.8), which measures the local geometry, lifts the rails and packs ballast beneath the sleepers (Selig and Waters, 1994; Permanent Way Institution, 2001). Tamping tines, which typically vibrate at a frequency between 37 and 42 Hz, are used to squeeze and compact the ballast under the sleepers. The tine faces contact over about 2-4 particle diameters in depth, starting from about 10-15 mm beneath the base of the sleeper (Plasser & Theurer, 2016).

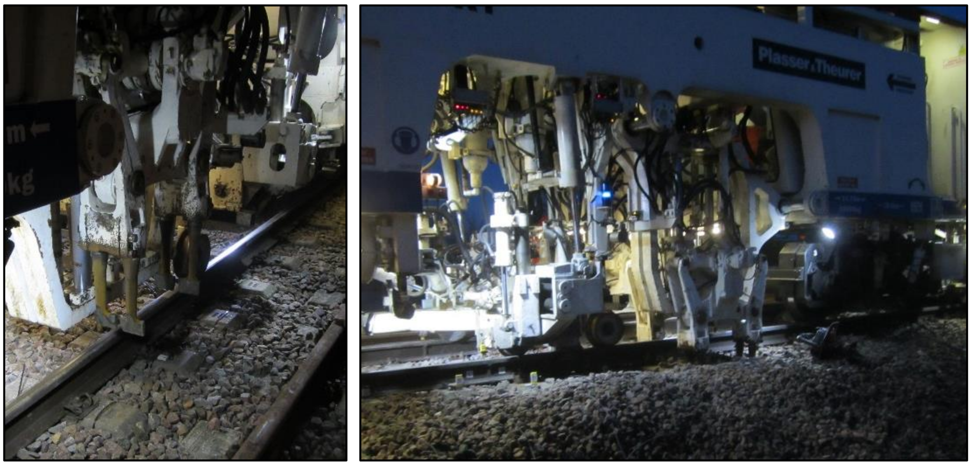

Figure 2.8 Photograph of tamping machine (a) tines above ballast (b) in operation.

Alternatively, repairs can be made manually by measuring the local geometry and lifting the track using jacks, then packing the ballast beneath the sleepers using hand-held pneumatic packing equipment such as Kango or Cobra packers (Network Rail, 2016), Figure 2.9.

Figure 2.9 Manual packing operation using Kango or Cobra packers (Network Rail, 2016).

The geometry lift is specified using data from track recording vehicles or local measurements. Maintenance may involve replacement of worn track components or replacement of “spent” ballast. Although these maintenance practices restore tolerable track geometry, the repairs are not permanent, with infrastructure managers often reporting that the geometry within defect zones deteriorates again relatively rapidly (Network Rail High Speed, 2013).

2.7 Conclusion

2.7.1 Summary

The aim of this research is to improve lineside monitoring to improve the understanding of performance issues on a ballasted high-speed railway and for use in condition monitoring and specifying maintenance. This review has shown that there are several potential track behaviours or performance issues that lineside monitoring techniques could be used to investigate; they could also be used to diagnose performance issues and evaluate remediation techniques. Both the short-term elastic behaviour (track vibration) and the long-term accumulation of differential plastic deformation (track settlement) are important for performance.

There are a variety of techniques that can be used to measure, model and interpret instantaneous elastic behaviour. Track deflection and track stiffness can be obtained from monitoring and used to quantify system performance and obtain relevant properties. Current techniques can be used to show the current state of the track, compare performance before and after maintenance and possibly highlight adverse conditions or processes affecting the track. Current data interpretation techniques are often time-intensive, complex and may involve uncertainty.

Long-term behaviour is more challenging to monitor and is less well understood. There are various empirical approaches for forecasting the settlement of the track, although these do not necessarily account for the mechanisms of deterioration. Measurements of cyclic behaviour of ballast and other track bed materials in the laboratory and methods to model that behaviour are the subject of ongoing research. To relate this to the actual performance of operational railways, there is a need to understand how the performance, properties and applied loading of railway track varies and changes both with time and along the length of the track.

Measuring the long-term behaviour in the field is challenging as the majority of instrumentation used for lineside monitoring is intended to measure track vibration, and is not routinely deployed for extended periods. Where long-term studies have been conducted, vibration measurements tend to be made periodically rather than continuously. Techniques that can be used for measuring settlement are sometimes invasive (deflectometers), in which case they do not reflect the state of the track prior to installation or require substantial amounts of track access (surveying) and would be supplementary to other forms of measurement. To assess the potential for deterioration of the track, it will be necessary to understand the rate of change of performance, how it varies along the track and how this is related to the system properties.

Track vibration measurements could be used to provide evidence regarding both the rate and nature of the changes in performance. This would require very regular or near-continuous measurements taken over an extended time period, possibly at several measurement locations. The frequency of measurements must be increased and deployments extend over an informative timescale, which would have consequences for the choice of transducer and the feasibility of analysis. Considering this, the requirements for lineside monitoring system, with reference to transducer choice for this research, are developed in the following subsection.

2.7.2 Requirements of a lineside monitoring system

The lineside environment is hazardous and current lineside monitoring technologies are not well suited to extended deployment. Monitoring equipment will be exposed to a range of environmental conditions and could be damaged during train operation or maintenance activities. Equipment must be sufficiently robust for an extended lineside deployment of several months to a few years, without any deterioration in system performance. There is also an incentive to minimise the capital cost of the transducers and the data acquisition system. Reducing the system cost will enable a greater number of lineside deployments to be made involving a greater number of transducers. This will be useful for research and make this approach more viable for condition monitoring by the industry. Minimising the transducer cost means that the risk of damage to the equipment is more acceptable. However, the data quality must be sufficient to quantify movement of the track accurately. This means that a transducer needs to be suitable for use under a range of track conditions: it should remain functional when track movement becomes severe within problem zones, and the signal should not be affected by transducer noise when movements are small.

These factors lead to the following requirements:

- data must be of sufficient quality to allow track deflection to be determined for a range of conditions,
- transducers must be low-cost,
- transducer must be easy to install and not change the behaviour of the track,
- transducers must be robust for extended deployment in the lineside environment.

Table 2.2 presents reasons for why certain monitoring technologies reviewed in this chapter were or were not used for different applications in this research. The data quality and ease of deployment meant geophones and high-speed video were used for more conventional short-term monitoring, whereas cost and robustness meant that the use of MEMS accelerometers for long-term applications has been investigated further.

Table 2.2 Proposed use of different monitoring systems in this research.

Transducer	**Applications**	**Reasons**
Geophone	Short-term monitoring, validating other sensors.	+ High quality data, processing issues understood. - Concern for long term robustness and operational range within defect zones, high cost per sensor.
Piezoelectric accelerometer	Not used.	- High cost per sensor, more processing issues than a geophone, suitability for low frequency applications.
MEMS accelerometer	Sensor validation, long term monitoring.	+ Low cost per sensor, can be ruggedized, potential for widespread long-term deployment. - More processing issues than a geophone, possible data quality issues.
High speed video for DIC	Short-term deployments with large deflections.	+ Direct measurement of displacement, high quality data, potential for reduced access requirements. - Effects from wind and ground borne vibration, significant labour and data storage requirements, requires line of site.
Multi-depth deflectometer	Not used.	+ Direct measurement of displacement. - Complex and invasive installation requirements, challenging permissions for deployment on track.
Laser System	Not used.	+ Direct measurement of displacement. - Requires both line of site and track mounted equipment, effects from wind and ground borne vibration.

With a suitable transducer, extended or pervasive lineside monitoring may become feasible. This means that data can be recorded for every train that passes the instrumented section of track. These data need to be processed and interpreted for further analysis. However, existing analysis methods have limitations and may become unmanageable if applied to large datasets. Improved interpretation methods are therefore required which are capable of:

- being automated,
- identifying the train type,
- giving measures of performance and system properties, i.e. deflection and stiffness.

Hardware suitable for extended lineside deployment, accompanied by appropriate methods to analyse large datasets, need to be developed: together these can form a system for track condition monitoring. Procedures for data retrieval, transmission and possibly online analysis would need to be developed if lineside monitoring techniques were to be commercialised.

This type of approach is demonstrated here through the validation of low-cost sensors in Chapter 4, development of new analysis techniques in Chapters 5, 6 and 7 and application of these technologies and techniques for lineside monitoring purposes in Chapters 8 and 9. It has enabled more long-term assessment of whether the effects of maintenance were sustained and provided evidence for progression of deterioration, valuable for research and for improving maintenance practice.

Chapter 3: Lineside monitoring on HS1

3.1 Introduction

This chapter describes background to HS1, supplies relevant supporting data sources and introduces the study sites used for lineside monitoring in this research.

3.2 Background to High Speed One

3.2.1 Route

HS1 is a 109 km long high-speed railway connecting London St Pancras to the Channel Tunnel, through Essex and Kent via Stratford, Ebbsfleet and Ashford stations. The railway was constructed in two phases, which form the basis for the two operational sections. Section 1 was constructed first and runs from beyond Ebbsfleet station to the Channel Tunnel boundary, while Section 2 runs from St Pancras to beyond Ebbsfleet station. The line speed for Section 1 is 300 km/h, whereas for Section 2 it is 230 km/h. The route is shown in the map in Figure 3.1.

This research has involved instrumenting, monitoring and analysing performance at six different sites, using the technologies and analysis techniques developed and validated during the research as well as more conventional techniques where appropriate. The locations of these sites are indicated in Figure 3.1.

CAMPBELL SCIENTIFIC CX9000 data loggers were used for both long term and conventional approaches to monitoring. These are capable of functioning unattended on battery power. This equipment can be programmed to trigger automatically if a train is detected. Data were retrieved by NRHS and transferred back to the University of Southampton for analysis.

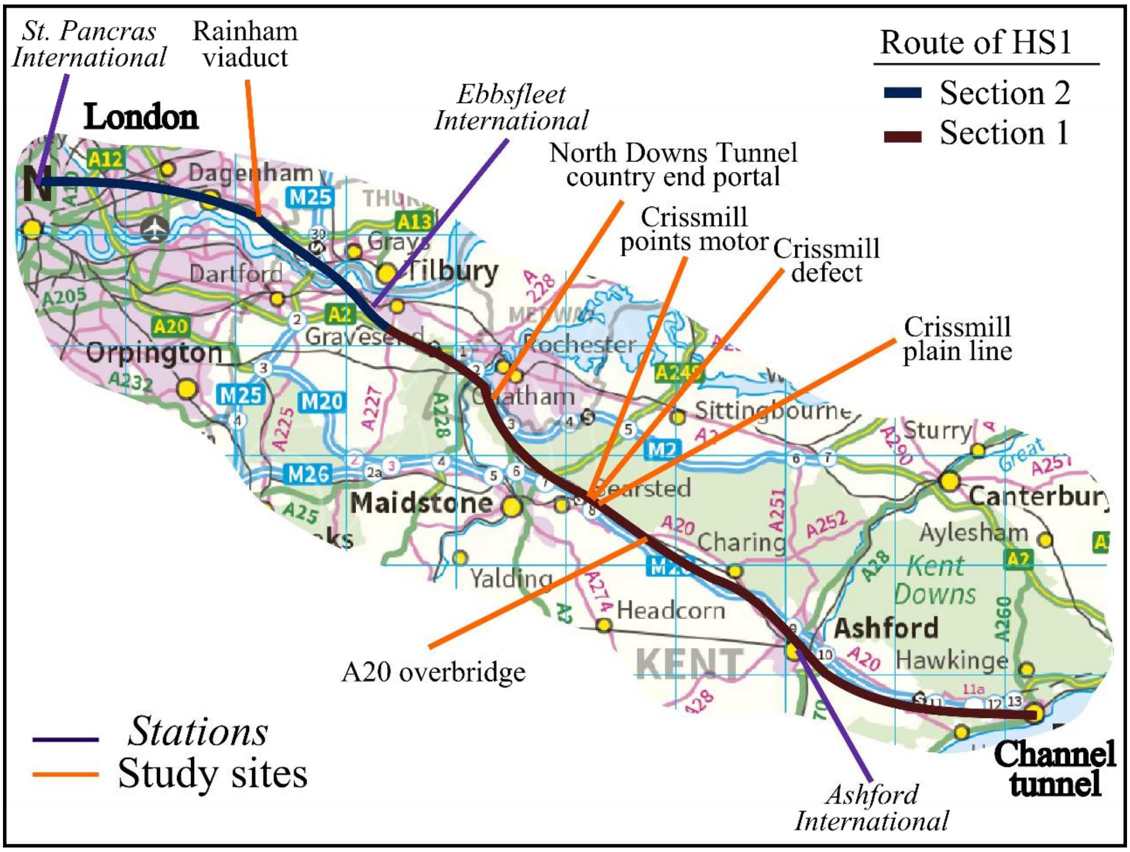

Figure 3.1 Map of study sites used for this research (Ordnance Survey, 2015).

The Crissmill plain line site was chosen to represent normal performance at high speeds; the other five sites were afflicted by different performance issues identified by NRHS. Two of these sites were on bridges and the other three were associated with features such as Under Track Crossings (UTX) or Switches and Crossings (S&C). Data from the Crissmill plain line site has been used extensively in Chapters 4-8; a more detailed description of the site including details of the instrumentation used is given in Section 3.4. Brief descriptions of the track fault and bridge sites follow in Sections 3.5 and 3.6 respectively. Details of instrumentation used for the fault sites are given together with results from monitoring in Chapters 8 and 9.

3.2.2 Trackform

Ballasted track is used for the majority of the route, including on bridges, with the exception of the London tunnels in which slab track was used. Generally, the plain line track superstructure employs continuous welded rail with a UIC 60 section. Two types of rail pads are used: a softer one and a stiffer one. Koroma (2015) found that the stiffer pad had a static stiffness of 115 MN/m and the softer pad 84 MN/m. Vossloh clips are used to fasten the rail to concrete duo-block bearers, which are on average spaced at 0.6 m centres. For S&C, combinations of long bearers and mono-block concrete sleepers are used. HS1 uses its own ballast specification (Rail Link Engineering, 1998), which requires a Los Angeles abrasion coefficient of ≤19 and a Micro Deval Index of ≤ 6. The ballast used came from two quarries: Glensanda in Scotland and Halsvik in Norway. These are granite and gneiss rocks respectively. Glensanda ballast was used predominantly for Section 1, and the Halsvik ballast was used for Section 2.

The trackbed and sub-structure vary between Sections 1 and 2, owing to the route and properties of the subgrade. The majority of Section 1 is built on an engineered track bed on the subgrade, which is chalk or clay. Bridge structures were generally used for major road and water crossings; and tunnels, embankments and cuttings for maintaining gradient (O'Riordan and Phear, 2001; O'Riordan, 2003). Poor ground conditions in the Rainham marshes on Section 2 meant more structures and ground improvement work was required outside the tunnels (Dyson and Kirk, 2006; O'Riordan and Kirk, 2007). The track bed was designed using UIC code 719R (International Union of Railways, 1994), French LGV best practice and the work of Li and Selig, (1998a; 1998b).

3.2.3 Train types

Three types of passenger train run on HS1, as well as some freight. Domestic high-speed services are operated using Class 395 Javelin trainsets in 6- and 12-vehicle configurations (the latter being formed of two six vehicle trainsets coupled together). International high-speed services use 20-vehicle Class 373 TGV-based Eurostar and 16-vehicle Class 374 Velaro trainsets. These will be referred to as Javelin, Eurostar and Velaro; photographs of these trains are given in Figure 3.2 (a) to (c) respectively.

Figure 3.2 Photographs of (a) Javelin, (b) Eurostar, (c) Velaro trains.

A Javelin trainset is an electric multiple unit with distributed traction, comprising six vehicles with near-identical geometry. The Eurostar can be split into two half trainsets, each comprising a driving vehicle and two semi-articulated passenger vehicles at each end of seven articulated passenger vehicles. The Velaro is an electric multiple unit with distributed traction, consisting of 16 vehicles with near-identical geometry. The Velaro entered service in November 2015. Train and vehicle geometries are summarised in Table 3.1. The vehicle geometry is described by the vehicle length L_v, bogie spacing L_b and axle spacing L_w. These are shown for twin bogie and articulated vehicle types in Figure 3.3.

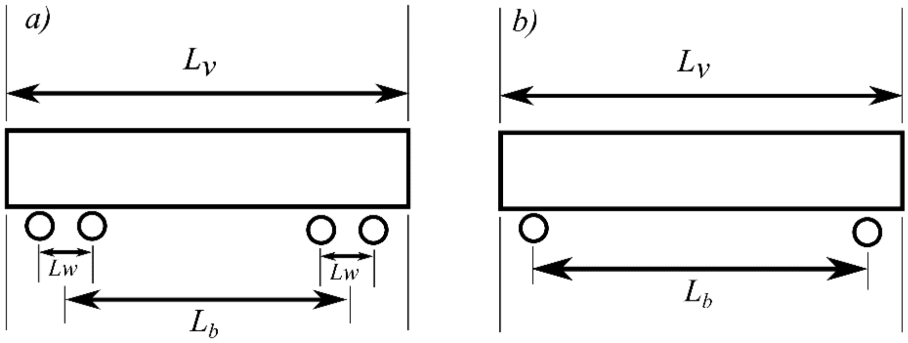

Figure 3.3 Typical vehicle geometry: (a) twin bogie vehicle, (b) articulated vehicle. L_v is the vehicle length, L_b is the bogie spacing and L_w is axle spacing within a bogie.

Table 3.1 Table of train and vehicle geometries for passenger trains operated on HS1.

Trainset	**Train length L_t (1st to last wheel)**	**Vehicle length L_v**	**Bogie spacing L_b**	**Bogie wheelbase L_w**	**Trainset coupling L_c**
Class 395 Javelin	116.8	20.0	14.2	2.6	-
12 vehicles	238.4	20.0	14.2	2.6	4.8
Class 373 Eurostar	396.4				
Driving vehicle	-	21.0	14.8	3.0	-
Semi-articulated	-	21.9	18.7	3.0	3.3
Articulated vehicle	-	18.7	-	3.0	-
Class 374 Velaro	391.9	24.8	17.4	2.5	-

3.2.4 Train loads

Variation in the static axle and wheel loads between and within trains are sources of uncertainty in lineside measurements. Inter-train variation from variable occupancy and differences between vehicles means the load applied to the track, hence the resulting deflection, could vary significantly from one train to another. Intra-train variation (i.e. differences in axle or wheel loads within a train) depends on how the passengers are distributed within a train. This may lead to more variable patterns of deflection. Measurements from a weighing-in-motion system can be used to investigate the inter- and intra-train variability of loading. This system self-calibrates using known trainsets and is claimed to be accurate to within 5% of the actual load. It provides data for the static axle and wheel loads and peak dynamic load from wheel out-of-round (Gotcha Montioring Systems, 2011). NRHS supplied quasi-static wheel load data for a single day of measurements for 99 Javelin trainsets each with 24 axles, and 28 Eurostar each with 48 axles. These trains passed a pair of weighing-in-motion systems located on opposite lines on straight and level track at close to the line speed of 230 km/h. This data was obtained May 2015. Histograms are given in Figure 3.4. Data were not made available in 2016, hence there is no comparable figure for the Velaro.

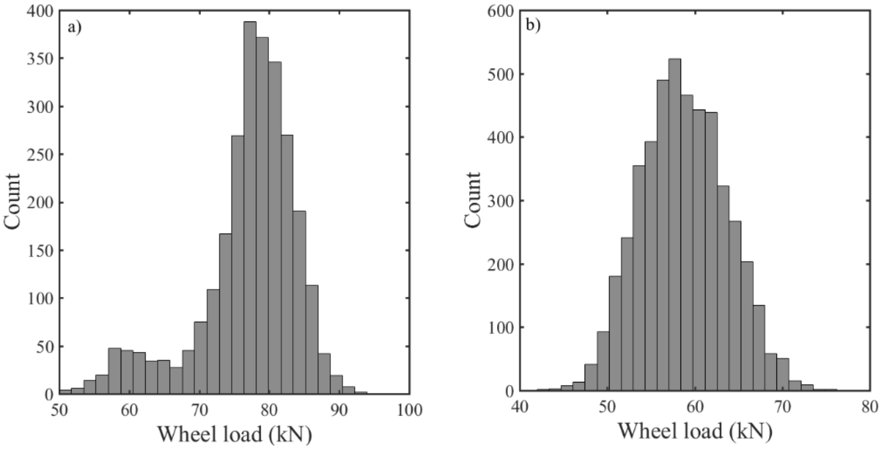

Figure 3.4 Histogram of quasi-static wheel loads for (a) Eurostar and (b) Javelin, obtained from weighing-in-motion systems on HS1.

The data for the Eurostar consists of two populations, each associated with one of the two different bogie configurations used in these trainsets (see Table 3.1). The smaller population of lower wheel loads is associated with the conventional bogie arrangements found in the driving cars at the either end of each articulated section. The larger population of higher wheel loads is associated with the articulated bogies used for the passenger vehicles in the trainset. The data should be split and analysed by population to understand the variation. Practically this means that time histories for the Eurostar should be analysed in sections based on these populations.

The data for the Javelins belong to a single population. Graphical analysis using a quantile-quantile plot suggests the data are normally distributed, with a mean and standard deviation of 58.7 and 4.9 kN respectively, giving a coefficient of variation of 8.4%. These statistics reflect both the inter- and intra-train variability. To investigate inter-train variability of wheel loads, it is appropriate to look at the distribution of the mean wheel loads from each train (mean axle load or train weight would also be suitable). To determine typical intra-train variability, the wheel loads in each train were normalised by the mean wheel load for that train. Histograms for these data are given in Figure 3.5. The distribution of mean wheel loads has a positive skew, suggesting higher loading at peak times. The normalised wheel loads are normally distributed, with a coefficient of variation of 4%.

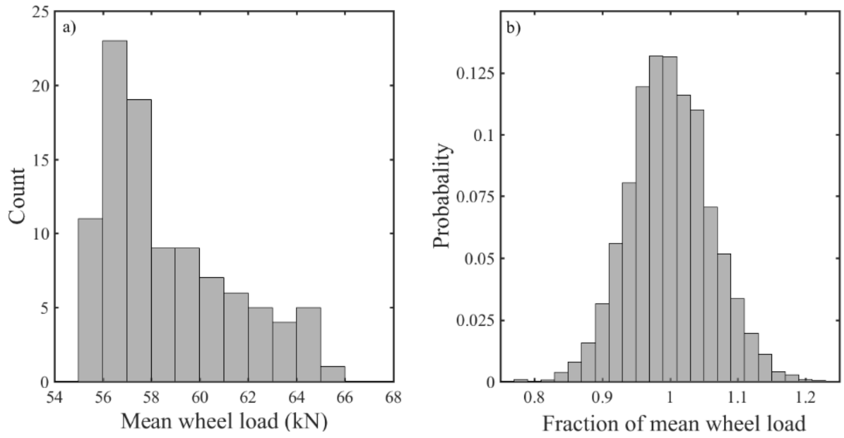

Figure 3.5 (a) Histogram of mean wheel load for 99 Javelin trains, (b) Histogram of wheel loads dived by the mean wheel load of each particular train.

Figure 3.6 shows the mean normalised wheel load at each axle location averaged over all trains from the Javelin data; the vehicles are separated by the dashed vertical lines. The vertical axis is restricted to 0.9 and 1.1 times the mean. This suggests that the heaviest wheels occur on the first and last bogies are the heaviest, and that the intermediate vehicles (vehicles 3 and 4), are the lightest.

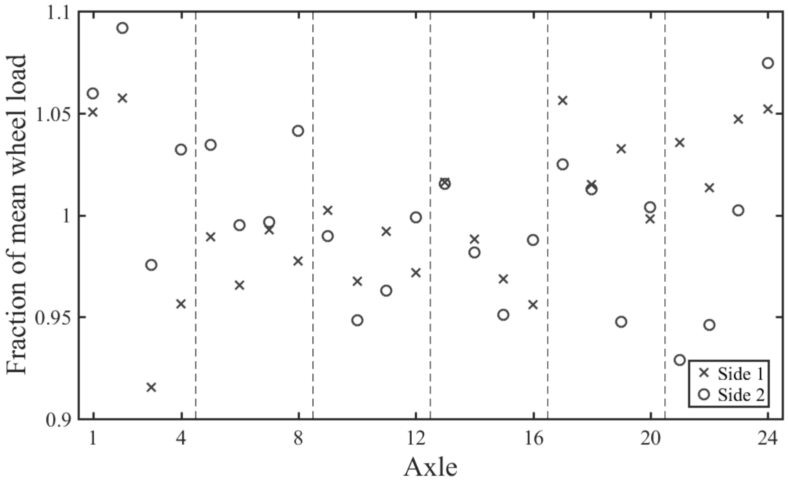

Figure 3.6 Mean normalised wheel load at each axle position for a Javelin train. The dashed vertical lines separate individual vehicles.

3.3 Crissmill plain line site

The Crissmill plain line site was selected to provide a benchmark for normal performance at high speed, as an example of well-performing plain line track, although in practice it was found that a proportion of the site is affected by voiding. It is situated just beyond the Crissmill crossovers on the down line, about 66.8 km from St Pancras on Section 1 of HS1 (Figure 3.1). The track is straight, descending with a gradient of around 1.4% and a line speed of 300 km/h. The site is in a wide sandy cutting and is shown in Figure 3.7. This site was also used for a collaborative study with the University of Birmingham investigating the respective roles of train aerodynamics and track vibration in ballast flight (Soper et al., 2017), discussed in Appendix C.

Figure 3.7 Photograph of the Crissmill plain line site instrumented during combined track vibration and aerodynamic measurements (Watson, 2016).

A conventional approach to site monitoring was taken at this site, with instrumentation being deployed for one or two days at a time. Instrumentation was placed and recovered during night-time possessions. Visits were made in May 2015, November 2015, May 2016 and December 2016. A variety of instrumentation was used for the track vibration measurements. For all visits, 20 vertical geophones were placed on sleeper ends at the locations shown in Figure 3.8 (see key on page xxxvii). Various configurations of MEMS accelerometers were used on different visits to supplement the geophone data. In May 2015, three MEMS accelerometers were fixed to the ends of the sleepers at 5.4_{O}, 5.4_{I} and 6.6_{O}; in May 2016, ten MEMS accelerometers were used to extend the study area ahead of the main site as shown in Figure 3.8; and in December 2016, six digital MEMS accelerometers were deployed alongside the geophones on both ends of the sleepers at 0.0, 1.2 and 2.4 m. Track vibration data obtained using geophones and accelerometers were sampled at 500 Hz for 20 s for each train passage. Displacements were obtained using 2 and 40 Hz high- and low-pass cut-off frequencies.

Aerodynamic instrumentation was installed on a gauge bar between the sleepers 3.0 m and 3.6 m away from the first geophone. Ballast acceleration measurements were made using instrumented ballast grains (Milne et al., 2016a), between the sleepers 3.6 and 4.1 m.

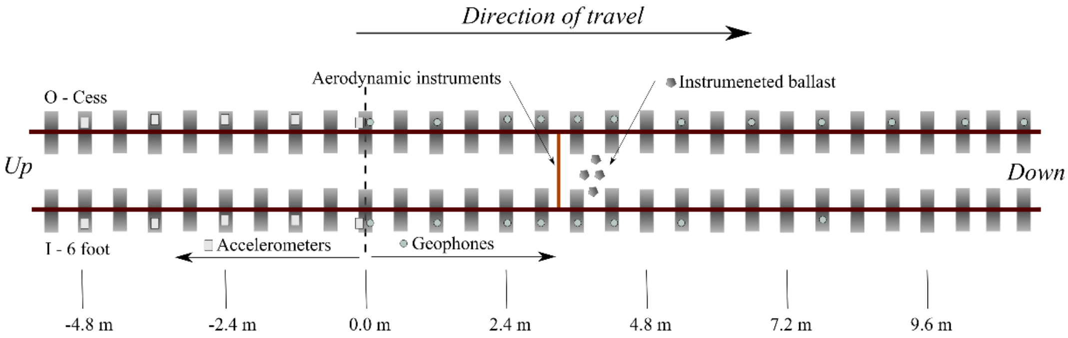

Figure 3.8 Primary instrumentation positions used for track vibration measurements at the Crissmill plain line site.

3.4 Fault sites: track

This section provides background regarding the fault sites studied using lineside monitoring during this research. Details of the instrumentation used and diagrams of transducers are presented with the results from monitoring in Chapters 8 and 9.

3.4.1 Crissmill defect site

The Crissmill defect site is at the end of the Crissmill crossovers at about 66.7 km away from London on the Down line (about 100 m closer towards London than the plain line site). The track is straight, descending at a gradient of around 1.4%. Here there was a defect just beyond a change in the trackform from mono-block sleepers used for the crossing back to duo-block sleepers used for plain line (Figure 3.9). A shallow UTX passes beneath the track at the same location. This site has been subject to extensive long-term monitoring as part of this research, looking at the effects of different maintenance interventions including shimming, tamping and the installation of under-sleeper pads.

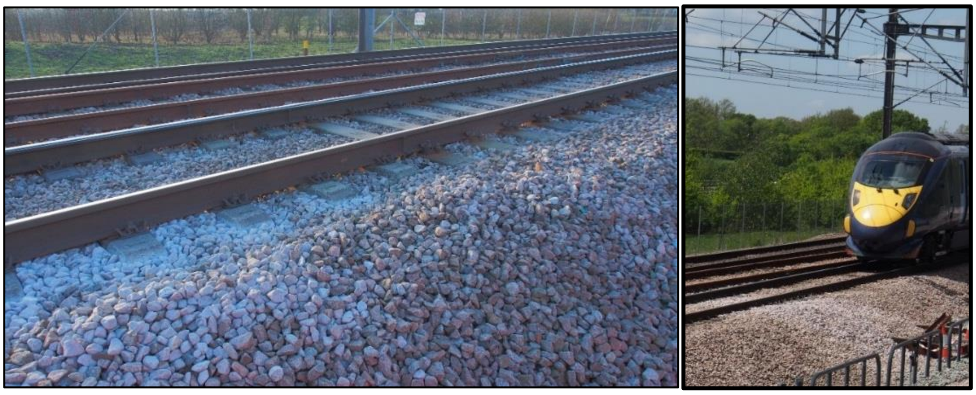

Figure 3.9 Photographs of Crissmill defect site, (a) before and (b) after remediation (Watson, 2016).

3.4.2 North Downs Tunnel country end portal

This site is about 30 m away from the south-eastern portal of the North Downs Tunnel (Figure 3.1), about 57.7 km from London on the down line. Here the track is on a curve with a radius of 4900 m and a design cant of 130 mm, descending with a gradient of about 1%. Monitoring was used to investigate a defect zone just beyond a pair of shallow UTXs (Figure 3.10). These shallow UTXs are a simple construction. Shallow trenches are excavated into the prepared sub-base, crossing the track just below the bottom of the ballast. Conduits for services are placed into these trenches and the trenches back-filled with concrete (Figure 3.11a). The conduits passing through the UTX terminate into inspection chambers on either side of the track (Figure 3.11b). The presence of these UTXs introduces a hard or stiff spot just beneath the ballast; what is not certain is whether the different in stiffness is sufficient to be significant.

Monitoring was conducted over a five-month period and was used directly to inform and evaluate the effectiveness of the maintenance and remedial measures applied.

Figure 3.10 Photographs of defects near the North Downs Tunnel portal (Watson, 2016).

Figure 3.11 (a) surface view of UTX and inspection chambers next to the ballast shoulder, (b) view inside UTX inspection chamber.

3.4.3 Crissmill points motor

This site involved monitoring a points motor used for the Crissmill crossover. The points motor is cantilevered out from supporting sleepers on a bracket. Problems associated with the excessive vibration of the points motor and voiding of the supporting sleepers, led to concern that the points motor or support bracket might fail. This site was instrumented to help to understand the behaviour of the track and of the points motor itself, and to provide frequent and timely data to allow NRHS to monitor the condition of the track in this critical zone.

Figure 3.12 Photograph of points motor at Crissmill crossovers.

3.5 Fault sites: bridges

Track defects are frequently found on and near bridges and, in the literature, they are frequently associated with the transition zone between the main trackform and the fixed structure. On HS1, faults have been identified in the vicinity of structural expansion/movement joints. One joint detail in particular, where the ballast remains continuous across the joint, is problematic.

Figure 3.13 Photograph of expansion joint plate at Rainham.

Two sites with this detail have been studied. These are the Rainham Viaduct and the A20 overbridge (Figure 3.1). Although the bridge designs differ slightly, the principles behind the joint detail are similar. At Rainham the joint studied is between bridge decks (Figure 3.14a) whereas on the A20 bridge they are between the bridge deck and the abutment (Figure 3.14b).

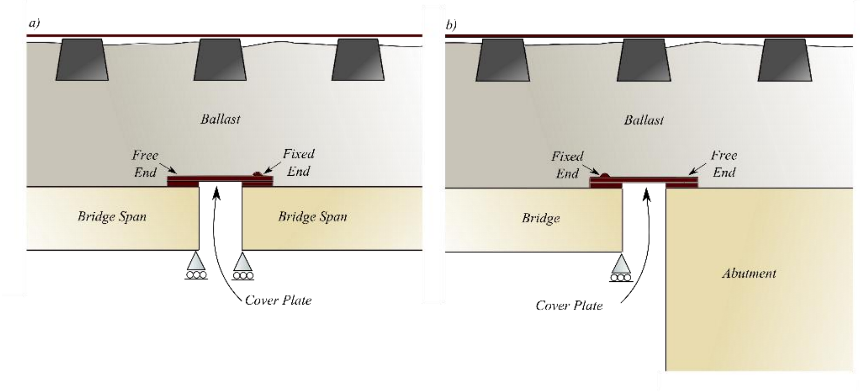

Figure 3.14 Simple spanning plate supporting continuous ballast, structural joint detail used on HS1 (a) between two adjacent bridge decks, (b) between a bridge deck and an abutment.

3.5.1 Rainham Viaduct

Rainham Viaduct is one of the major structures on Section 2 of HS1. This is a 454 m long viaduct consisting of five decks each with three spans. The bridge crosses an area of soft ground and existing services (a road and pipes for a water treatment plant). The bridge is about 23.5 km from St Pancras. Each span is 30 m long, giving 90 m long decks, with the exception of the 34 m central span in the middle (third) deck of the bridge, as illustrated in Figure 3.15. The deck supports both the up and the down lines.

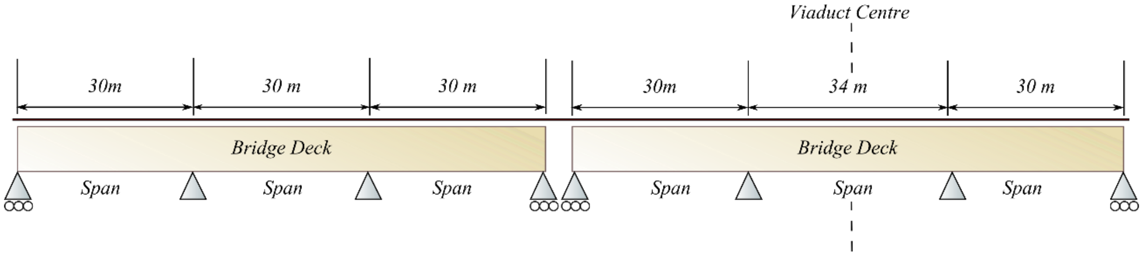

Figure 3.15 Example arrangement of bridge decks at Rainham Viaduct.

The bridge is a composite structure. The typical cross-section is a 0.3 m thick concrete slab resting on 2 m deep steel girders. The depth of the girder was reduced to 1.4 m to provide sufficient headroom when crossing over a highway (Dyson and Kirk, 2006). Between each deck there are structural expansion/movement joints. These have a simple design: a steel plate spans across the joint (Figure 3.14(a)). This plate is fixed to one of the decks and free to slide on the other. Ballasted track with continuous welded rail is used across the entire bridge, without rail expansion devices. This means that the ballast layer is continuous across the joint. There are signs of accelerated deterioration of the ballast above every joint, although this is more severe above some joints than others, see Figure 3.16.

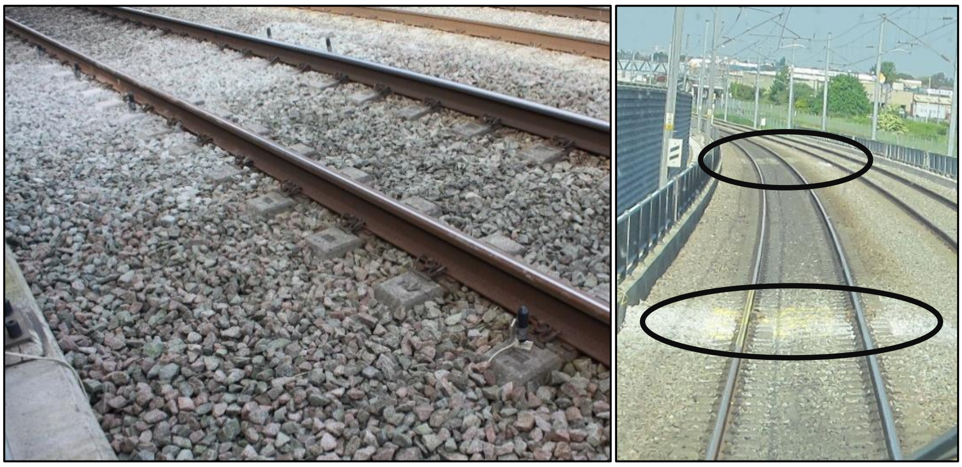

Figure 3.16 Photograph of track defect on Rainham Viaduct, (a) from the cess and (b) from the cab of a train on the Up line looking towards London.

The track alignment across Rainham Viaduct is quite complex and involves a combination of horizontal and vertical curves for much of the bridge. The horizontal alignment of the track on the bridge is a curve with a design radius of 2402 m and a cant of 160 mm. The vertical alignment changes over the bridge. Travelling away from London, the first 109 m of track across the bridge ascends at a gradient of 1.8%. For the next 324 m, there is a vertical curve with radius of 1000 m leading into a descending slope with a gradient of 1.4% for the remainder of the structure.

The study at Rainham was directed at the most severe defect on the bridge at the joint between the second and third (central) decks away from London on the Up line. This site is studied first using more conventional monitoring techniques to understand performance within the defect zone, consider the effects of bridge and ballast interaction and evaluate a tamping intervention. Later the continuous approach to monitoring has also been used. The outcomes from these different approaches to monitoring are presented in Chapters 9 and 8 respectively.

3.5.2 A20 overbridge

The A20 bridge carries HS1 across the A20 road near Maidstone Kent on ballasted track, around 69.7 km from London. The track is curved with a radius of 4650 m, a cant of 135 mm and a gradient of 0.9% descending away from London. Each line is carried by a separate triple-span deck. The decks share the abutments at either end of the structure but have separate intermediate supports. The decks are fabricated using composite construction with a concrete slab and steel girders. Both decks have spans of 22.3 m, 32.9 m and 22.3 m, as shown in Figure 3.17.

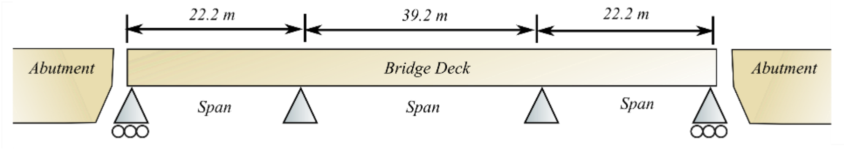

Figure 3.17 Layout of A20 bridge deck.

A similar joint detail to that used at Rainham Viaduct is used between the bridge deck and the abutments of the A20 bridge (Figure 3.14(b)). A steel plate has been fixed to the end of the bridge deck, which spans across the joint and is free to slide over the wall of the abutment. Ballasted track is used across the bridge, with continuous welded rail without the use of a rail expansion joint. The ballast is continuous across the joints. Defects could be observed at either end of the bridge deck. At this site, geophones were used to measure bridge vibration and high-speed video was used to assess the performance of the track. Results are presented in Chapter 9.

Figure 3.18 Photographs of track defects either end of the A20 overbridge (Watson, 2016).

3.6 Summary

The Chapter has given background to the route, the trackform, the trains operated on the line and locations of the different study sites used in this research. A detailed description was given of the Crissmill plain line site including details of the instrumentation used to obtain data that has been used extensively for validating MEMS accelerometers and in the development and testing of new analysis methods in Chapters 4–8. Shorter summaries were given to introduce the fault sites which are studied in greater detail in Chapters 8 and 9, through the application of both continuous and conventional approaches to lineside monitoring.

Chapter 4: Low cost transducers for lineside monitoring

4.1 Introduction

In Chapter 2 it was proposed that a system suitable for widespread, long term lineside monitoring needs to be robust, offer semi-autonomous operation and is likely to be more viable if it is based on low-cost transducer technologies. A number of different types of transducers that have been, or could be used for lineside monitoring have been reviewed. Of these, MEMS accelerometers offer the lowest cost per transducer. They have a small size, which means that they can be packaged robustly or embedded within track components. This type of sensor has not been proven for lineside monitoring applications, owing to concerns regarding transducer noise, accuracy and reliability. However, as the technology continues to improve, this assumption may no longer be valid. If MEMS accelerometers were sufficiently accurate, they would be suited for deployment on the track. In this Chapter, newer sensors are assessed through laboratory testing and field trials to determine their suitability as an alternative track-mounted motion transducer for lineside monitoring. Some of the material presented in this Chapter has been published in Milne et al. (2016b). This has been extended with further laboratory and field tests.

4.2 MEMS accelerometers

There are a variety of commercially available MEMS accelerometers. These output two types of signal: analogue and digital. In this research, analogue sensors were chosen, to be compatible with the CAMPBELL SCIENTIFIC CX9000 data acquisition system. This system allowed for direct comparison with similarly logged ION SENSOR low frequency geophones and is suitable for autonomous long-term monitoring applications. Although digital MEMS accelerometers are widely available, it would have been necessary to obtain or develop a data acquisition system suited to long-term deployments if they had been used. Use of digital MEMS accelerometers for short-term and more innovative uses is considered towards the end of the Chapter with respect to commercial devices, for which suitable, inexpensive data acquisition systems were already available.

Two low-cost analogue accelerometers were identified as potentially suitable for measurement of low frequency track vibration. These were the ADXL326 and the ADXL335, both manufactured by ANALOG DEVICES. These are both triaxial accelerometers with three orthogonal measurement axes. They have a maximum measurement range of ±16 g and ±3 g respectively. Both devices operate up to 550 Hz for the vertical axis (Z) and up to 1600 Hz for the horizontal axes (X and Y). Both cost about £3 for the basic chip.

For an analogue sensor, analogue-to-digital conversion of the voltage signal is performed by an external data acquisition system. The sample rate, resolution of the analogue-to-digital convertor (ADC), over-sampling and anti-aliasing depend on that equipment. The operational range and sensitivity of analogue transducers are normally fixed. Additional analogue filters can be included between the transducer and the ADC. Cables typically up to 20 m in length can be used to transmit the signal between the sensor and data acquisition system and to supply power. Sensor hardware was supplied on breakout boards, as shown in Figure 4.1(a), costing around £20 each. These were equipped with a first-order low-pass anti-aliasing filter. This had a 50 Hz cut-off frequency provided by a resistor-capacitor (RC) circuit to attenuate the signal at higher frequencies. These sensors use a 32 kΩ resistor and a 0.1 μF capacitor. The sensors were encapsulated in epoxy resin within a robust enclosure and attached to shielded cables for deployment on track (Figure 4.1(b)).

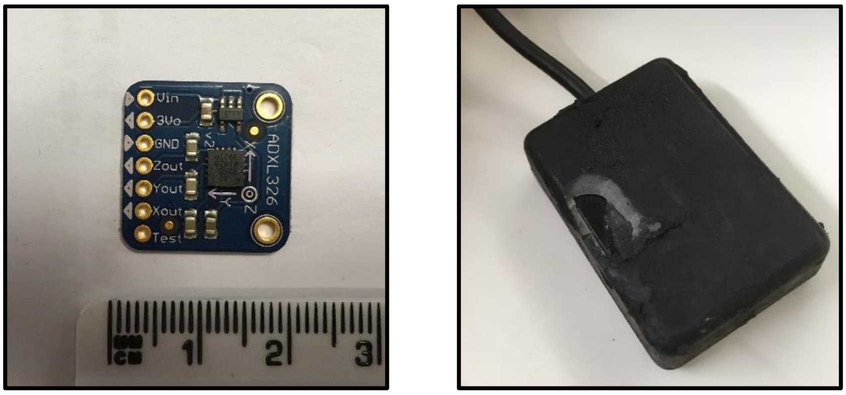

Figure 4.1 Photographs of (a) ADXL326 breakout board and (b) sensor package recovered from track.

4.3 Testing

Benchmarking a new sensor against one of a known quality is a common method of investigating transducer performance. This was done by mounting the MEMS accelerometers and a high-quality ION SENSOR low frequency geophone together on the test apparatus and subjecting them to the same excitation. The output signals were compared directly in the time domain, and by finding the transfer function between the two in the frequency domain. For lineside monitoring, the very low frequency performance (< 40 Hz) of the transducer is important. Different test apparatus was required to test within the frequency range. A hydraulic actuator was used for testing below 5 Hz, and an electrodynamic shaker for the tests above 5 Hz. In further testing servo-controlled apparatus allowed control of the input waveform and amplitude. This was used in the present study for replicating typical railway track motions in the laboratory. Together these three pieces of test equipment were used to investigate the performance of the transducers to check their performance for use in the field.

4.3.1 Laboratory testing

Initial tests were used to benchmark the analogue ADXL326 and ADXL335 sensors against a geophone. At low frequencies (< 5 Hz), a hydraulic actuator (Figure 4.2(a)) was used to apply a sinusoidal excitation at different fixed frequencies for a given number of cycles and amplitudes. For higher frequencies (5 – 45 Hz), an electrodynamic shaker (Figure 4.2(b)) was used to perform a frequency sweep. The signals were sampled using the same data acquisition system at 500 Hz. The outputs from the geophone and MEMS accelerometer were compared in both the time and frequency domains.

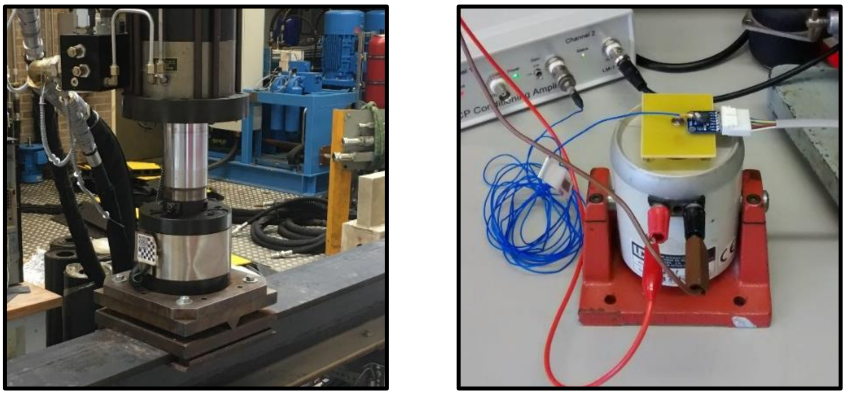

Figure 4.2 Photographs of hydraulic actuator and electrodynamic shakers used for low and high frequency testing.

Figure 4.3 shows a selection of displacement-time histories obtained by processing the data from the geophones and the accelerometers. Data were processed by filtering and integrating the velocity and acceleration signals in the time domain, once and twice respectively. The same high- and low-pass Butterworth filters, with cut-offs of 0.8 Hz and 8 Hz respectively, were used for both signals. The mean range of displacement obtained agreed to within ±1% of the test amplitude for the different sensor types.

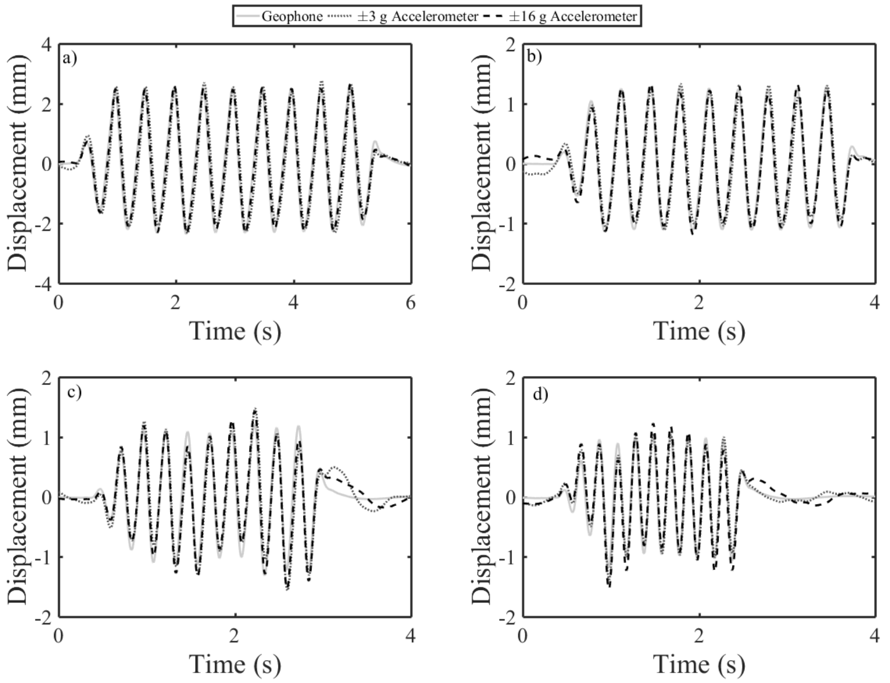

Figure 4.3 Displacement time histories for fixed frequency sinusoidal excitation at (a) 2 Hz, (b) 3 Hz, (c) 4 Hz, (d) 5 Hz, measured using a geophone and ±3 g and ±16 g accelerometers.

Transducer performance was verified in the frequency domain by calculating the transfer function between the geophone and accelerometer signals. Acceleration data were integrated in the frequency domain to obtain velocities for this comparison. As the transducers were subjected to the same excitation, the expected magnitude of the transfer function for calibrated velocity data is unity. In the actuator tests, only the test frequencies and their harmonics were excited. The transfer function has been evaluated at each test frequency for the actuator tests and is shown in Figure 4.4(a). The higher frequency performance was also investigated in the frequency domain using an electrodynamic shaker to perform a frequency sweep, produced using a signal generator, between 5 Hz and 45 Hz. The magnitude of the transfer function has been calculated using the cross spectrum from this test and converted into standard 1/3 octave bands. This is shown in Figure 4.4(b). The frequency response for the 1st order RC antialiasing filter with a 50 Hz cut-off frequency has been plotted to show the expected attenuation of the signal from the accelerometer relative to the signal from the geophone.

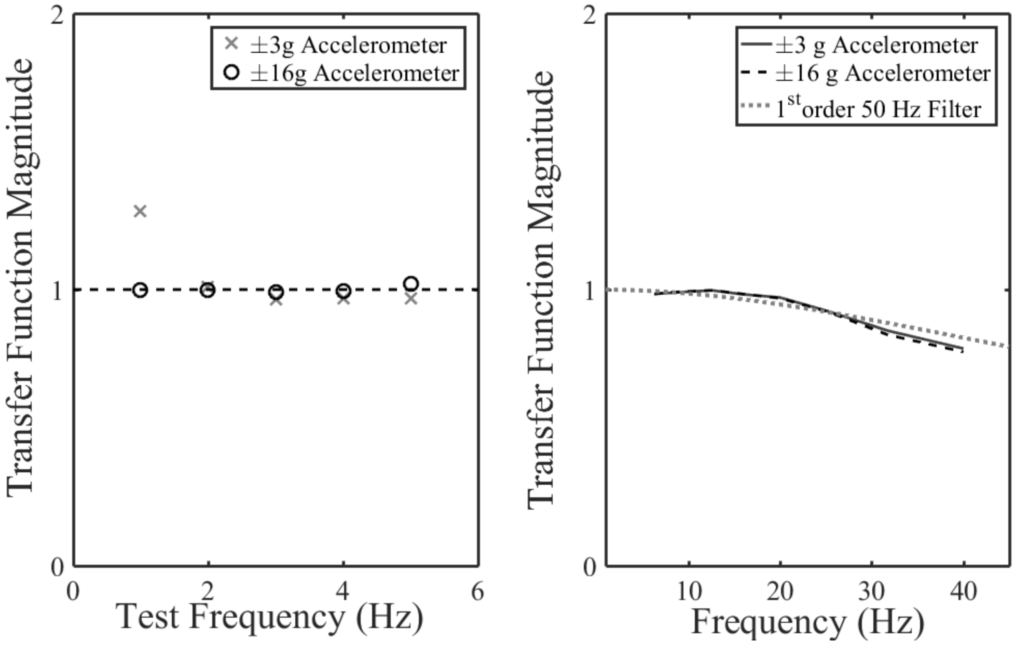

Figure 4.4 Transfer function magnitude between ±3 g and ±16 g accelerometers and a geophone (a) at each test frequency, (b) at the harmonics of each test frequency and for a frequency sweep between 5 and 45 Hz, expressed in 1/3 octave bands, and the frequency response of the antialiasing filter.

At frequencies between 1 Hz and 5 Hz the transfer function between the accelerometers and the geophone was close to unity, indicating agreement between sensors. Only the ±3 g accelerometer did not agree for the 1 Hz test. At higher frequencies, the transfer functions between the accelerometers and geophone were equivalent to the expected attenuation from the filter, indicating agreement between transducers.

More advanced testing was carried out on the ±16 g ADXL326 accelerometer using an INSTRON ELECTROPULS E1000 servo-controlled actuator (Figure 4.5). Displacement control of this equipment enabled testing using waveforms typical of track deflection determined from the BOEF model. The MEMS accelerometers were benchmarked against the output signal from test equipment’s own displacement transducers. Both signals were sampled at 500 Hz using a CAMPBELL SCIENTIFIC data acquisition system.

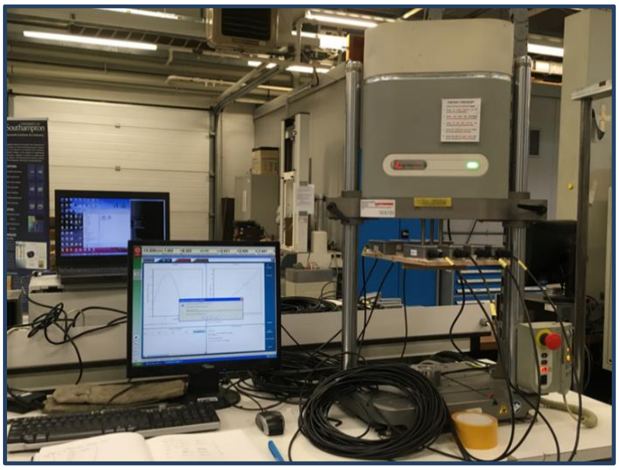

Figure 4.5 Instron electropuls E1000 servo-controlled actuator used to apply a simulated track deflection waveform.

Figure 4.6 compares displacement data obtained from the accelerometer with the movement of the actuator. This is shown in (a) the time domain and (b) the frequency domain; a vertical logarithmic scale has been used to show more clearly the differences between high and low amplitude frequency content. The waveform specified was designed to represent typical operating conditions on HS1, i.e. a 0.5 mm amplitude sleeper deflection on a track system support modulus of 40 MN/m^2 with Javelin vehicle geometry passing at 60 m/s. There is close agreement in both time and frequency domains, suggesting the transducer would be suitable for use in the field.

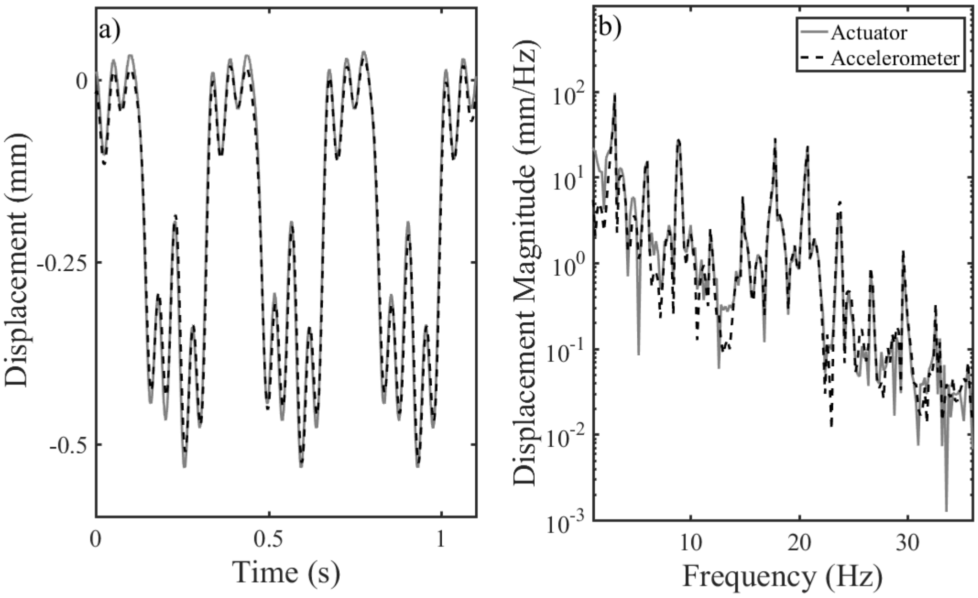

Figure 4.6 (a) Displacements obtained using actuator LVDT and MEMS accelerometer, (b) displacement spectra for a waveform representative of typical sleeper deflections on HS1 for Javelin vehicles travelling at 60 m/s.

Figure 4.7 compares the result for a similar waveform in the time domain only. In (a) the length of the waveform was increased to represent a train moving at 25 m/s and then in (b) the input deflection was increased to 3 mm to represent poorly performing track. Larger deflections at higher speeds were not possible with the test machine. The agreement between the accelerometer and the actuator output is less good for the data representative of the slower train, but is better when deflections are increased. This is expected, as slowing the train will lower the frequencies of interest and reduce their acceleration amplitudes. Increasing the deflection will raise the amplitude of the low frequency components. This suggests that it may become challenging to obtain displacement data from slower moving trains using these accelerometers, and that measurements are more likely to be successful where deflections are large.

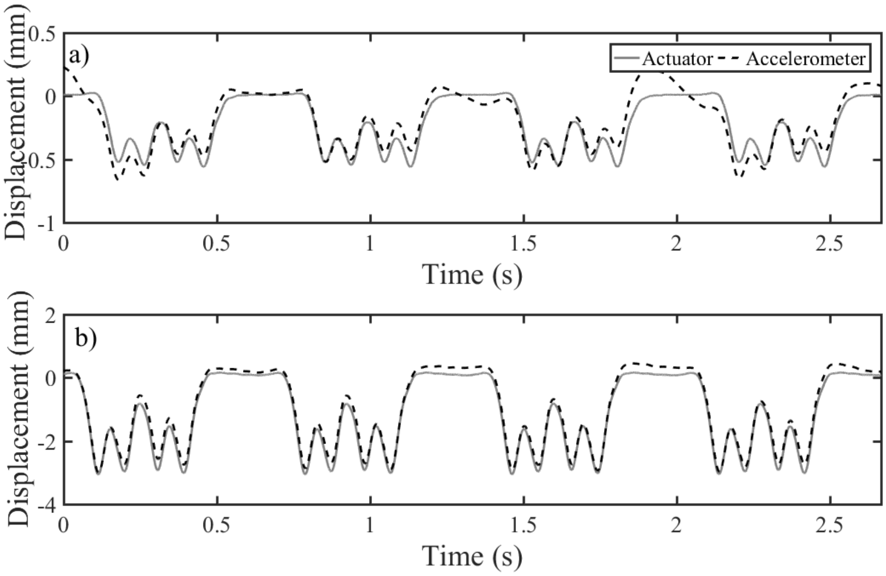

Figure 4.7 Comparison of displacement data obtained using actuator LVDT and MEMS accelerometer for waveform representative of (a) 0.5 mm deflections from Javelin vehicles travelling at 25 m/s and (b) 3 mm deflections for the same speed.

4.3.2 Field trials

Having shown that displacements could be obtained reliably using ADXL326 MEMS accelerometers in laboratory tests, the same sensor was trialled in the field. The sensors were fixed on sleeper ends next to geophones, as shown in Figure 4.8.

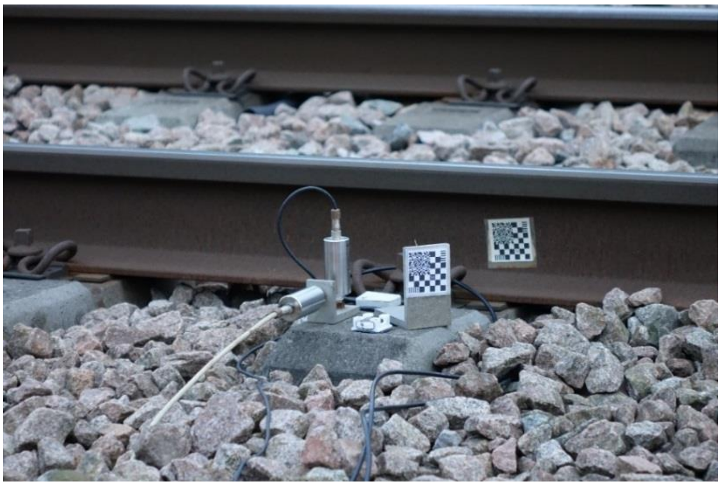

Figure 4.8 Photographs of geophones, MEMS accelerometers and targets for DIC mounted on a sleeper end (Watson, 2016).

Figure 4.9 presents displacement data obtained using a geophone and an accelerometer on the same sleeper end during the passage of a Javelin. The signals were both sampled at 500 Hz. Deflections we obtained by filtering and integrating once and twice for the velocity and acceleration signals respectively. The cut-off frequencies were 2 and 40 Hz for the high- and low-pass filters respectively. In Figure 4.9(a), there is reasonable agreement in terms of the overall pattern and range of movement in the time domain. The frequency and magnitude of the dominant peaks in the spectrum agree well in Figure 4.9(b), although the displacement spectrum from the accelerometer is much noisier than that from the geophone. Figure 4.10 shows that the acceleration data from the MEMS accelerometer is much nosier than the velocity data from the geophone, by plotting the signal-to-noise (SNR) ratios in standard 1/3 octave bands.

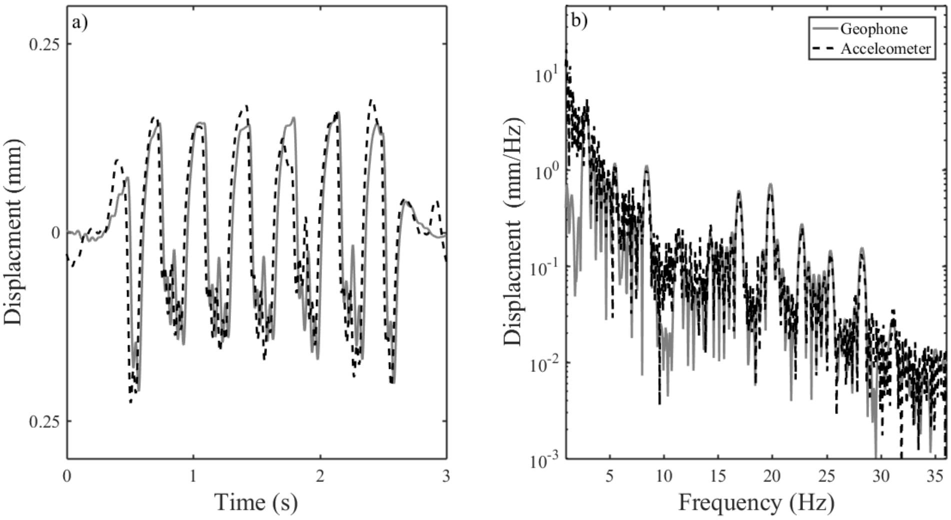

Figure 4.9 Comparison of displacement data obtained using a geophone and MEMS accelerometer on the same sleeper end in (a) the time domain and (b) frequency domain. Data were sampled at 500 Hz and filtered with 2 and 40 Hz high- and low-pass cut-off frequencies, before integration.

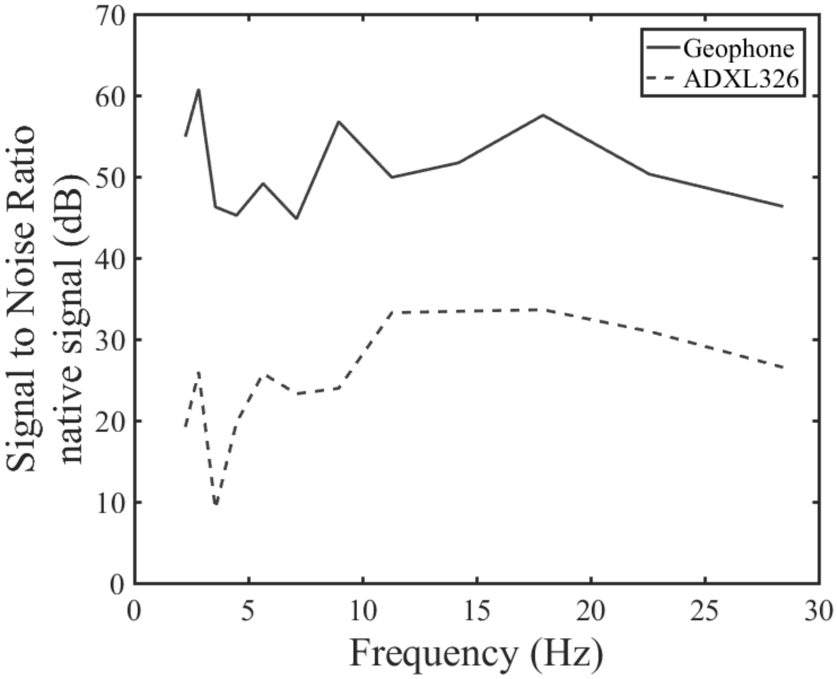

Figure 4.10 Signal-to-noise ratio between train passage and background signal data for accelerometer and geophone data from Figure 4.9 in 1/3 octave bands.

Not all the results agreed as well as those shown in Figure 4.9. Figure 4.11 presents geophone and accelerometer data from a different sleeper, processed in the same way as before. A low frequency phenomenon has affected the accelerometer results. The magnitude of the first dominant frequency is much greater in the spectrum for the accelerometer data than for the geophone. This may be the influence of low frequency transducer noise, or possibly sleeper rotation. Variation in the component of gravitational acceleration in the measurement axes from rotation could influence the result from a MEMS accelerometer. A gyroscope would be needed to measure angular velocity for investigating the significance of sleeper rotation (Gao et al., 2017).

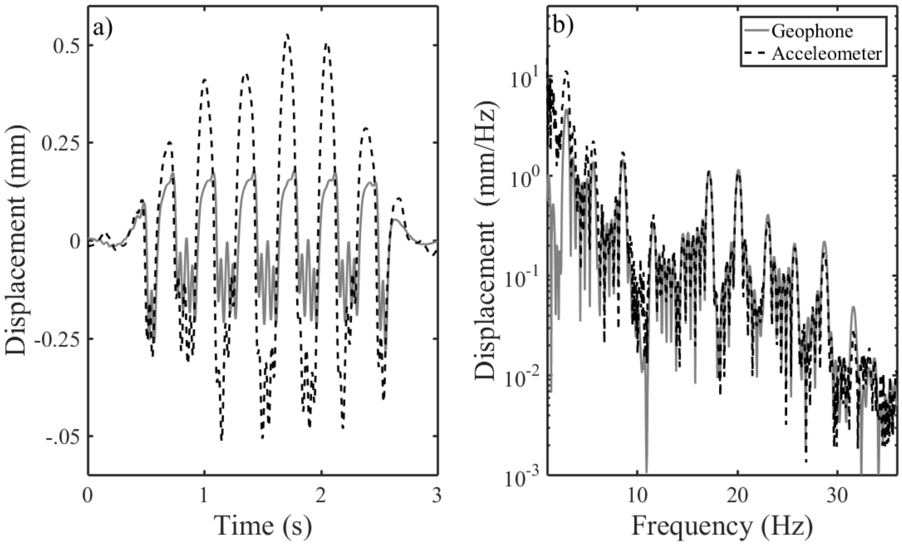

Figure 4.11 Comparison of displacement data obtained using a geophone and MEMS accelerometer on the same sleeper end in (a) the time domain and (b) displacement spectra where the MEMS accelerometer has been affected some low frequency phenomenon. Data were sampled at 500 Hz and filtered with 2 and 40 Hz high- and low-pass cut-off frequencies before integration.

The previous results were for small amplitude sleeper deflections less than 0.5 mm. One reason for using an MEMS accelerometer is that they may be more suited to poorly performing track where deflections tend to be larger. Figure 4.12 shows displacement data obtained from a geophone and a MEMS accelerometer on a sleeper end that was moving by about 1.5 mm. There is close agreement between the results from the two sensors

No data was available to perform a direct comparison between the MEMS accelerometers and another system (i.e. DIC) for very large deflections. However, as displacements were obtained with reasonable accuracy when deflections were small it would be reasonable to assume the system will be accurate when the acceleration signal is larger (as in the laboratory tests), providing the accelerometers do not go off scale.

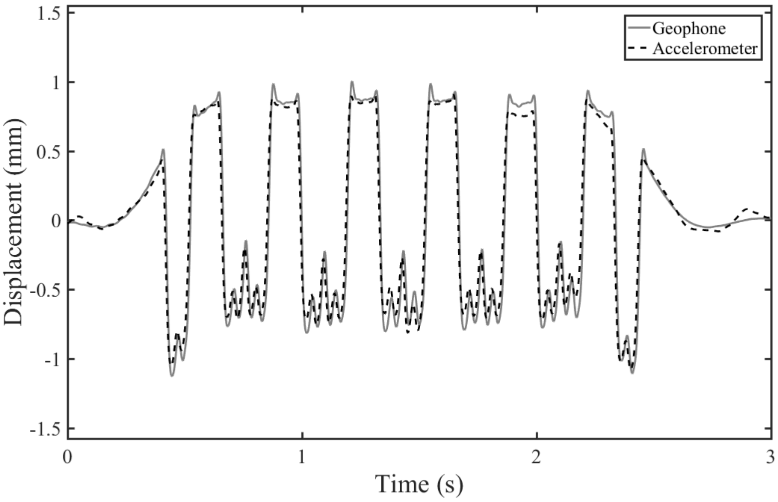

Figure 4.12 Comparison of sleeper deflection data obtained using a geophone and a MEMS accelerometer position on the same sleeper, thought to be affected by voiding. Data were sampled at 500 Hz and filtered with 2 and 40 Hz high- and low-pass cut-off frequencies before integration.

4.4 Digital sensors

Most data collection for the case studies presented in Chapter 9 was carried out using the analogue ADXL326. However, some attention has been given to trialling physically similar digital MEMS accelerometers, as there is potential for reducing the cost and size of the data acquisition system and simplifying the transmission of vibration data with a digital system. This would be important in facilitating the adoption of widespread condition monitoring and could enable novel measurements.

With a digital sensor, analogue-to-digital conversion is performed on the sensor hardware at a programmable rate, rather than using an external ADC. This can include the application of digital filters and other noise reducing techniques. The operational range is also programmable. However, this reduces the data size rather than the sensor’s resolution. Acceleration measurements are stored in data registers on the hardware. These are updated at the specified rate. A microcontroller is required to read the data from the sensors and store it to permanent memory. If the output data rate of the hardware is higher than the desired output sample rate, over-sampling can be employed to increase the effective resolution of the ADC. Only short cables, typically less than 1 m length, can be used between the sensor and the microcontroller for high data acquisition rates. Ideally the transducer and the microcontroller should be co-located. Data can either be stored by the microcontroller or transmitted to another system.

Trials on digital MEMS have focused on the ADXL345, a popular and inexpensive digital accelerometer manufactured by ANALOG DEVICES. This sensor is a triaxial transducer, with a scalable range of up to ±16 g at 13-bit resolution. The resolution reduces by one bit as the dynamic range is halved. The device can output data at up to 3200 Hz.

Two commercially available systems that use this sensor were trialled: first the AXIVITY AX3 and later the GULF COAST DATA CONCEPTS X16. Both systems comprise an ADXL345 accelerometer, a microcontroller, clock, internal storage and a battery, allowing stand-alone operation. Functionally, the X16 was more advanced than the AX3, with the ability to oversample, and hence increase the effective resolution, as well as filter and time stamp the data. The AX3 simply attempts to sample and time stamp the data at a specified rate. In principle, the device can operate up to 3200 Hz; but in practice rates above 400 Hz resulted in dropped records, suggesting the microprocessor was not sufficient for the data acquisition system. Sacrificial brackets were designed and produced from Acrylonitrile Butadiene Styrene (ABS) plastic using a 3D printer for both devices. These were glued to the track to hold the sensor securely, while enabling quick retrieval of the sensors. Figure 4.13 shows the two systems deployed on a sleeper on track.

Figure 4.13 Photographs of (a) AX3 and (b) X16 accelerometers deployed on track.

These systems were both trialled in the laboratory and in the field on separate occasions. This showed that both systems were acceptable for measuring acceleration, where the higher frequency components are the more significant part of the signal. However, only the X16 was capable of producing data suitable for obtaining displacements, which requires low noise data for the lower frequency components of the signal. As the devices use the same transducer and were fixed to the track in similar ways, this result must be due to differences in the ability of each data acquisition system to obtain low noise data at low frequency. Figure 4.14 shows examples of deflection data for (a) Javelin and (b) Eurostar trains obtained using the X16, results from the AX3 are not shown.

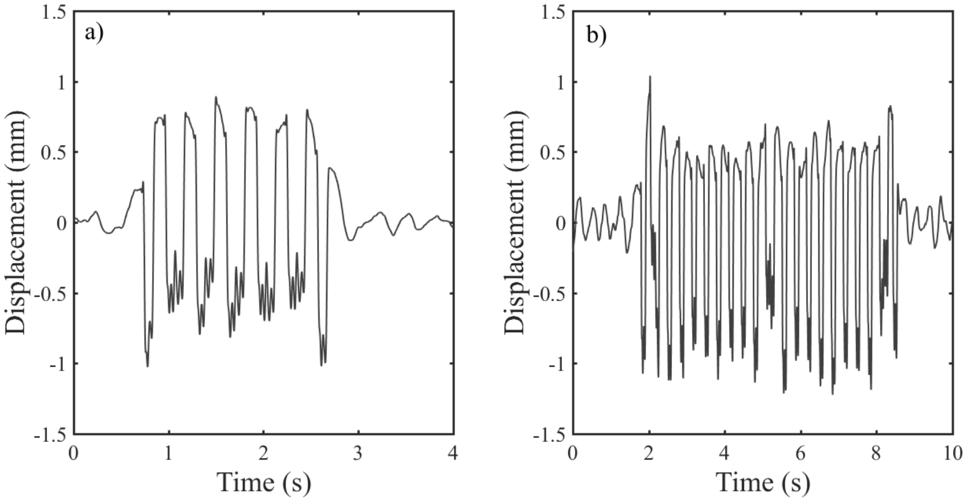

Figure 4.14 Track displacement data obtained using an X16 self-contained MEMS accelerometer and data aquistion system for (a) a Javelin and (b) a Eurostar, sampled at 400 Hz and filtered with 2 and 40 Hz high- and low-pass cutoffs before integration.

Self-logging digital accelerometers have also enabled development of instrumented ballast grains, in which the accelerometers have been embedded into ballast grains as shown in Figure 4.15 (Milne et al., 2016a). Data from these sensors has been used for studies on ballast flight phenomena (Soper et al., 2017) and ballast vibration (Zhang et al., 2016) More details of this are given in Appendix C.

Figure 4.15 Instrumented ballast grain.

4.5 Conclusions

Laboratory trials have shown that data from MEMS accelerometers generally agree with data from higher quality geophones. This was tested using low frequency sinusoidal signals, a frequency sweep and simulated track deflection signals in the frequency range applicable to track deflection for a plausible range of train speeds and deflection amplitudes. Results were compared in both the time and frequency domains with good agreement. Generally, reproduction of measured track deflections improves for larger deflections and faster trains.

The low-cost sensors were shown to be suitable for lineside monitoring on high speed railways through field trials. Good agreement was found between geophones and the accelerometers for a range of track conditions. On occasions however, the MEMS result was affected by low frequency phenomena, leading to spurious amplification seen in some time histories for track deflection. It is difficult to ascertain whether this was due to poor transducer performance at low frequency or sleeper rotation, which would affect a MEMS transducer but not a geophone. To investigate this further it would be worthwhile to extend lineside monitoring measurements to study sleeper rotation using a gyroscope. The larger dynamic range of a MEMS sensor means that it will remain functional in poor track conditions where the track velocities may exceed the operational range of a geophone on high speed track. This means MEMS accelerometers are well suited for making measurements of poorly performing track in defect zones.

It is concluded that the MEMS accelerometers considered would be a suitable transducer for a lineside monitoring system used for extended deployments on a high-speed railway with speeds greater than 55 m/s, particularly in defect zones where track movements may be severe. As MEMS sensors are small it is practical to ruggedize the sensor for extended deployment. For research purposes, the reduction in cost over a geophone means that larger or dedicated deployments are possible and the risk of damage to a sensor is more acceptable. This means that trialling long-term lineside monitoring deployments and using the resulting data to study deterioration is feasible. This is demonstrated by the application of these technologies in this way described in Chapters 8 and 9. In an industrial context, the lower cost may mean that the business case for deploying such a system is stronger. Successful use of digital sensors combined with low-cost microcontrollers for data acquisition, transmission or storage depends on the specification of the microcontroller and data acquisition software.

Chapter 5: Lineside monitoring: Low frequency track vibration

5.1 Introduction

A system for lineside monitoring suitable for long term or larger monitoring deployments requires methods for analysing and interpreting the track vibration data that can be automated. In Chapter 4 it was shown that low-cost transducer technologies that could enable larger, longer term deployments at reasonable cost are suitable for use on the track. Extended deployments have the potential to provide data at regular enough intervals to determine how the performance of the track is changing. Large quantities of track vibration data will need to be processed and interpreted in order to study the changes. This chapter uses the BOEF model to study the properties of low frequency track vibration signals. The sensitivity of the trainload dominant frequency to train geometry, vehicle geometry and variation in wheel loads is investigated. The properties are used in Chapter 6 to develop new methods to identify the train type in each vibration record and characterise the magnitude of track displacement, as well as in Chapter 7 to develop new methods to determine the track system support modulus in the frequency domain. Some of the material in this Chapter have been published in Le Pen et al. (2016) and Milne et al. (2017).

5.2 Low frequency track vibration

Processed track vibration data can be used to obtain track deflection signals such as those shown in Figure 5.1. These results are for the Crissmill plain line site described in Chapter 3, and were obtained using geophones for all the train types operated on HS1.

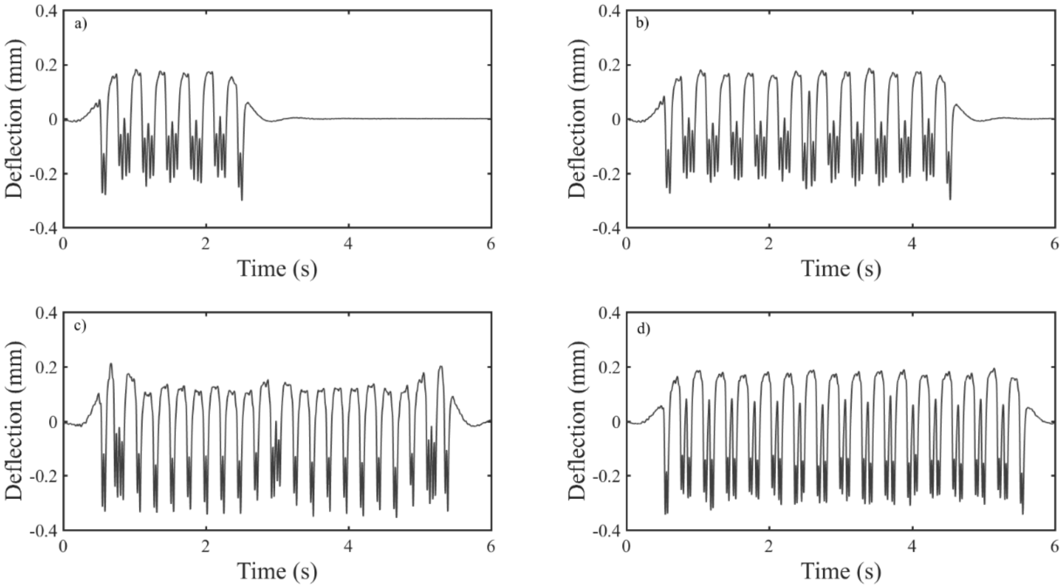

Figure 5.1 Example track deflections for each train type operating on HS1. Obtained using geophones sampled at 500 Hz. Filtered for integration using 2 Hz and 40 Hz cut-off frequencies. (a) Six-vehicle Javelin, (b) two six-vehicle Javelin coupled together, (c) 20-vehicle Eurostar, (d) 16-vehicle Velaro.

Chapter 2 discussed how different models can be used to simulate and understand track vibration signals, depending on the behaviours of interest. Here, neglecting inertial effects and rail roughness, the BOEF model is used to study the fundamental deflection behaviour of railway track.

Consider an Euler-Bernoulli beam, representing a rail with bending stiffness *EI*, on a uniform elastic foundation with a system support modulus *k*, as shown in Figure 5.2.

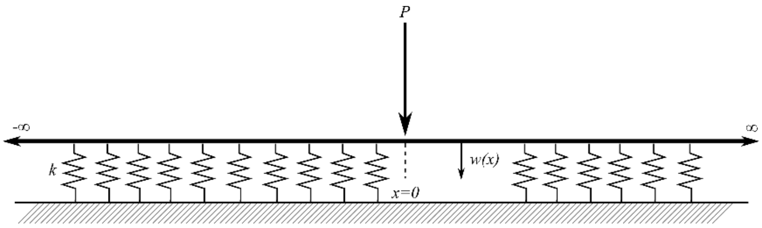

Figure 5.2 Beam on and elastic foundation subject to a point load.

The static deflection *w* at a distance *x* along that beam obeys the governing equation:

$$EI\frac{d^4w(x)}{dx^4} + kw(x) = 0 \tag{5.1}$$

For the deflection w due to a single load P acting at x=0 this has the solution:

$$w(x) = \frac{P}{2kL}\mathrm{e}^{-\frac{|x|}{L}}\left(\cos\left(\frac{|x|}{L}\right) + \sin\left(\frac{|x|}{L}\right)\right) \tag{5.2}$$

where L is the characteristic length:

$$L = \sqrt[4]{\frac{4EI}{k}} \tag{5.3}$$

A point on the track subject to a load moving at a constant speed v experiences this deflection as a function of time $t = x/v$. The solution for the time-varying displacement of the track at a point due to a moving unit load may therefore be written:

$$w(t) = \frac{P}{2kL}\mathrm{e}^{-\frac{v|t|}{L}}\left(\cos\left(\frac{v|t|}{L}\right) + \sin\left(\frac{v|t|}{L}\right)\right) \tag{5.4}$$

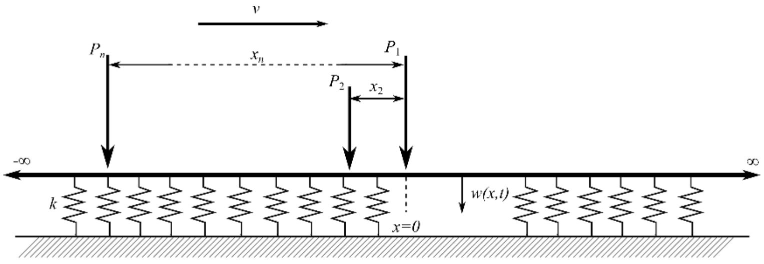

Figure 5.3 Beam-on-elastic-foundation subject to a train of moving loads.

For a train of moving loads P_m, each separated from the first load by a distance, x_m, as shown in Figure 5.3, the total rail deflection can be found by summing the effect of each wheel load.

$$w(t) = \sum_m \frac{P_m}{2kL}\mathrm{e}^{-\frac{v\left|t-\frac{x_m}{v}\right|}{L}}\left(\cos\left(\frac{v\left|t-\frac{x_m}{v}\right|}{L}\right) + \sin\left(\frac{v\left|t-\frac{x_m}{v}\right|}{L}\right)\right) \tag{5.5}$$

Figure 5.4 shows example rail deflections obtained using Eq.(5.5) for a six vehicle Javelin with wheel loads of 65 kN, moving at a speed of 60 m/s along a track with a UIC 60 rail (EI = 6.42 MNm^2) and track system support modulus per rail of 40 MN/m^2. These track properties are typical of HS1.

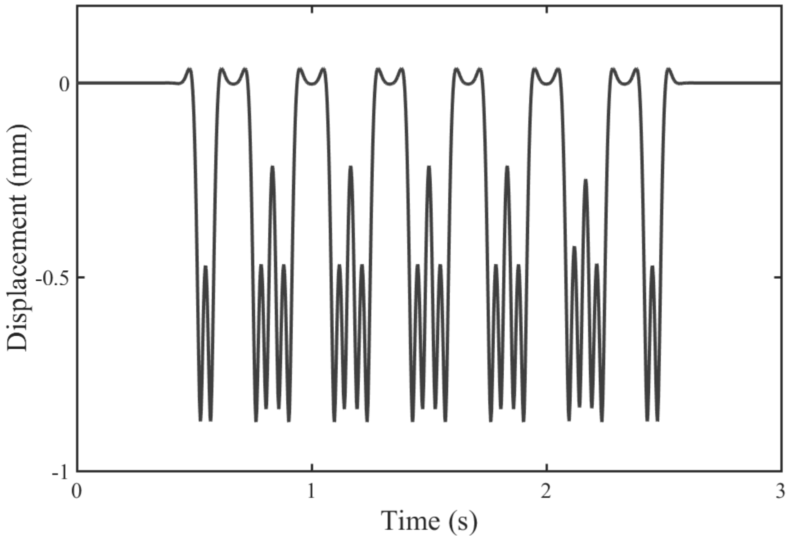

Figure 5.4 Rail deflections obtained using Eq.(5.5) for a train comprising six 20 m vehicles with wheel loads of 65 kN, moving at 60 m/s along a track with a UIC 60 rail and a track system support modulus of 40 MN/m^2.

As discussed in Chapter 2, the track system support modulus is an important parameter for the static (and quasi-static) deflection of the track. It influences both the amplitude and width of the deflection beneath a wheel load, and hence interaction between wheels. Figure 5.5(a) shows the deflection with different track system support moduli for a load of 50 kN. By plotting the deflection normalised by its maximum value, it is clear that the deflection bowl increases in width as the track system support modulus reduces (Figure 5.5(b)). As the width of the deflection bowl increases the interaction where the is overlap between adjacent wheels is more significant, leading to reduced recovery between wheels on softer track.

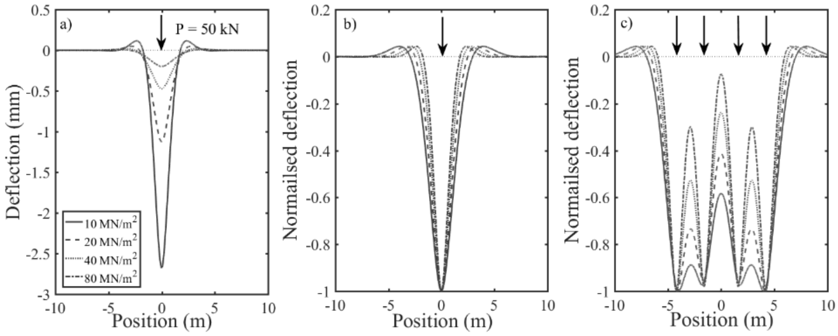

Figure 5.5(a) Static deflection of a UIC 60 rail on elastic foundation with a range of plausible track system support moduli subject to a 50 kN point load, (b) normalised deflection for the same track, (c) normalised deflection for the same track due to wheels on the bogies from adjacent vehicle ends.

Eq.(5.5) is a convolution of the solution for a single unit moving load *d*(*t*), obtained by setting $P = 1$ in Eq.(5.4) and a sequence of loads *f*(*t*) representing the wheel loads of a train (Le Pen et al., 2016).

$$w(t) = d(t) * f(t) \tag{5.6}$$

The load function *f*(*t*) can be written as a sequence of Dirac delta functions.

$$f(t) = \sum_m P_m \delta\left(t - \frac{x_m}{v}\right) \tag{5.7}$$

The convolution in Eq.(5.6) corresponds to a product in the frequency domain.

$$W(f) = D(f)F(f) \tag{5.8}$$

where *D*(*f*) and *F*(*f*) are the Fourier transforms of *d*(*t*), and *f*(*t*), respectively. This means that the influence of the track and the train of loads on the spectrum of track vibration can be studied independently of each other. Figure 5.6 shows the Fourier transform for the example rail deflections shown in Figure 5.4 obtained using Eq.(5.8).

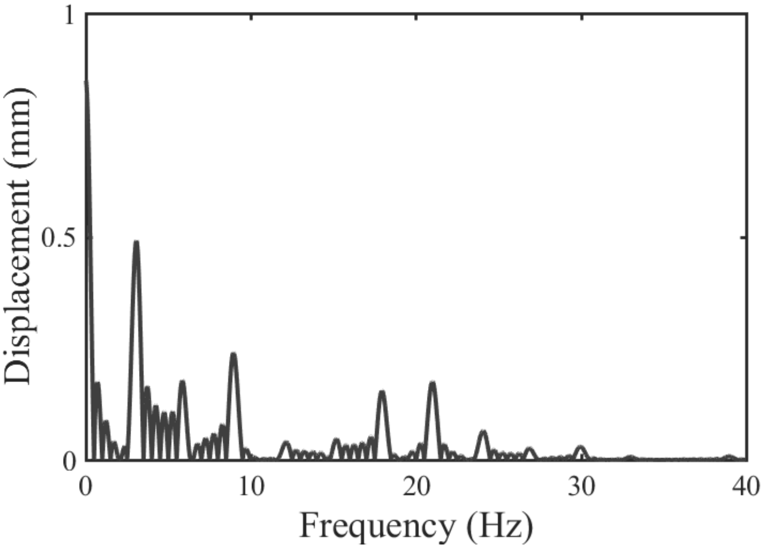

Figure 5.6 Fourier transform for example rail deflections from Figure 5.4 obtained using Eq.(5.8).

An important property discussed in Chapter 2 is that the dominant frequencies in spectra of low frequency track vibration occur close to multiples of the vehicle-passing frequency (see Eq.(2.1)). This property arises due to repetition of near identical vehicles within a train, and be seen clearly in both the spectrum from the BOEF model in Figure 5.6, as well as in spectra of vertical velocity measured on the sleeper for each of the four train types that operate on HS1 in Figure 5.7. These results were obtained from the velocity signals used to obtain the track deflections shown in Figure 5.1. The frequency axis has been non-dimensionalised by the vehicle-passing frequency so that $N=f/f_1$.

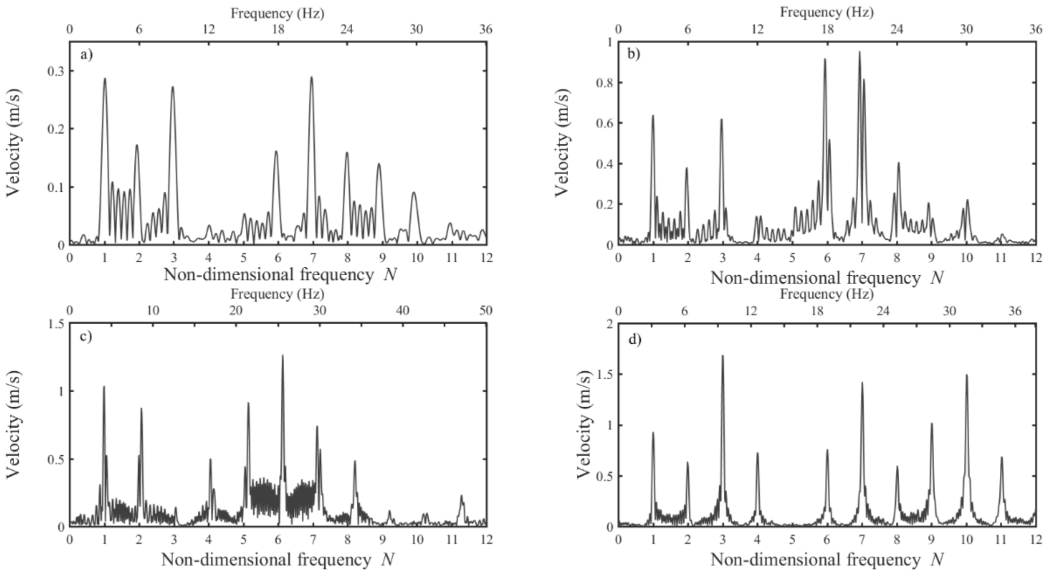

Figure 5.7 Spectra of sleeper velocity measurements plotted against non-dimensional frequency $N=f/f_1$ for (a) six vehicle Javelin, (b) two six-vehicle Javelin coupled together, (c) 20-vehicle Eurostar, (d) 16-vehicle Velaro.

Here, a further study of the role of the track and the dominant train load frequencies is presented. This leads to a more in-depth understanding of their properties, which are used to develop methods for interpreting spectra from lineside measurements in Chapters 6 and 7.

5.3 Role of the track

First, it is useful to consider the effect of the track on the spectrum of low frequency track vibration. The Fourier transform of the deflection of a BOEF subject to a moving unit load is given by:

$$\begin{aligned} S(f) &= \frac{1}{2kL}\int_{-\infty}^{\infty} \mathrm{e}^{-\frac{v|t|}{L}}\left(\cos\left(\frac{v|t|}{L}\right)+\sin\left(\frac{v|t|}{L}\right)\right)e^{-i2\pi ft}\,\mathrm{d}t \\ &= \frac{2v-\mathrm{i}2L\pi f}{2k(v^2+(v-\mathrm{i}2L\pi f)^2)}+\frac{2v+\mathrm{i}2L\pi f}{2k(v^2+(v+\mathrm{i}2L\pi f)^2)} \\ &= \frac{4v^3}{4kv^4+16\pi^4kL^4f^4} \end{aligned} \tag{5.9}$$

The corresponding Fourier transforms of track velocity and acceleration may be obtained by multiplication by $i2\pi f$ and $-4\pi^2f^2$, respectively.

Figure 5.8(a) shows the track deflection obtained from Eq.(5.4) for a 50 kN load moving at 50 m/s, for a range of plausible track system support moduli. Figure 5.8(b) shows the magnitude of the corresponding Fourier transforms normalised with respect to the maximum deflection in each case. The frequency axis has been expressed in terms of the non-dimensional frequency normalised vehicle-passing frequency for a Javelin vehicle (20 m length). These results show the influence of the track stiffness in both the time and the frequency domains. Increasing the track system support modulus shortens the deflection bowl in the space or time domain and increases the relative importance of the higher frequency components in the frequency domain. This is an important property because the shape of the spectrum of measured track vibration depends on the system support modulus, which means the spectrum of track vibration can be used to determine the track system support modulus (Chapter 7).

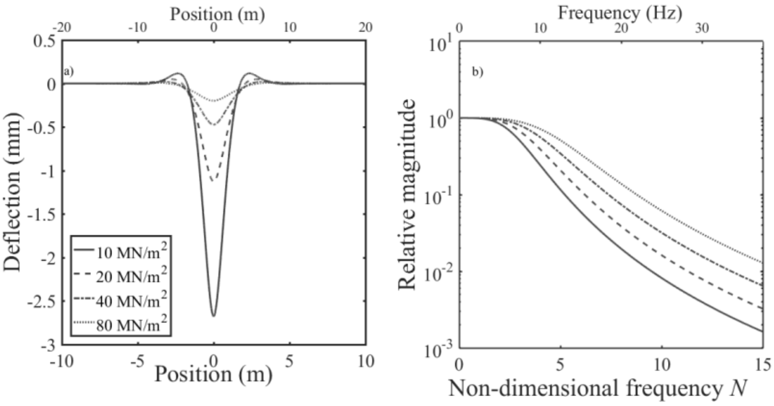

Figure 5.8 (a) Track deflection due to a 50 kN moving load at 50 m/s for a range of track support moduli, (b) Normalised magnitude of the Fourier transform for track deflection for non-dimensional frequency for a range of track support moduli.

5.4 Role of the train geometry

A train of moving wheel loads, P_m, separated from the first load by distance, x_m, can be represented as a series of Dirac delta functions (Eq.(5.7)). The Fourier transform of Eq.(5.7) describes the frequency content of the loading:

$$F(f) = \int_{-\infty}^{\infty} \sum_{m} P_m \delta\left(t - \frac{x_m}{v}\right) e^{-i2\pi f t}\,\mathrm{d}t \;= \sum_{m} P_m e^{-\frac{i2\pi f x_m}{v}} \qquad (5.10)$$

The most prominent frequencies in the load spectrum depend on the geometry of the train and the relative amplitudes of the wheel loads. If the wheel loads are equal, the frequencies and magnitudes depend only on the train geometry.

Trains often consists of repeating near-identical vehicles with the same axle configuration, giving periodicity in the loading. This periodicity causes the dominant frequencies to occur close to multiples of the vehicle-passing frequency. This is implicit in Eq.(5.7) and therefore Eq.(5.10). In this section, explicit consideration of vehicle geometry both in idealised and realistic configurations is used to show the importance of train geometry, train length and vehicle geometry for the dominant train load frequencies and their magnitudes.

The Javelin and the Velaro trains contain only vehicles with the same axle configuration and near-uniform wheel loads. This type of train may be described as ‘periodic’. Initially, only periodic trains are considered as the properties of their Fourier transform explain both the *frequency* and *magnitude* of the peaks in the train load spectra. Later, the effects from coupling two trainsets together and having multiple vehicle types within a train are considered with reference to a 12 car Javelin and a Eurostar. Examples shown are based on the Javelin vehicle geometry (see Table 3.1) unless otherwise stated.

5.4.1 Infinite train

Consider an infinitely long train consisting only of identical repeating vehicles. As this infinite train is periodic, the train loads can be represented as a Fourier series. In this form, the frequencies of loading only exist at integer multiples (N) of the vehicle-passing frequency. The amplitudes of these discrete frequencies are the Fourier series coefficients, U_N, which can be evaluated over one period of the train, L_v/v. It is convenient to define one period as a single vehicle (Figure 5.9).

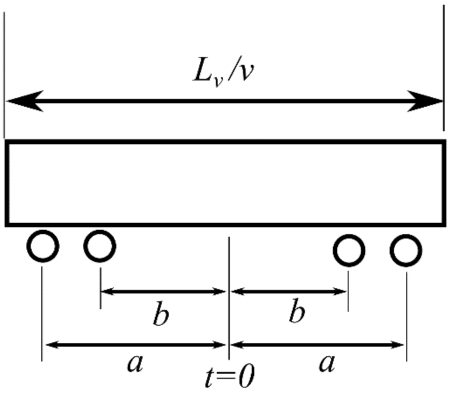

Figure 5.9 A single repeated vehicle, $a=(L_b+L_w)/2v$, $b=(L_b–L_w)/2v$.

Thus, the load function can be written as:

$$f(t) = \sum_{N=-\infty}^{\infty} U_N e^{-\frac{i2\pi Nvt}{L_v}} \tag{5.11}$$

and the Fourier series coefficients are found from:

$$U_N = \frac{v}{L_v}\int_{-\frac{L_v}{2v}}^{\frac{L_v}{2v}} \big(\delta(t+a)+\delta(t+b)+\delta(t-b)+\delta(t-a)\big)e^{-\frac{i2\pi Mvt}{L_v}}\,dt$$

$$= \frac{v}{L_v}\left(e^{\frac{i2\pi Nav}{L_v}} + e^{\frac{i2\pi Nbv}{L_v}} + e^{-\frac{i2\pi Nbv}{L_v}} + e^{-\frac{i2\pi Nav}{L_v}}\right) \tag{5.12}$$

where $a = (L_b + L_w)/2v$, $b = (L_b – L_w)/2v$.

This can be rearranged to give:

$$U_N = 4\frac{v}{L_v}\cos\left(\frac{\pi N L_b}{L_v}\right)\cos\left(\frac{\pi N L_w}{L_v}\right) \tag{5.13}$$

Eq.(5.13) describes the relative amplitudes of the discrete train-load frequencies that occur at integer values of N for an infinite train. Figure 5.10 shows the magnitude of these (i.e. positive values), with the factor $4v/L_v$ omitted, evaluated at the first 12 integer values of N for the Javelin vehicle geometry. This function has also been plotted for continuous values of N, which shows how the function envelopes the values at the discrete frequencies.

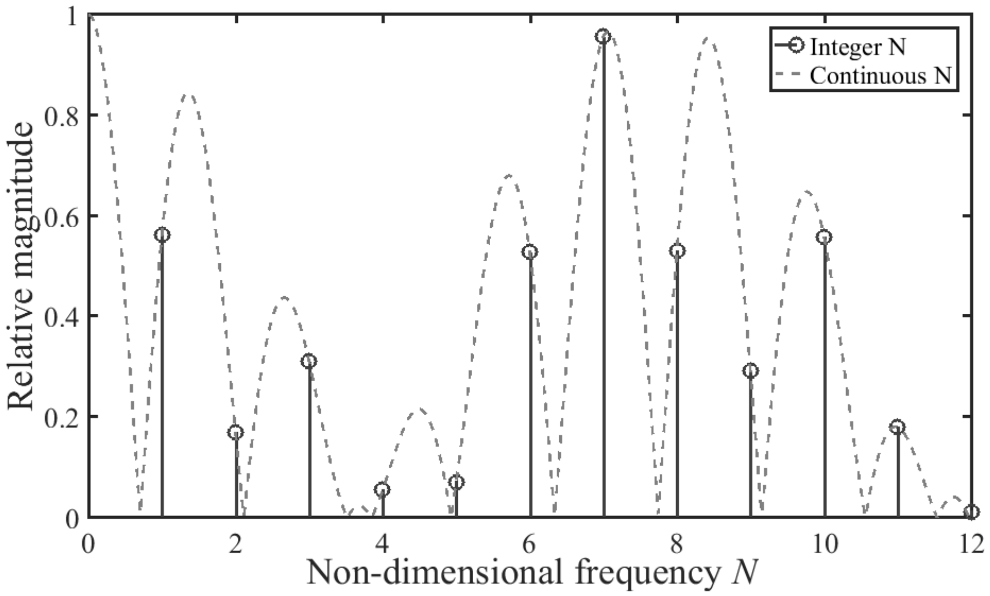

Figure 5.10 Discrete load frequencies for an infinite train consisting of 20 m long Javelin vehicles and weighting function due to vehicle geometry from Eq.(5.13).

The train loading frequencies of an infinite periodic train are thus discrete and occur at integer multiples of the vehicle-passing frequency. However, for a finite length train the trainload spectrum is continuous and obtained from a Fourier transform $F(f)$ rather than a Fourier series. This will now be explored for a single vehicle, a train with an explicit periodic structure and a train that consists of more than one vehicle type.

5.4.2 Single vehicle

The train load spectrum for a single vehicle, with four equal wheel loads P, is found from the Fourier transform:

$$F(f) = P \int_{-\infty}^{\infty} \big(\delta(t+a) + \delta(t+b) + \delta(t-b) + \delta(t-a)\big) e^{-i2\pi f t}\, dt$$

$$= P\big(e^{i2\pi f a} + e^{i2\pi f b} + e^{-i2\pi f b} + e^{-i2\pi f a}\big) \qquad (5.14)$$

where $a = (L_b + L_w)/2v$, $b = (L_b - L_w)/2v$ as before.

This can be normalised and expressed in terms of the non-dimensional vehicle-passing frequency N (which is now not necessarily an integer):

$$F(N) = 4\,P\cos\left(\frac{\pi N L_b}{L_v}\right)\cos\left(\frac{\pi N L_w}{L_v}\right) \qquad (5.15)$$

The shape of the load spectrum for a single vehicle, Eq.(5.15) is given by the same function that describes the Fourier series coefficients for an infinite train, Eq.(5.13) However, Eq.(5.15), is the continuous train loading spectrum for a single vehicle whereas the mathematically equivalent Eq.(5.13) weights the discrete frequency components for an infinite train. These expressions depend on the regular wheel separations defined by the axle and bogie spacings. Figure 5.11 shows the two cosine functions in these equations and how they combine to form the load spectrum for a single vehicle; for clarity, these are shown as magnitudes, i.e. always positive values. For the single vehicle (Figure 5.11(c)) the spectral peaks are broad; they do not occur at integer multiples of the vehicle-passing frequency, but depend on an interaction between the axle spacing (Figure 5.11(a)) and the bogie spacing (Figure 5.11(b)). In the spectrum, certain frequencies are suppressed; these occur when Eq.(5.15) is equal to zero, i.e. at $N=rL_v/2L_w$ from the axle spacing and $N=rL_v/2L_b$ for the bogie spacing, where r = 1, 3, 5… These suppressions arising from the axle and bogie spacings, are periodic in the frequency domain, although in general the combined function is not.

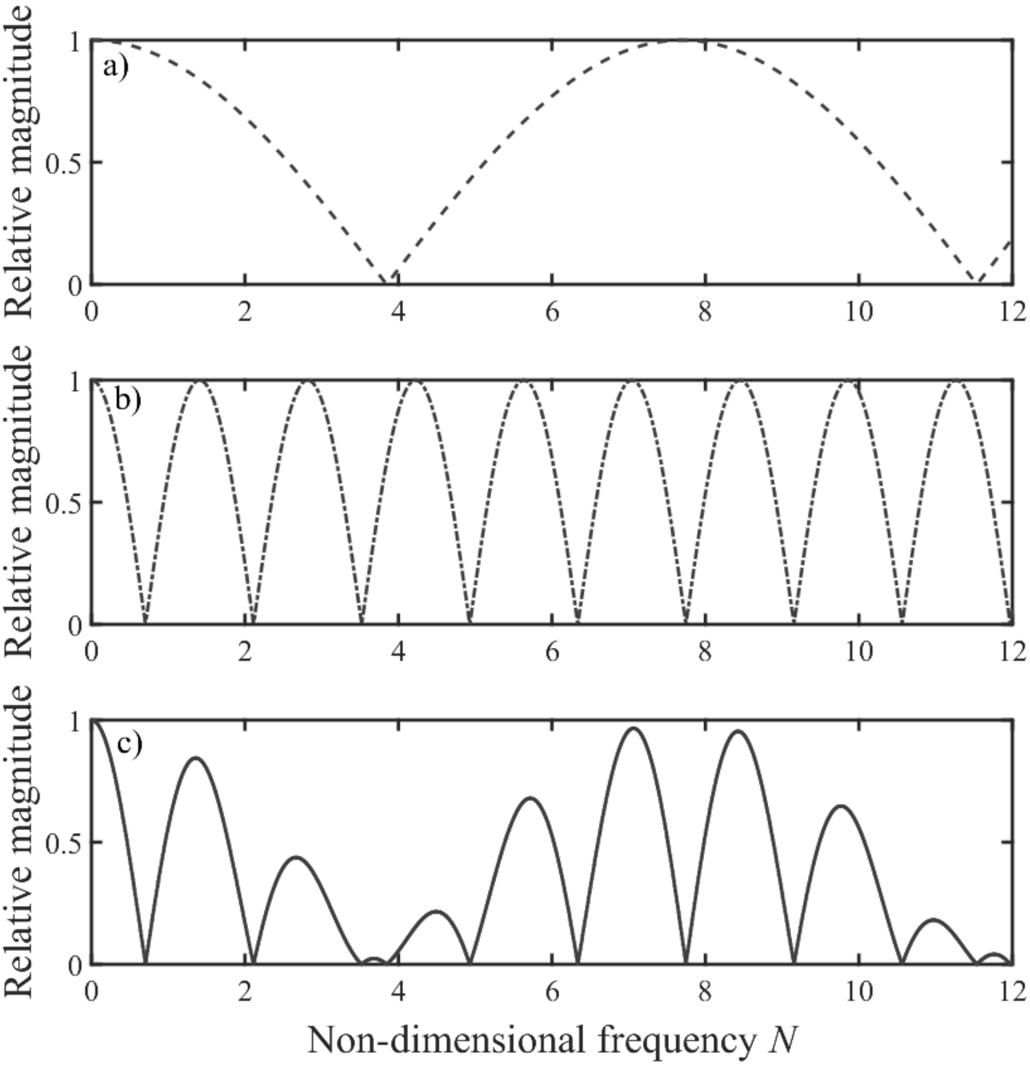

Figure 5.11 Components of the single vehicle spectrum (a) contribution of axle spacing (b) contribution of bogie (c) single vehicle spectrum for a 20 m Javelin vehicle from Eq.(5.15).

5.4.3 Periodic train

For a train consisting of a number of near-identical vehicles, the resulting periodicity gives rise to a train loading spectrum that exhibits properties similar to those for an infinite train. The Fourier transform of the wheel loading function from a train of N_C cars is found from:

$$F(f) = \mathrm{P} \sum_{m=0}^{N_c - 1} \int_{-\infty}^{\infty} \left(\delta\left(t + a - \frac{mL_v}{v}\right) + \delta\left(t + b - \frac{mL_v}{v}\right) \right.$$
$$\left. + \delta\left(t - b - \frac{mL_v}{v}\right) + \delta\left(t - a - \frac{mL_v}{v}\right) \right) e^{-i2\pi f t} dt$$
$$= P \sum_{m=0}^{N_c - 1} e^{-i2\pi f \frac{mL_v}{v}} \left(e^{i2\pi f a} + e^{i2\pi f b} + e^{-i2\pi f b} + e^{-i2\pi f a}\right) \tag{5.16}$$

where a and b are as before. This can be rearranged and written in terms of the non-dimensional frequency:

$$\mathrm{F}(N) = 4P \cos\left(\frac{\pi N L_b}{L_v}\right) \cos\left(\frac{\pi N L_w}{L_v}\right) \sum_{m=0}^{N_c - 1} e^{-i2\pi N m} \tag{5.17}$$

Eq.(5.17) contains two parts: a weighting function and a series. The weighting function is identical to the spectrum for a single vehicle, Eq.(5.15), and the function for the Fourier series coefficients for an infinite train, Eq.(5.13). The axle and bogie spacings are responsible for the suppression of certain frequencies in the spectrum, as before.

Figure 5.12 shows the magnitude of the series term in Eq.(5.17) for increasing numbers of vehicles. This implicitly contains information about the train’s periodicity. For two or more vehicles, there will be a peak at the vehicle-passing frequency and integer multiples of it. As the number of repeating vehicles within the train increases, the spectral peaks become narrower at these frequencies, but do not reduce in magnitude. For N_C vehicles, there are $N_C - 1$ subsidiary peaks between each main peak.

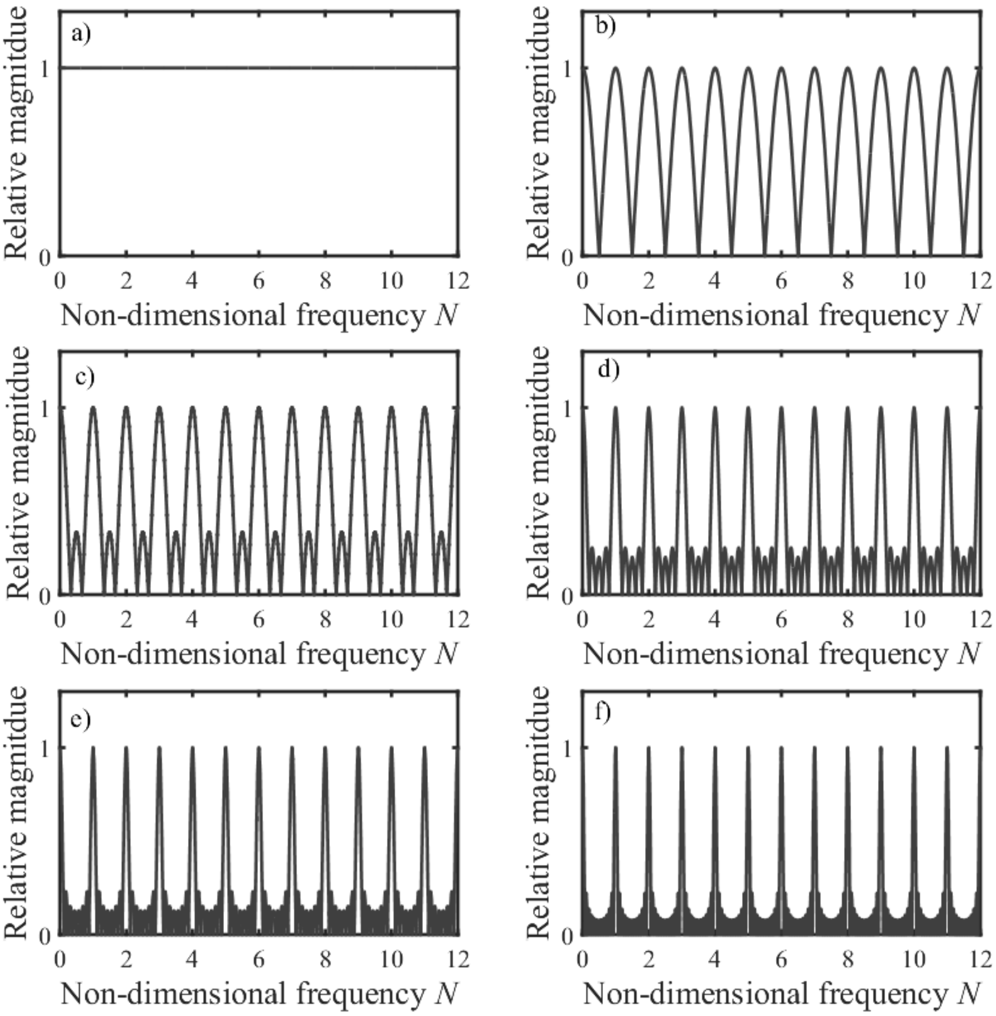

Figure 5.12 Effect of increasing the number of vehicles in a train on the train load spectrum due to the series in Eq.(5.17) length of: (a) 1 vehicle; (b) 2 vehicles; (c) 3 vehicles; (d) 5 vehicles; (e) 8 vehicles; (f) 13 vehicles.

Combining these results with the weighting function from Figure 5.11(c), the normalised full load spectrum determined from Eq.(5.17) is obtained as shown in Figure 5.13 for trains consisting of Javelin vehicles. Here, the spectral peaks do not occur exactly at integer multiples of the vehicle-passing frequency, especially for short trains. However, as the number of vehicles increases, the peaks increase in sharpness and tend to integer multiples of the vehicle-passing frequency.

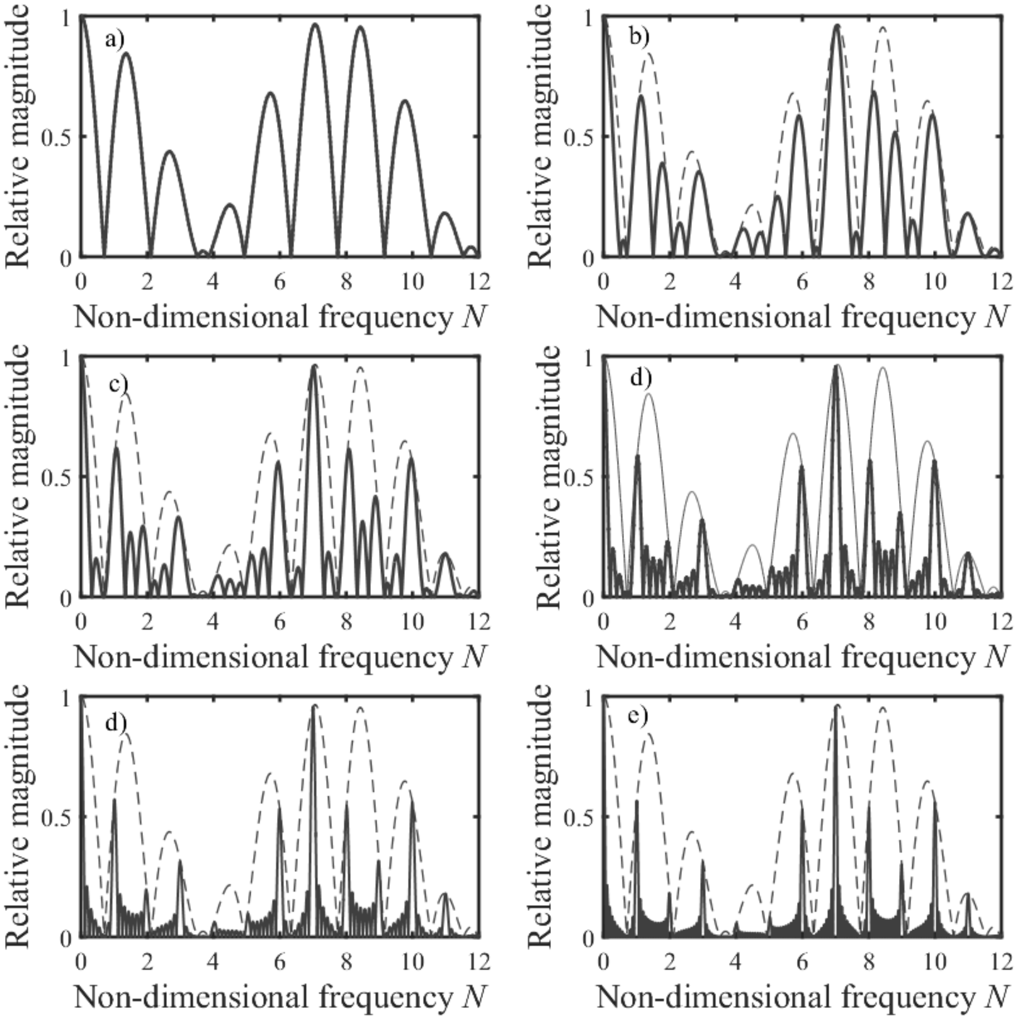

Figure 5.13 Normalised train load spectrum for a train of 20 m Javelin vehicles comprising: (a) 1 vehicle; (b) 2 vehicles; (c) 3 vehicles; (d) 5 vehicles; (e) 8 vehicles; (f) 13 vehicles. Single vehicle spectrum '- - -', from Eq.(5.17).

Now, the relative magnitudes of these peaks are modulated by the weighting function. This means that Eq.(5.13) or (5.15) can be used to determine the magnitude of the peak at multiples of the vehicle-passing frequencies for periodic trains, using the vehicle geometry alone. This is shown in Figure 5.14 for (a) the Javelin and (b) the Velaro, using the full train geometry and the weighting from a single vehicle. These results for the full train geometry have a similar shape to those shown in Figure 5.7(a) and (d), but with different amplitudes.

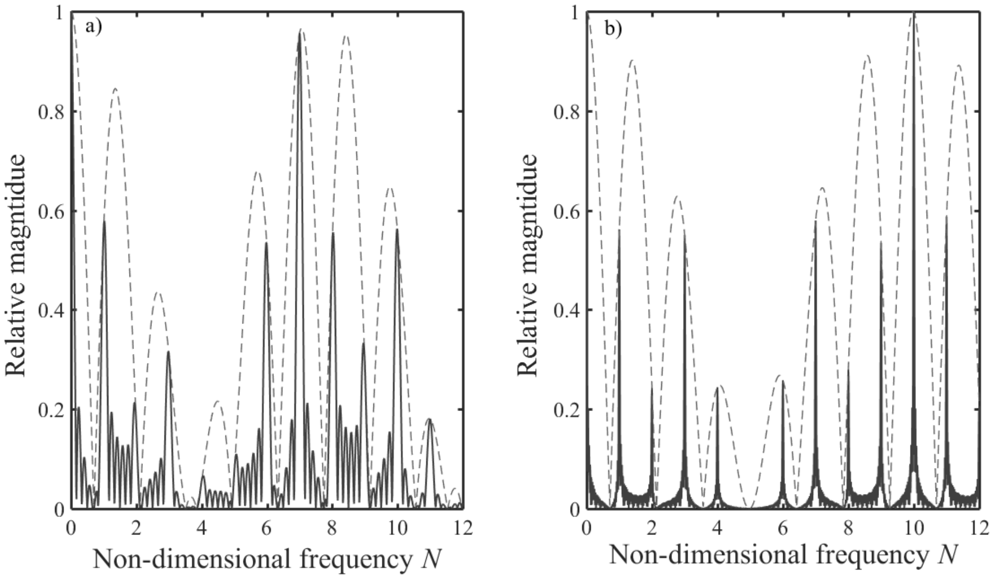

Figure 5.14 Normalised train load spectrum '—' and weighting '- - -' from a single vehicle for (a) Javelin and (b) Velaro.

5.4.4 Effect of coupled of trainsets

Trainsets are often coupled to form longer trains, for example the 12 vehicle Javelin. The coupling length between trainsets may be different from the coupling length between vehicles within a trainset. This introduces a phase shift between trainsets, which can cause localised suppressions of peaks as seen in Figure 5.15, which shows results for coupled Javelin trainsets. This can also lead to twin peaks, such as that close to the 7th harmonic of the vehicle-passing frequency, shown in the insert within Figure 5.15. This can also be seen in the measured results in Figure 5.7(b).

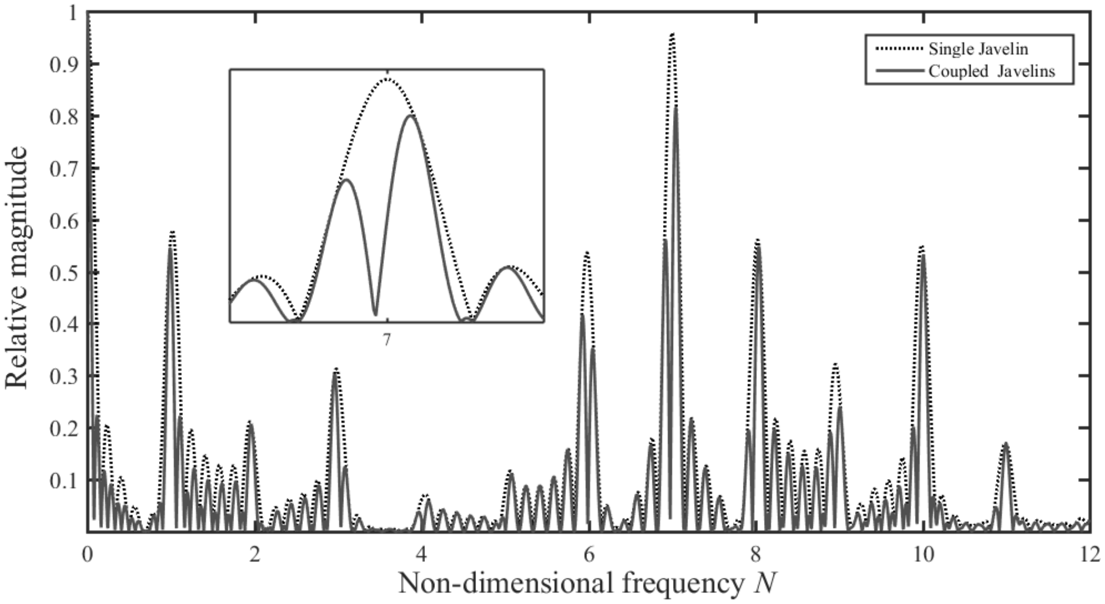

Figure 5.15 Relative magnitude of the Fourier transform for the train loads from a six vehicle Javelin trainset and two six vehicle trainsets with an additional coupling length of 1.4 m.

The Fourier transform for two coupled trainsets $F_c(N)$, can be written as the Fourier transform for the single trainset $F(N)$, together with a phase shift:

$$F_c(N) = F(N)\left(1 + e^{\frac{-i2\pi N(L_t+L_c)}{L_v}}\right) \tag{5.18}$$

where L_t is the trainset length and L_c is the additional coupling length. The effect on the spectrum depends on the phase difference introduced by the coupling between the two trainsets.

5.4.5 Effects of multiple vehicle lengths and coupling

The Eurostar consists of two coupled trainsets of 10 vehicles each (Figure 5.1(c)). Each trainset contains three different vehicle types: seven articulated passenger vehicles, two semi-articulated passenger vehicles, and a powered driving vehicle with conventional bogies. Figure 5.16 shows the relative magnitudes calculated for the nine articulated vehicles, a single trainset and two coupled trainsets forming a complete 20 vehicle train. When only the passenger vehicles are considered (Figure 5.16(a)), the train has a periodic structure; the spectral peaks are at the multiples of the vehicle-passing frequency and their amplitudes can be obtained from Eq.(5.13) or Eq.(5.15). For these articulated vehicles, the weighting function depends only on the axle spacing. The introduction of a vehicle with a different geometry changes the spectrum (Figure 5.16(b)): the spectral peaks remain close to integer multiples of the vehicle-passing frequencies but their magnitudes are reduced. Coupling two trainsets changes the spectrum further (Figure 5.16(c)), splitting certain peaks. Furthermore, the different vehicle types from the Eurostar have different wheel loads. This is accounted for in Figure 5.16(d) using Eq.(5.3). Using the actual distribution of static wheel loads along the train has a negligible effect on the magnitudes or frequencies of the dominant frequencies.

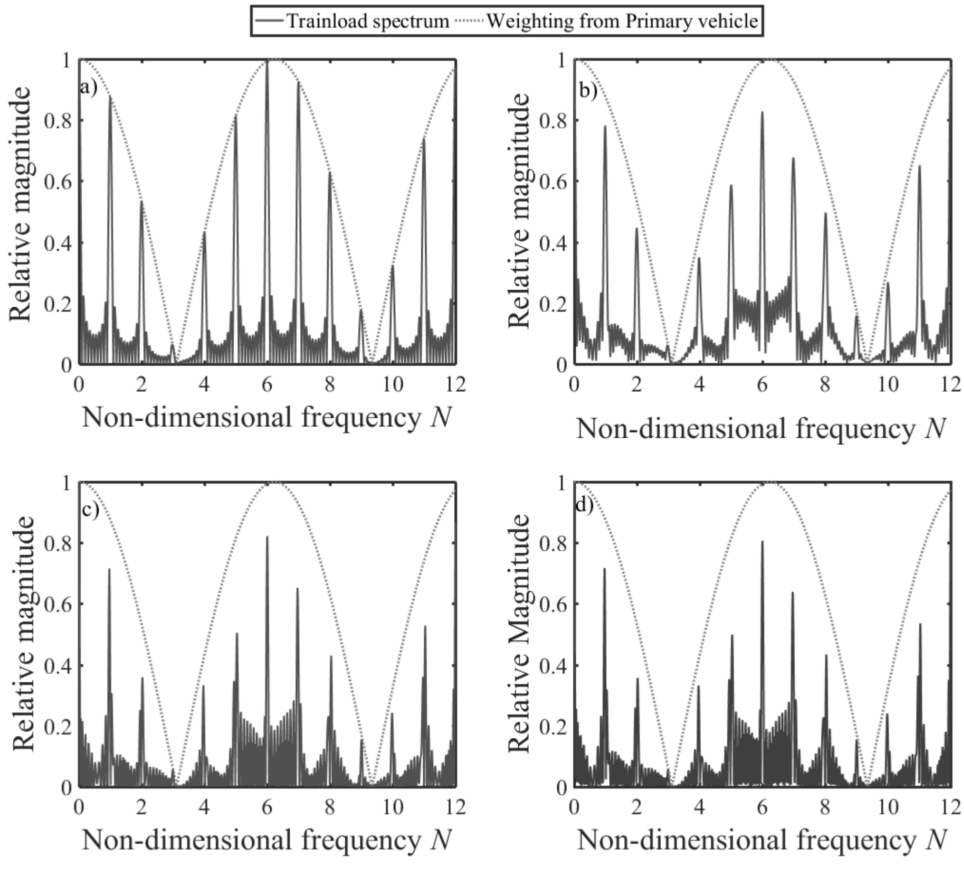

Figure 5.16 Relative magnitude of the Fourier transform for the train loads of: (a) the passenger saloons in a Class 373 Eurostar trainset; (b) drive car and passenger saloons in a single Eurostar trainset; (c) two coupled Eurostar trainsets; (d) two coupled trainsets with correct wheel loads.

5.4.6 Implications

This chapter has shown that for trains with a periodic structure, as the number of vehicles in the train increases, the spectral peaks occur at approximately integer multiples of the vehicle-passing frequency. Eq.(5.13) can thus be used to determine the magnitude of these peaks in the load spectrum. For trains with inhomogeneous geometries, these peaks are still likely to occur close to multiples of the vehicle-passing frequency for the primary vehicle type. However, the full train geometry, and possibly the variation in axle load, must be considered to determine the relative magnitudes of the spectral peaks. Coupling of trainsets changes the magnitudes and can lead to certain peaks close to multiples of the vehicle-passing frequency being split into two. This may make it more challenging to define which peak is dominant and to calculate an appropriate relative magnitude.

Knowledge of the frequencies and relative magnitudes of the dominant train load frequencies for periodic trains is used later in Chapter 7 to develop and then simplify methods for determining the track system support modulus. For this it is important to understand when Eq.(5. 13) is a valid approximation and the relative magnitudes of the train load frequencies can be determined from the vehicle geometry.

For any train with a single vehicle type and equal loads the train load spectra are weighted by the function of vehicle geometry given in Eq.(5. 13). If there are sufficient vehicles in the train, the spectral peaks occur at approximately integer multiples of the vehicle-passing frequency. Eq.(5.13) can thus be used to determine the amplitudes of these peaks in the load spectrum.

However, as shown in Figure 5.12, for shorter trains the peaks will be broader and there will be a difference between the actual and the nominal frequencies (nearest integer multiple of the vehicle-passing frequency) of the peaks. This difference in frequency also affects the relative magnitudes. Figure 5.17 shows the percentage difference in frequency for a Javelin with an increasing number of vehicles. The difference between the actual frequency (the exact frequency of the peak) and the assumed frequency (the nearest integer multiple of the vehicle passing frequency to the peak) is expressed as a percentage of the vehicle-passing frequency: moreover the difference between the actual amplitude (the exact amplitude calculated at the peak) and the nominal amplitude (an approximation found using Eq.(5.13) or (5.15) assuming the peak is at a multiple of the vehicle passing frequency) for each peak is also shown expressed as a percentage of the nominal amplitude. All these results are shown as positive to allow a logarithmic scale to be used. The results for the 7th nominal frequency are less than 0.1% in some cases and thus off the scale in Figure 5.17. Similar trends were obtained for the Velaro.

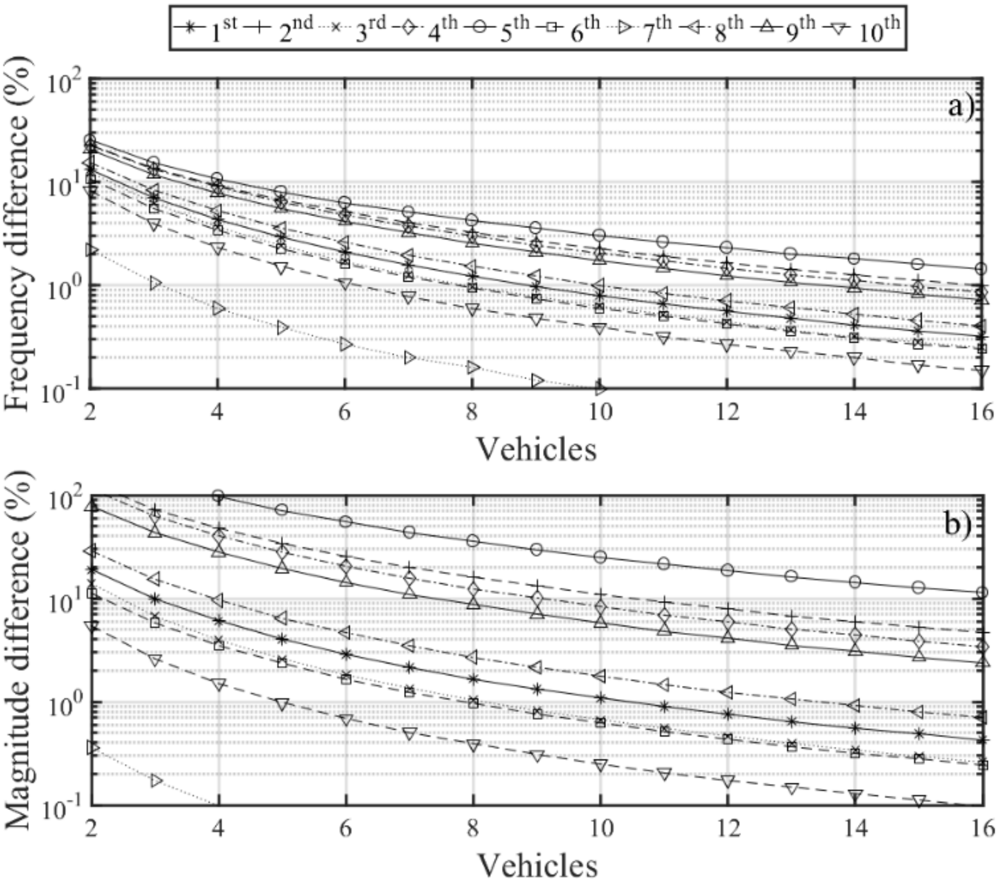

Figure 5.17 Relative differences between (a) actual and nominal frequency and (b) actual and nominal magnitude of spectral peaks in the train load spectrum for a Javelin train with different numbers of vehicles.

The differences in Figure 5.17 vary from one peak to another, depending on whether the peak is near a local maximum or a zero in the single vehicle spectrum. If a nominal frequency is near to a maximum in the single vehicle spectrum, for example the 1st, 3rd, 6th, 7th and 10th nominal frequencies in the present case, the spectral peak will be well-defined for any number of vehicles and there will be only a small difference between the actual and nominal peaks. Although the 8th nominal frequency has a similar magnitude to the 6th, the 6th is closer to the local maximum and therefore subject to a smaller error. If a peak is near a suppressed frequency, for example the 2nd and 5th nominal frequencies, it will be subject to greater error. From Figure 5.14 it can be seen that the 1st, 3rd, 6th 7th and 10th nominal frequencies are close to local maxima in the single vehicle spectrum for all the Javelin and the Velaro trains, whereas the 2nd and 5th nominal frequencies tend to be suppressed. For the Eurostar the 1st, 2nd, 4th, 5th, 7th and 8th are more prominent, with the 6th being the most prominent. The 3rd and 9th nominal frequencies are more suppressed. For the Javelin, the errors in frequency at the 1st, 3rd, 6th 7th and 10th nominal frequencies are less than ±3% of the vehicle-passing frequency.

5.4.7 Effects of variation in wheel load

In the above analysis, it has generally been assumed that all wheel loads are equal. In reality, there will be some variation between wheel loads owing to differences between vehicle equipment, occupancy and dynamic loading effects, which if significant may affect the spectrum. Measured static axle loads for 99 Javelin trainsets passing a weighing-in-motion system, given in Chapter 3 (Figure 3.5 and Figure 3.6) were found to have a relative standard deviation of the axle load of about 4%. Dynamic effects are likely to increase this variation.

Monte-Carlo simulations were performed for 1000 notional trains, in which each wheel load was modelled as a normally distributed random variable with a standard deviation of 4, 5, 10 and 20% of the mean. The track deflections were obtained in the time domain from the beam model and the spectrum was obtained from this numerically using a discrete Fourier transform. The variation in wheel load changes the train load spectrum and causes the magnitudes of the spectral peaks to vary. However, the frequencies do not change. Figure 5.18 shows the relative standard deviation of the magnitude of the spectral peaks for a 4% variation. These are expressed relative to the actual magnitude obtained for equal loads rather than relative to the nominal magnitude, so the errors are in addition to those in Figure 5.17. For greater variations in wheel load, these results increase in proportion to the standard deviation of the wheel load.

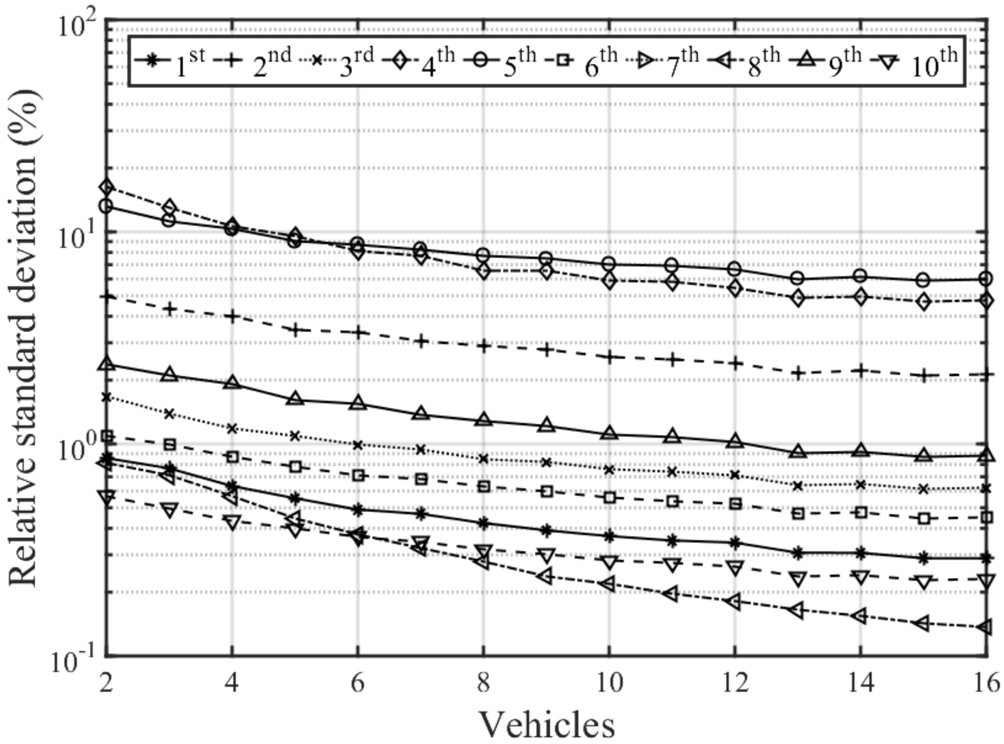

Figure 5.18 Variation of the expected magnitude at each spectral peak for a train consisting of increasing numbers of Javelin vehicles; each wheel load was modelled as a normally distributed random variable with a standard deviation of 4% of the mean load.

The relative standard deviation was found to vary from one peak to another. For this example of a Javelin train, the effects were smallest at the 1^{st}, 3^{rd}, 6^{th}, 7^{th} and 10^{th} nominal frequencies, which are again the dominant frequencies closest to local maxima in the single vehicle spectrum. The relative standard deviation for the 7^{th} nominal frequency was less than 0.1% and is therefore not visible on the graph. For each simulated load variation, the relative standard deviation of the peaks was less than half the specified relative standard deviation of the axle loads, for all train lengths studied, and reduced as the train length was increased. These results show that, for a typical variation in axle load, the effect on the magnitude of the 1^{st}, 3^{rd}, 6^{th}, 7^{th} and 10^{th} nominal frequencies was less than 2%. The magnitudes of these peaks may therefore be calculated reasonably accurately using Eq.(5.13).

5.5 Determination of train speed

The dominant trainload frequencies can be used to determine train speed. For measurements made on or very near the track, this can be done by simply identifying the vehicle-passing frequency and multiplying by the known vehicle length.

In previous studies (Ni et al., 2011; Kouroussis et al., 2013) the speed associated with each dominant frequency was found and an average taken. However, the accuracy of these frequency domain approaches depends on whether the actual frequency of a spectral peak corresponds to an exact multiple of the vehicle-passing frequency, which varies from on peak to another (Figure 5.17(a)). Thus, it is likely to be more accurate (or at least quicker) to identify the vehicle-passing frequency from a spectral peak that theoretically always occurs at an integer multiple of the vehicle-passing frequency f_N (Figure 5.17) and is not influenced by variations in wheel load (Figure 5.18), rather than to find an average speed by using many peaks. For example, N = 7 should be used for the Javelin, N=6 for the Eurostar and N=7 or 10 for the Velaro.

The velocity is obtained from:

$$v = \frac{f_N}{N} \times L_v \tag{5.19}$$

5.6 Conclusion

This chapter has studied the properties of low frequency track vibration signals in the frequency domain. It has been shown that spectra of track vibration depend on the track system support modulus and the train load frequencies. This dependence is used to measure track stiffness in the frequency domain in Chapter 7. The dominant train load frequencies tend to occur at integer multiples of the vehicle-passing frequency, and their frequency and magnitude depend primarily on the trainset geometry. For trains with repeating near-identical vehicles, the dominant frequencies depend on vehicle geometry alone. Variation in wheel load was shown to have a small effect on the spectrum compared with the train or vehicle geometry.

Chapter 6: Interpreting track deflections

6.1 Introduction

Lineside monitoring is often used to obtain track deflection. The routines used to obtain track deflection by filtering and integrating velocity or acceleration measurements can readily be automated. However, the resulting displacement-time histories are normally inspected manually to determine the train type and to obtain a single value of track deflection, taken to be typical or ‘characteristic’ of a train passage. For large volumes of data from continuous monitoring schemes this should be implemented using an algorithm to prevent the process from becoming unmanageable.

This chapter proposes a method for identifying the train type from a track vibration recording and two approaches for classifying the range of track movement. An algorithm for characterising the range of track deflection must account for artefacts from signal processing, including the transients affecting the data around the first and last bogies of the train and the shift in the ‘at-rest position’ within the stationary region of the signal (see Figure 2.7). Additionally, the variability of the signal resulting from differences in occupancy and dynamic behaviour along the train should be taken into account as well as uplift effects between wheelsets. Of the two approaches given, one relies on turning point analysis and the other on analysing the cumulative distribution function (CDF) for track deflection. First, however it is necessary to remove artefacts at the start and end of the data.

6.2 Identifying train types

The analysis methods developed in this chapter and Chapter 7 require knowledge of the train type so the correct train or vehicle geometry, as well as typical loads can be associated with that record for analysis. For long-term lineside monitoring the equipment will be left unattended and it is unlikely that there will be a direct record of which train corresponds to which measurement. It is beneficial if this information can be determined from the vibration signal in advance of other analysis. Two relevant statistics can be found from a track vibration-time history and its spectrum in advance of further analysis. These are the train passage time t_t, the time between the first and last wheels of the train passing the transducer and the vehicle-passing frequency f_1 (Eq.(2.1)).

The duration of the train passage could be estimated from the amount of time the track vibration signal is non-zero (or deviates from the D.C. value), or by using a peak-finding algorithm to identify the first and last wheels of the train. Thresholds might be more appropriate for the native signal (velocity or acceleration), whereas peak finding may be more effective when applied to a displacement signal. An example is shown in Figure 6.1(a) in which a threshold is applied to a velocity signal and (b) in which peak-finding is applied to the displacement signal. The estimate of the train-passing time will depend on the method. Using peak finding to identify the first and last wheels will provide a time that should correspond to the exact wheelbase of the train. However, thresholding the native signal will still provide a reasonable estimate of the passing time, especially for longer trains.

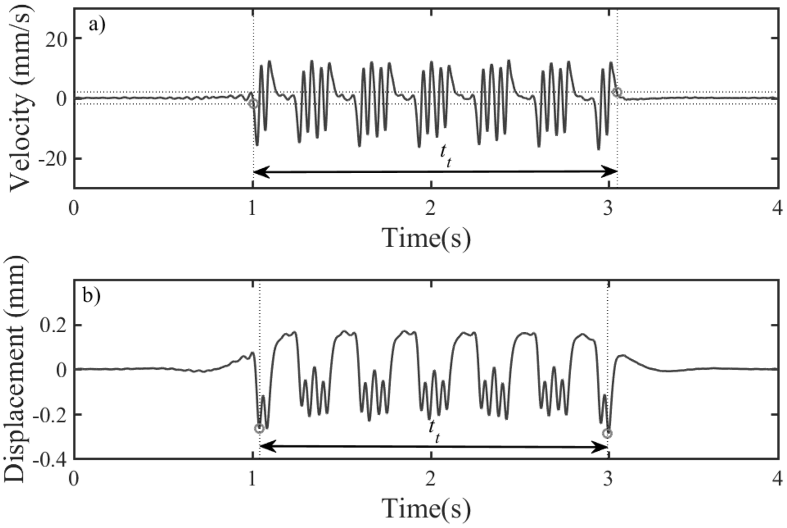

Figure 6.1 Example of (a) using a threshold on the native signal and (b) using peak finding to find the first and last wheel to determine the passing time for the train.

The vehicle-passing frequency can be identified by applying a peak-finding algorithm to the magnitude spectrum of track vibration to identify the frequencies of the dominant peaks, and then finding their common factor.

Different methods can be used to identify train types, including axle counting or employing a neural network that has been trained to recognise signatures for different train types (Ah Fat, 2017).

One of the simplest approach to identify the train type would be to use the train passing time and speed to find the train length and compare this with known lengths. However, without knowledge of the train type the train or an independent measurement, the train speed will also be unknown. Furthermore, trains might be of similar lengths and operate at similar speeds making it difficult to differentiate between different types such as the Velaro and the Eurostar, which both operate around 80 m/s and are close to 400 m long.

This section describes how train-passing time and the vehicle-passing frequency was used to account for different vehicle types and help distinguish between train types encountered during this research on HS1. By assuming a notional vehicle length L_{ve} the vehicle-passing frequency can be used to determine an equivalent speed v_e:

$$v_e = f_1 \cdot L_{ve} \tag{6.1}$$

This equivalent speed can be used to find a notional train length L_{te} from the train passage time,

$$L_{te} = t_t \cdot v_e \tag{6.2}$$

Every train will have notional length for an assumed vehicle type, which will be different for trains with similar lengths but different vehicle types. The notional lengths can be used to identify the train type. However, these may not always be unique, which means the method will only work for railways with a suitable mix of traffic as there is the risk that the combination of train and vehicle lengths on a different railway would not give unique notional lengths, although this would be simple to check.

Table 6.1 list the actual and equivalent lengths for the trains operated on HS1 for a notional vehicle length of L_{ve}=20 m. For these trains, the differences in equivalent lengths between train types are more significant than the differences between their actual lengths. This means that in this case it is easier to differentiate between trains using the equivalent length than the actual length (which would only be possible with an independent measure of train speed).

Table 6.1 Notional trainset lengths for a 20 m vehicle.

Train type	**Actual primary vehicle length (m)**	**Train length (m)**	**Notional length (m) L_v=20 m**
Javelin (6 Car)	20	116.8	116.8
Javelin (12 Car)	20	237	237
Eurostar	18.7	386	412
Velaro	24.8	389.4	314

In this research, the method proved effective for identifying the train type allowing correct geometry to be assigned for analysis. Every train in a sample of 149 trains was identified correctly using a threshold of ±5% of the notional length. Data were obtained from the Crissmill plain line site in May 2016. This was checked by determining the train type present in each record manually by inspection. This method works for the trains operating on HS1.

6.3 Truncating to stationary region

Track displacement data obtained from velocity or acceleration measurements will be affected by artefacts from signal processing. Assuming that the data have been filtered appropriately, and that the train is sufficiently long there should be a stationary region within the displacement signal, unaffected by the start-up transients that affect the data for the first and last bogies (Figure 2.7). Displacement data should be truncated to this stationary region for characterising track deflection. Train architecture facilitates this. It has already been shown in Chapter 5 that repetition of near-identical vehicles within a train causes periodicity in the pattern of loading, with a vehicle forming one period.

When truncating measurements in the time domain, it is convenient to define one period as one vehicle length containing two half vehicles as shown in Figure 6.2, rather than a whole vehicle as was shown in Figure 5.9, as under most circumstances this will allow consideration of the longest section of data from the stationary region.

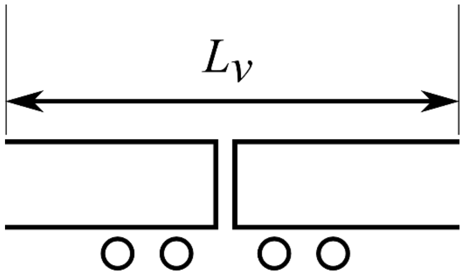

Figure 6.2 Paired half-vehicle period.

As proposed in Section 6.2, peak-finding algorithms can be used to determine the time associated with the first and last wheels t_s and t_e of the train from the deflection data and the train passing time t_t. Then, provided that the train type and its speed are known, suitable boundaries, t_1, t_2… for truncating the stationary region can be found from the known trainset geometry. There may be multiple regions if the signal is being truncated to a single vehicle type or to avoid effects from the coupling of trainsets. These ordinates can be expressed as a proportion of the train passing time. Figure 6.3 shows how displacement signals for a Javelin and a Eurostar could be truncated to avoid start up transients and in the case of the Eurostar, to limit analysis to a single vehicle type. Possible ordinates for truncating the different train types operating on HS1 are given in Table 6.2.

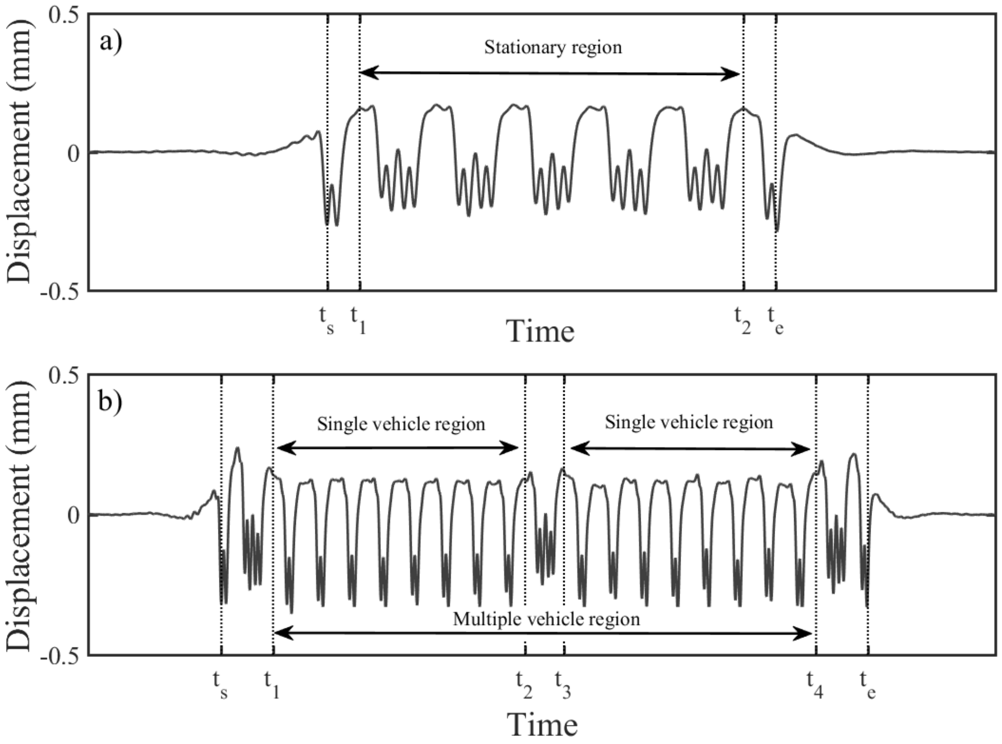

Figure 6.3 Boundaries for truncating displacement signals into stationary regions for (a) Javelin and (b) Eurostar.

Table 6.2 Possible ordinates for truncating displacement signals into stationary regions containing single or multiple vehicle types.

Train Type	**Proportion of train passing time (t_e - t_s)**			
	t_1	t_2	t_3	t_4
Javelin (6 car)	0.07	0.93	-	-
Javelin (12 car)	0.04	0.46	0.54	0.96
Eurostar (20 car)	0.08	0.47	0.53	0.92
Velaro (16 car)	0.05	0.95	-	-

6.4 Characterising deflection: peak-finding

Displacement-time histories from the BOEF model and from measurements contain distinct turning points associated with downward displacement, maximum uplift and minimum uplift. The latter corresponds to the at-rest position. These define the range of the displacement. As an example, these are shown in Figure 6.4 from calculations using the BOEF model for Javelin vehicles, with 50 kN wheel loads moving at 50 m/s over a track with a support modulus of 40 MN/m^2.

Turning point analysis can be used to identify these features from the model and from measurements. If there are distinct uplift features in the signal, the minimum uplift may be identifiable. Statistical interpretation of these points can provide a datum for each of the downward deflection w_l, and the maximum uplift w_u and an estimate of the at-rest position w_r, either by taking an average of the turning points. The range of movement $w_v = w_u - w_l$ and the characteristic downward displacement $w_t = w_r - w_l$, can be found. These allow quantification of uplift. The turning points and the three different datum levels identified using the averages of the turning points are identified in Figure 6.4.

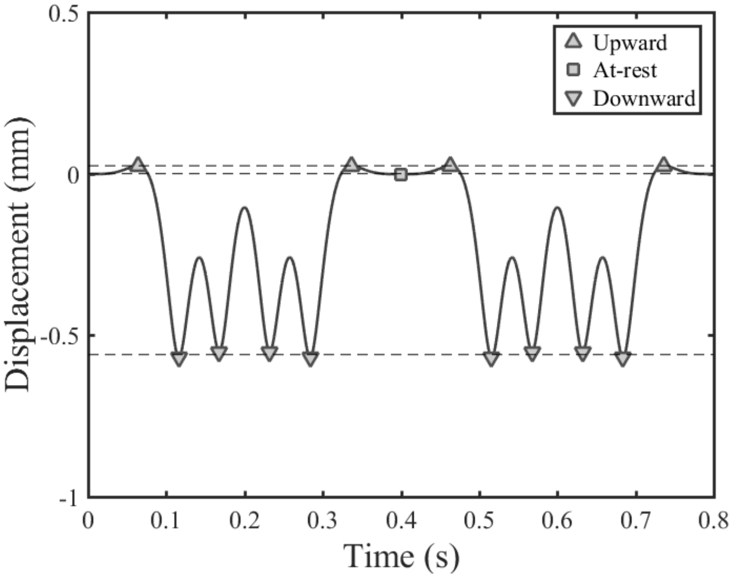

Figure 6.4 Turning point analysis using data from the BOEF model Javelin vehicle geometry.

The same method has been employed using measured data to estimate a datum for upward, downward and at-rest displacement, for a Javelin, a Eurostar and a Velaro, in Figure 6.5. The positions corresponding to the uplift, at-rest position and typical downward deflection are indicated. These were found from the mean of the associated data points. Measured data are often more variable than the regular shaped results obtained from modelling (Figure 6.4), and can contain features that are not present in the model such as high dynamic loads from wheel flats. These may result in additional turning points during the analysis, like the multiple turning points identified and then associated with the at-rest position in Figure 6.5(b) and (c) which influenced the results. Therefore, an alternative approach is explored.

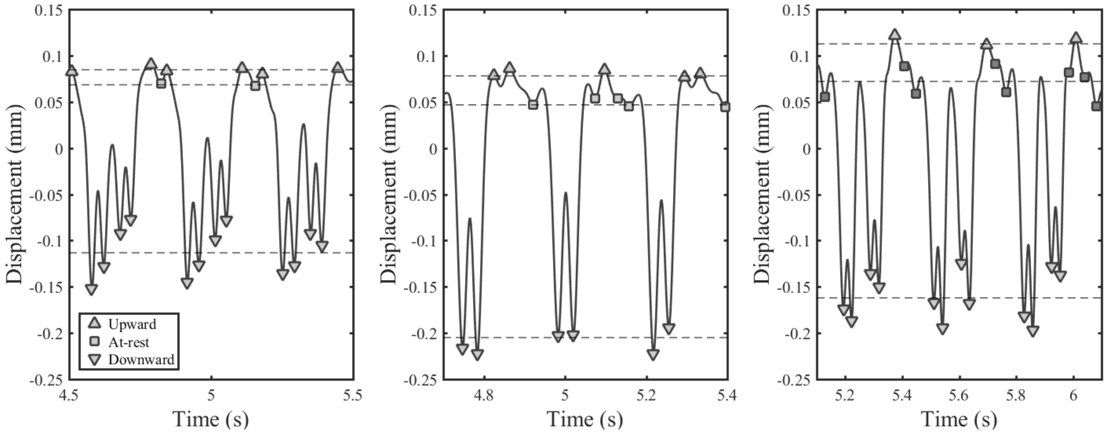

Figure 6.5 Turning point analysis using measured displacement data for (a) Javelin (b) Eurostar (c) Velaro.

6.5 Characterising deflection: statistical method

Track deflections calculated using the BOEF model are distributed according to the model’s solution. This is a function of the track stiffness, wheel load and train geometry. The CDF for the results of the BOEF model can be used to determine the proportion of the time that the track is expected to be below, at or above the at-rest position for a given time period. The stationary region in a displacement time history obtained from lineside measurements is expected to have a similar distribution to that obtained from the BOEF model. This means that the probability P of the measured track deflection w_m being less than or equal to the at-rest position w_r is assumed to be the same as the probability of the modelled displacements w being less than or equal to zero for equivalent time periods or lengths of track.

$$P(w_m \leq w_r) = P(w \leq 0) \qquad (6.3)$$

Finding these probabilities involves comparing the CDF for the model and the measurements using equivalent time windows. The theoretical basis for this approach will now be demonstrated, and a practical approach for implementation proposed.

6.5.1 Theory

The CDF $c(w)$ for a variable distributed according to a function can be found analytically from the normalised inverse of that function (Riley et al., 2002), or numerically using the product limit estimator (Kaplan and Meier, 1958). For simplicity, this analytical example uses the static solution for the BOEF model subject to a single point load, rather than a train of loads. The result for a train or a vehicle would need to be evaluated for different regions. The static solution for a force Q applied at x=0 is given by:

$$w(x) = \frac{Q}{2kL} \mathrm{e}^{-\frac{|x|}{L}} \left(\cos\left(\frac{|x|}{L}\right) + \sin\left(\frac{|x|}{L}\right) \right) \tag{6.4}$$

The CDF $c(w)$ for the function can be written:

$$c(w) = \int_{w_1}^{w} \frac{x(w)}{A} \, dw \tag{6.5}$$

where w_1 is the minimum value of w and $x(w)$ is the inverse of $w(x)$

$$x(w) = w^{-1}(x) \tag{6.6}$$

normalised by A

$$A = \int_{w_1}^{w_2} x(w) \, dw \tag{6.7}$$

where w_2 is the maximum value of w

For the function $w(x)$ to be invertible, it must be unique for each value of x. In this example $w(x)$ does not satisfy this condition. To find the inverse, the domain of the function must be restricted to monotonic regions. In such regions, $[x_1, x_2]$, the inverse function $x(w)$ is defined implicitly over $[w_1, w_2]$, which are now the values of w at x_1, x_2.

$$\int_{w_1}^{w_2} x(w) \, dw = \int_{x_1}^{x_2} w(x) \frac{dw}{dx} dx \tag{6.8}$$

Integration by parts gives:

$$\int_{x_1}^{x_2} w(x)\frac{dw}{dx}dx = [xw(x)]_{x_1}^{x_2} - \int_{x_1}^{x_2} w(x)dx \qquad (6.9)$$

Each region of the solution to the BOEF model can be evaluated analytically since:

$$\int_{x_1}^{x_2} w(x)dx = \left[\frac{Q}{2k}\mathrm{e}^{-\frac{|x|}{L}}\cos\left(\frac{|x|}{L}\right)\right]_{x_1}^{x_2} \qquad (6.10)$$

The CDF for the entire function may be evaluated by integrating over all the regions.

For a single load, the boundaries of the monotonic regions occur approximately at $|x|/L=n\pi$. These are shown for the response of a BOEF normalised to the maximum deflection in Figure 6.6(a). The cumulative distibution function for the region [0, 2π] has been evaluated analytically and is shown in Figure 6.6(b). The CDF has a distinctive shape, with a shallow section then a change of gradient into a steep region associated with zero deflection. This facilitates using the CDF to estimate the at-rest position.

Although it is possible to determine the CDF for an entire train it is far more onerous, as the boundaries for the monotonic regions will depend on the train geometry and the track system support modulus. The alternative is to discretise the solution and find the CDF numerically. This has been done for the same region as the analytical solution in Figure 6.6(b). The result for the region [-2π , 0] hence [-2π, 2π] would be the same owing to symmetry. Outside this region there is approximately zero deflection. The discrete CDFs determine the probability according to the numer of samples that are less than or equal to each unique value of deflection and the total number of samples (Kaplan and Meier, 1958). Both approaches can be seen to give the same result. This is important as the numerical approach will be required for obtaining the cumulative CDF from lineside measurements.

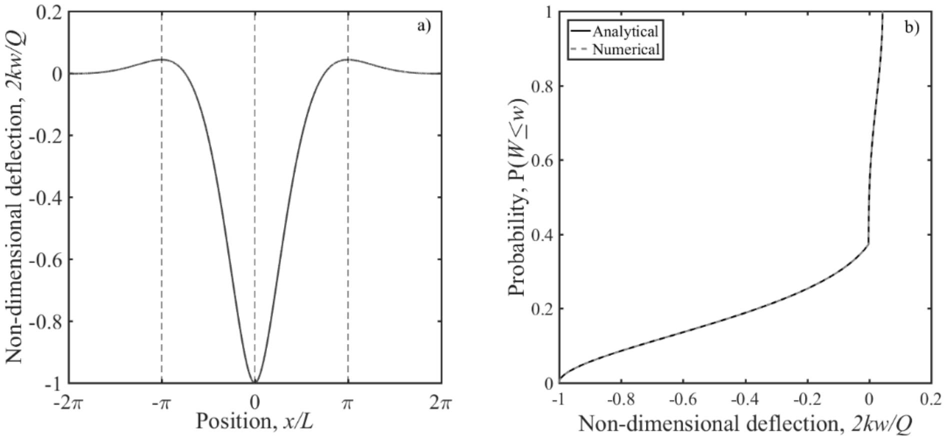

Figure 6.6a) Non-dimensionalised displacement *2kw/Q* at a position of *x/L* on a BOEF. The boundaries between monotonic regions have been highlighted using dashed lines. (b) CDF for the region [0, 2π] (hence [-2π, 2π]) evaluated analytically and numerically.

6.5.2 Accounting for train geometry

The track deflection due to multiple wheel loads is a function of the vehicle geometry and the track system support modulus. The vehicle geometry fixes where the loads are positioned relative to each other and the track system support modulus controls the size of the deflection bowl beneath each load and the interaction between adjacent loads. This means that both the vehicle geometry and the track stiffness affect the distribution of deflection. The numerical rather than the analytical approach has been used to study the effect of this. This is because the numerical approach allows different train geometries and the influence of track system support modulus to be considered without the need to find the boundaries to the monotonic regions for each case.

The proposed method requires the CDFs to be found for a predefined length or time window, such as a number of pairs of half-vehicles (Figure 6.2). The deflections within one period will be distributed in the same way as for multiple periods. Hence, evaluating the cumulative distribution using measurements from several vehicles implicitly averages the data. Figure 6.7 shows the expected deflection profile and CDF for two half vehicle pairs for Javelin, Eurostar and Velaro vehicle geometries. These have been determined for a range of plausible track support moduli and nominal wheel loads of 50 kN. The wheel load will change the magnitude of the deflection but not its distribution, which depends on the track system support modulus and vehicle geometry.

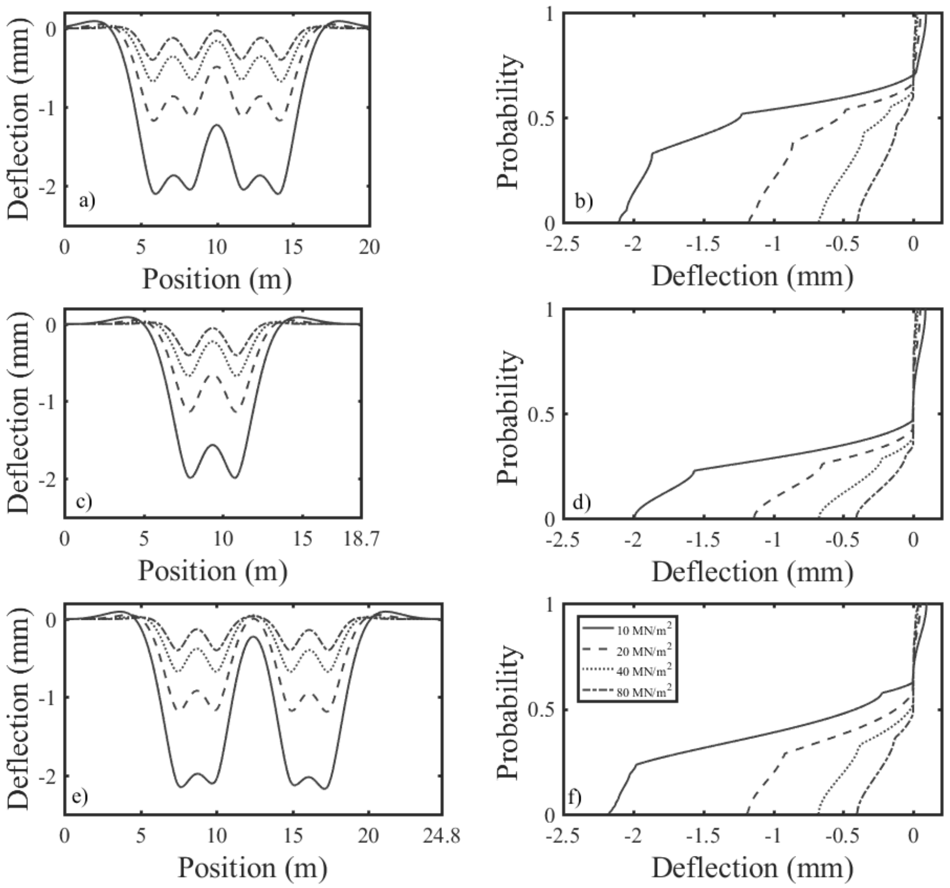

Figure 6.7 (a) Displacements for two half Javelin vehicles, (b) corresponding CDF for the Javelin, (c) displacements for two half Eurostar vehicles, (d) corresponding CDF for the Eurostar, (e) displacements for two half Velaro vehicles, (f) corresponding CDF for the Velaro, evaluated for a nominal 50 kN wheel loads for a range of plausible track support moduli.

In Figure 6.7(b), (d) and (f) the region of the CDF associated with the at-rest position *w* = 0 is very steep compared with other parts of the function and comes after a significant change in gradient. This means that the region associated with the at-rest position is clearly identifiable in the CDF. A single value of probability can be used to identify the at-rest position in data from lineside measurements. This probability, *P*(*w*=0), has been determined for the three vehicles, for a range of track support moduli, as shown in Figure 6.8.

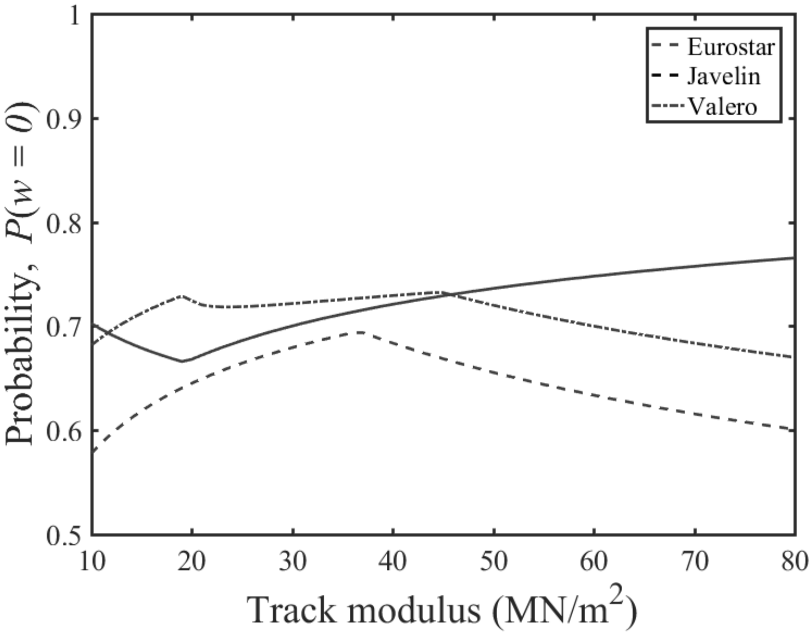

Figure 6.8 Probability corresponding to the at-rest position $P(w= 0)$ expressed as a function of track support moduli for Javelin, Eurostar and Velaro vehicle types.

If the track system support modulus is known, the theoretical probability can be found. However, this is unlikely as a measurement of displacement is a precursor to finding the track system support modulus using traditional methods. Figure 6.8 shows that for a wide range of plausible track support moduli (10-80 MN/m^2), $P(w=0)$ takes a limited range of values: 0.66-0.75, 0.52-0.70 and 0.65-0.73 with mean values of 0.7, 0.65 and 0.7 for the Javelin, Eurostar and Velaro respectively. For automatic processing, it would be convenient to have a single value deemed to be an acceptable approximation of $P(w=0)$ that could be applied to the majority of data. In the CDF, there is a steep region where a range of probability values could be associated with the at-rest position. The steep gradient means that estimates of the rest position from measurements will not be sensitive to slight variations in the value of probability used to identify it within that region.

Figure 6.9(a) shows the probability value associated with an over- or under-estimate of the at-rest position by 1% of the downward deflection on a track with a system support modulus of 25 MN/m^2 for a Javelin vehicle. This indicates the sensitivity to the value of probability used to identify the rest position. There is quite a significant change in probability for a small change in the assumed at-rest position, due to the steepness of the function. The results of the analysis for a range of plausible track system support moduli are shown in Figure 6.9(b). The thick line shows the probability values for $P(w=0)$; either side of this, thin lines show the values for $P(w=\pm0.01)$, corresponding to a small error in the estimate of the rest position, i.e. 1% of the downward deflection.

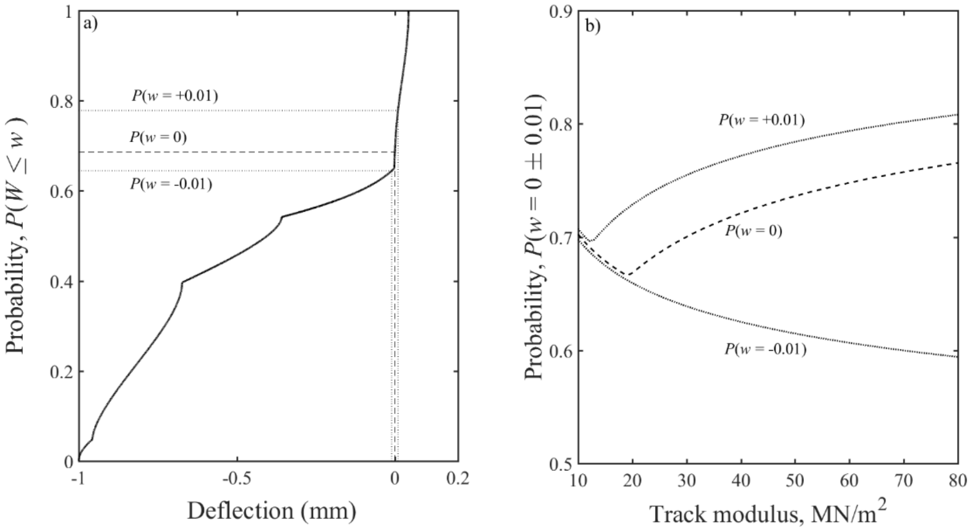

Figure 6.9(a) Change in probability value associated with a over- or under-estimate of the at-rest position by 1% of the downward deflection for a Javelin trainset on track with a system support modulus of 25 MN/m^2. (b) Probability values for $P(w=\pm0.01)$, for a Javelin on a track with a range of plausible track system support moduli.

The analysis has been repeated for the Eurostar and Velaro vehicles, see Figure 6.10. The significance of the change in probability depends on both the vehicle geometry and the track system support modulus. For the vehicles studied, on track with a track system support modulus $k > 20$ MN/m^2, a change in the assumed probability used to identify the at-rest position, of $\Delta P \approx \pm0.1$ is unlikely to change the estimate of the at-rest position significantly. This level of variation covers the range of probability values corresponding to the at-rest position from Figure 6.8. Overestimating the probability value will tend to give a smaller margin of error for an increasing track system support modulus, than underestimating it, where the margin for error will increase with the track system support modulus.

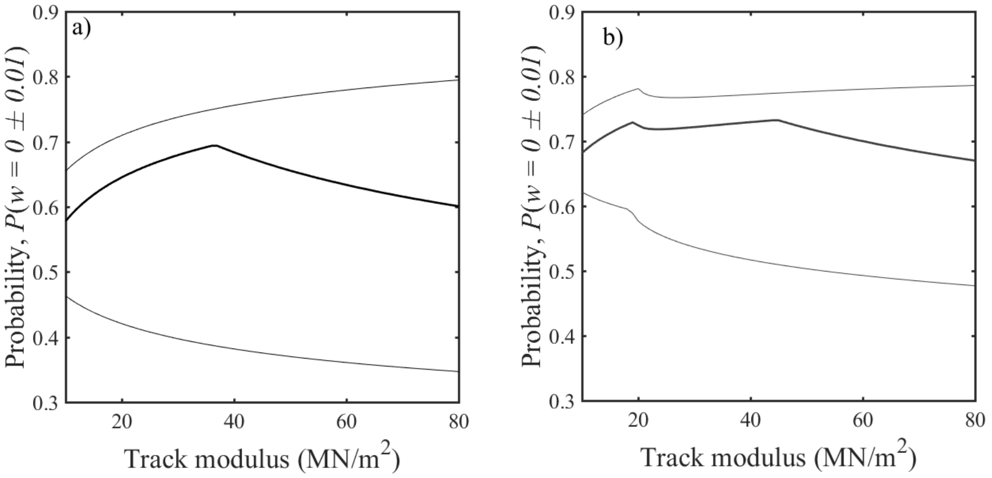

Figure 6.10 Probability values for $P(w = 0 \pm 0.01)$ of normalised displacement for(a) Eurostar and (b) Velaro on a track with a range of plausible track system support moduli.

6.5.3 Examples

The utility of the method is studied using deflection data obtained for a sleeper on well-performing track and a sleeper above a void, in both cases for a Javelin train. Figure 6.11(a) shows sleeper displacement data obtained using a geophone for a six-vehicle train moving at 60.2 m/s. Data were sampled at 500 Hz and filtered with high- and low-pass cut-off frequencies of 2 and 40 Hz respectively. The track had a system support modulus of 36.3 MN/m^2 , determined using the method from Chapter 7 and in Le Pen et al. (2016). The sleeper can be seen to move by about 0.35 mm. Figure 6.11(b) shows results for the same train calculated using the BOEF model. The CDFs for the stationary region highlighted in the measurements and for the equivalent period from the model are shown in Figure 6.11(c). Generally, the distribution of the measurements is similar to that obtained from the model, although the measurements are offset to the right by the unknown difference in the at-rest position. The steep region in the measurements is likely to be associated with the at-rest position, and can be used to estimate this position. The location of the at-rest position in the measurements has been estimated using probability values of P = 0.66, 0.70 and 0.75. These probability values are the minimum, exact, and maximum possible values for a Javelin on a track where the rail pad stiffness limits the possible track system support modulus to 60 MN/m^2 and give estimates of the at-rest position of 0.135, 0.145 and 0.150 mm respectively.

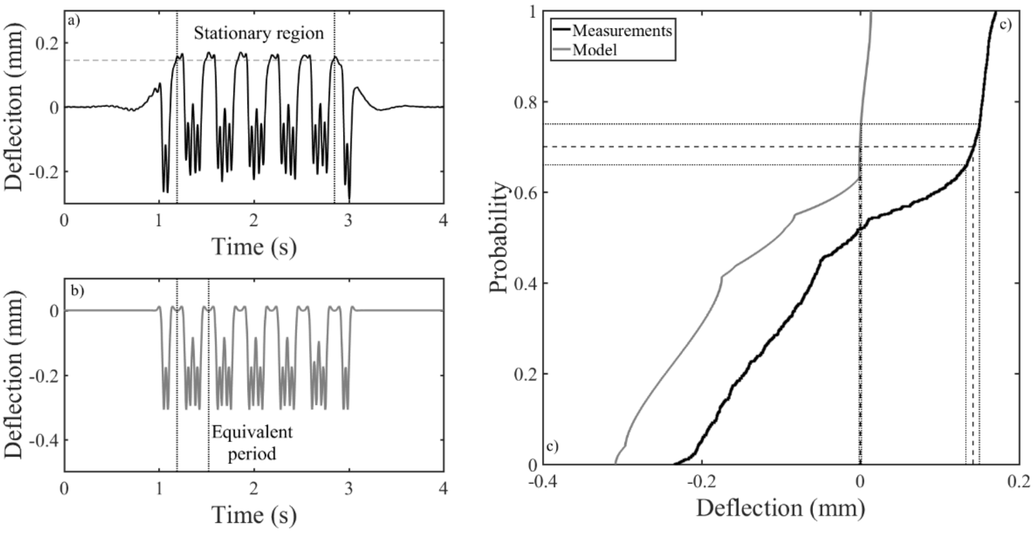

Figure 6.11 Displacement data for a well-performing sleeper, (a) obtained from measured geophone data, sampled at 500 Hz, filtered with 2 and 40 Hz high- and low-pass cut-offs, (b) obtained using the beam-on-elastic-foundation model, (c) the CDFs for the measured and modelled data.

Figure 6.12(a) shows deflection data obtained using a MEMS accelerometer, for a sleeper that was moving by about 4 mm under passing trains suggesting a gap beneath the sleeper. Data were sampled at 500 Hz and filtered with high- and low-pass cut-off frequencies of 2 and 40 Hz respectively. The CDF for the stationary region identified in Figure 6.12(a) is shown in Figure 6.12(b). The probability values used previously give estimates of 1.7, 1.9 and 2.0 mm for the at-rest position.

The shape of the distribution below the at-rest position is of interest. There are two distinct regions with constant gradients. Between $P \approx 0.03$ and 0.50 the CDF is quite steep. This gradient reduces between 0.5 and 0.65, and the shape differs from the distribution that would be obtained from the model even with very soft track support $k <$ 10 MN/m^2. These features are a consequence of voiding.

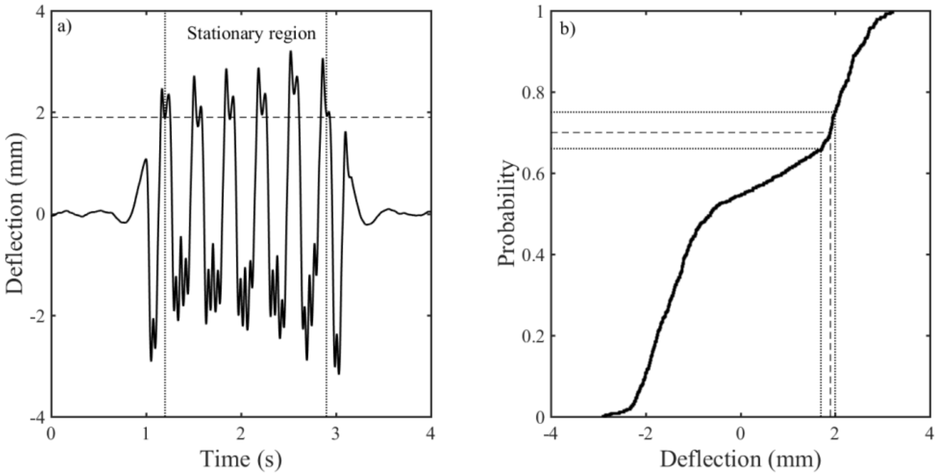

Figure 6.12(a) Displacement data for a voided sleeper obtained using a MEMS accelerometer, sampled at 333 Hz and filtered with 2 and 40 Hz high- and low-pass cut-offs. (b) CDF for that displacement data.

Practically it would be useful to be able to select a single probability value to represent the at-rest position as this would enable rapid analysis of deflection data. In the results shown in Figure 6.11 and Figure 6.12, the differences between the at-rest positions obtained from the measurements using different probability values were more significant than expected from the theoretical analysis. The differences between the estimate of the at-rest position found using *P* = 0.66 and 0.70 were smaller than between *P* = 0.70 and 0.75.

6.5.4 Characterising the range of movement

The CDF provides a basis for characterising the typical range of deflection which, together with an estimate of the at-rest position, can be categorised as either downward deflection or uplift. Differentiating between upward and downward movement from the at-rest position is important. Most of the track deflection is expected to be in the downward direction, and the deflection beneath a wheel load is commonly used as an input to assess the track stiffness. Conversly, uplift effects are expected to be small (up to around 4% of the downward deflection according to the BOEF model), and significant uplift may indicate atypical behaviour. This can be analysed by selecting probability values representing typical upper and lower limits of track movement. Although the pattern of track deflection tends to be repeated for similar vehicles, there will be variations due to different vehicle weights, occupancy and the dynamic behaviour of each wheel, including wheel flats. This means that it would be inappropriate to select either the maximum upward or downward deflection (i.e. at P = 1 or 0) to characterise the typical range of movement. Instead values that encompass the majority of the typical range of movement yet avoid irregular movements from wheel impacts should be chosen.

The CDF for the BOEF model can provide guidance for selecting appropriate values. Figure 6.13(a) shows simulation results giving the difference between the exact and approximate positions for downward deflection found using probability values of P = 0.01, 0.025 and 0.05 (in the model P = 0 corresponds to the exact deflection). Figure 6.13(b) shows corresponding results for the uplift determined using P = 0.99, 0.975 and 0.95. Both graphs show the results for a range of plausible track system support moduli. For clarity, these results are shown only for the Javelin. Both are expressed as a percentage of the exact downward deflection or uplift and indicate the extent to which each probability value would give a reasonable approximation to the exact value for each direction. As the amount of uplift is small, the absolute error will be small. These results show that the difference between the theoretical deflection and the corresponding approximation can be less than 2% for P = 0.025 and 0.975. Results were found to be similar for the other train types studied. Adopting such values rather than the maximum and minimum helps to mitigate against irregular or extreme movement that may influence a small part of the train passage.

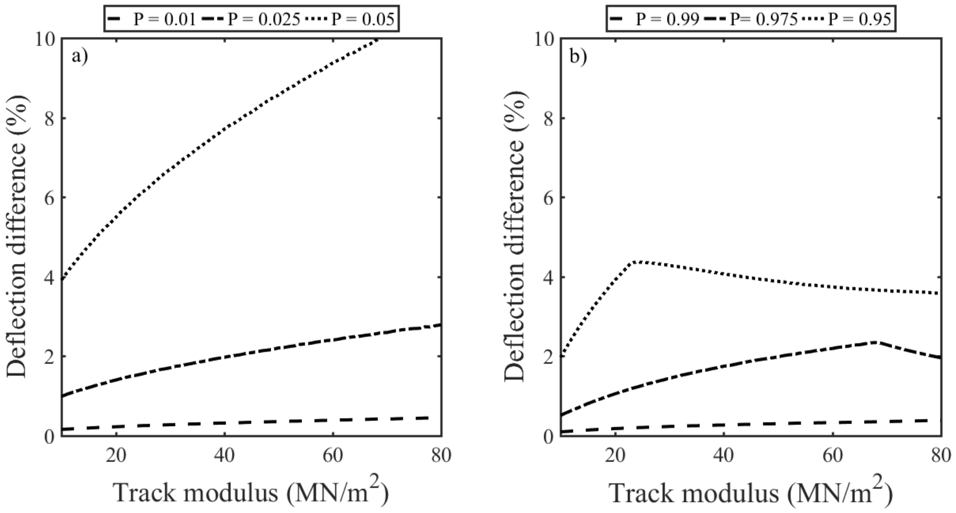

Figure 6.13 Difference between exact and approximate deflection determined using confidence intervals, (a) for the downward deflection and (b) for the uplift.

Figure 6.14(a) and (b) shows the results of applying the probability values used in Figure 6.13 to the stationary region of the displacement data from Figure 6.11(a) and Figure 6.12(a) respectively. The positions associated with the at-rest level and the typical extents of movement have been identified. These can be used to find the total range of movement, the characteristic downward deflection and the amount of uplift. The at-rest position found using P = 0.7 in Figure 6.14(a) is close to where it would have been placed by inspection. The downward deflection was identified using P = 0.01, 0.025 and 0.05, and the uplift using P = 0.99, 0.975 and 0.95.

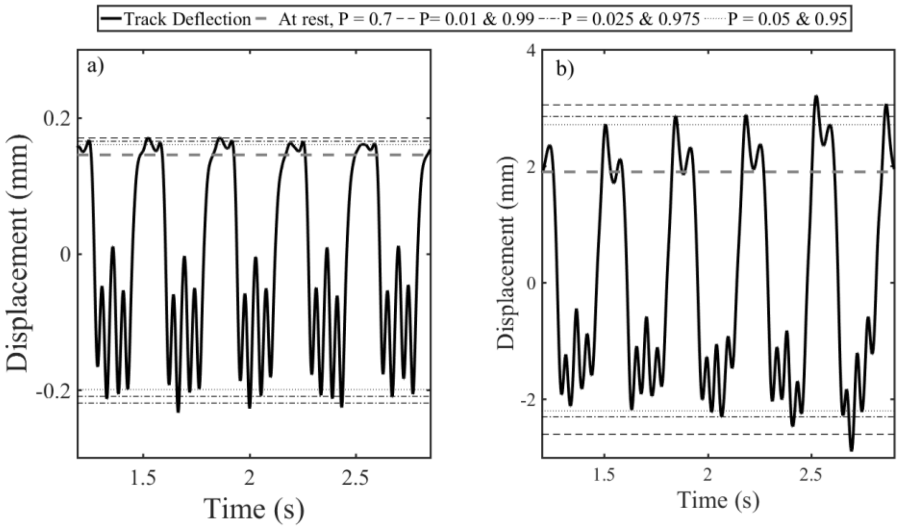

Figure 6.14 Identification of typical characteristic upward and downward deflection and at-rest position for(a) track with well-performing and(b) track with voided sleepers.

The results indicated in Figure 6.14 are given in Table 6.3. Those found using P = 0.01 and 0.99 are more influenced by the extremes of movement than the others. Here both P = 0.025 and 0.975 and P = 0.05 and 0.95 give reasonable estimates for the typical total range of movement. Figure 6.14 indicates that P = 0.025 and 0.975 would be more representative of the total range of movement in the absence of variable or irregular track movements. In Figure 6.14(a), the at-rest position estimated by inspection would have been closer to that found using P = 0.75, but this is not very significant as the difference was less than 1.5% of the middle estimate for the downward deflection. However, this would affect the estimate of uplift.

Table 6.3 Typical characteristic downwards and upwards track deflections identified using different probability values from displacement data for track with well-performing sleepers and track with voided sleepers from Figure 6.14.

Probability values	Deflections (mm)					
	Well-performing sleeper			Voided sleeper		
	Downward	Upward	Total	Downward	Upward	Total
0.010, 0.990	0.36	0.03	0.39	4.50	1.15	5.65
0.025, 0.975	0.35	0.02	0.37	4.20	0.95	5.15
0.050, 0.950	0.34	0.02	0.36	4.10	0.81	4.91

6.5.5 Further testing

Figure 6.15, Figure 6.16 and Figure 6.17 show example sections of displacement-time histories for six sleeper ends for a Javelin, a Eurostar and a Velaro respectively from the Crissmill plain line site. The CDF for each section has been evaluated using three vehicle periods for each sleeper end. The upper, lower and mean estimates for $P(w=w_r)$ for each train have been marked on the CDF to allow the at-rest position to be found. These are P = 0.66, 0.7, 0.75 for the Javelin; P = 0.52, 0.65 0.7 for the Eurostar; and P = 0.65, 0.7 and 0.74 for the Velaro, which were obtained from the BOEF model (Figure 6.8). The probabilities corresponding approximately to the extents of downward (P = 0.01, 0.025 and 0.05) and upward movement (P = 0.99, 0.975 and 0.95) have also be marked.

Track movements determined using these analyses are tabulated in Table 6.4, Table 6.5 and Table 6.6 for the same Javelin, Eurostar and Velaro train passages. The differences between the upper, mean and lower estimates for the characteristic downward movement are small for this well-performing track. The CDFs are steep in this region, so the estimates of the at-rest position are not sensitive to slight changes in the value for $P(w_m=w_r)$. This confirms that it is reasonable to select a single probability for estimating the at-rest position for all train types, say P = 0.7. This approach allows a consistent and comparable algorithm to be applied to a large dataset from continuous monitoring, to determine the characteristic total and downward deflection.

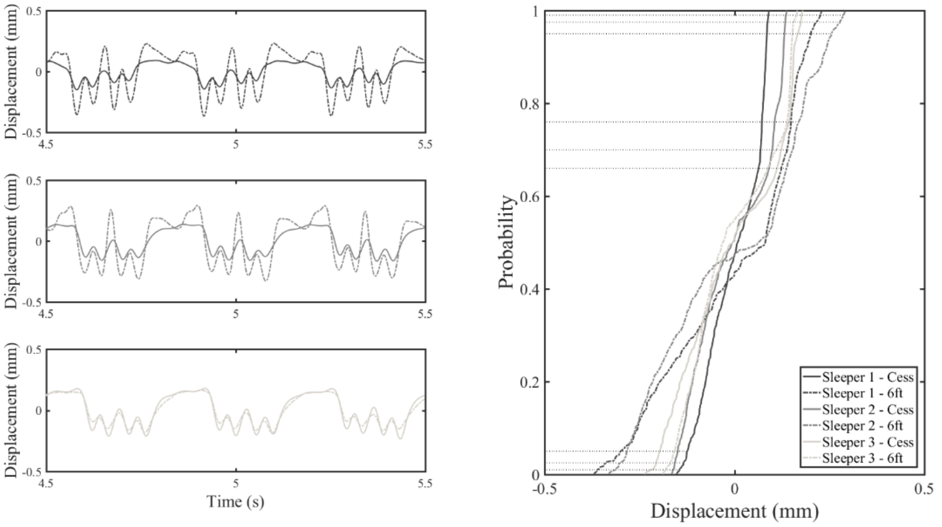

Figure 6.15 (a), (b) and (c) Three-vehicle-length windows of displacement time histories obtained at either end of three different sleepers at Crissmill plain line site. (d) The empirical CDF for each of these displacement time histories for the passage of a Javelin.

Table 6.4 Characteristic range of total and downward displacement found from measured Javelin displacement data from Figure 6.15.

	Deflection (mm)											
	Range			**Upper downward**			**Middle downward**			**Lower downward**		
Probabilities	0.99-0.01	0.975-0.025	0.95-0.05	0.75-0.01	0.75-0.025	0.75-0.05	0.70-0.01	0.70-0.025	0.70-0.05	0.66-0.01	0.66-0.025	0.66-0.05
Sleeper 1												
Cess	0.23	0.22	0.21	0.22	0.20	0.20	0.21	0.20	0.19	0.21	0.19	0.19
6-foot	0.59	0.56	0.50	0.51	0.49	0.45	0.50	0.48	0.44	0.49	0.46	0.42
Sleeper 2												
Cess	0.30	0.29	0.28	0.27	0.26	0.25	0.26	0.26	0.25	0.25	0.25	0.24
6-foot	0.60	0.58	0.54	0.48	0.47	0.45	0.47	0.45	0.44	0.45	0.44	0.42
Sleeper 3												
Cess	0.40	0.38	0.37	0.36	0.35	0.34	0.34	0.33	0.32	0.33	0.32	0.31
6-foot	0.35	0.32	0.31	0.32	0.31	0.30	0.29	0.28	0.27	0.27	0.25	0.25

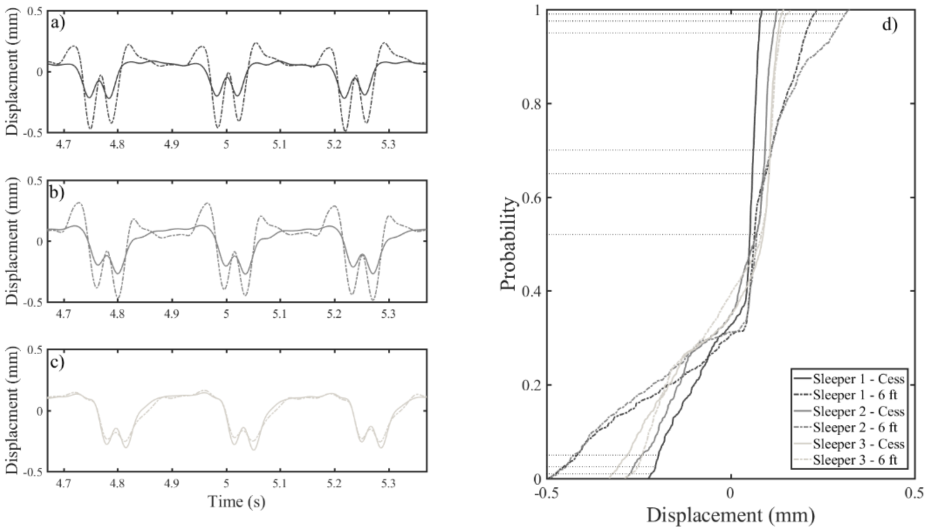

Figure 6.16 (a), (b) and (c) Three-vehicle-length windows of displacement time histories obtained at either end of three different sleepers at Crissmill plain line site. (d) The empirical CDF for each of these displacement time histories for the passage of a Eurostar.

Table 6.5 Characteristic range of total and downward displacement found from measured Eurostar displacement data from Figure 6.16.

	Deflection (mm)											
	Range			**Upper downward**			**Middle downward**			**Lower downward**		
Probabilities	0.99-0.01	0.975-0.025	0.95-0.05	0.70-0.01	0.70-0.025	0.70-0.05	0.65-0.01	0.65-0.025	0.65-0.05	0.52-0.01	0.52-0.025	0.52-0.05
Sleeper 1												
Cess	0.30	0.28	0.27	0.28	0.27	0.26	0.28	0.26	0.26	0.27	0.26	0.25
6-foot	0.70	0.67	0.62	0.59	0.57	0.53	0.57	0.55	0.51	0.54	0.52	0.48
Sleeper 2												
Cess	0.40	0.39	0.36	0.37	0.36	0.33	0.36	0.35	0.33	0.34	0.33	0.31
6-foot	0.79	0.74	0.71	0.59	0.56	0.54	0.57	0.54	0.52	0.55	0.52	0.50
Sleeper 3												
Cess	0.46	0.44	0.41	0.43	0.41	0.39	0.43	0.41	0.38	0.41	0.39	0.37
6-foot	0.43	0.39	0.37	0.38	0.36	0.35	0.38	0.35	0.34	0.35	0.33	0.32

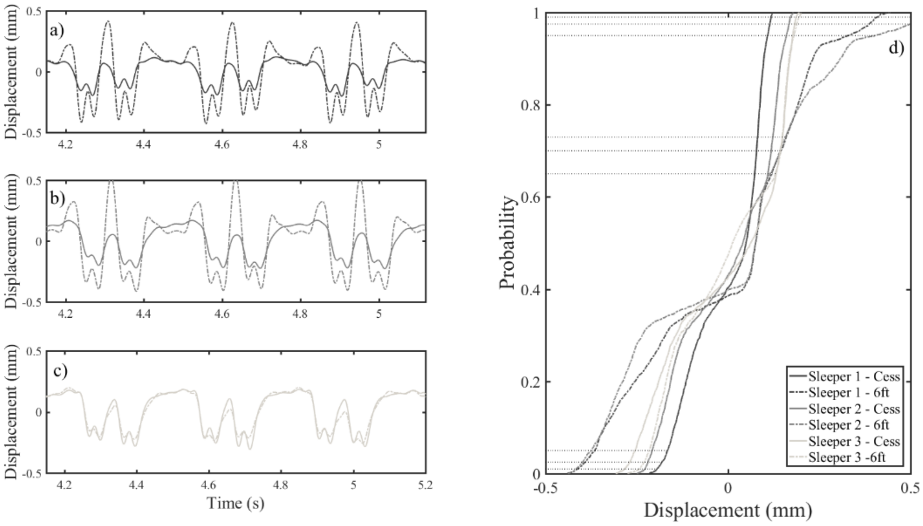

Figure 6.17 (a), (b) and (c) Three-vehicle-length windows of displacement time histories obtained at either end of three different sleepers at Crissmill plain line site. (d) The empirical CDF for each of these displacement time histories for the passage of a Velaro.

Table 6.6 Characteristic range of total and downward displacement found from measured Velaro displacement data from Figure 6.17.

	Deflection (mm)											
	Range			**Upper downward**			**Middle downward**			**Lower downward**		
Probabilities	0.99-0.01	0.975-0.025	0.95-0.05	0.74-0.01	0.74-0.025	0.74-0.05	0.7-0.01	0.7-0.025	0.7-0.05	0.65-0.01	0.65-0.025	0.65-0.05
Sleeper 1												
Cess	0.31	0.30	0.27	0.28	0.26	0.25	0.27	0.26	0.24	0.27	0.26	0.24
6 foot	0.82	0.78	0.69	0.57	0.55	0.52	0.56	0.54	0.51	0.53	0.51	0.48
Sleeper 2												
Cess	0.40	0.39	0.37	0.35	0.34	0.33	0.35	0.34	0.33	0.34	0.33	0.32
6 foot	0.94	0.9	0.78	0.58	0.56	0.53	0.56	0.54	0.52	0.53	0.52	0.49
Sleeper 3												
Cess	0.47	0.45	0.43	0.44	0.42	0.40	0.43	0.41	0.40	0.42	0.40	0.39
6 foot	0.44	0.42	0.39	0.39	0.38	0.36	0.39	0.37	0.36	0.37	0.36	0.35

6.6 Comparison of turning point and CDF analyses

Two methods have been proposed in the previous sections for interpreting track deflection data from lineside measurements. Both could be used to characterise automatically the ranges of total and downward deflection. The first method relies on turning point analysis to find the range of track movement, while the second uses the CDF for track deflection. The characteristic total and downward deflections have been found using both methods from the data in Figure 6.15, Figure 6.16 and Figure 6.17, these are tabulated in Table 6.7. The CDF approach used P = 0.7 for the at-rest position and P = 0.025 and 0.975 for the range of deflection for all train types. The results are similar for both methods.

Table 6.7 Comparison of the characteristic range of total and downward displacement found using turning point analysis and the CDF method, with $P(w \leq 0) = 0.7$ for measured track displacements.

	Javelin Displacement (mm)				**Eurostar Displacement (mm)**				**Velaro Displacement (mm)**			
	Range		**Downward**		**Range**		**Downward**		**Range**		**Downward**	
	TP	CDF	TP	CDF	TP	CDF	TP	CDF	TP	CDF	TP	CDF
Sleeper 1												
Cess	0.20	0.22	0.18	0.20	0.28	0.28	0.26	0.27	0.26	0.30	0.23	0.26
6-foot	0.48	0.56	0.41	0.48	0.66	0.67	0.50	0.57	0.68	0.78	0.44	0.55
Sleeper 2												
Cess	0.28	0.29	0.27	0.26	0.36	0.39	0.33	0.36	0.35	0.39	0.32	0.34
6-foot	0.51	0.58	0.41	0.45	0.69	0.74	0.50	0.56	0.80	0.9	0.44	0.56
Sleeper 3												
Cess	0.36	0.38	0.35	0.33	0.43	0.44	0.40	0.41	0.43	0.45	0.41	0.42
6-foot	0.30	0.32	0.30	0.28	0.39	0.39	0.35	0.36	0.38	0.42	0.36	0.38

*TP-*Turning point analysis*, CDF-*Cumulative distribution function* (Total: P = 0.975 & 0.025. Downward: P = 0.7 & 0.025).

The CDF approach is based on integration, whereas turning-point analysis uses differentiation; this gives the former some advantages. Determining the empirical CDF requires less computation time than turning point analysis, which requires numerical differentiation. The CDF approach uses all the data rather than a few turning points, meaning that it is likely to be less sensitive to extreme values. It has also been shown that $P(w=0)$ can be approximated by a range of values without significantly changing the result. This means the CDF approach is likely to be both faster and more robust.

6.7 Deflected track bed geometry

Each load applied to the track is spread by bending of the rail, leading to a deflection bowl beneath each load. This effect can be seen in time histories of track movement for individual sleepers. The signal processing required to integrate track acceleration or velocity and obtain displacement results in the loss of the at-rest position. This means that there is no common datum for aligning data from different transducers. As discussed in the previous section, the method for interpreting track displacement using its CDF allows this at-rest position to be estimated. This is comparatively straightforward, as it can generally be assumed that $P(w=0) \approx 0.7$ for the trains operating on HS1 for a plausible range of track stiffness. The method allows measurements from multiple transducers to be aligned relative to a common datum, assumed to be the at-rest position of the rail. However, this at-rest position is equivalent to the unloaded track geometry and may be irregular. Provided that the measurements share a common timestamp, it is possible to interpolate between the transducers to determine the deflection along the rail at a given instant, allowing visualisation of the deflection bowl beneath the train. This shows how different locations along the track deflect relative to each other, which may highlight any performance variation.

The method of interpolation used will influence the deflection obtained. Linear interpolation will allow visualisation and comparison of the deflection across measurement locations. However, other functions that account for the bending of the rail may also be used for interpolation. Given that the measurements are all along the same rail (although potentially on a non-uniform foundation), the data from monitoring must satisfy an equation that includes the bending of the rail. For a simple case, the form of the solution to the BOEF model for a train of variable loads with known may be used as the objective function to fit the model of track deflection. However, this function may not cope well with non-uniformity of stiffness along the length of the track bed or non-linearity from voiding.

It may be more effective and quicker to take a non-parametric approach that satisfies beam bending by preserving a continuous slope, but does not explicitly account for material behaviour. For multiple wheel loads on a rail, a suitable function must have continuous first and second derivatives. This means that a ‘spline’ cubic polynomial may be a reasonable function for interpolating between lineside measurements points to visualise the deflection bowl. This technique has been used in Figure 6.18, with linear and cubic interpolants used to aid visualisation of the instantaneous deflection of the track along the well-performing section of the Crissmill plain line site under loads from a train. This approach can also be used to animate movements along a length of track beneath a passing train.

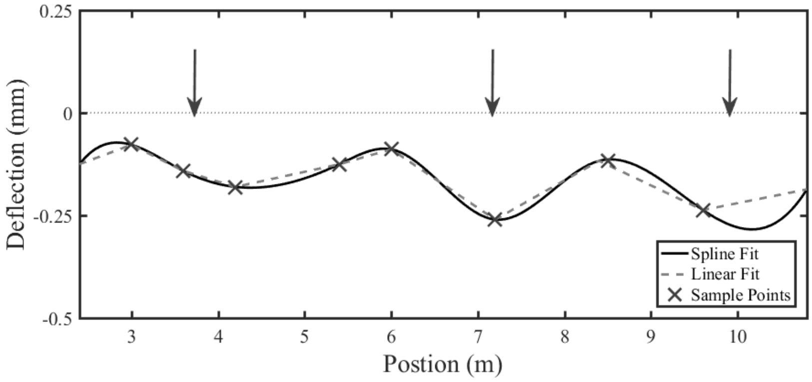

Figure 6.18 Visualisation of the deflected shape of the track under load found by interpolating between transducers aligned to a common datum using the CDF for the track deflection at each location.

Interpolating between lineside measurements made at a number of locations aligned to a common datum provides an estimate of the spatial record of track deflection in time. By recording the maximum deflection at each point this approach can be used to infer the deflected shape of the track bed under loading relative to the unloaded level of the rail. This is used later, in Chapter 9, to visualise the impact of voids on the deflected track geometry in and around defect zones.

The reliability of this method will depend on the transducer spacing. This is shown in Figure 6.19 where track deflections simulated using the BOEF model for UIC60 rail with a track system support modulus of 40 MN/m^2 and two half Javelin vehicles have been interpolated using a ‘cubic spline’. The model was sampled twice at locations representative of (a) 0.6 m transducer spacing (every sleeper), and (b) 1.2 m transducer spacing (every other sleeper). In sample 1 the sample locations align closely with the wheels. In sample 2 the wheels are centred between two points. When sample points are every 0.6 m the pattern of deflection is reliably reproduced. However, when the sample spacing is increased to 1.2 m the downward deflection between the sample points was underestimated. A close transducer spacing would be required to be able to visualise the deflection bowl without underestimating the deflection between measurement locations.

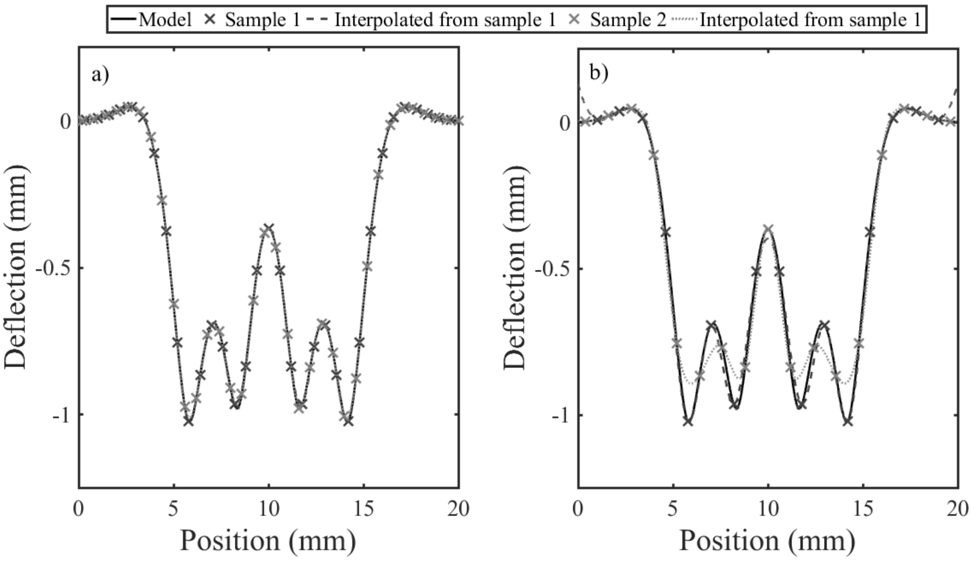

Figure 6.19 Reliability of visualising a deflection bowl simulated using the BOEF model with a UIC60 rail and a track system support modulus of 40 MN/m^2 using a ‘cubic spline’ for interpolation for two positions relative to the wheels of a Javelin for (a) 0.6 m transducer spancing and (b) 1.2 m transducer spacing.

6.8 Rail deflection

In this research, lineside measurements have been made mainly on the sleepers. However, results from the BOEF model are for displacement of the rail. Inclusion of a resilient rail pad between the rail and the sleeper means the displacements of the rail and the sleeper will be different. A compensating correction is required if sleeper displacements are to be used to determine other parameters on the basis the model.

At the rail, the system deflection $w_{s,}$ is the sum of track bed deflection w_t and the rail pad deflection w_p:

$$w_s = w_p + w_t \tag{6.11}$$

At any rail fastener, ignoring inertial effects, the rail pad and track bed can be considered to form two resilient spring elements acting in series:

$$\frac{1}{s} = \frac{1}{s_p} + \frac{1}{s_t} \tag{6.12}$$

where s, s_p and s_t are the system, rail pad and track bed stiffness. By definition $s < s_p$ and $s < s_t$. Eqs.(6.11) and (6.12) can be rearranged to express the system displacement in terms of the measured displacement at sleeper level and the system and rail pad stiffness. These stiffnesses could be replaced with moduli (stiffness per unit length).

$$w_s = \frac{w_t}{1 - \frac{s}{s_p}} \tag{6.13}$$

Eq.(6.13) can be used as a correction between the displacement of the rail and the measured displacement of the sleeper provided the rail pad and system modulus are known and the track is well-supported.

If the track system support modulus is unknown, it may be determined by the direct method in which an assumed (or measured) wheel load is required together with measurement of sleeper deflection. An iterative process is required to solve for both the rail deflection and the track system support modulus; this is described as well as an alternative method for determining the support modulus in Chapter 7.

6.9 Interaction between wheels

The two wheels in a bogie and adjacent wheels at vehicle ends are often close enough to each other for their deflection bowls to overlap. This means that there will be a difference between the measured deflection and that caused by a single wheel load. The deflection under a single wheel load is normally used for obtaining the track system modulus, e.g. (Raymond, 1985; Priest and Powrie, 2009). Kerr (2000) proposed that the spatial solution from the BOEF model should be used to account for the resulting interaction. If the track system support modulus is known, this can be used to find the displacement of the rail associated with a single wheel load w_0 from an estimate of the rail displacement w_s.

$$w_0 = \frac{w_s}{\left(1 + \sum_n \mathrm{e}^{-\frac{|l_n|}{L}} \left(\cos\left(\frac{|l_n|}{L}\right) + \sin\left(\frac{|l_n|}{L}\right)\right)\right)} \qquad (6.14)$$

where l_n is the distance to a neighbouring wheel and L is the characteristic length (see Eq.(5.3).

For plausible track system support moduli, it will be sufficient to consider only the influence of the nearest wheels. For a twin bogie vehicle, this would include wheels from adjacent bogies at vehicle ends. There will be differences in the result depending on whether the characteristic displacement is more representative of the deflection beneath a wheel closer to the vehicle end or the vehicle centre as indicated in Figure 6.20.

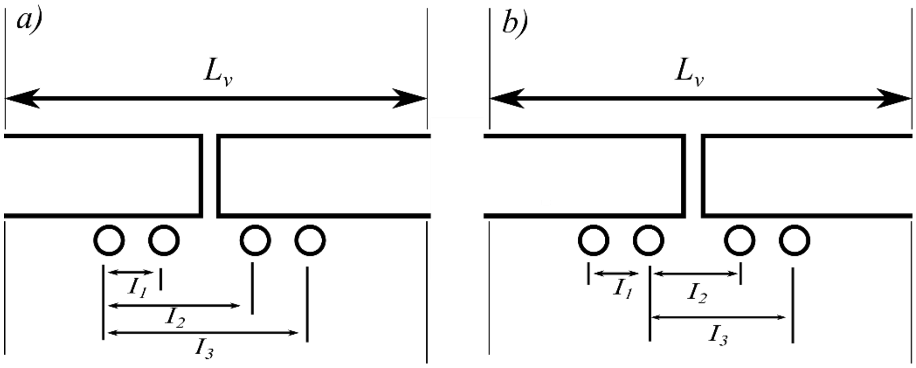

Figure 6.20 Wheel positions relative to a wheel closest to (a) the vehicle centre and (b) the vehicle end.

Figure 6.21 shows the expected ratio between the rail deflection due to a single wheel and the rail displacement accounting for interaction between neighbouring wheels on a vehicle. This was obtained from Eq.(6.15) for the wheel nearest the vehicle centre and nearest the vehicle end for the Javelin, the Eurostar and the Velaro trains and is plotted as a function of track system support modulus.

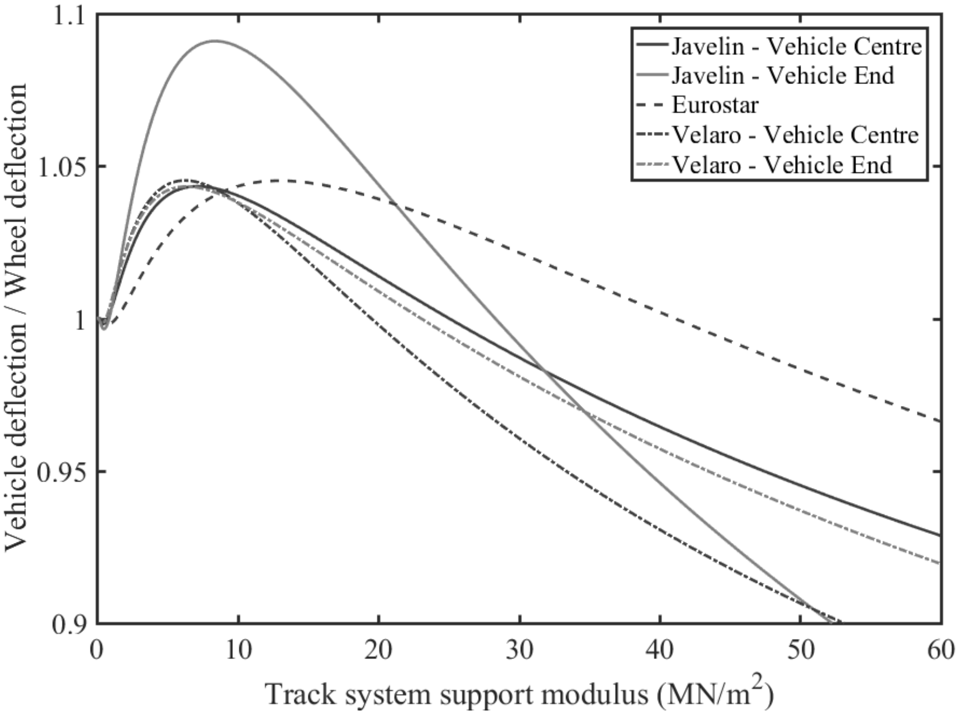

Figure 6.21 Ratio of downward rail deflection due to a vehicle and that from a single wheel for a track with a UIC60 rail and a range of plausible track system support moduli.

Figure 6.21 shows the ratio between the measured deflection and the deflection due to a single wheel load; the vertical axis is limited to 0.9 and 1.1 times the deflection from a vehicle. This ratio varies from one train to another and according which wheel is under consideration. It also shows that on softer track interaction between adjacent wheelsets tends to be additive and increase the maximum deflection, whereas on stiffer track interaction effects tend to reduce the maximum deflection as the adjacent wheel is in the region of uplift. This is shown in Figure 6.22 for a single wheel and a Javelin vehicle on a track with a UIC 60 rail and track system support moduli of 10 MN/m^2 and 40 MN/m^2. The wheel loads are 50 kN each and are moving at 50 m/s.

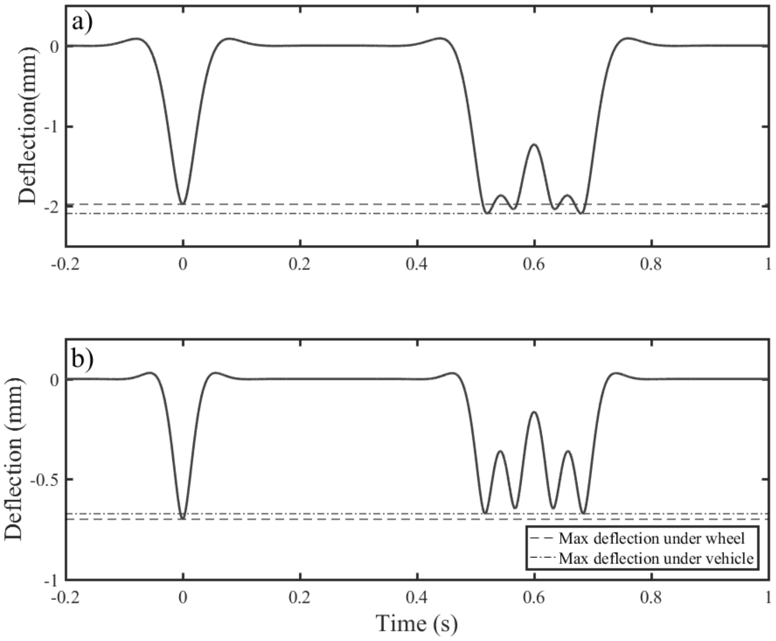

Figure 6.22 Comparison of maximum track deflection under a nominal wheel load of 50 kN moving at 50 m/s and from a Javelin vehicle with the same loads and speed (a) on softer track with a track system support modulus of 10 MN/m^2 and (b) on stiffer track with a track system support modulus of 40 MN/m^2. Both use a UIC 60 rail.

In this research, the downward rail deflection w_s has not been defined in a way that explicitly corresponds to deflection beneath a specific wheel. This means that it would be challenging to select an appropriate geometry correction. However, the results in Figure 6.21 suggest that for a plausible range of track system support moduli (10-50 MN/m^2) on well-performing track the likely difference between the measured deflection and the deflection from a single wheel will be no more than ± 9% for all the trains that operate on HS1.

6.10 Conclusion

Two different methods for characterising the range of total and downward track deflection have been proposed. The first method for characterising deflections was based on identifying the turning points in track deflection data and the second uses the CDF for track displacements. The CDF method is preferred, because it justifies a basis for identifying the at-rest position in the data, overcoming the artefacts from signal processing that make interpretation of these signals by numerical means challenging. The CDF method is quicker than turning point analysis, makes use of all the data rather than a few selected points, and can be used to average implicitly over multiple vehicles. This means that the method can be implemented so as to be less sensitive to extremes of movement, possibly from wheel flats, providing a result that is typical or characteristic of the regular track movement due to a passing train. Both methods could be used in the automated analysis of track vibration data.

Chapter 7: Analysing track stiffness

7.1 Introduction

Chapter 2 discussed how measures of track stiffness, in particular the track system support modulus, are often used for quantifying track performance. This chapter explains first how the track system support modulus can be determined from deflection data by using BOEF model to simulate measured rail deflection caused by a known load. An alternative is then explored, which utilises the properties of the Fourier transform for train loads and the response of the track model investigated in Chapter 5. Two implementations of this method are considered. Material from this chapter has been published in Le Pen et al. (2016) and Milne et al. (2017).

The methods given and developed here can be implemented automatically using a computer. They are tested here using data from the Crissmill plain line site obtained with the instrumentation described in Chapter 3. These methods have made it feasible to analyse significant quantities of track vibration signals obtained for the study sites presented in Chapter 8. This is useful for condition or performance monitoring as, together with a measure of track deflection, track vibration signals can be used to investigate the performance and properties of railway track.

7.2 Time domain methods

The BOEF model can be used to determine the track system support modulus from deflection data. Recall that this model is for rail deflection not sleeper deflection, see section 6.8. This means that a correction must be included in the calculation of the track system support modulus. This is an iterative process that uses a measurement of track bed displacement w_t and a measured or assumed wheel load P applied to the rail. A first approximation of the ‘track bed stiffness’ s_t can be found from:

$$s_t = \frac{P}{w_t} \tag{7.1}$$

P is likely to be an overestimate of the load applied to the track bed by a sleeper beneath a wheel, which is unknown. Often this is assumed to be half of the wheel load, although by finding the pressure distribution beneath the rail using the BOEF model and integrating over a sleeper bay suggests a lower value of between 24% and 40% of the actual wheel load for well-supported track with a system support modulus of 10-50 MN/m^2. This 'track bed stiffness' should be combined with the rail pad stiffness to obtain an initial estimate of the track support stiffness s.:

$$s = \frac{s_t s_p}{s_t + s_p} \tag{7.2}$$

This estimate of track stiffness can be used to estimate the deflection at the rail w_s from the measurements at the sleeper:

$$w_s = \frac{w_t}{1 - \frac{s}{s_p}} \tag{7.3}$$

Track stiffness may then be recalculated, Eq.(5.27):

$$s = \frac{P}{w_s} \tag{7.4}$$

Iteration continues until the rail displacement and track stiffness have converged for the applied wheel load. Then the track system support modulus can be found from:

$$k = \sqrt[3]{\frac{s^4}{64EI}} \tag{7.5}$$

This process produces results for the track system support modulus and rail deflection that are compatible with the assumed or measured load, the rail pad properties and the measured sleeper deflection.

As written, these equations are based on the assumption that interaction between wheels is negligible for the total displacement. In principle if *P* is the load from a single wheel, the correction from characteristic displacement w_s to the displacement due to a single wheel load w_0 using Eq.(6.14) should be incorporated into the calculation. However, the differences between w_s and w_0 are likely to be small. Alternatively, the measurements could be fitted to a train of applied loads using regression (Track Stiffness Working

Group, 2016). The applied load is often unknown so is a source of uncertainty in this calculation.

7.3 Frequency domain methods

The properties of the track system and the trainload frequencies control the shape of the spectra of low frequency track vibration. This was investigated extensively in Chapter 5. The low frequency track vibration may be thought of as the convolution of the response of the track to a single moving unit load, and a series representing the wheel loads from the train. This is a product in the frequency domain, which is given here for track displacement:

$$W(f) = \frac{4v^3}{4kv^4 + 16\pi^4 kL^4 f^4} \times P \sum_{m=1}^{M} e^{-\frac{i2\pi f x_m}{v}} \tag{7.6}$$

where *v* is the train speed, *k* the track system support modulus, *L* the characteristic length, *P* the wheel loads (assumed identical), *M* the total number of wheels and x_m the separation between the first and m^{th} wheel, as in Chapter 5.

Eq.(7.6) forms the basis for determining the track system support modulus in the frequency domain.

7.3.1 By analysis of the magnitudes of a pair of dominant trainload frequencies

As described in Le Pen et al. (2016), the frequency domain properties of the trainload frequencies can be used to determine the track system support modulus. The ratio is obtained of the amplitudes at two of the dominant frequencies which have peaks at N_a and N_b, which are at multiples of the vehicle-passing frequency. From Eq.(7.6 this is:

$$\frac{W(N_a)}{W(N_b)} = \frac{{L_v}^4 k + 16EI{N_b}^4\pi^4}{{L_v}^4 k + 16EI{N_a}^4\pi^4} \times \frac{\sum_{m=1}^{M} e^{-\frac{i2\pi N_a x_m}{L_v}}}{\sum_{m=1}^{M} e^{-\frac{i2\pi N_b x_m}{L_v}}} \tag{7.7}$$

This ratio is independent of train speed and wheel load. The corresponding equations for velocity and acceleration may be obtained by multiplying Eq.(7.7) by N_a/N_b and N_a^2/N_b^2, respectively.

The properties of periodic trains studied in Chapter 5 mean that Eq.(7.7) can be simplified using Eq.(5.15), allowing the method to be expressed using the geometry of a single vehicle rather than the whole train

$$\frac{W(N_a)}{W(N_b)} = \frac{kL_v^4 + 16\pi^4 EI{N_\mathrm{b}}^4}{kL_v^4 + 16\pi^4 EI{N_\mathrm{a}}^4} \times \frac{\cos\left(\frac{\pi N_\mathrm{a} L_b}{L_v}\right)\cos\left(\frac{\pi N_\mathrm{a} L_w}{L_v}\right)}{\cos\left(\frac{\pi N_\mathrm{b} L_b}{L_v}\right)\cos\left(\frac{\pi N_\mathrm{b} L_w}{L_v}\right)} \tag{7.8}$$

This equation can be used for periodic trains such as the Javelin and the Velaro. Eqs.(7.7) and (7.8) are the products of two terms: the first contains the effect of the track and the second is the ratio of amplitudes for a pair of the dominant trainload frequencies, depending on the train or vehicle geometry

The track system support modulus can be found by determining the ratio of the magnitudes at two dominant frequencies from the measurements. The appropriate form of Eq.(7.7) or Eq.(7.8) for displacement, velocity or acceleration can be used to find the track system support modulus as all other parameters, i.e. the rail bending stiffness and the train or vehicle geometry, are known.

In principle, any pair of frequencies could be used to give the same result. However, the analysis in Chapter 5 showed that the dominant frequencies and their amplitudes can be affected by different factors to a varying extent. This means that the pair of frequencies selected for evaluation can affect the success of the approach. The spectral peaks used should be prominent in both the measured and the theoretical trainload spectrum, be obtainable accurately and reliably from the vehicle geometry, insensitive to variations in wheel load, and not too close to one another so that good resolution can be achieved.

Certain peaks are more prominent, less influenced by train length and insensitive to inter-train variations in wheel load (e.g. the 1st, 3rd, 6th, 7th and 10th for the Javelin) as was seen in Figure 5.17 and Figure 5.18. These peaks are good candidates for determining track system support modulus by analysis of the ratio of the magnitudes at two dominant frequencies. Figure 7.1 illustrates the sensitivity to the track system support modulus of the ratio of the amplitudes at various pairs of frequencies for a Javelin vehicle, found using Eq.(7.8). Increased separation between peaks increases the sensitivity of the function to the track system support modulus. This suggests a ratio of the 10th or 7th to the 1st or 3rd harmonics of the vehicle-passing frequencies would be most suitable for determining the track system support modulus.

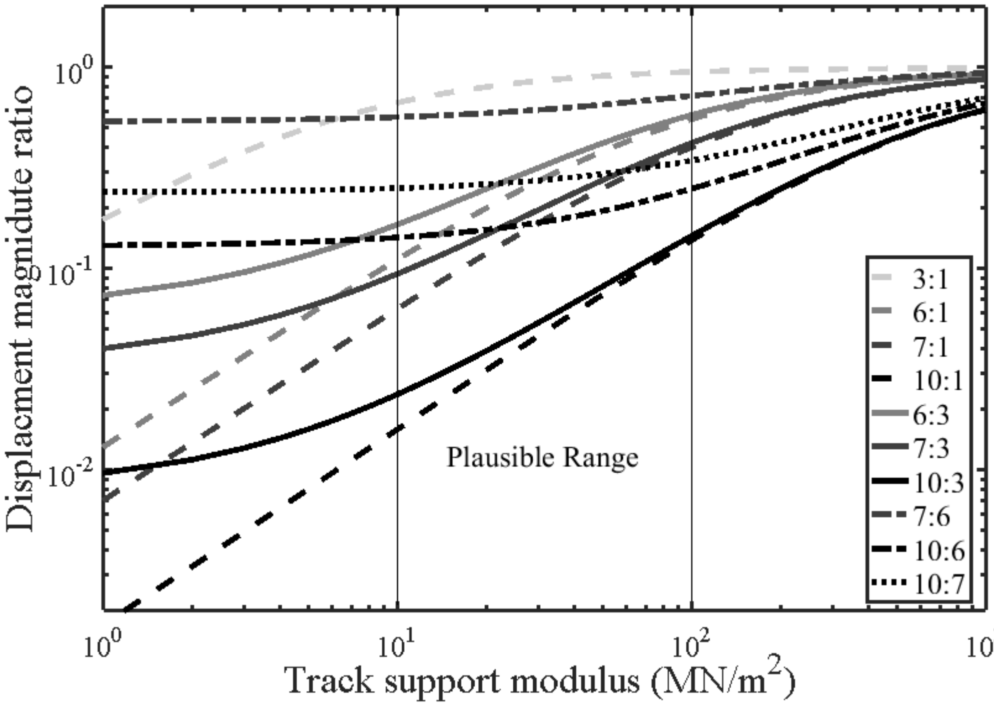

Figure 7.1 Displacement magnitude ratios between different pairs of dominant frequencies for a Javelin as a function of the track system support modulus. The plausible range of support modulus is also indicated.

Selection of the frequencies must also account for transducer performance. This means that lower frequency peaks should be avoided, particularly if using accelerometers. These peaks are likely to have low amplitudes and are more susceptible to transducer noise.

For a given pair of frequencies, the vehicle or trainset geometry can be used to compute calibration curves expressing the expected magnitude ratio as a function of track system support modulus for track displacement, or the equivalent for velocity or acceleration. Example curves for the expected displacement magnitude ratio between the 7th and 3rd harmonics of the vehicle-passing frequency for Javelin and the Velaro found using Eq.(7.8) and for the Eurostar using Eq.(7.7) with the 6th and 2nd harmonics are given in Figure 7.2. The result for the Eurostar takes account of the complex geometry and variations in wheel load along the train. By comparing the ratio of magnitudes at these frequencies obtained from measurements with these calibration cures the track system support modulus can be obtained.

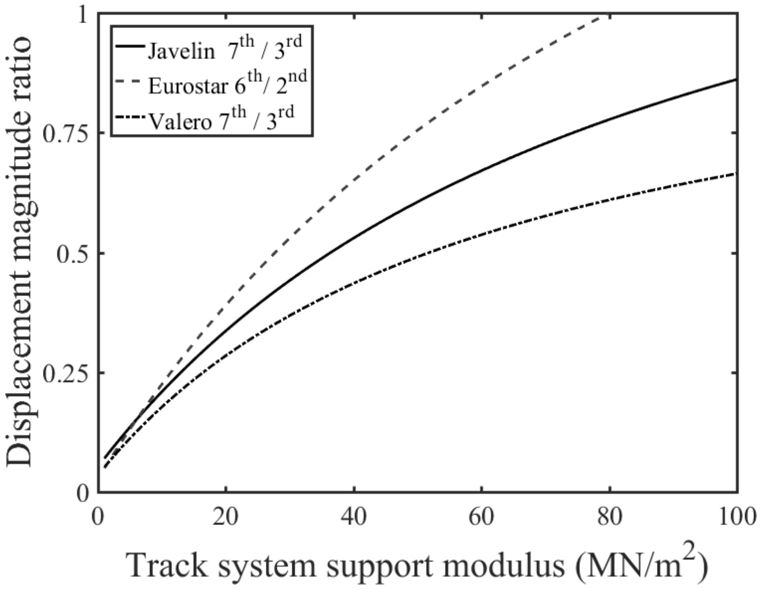

Figure 7.2 Expected displacement magnitude ratio for different track system support moduli for the Javelin and Velaro using the ratio between the 7th and 3rd dominant frequencies and the Eurostar using the ratio between the 6th and 2nd.

This method has been used to obtain the track system support modulus from the Javelin, Eurostar and Velaro data obtained on the same sleeper for which data were shown in Figure 5.7. The results are given in Table 7.1. The results for all trains are close, although the results for the heavier and faster Eurostar and Velaro give lower values than for the lighter Javelin.

Table 7.1 Track system support moduli obtained from ratio of the magnitudes at two dominant train load frequencies from the track vibration spectra for three different train types given in Figure 5.7.

Train	**Frequencies analysed**	**Velocity magnitude ratio**	**Track system support modulus (MN/m^2)**
Javelin	7th/3rd	1.11	33
Eurostar	6th/2nd	1.45	27
Velaro	7th/3rd	0.84	29

Peak finding algorithms can be used to determine the magnitude of the dominant frequencies in spectra for lineside measurements. Eqs.(7.7) or (7.8) can then be used to obtain the track system support modulus from measured ratios between the magnitudes at two of the dominant trainload frequencies as part of an automatic routine.

The frequency domain approach enables the track system support modulus to be determined without knowledge of the wheel load. This means that the characteristic rail deflection, obtained by the methods given in Chapter 6, can be used to estimate the loads applied locally to the track:

$$P = 2kLw_{\mathrm{s}} \tag{7.9}$$

7.3.2 Numerically by regression

Analysis in Chapter 5 showed that there are often several dominant frequencies that would be suitable for use. For example, the 1st, 3rd, 6th, 7th and 10th peaks may be suitable for the Javelin. Analysing the ratio between the magnitudes at a pair of dominant frequencies to determine the track stiffness disregards information from the measurements that could be used to inform and possibly improve the calculation. Solving the problem numerically using regression rather than solving it deterministically would allow more data to be taken into account.

Chapter 5 explained how that the magnitude of the Fourier transform from lineside measurements $|W(N)|$ can be expressed non-dimensionally in terms of the vehicle-passing frequency. Using this frequency axis makes it more straightforward to divide by the expected relative magnitudes of the train load frequencies from Eq.(5.17) to obtain an estimate of the magnitude of the Fourier transform for the track vibration shape function $|\hat{S}(N)|$.

$$\left|\hat{S}(N)\right| = \frac{|W(N)|}{\left|\cos\left(\frac{\pi N L_b}{L_v}\right)\cos\left(\frac{\pi N L_w}{L_v}\right)\sum_{m=0}^{N_c-1} e^{-i2\pi N m}\right|} \tag{7.10}$$

Eq.(7.10) is based on the result for a periodic train, although the complete train geometry can be used for more complex cases. If the track is behaving normally, the track vibration shape function Eq.(5.9) should fit these data. Fitting this function by regression can be used to find the track system support modulus.

In a solution by least squares, the objective is to minimise the sum of the squares of the residual errors r_d:

$$R = \sum_d {r_d}^2 \tag{7.11}$$

These are given by

$$r_d = a_d - f(N, \{A, k\}) \tag{7.12}$$

where $f(N, A, k)$ is a function that describes the effect of the track stiffness on the spectrum for track vibration, from the shape function Eq.(5.9). For track displacement, this is:

$$f(N, A, k) = A \frac{{L_v}^4}{\left(k{L_v}^4 + 16\pi^4 EIN^4\right)} \tag{7.13}$$

Equivalent functions for track velocity and acceleration can be found by multiplication of Eq.(7.13) by N and N^2 respectively. A is an amplitude term and k is the track system support modulus. In theory, A is related to the train speed and the total load applied during the train passage; however this is not important here. Figure 7.3 shows an example of the velocity shape spectrum fitted to data from sleeper velocity measurements for the Javelin track vibration spectrum from Figure 5.7(a). The amplitude has been normalised by A. The track system support modulus was found to be 33 MN/m^2; which is the same as the result found from the ratio of magnitudes of the 7th and 3rd dominant frequencies (Table 7.1).

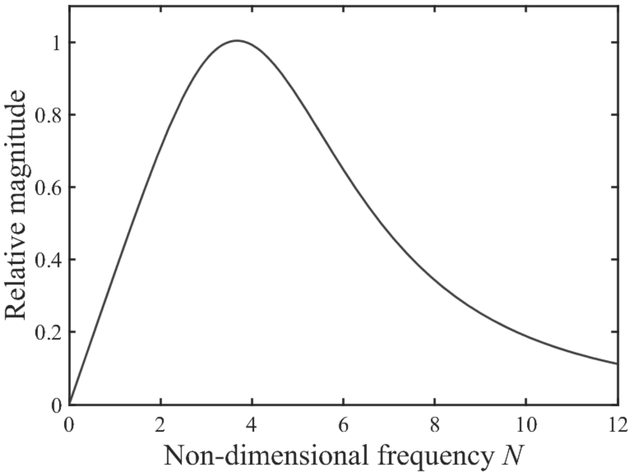

Figure 7.3 Velocity shape function obtained for Javelin data used to estimate the track system support modulus of 33 MN/m^2 by fitting the BOEF model in the frequency domain using regression.

7.4 Comparison of methods

7.4.1 Frequency domain implementations

The two different methods for finding the track system support modulus in the frequency domain using properties of the Fourier transform for track vibration both have their merits. Both require similar inputs: vehicle or train geometry, rail type and magnitudes at the dominant frequencies from lineside measurements. Analysing the magnitude ratios is deterministic and is computationally faster than regression. In theory, both methods should give the same result provided that the track behaviour conforms to the model. However, analysing a single pair of dominant frequencies relies on very little data; this means it may be sensitive to factors that affect the magnitudes of the peaks used. The regression method uses more data so should be less sensitive to factors affecting individual peaks. Figure 7.4 compares results obtained using regression and ratio analysis for May 2015 and 2016 geophone data from the Crissmill plain line site. For May 2015, the two methods generally agree for the entire site. The agreement is less good for certain sleepers in May 2016.

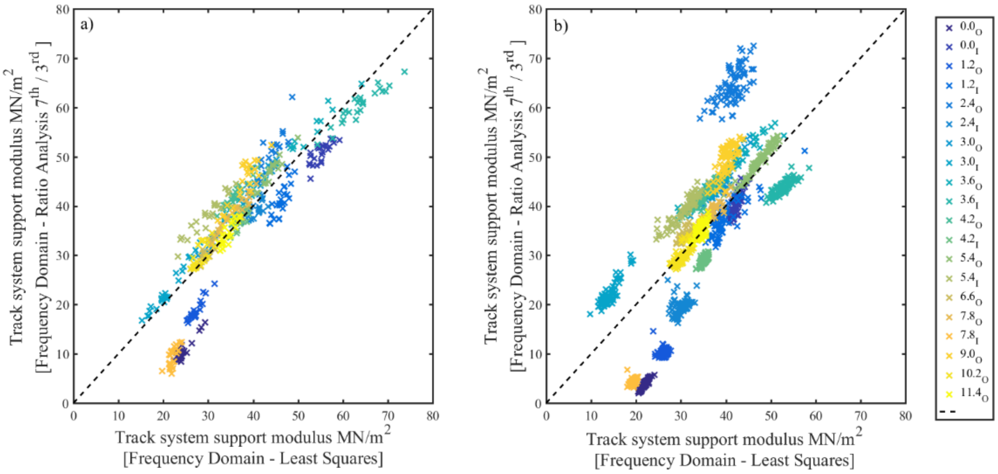

Figure 7.4 Comparison between track system support modulus obtained using numerical regression and ratio analysis for (a) May 2015 and (b) May 2016.

To investigate this, further comparisons are made with conventional estimates using the load deflection method.

7.4.2 Frequency and time domain implementations

Comparing the conventional time domain load-deflection method with the results from the frequency domain methods provides a means of testing the effectiveness of the new frequency domain based methods. To do this, the track system support modulus was obtained from the estimates of characteristic downward deflection found using the CDF of sleeper deflection, which were then corrected to give the rail displacement using a pad stiffness of 84 MN/m. As the applied wheel load was uncertain, the calculation was repeated with nominal wheel loads of 59±15 kN for both occasions (based on the mean and 3σ from Figure 3.4(b)). These results are based on the analysis of 49 Javelins for May 2015 and 65 Javelins for May 2016. The results are compared with data obtained using the two different implementations of the frequency domain method in Figure 7.5.

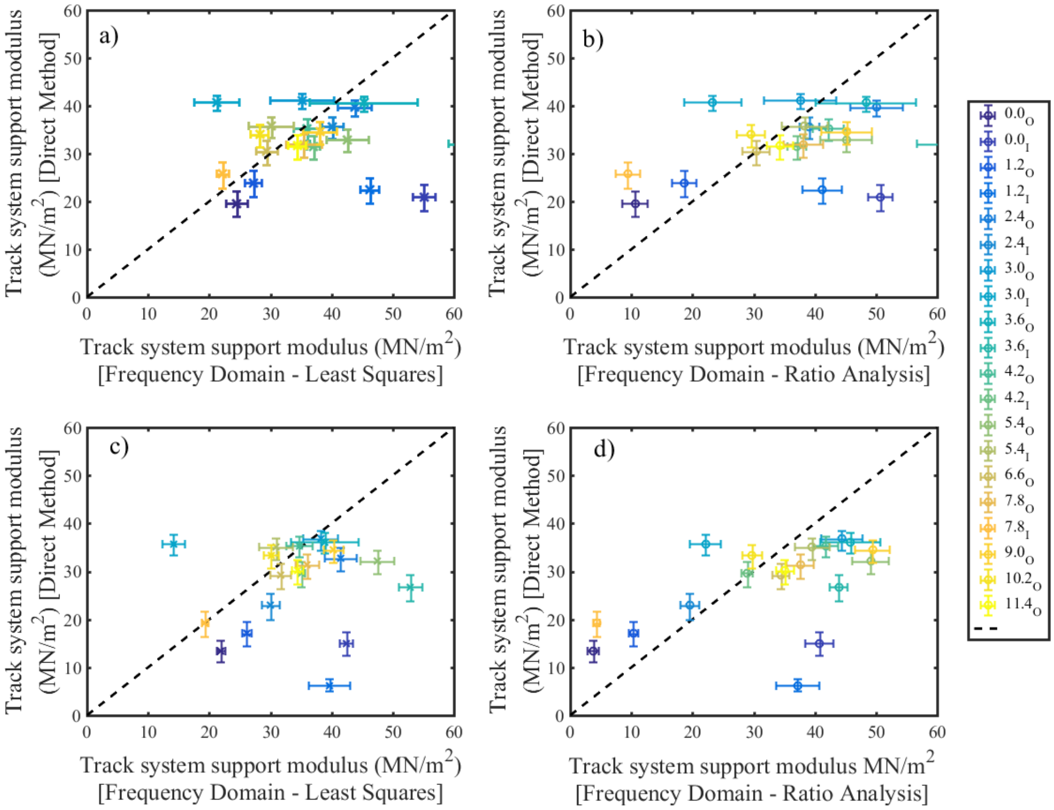

Figure 7.5 Comparison between track system support modulus obtained directly using a range of assumed loads with measured deflections, corrected for a pad stiffness of 84 MN/m with (a) numerical regression and (b) ratio analysis of the 7th/3rd dominant frequencies for 49 Javelins in May 2015 and (c) numerical regression and (d) ratio analysis of the 7th/3rd dominant frequencies for 65 Javelins in May 2016.

The results for the time domain and the frequency domain approaches are close. The values for track system support modulus determined using the track deflection and nominal wheel load agree more closely with those obtained by the regression method than from the ratio of magnitudes at the dominant frequencies. This difference is more pronounced for the more recent data, where the results from ratio analysis and from the least squares fit did not agree at specific sleepers (Figure 7.4).

There are some outliers where the results from the different approaches disagree. This might indicate that the assumed load is too low or too high or that a hanging sleeper might be influencing the behaviour. If a sleeper were unsupported, causing a large deflection, a low stiffness would be calculated in the time domain. The effect of a hanging sleeper on the spectrum of track vibration might be different and requires further study to understand the effects.

7.5 Conclusion

The insights into the train load frequencies and role of track stiffness gained in Chapter 5 has allowed development of new methods to determine the track system support modulus from a spectrum of track vibration. The first method analyses the ratio of the magnitudes found at a pair of dominant train load frequencies to determine the track system support modulus. This method can be simplified to use the geometry for a single vehicle rather than for a whole train for finding the relative magnitude at the dominant frequencies. An alternative approach, which involves estimating the track system support modulus by fitting the track vibration shape function in the frequency domain, was also proposed. Generally, this approach offered better agreement with results obtained using measured deflection and a range of plausible assumed loads than analysing the ratio of the magnitudes of the peaks at the 7th and 3rd dominant frequencies. However, curve fitting is more computationally expensive than ratio analysis.

Chapter 8: Application of continuous monitoring

8.1 Introduction

The methods of analysis developed in Chapters 5, 6 and 7 allow for the automated processing needed to interpret large volumes of vibration data that would be generated by long-term continuous application of lineside monitoring systems. First this chapter tests these methods using data from the Crissmill plain line site, and then demonstrates their application for long-term lineside monitoring with respect to three defect sites on HS1.

Monitoring systems based on the MEMS accelerometers that were validated in Chapter 4 have been used in extended deployments to study the performance of the track at the Crissmill defect site, the North Downs Tunnel portal site and the Rainham Viaduct site (which were described in Chapter 3). Data from these sites have been processed and then interpreted using methods developed in Chapters 5-7. The results are used to demonstrate the utility of the methods for obtaining a record of how the performance and properties of the track are changing, and understanding the effects of maintenance interventions. In the subsequent figures, a maintenance intervention is indicated by dashed vertical lines.

All deflection data presented for the defect sites was obtained from acceleration signals. The signals were sampled at 500 Hz, unless otherwise stated. Processing by double integration used high- and low-pass Butterworth filters with 2 and 40 Hz cut-off frequencies respectively. The characteristic total and downward deflections were obtained using the CDF for track deflection assuming P = 0.025, 0.7 and 0.975 (see Chapter 6). These correspond to the typical extent for downward movement, the at-rest position and the typical extent for upward movement respectively for all train types recorded. For expedience, the track system support modulus was found in the frequency domain by analysing the ratio of the magnitudes of the 7th and 3rd dominant frequencies in the spectrum for track vibration (see Chapter 7). This was done for the Javelin and Velaro only (once the latter was in operation after November 2015), using vehicle rather than trainset geometry. The mixture of vehicles and coupling of trainsets within the

Eurostar meant these data were less reliable for determining the track system support modulus than the other trains. The characteristic downward deflection and track system support modulus were used to find an estimate of the typical wheel load applied at each location for the Javelin and the Velaro. Sleeper deflections were corrected to determine the rail displacement assuming a pad stiffness of 84 MN/m.

8.2 Testing of continuous monitoring

This section uses data from the Crissmill plane line site to test the analysis methods developed in Chapter 5, 6 and 7 for characterising the range of track deflection and determining the track system support modulus.

8.2.1 Typical results

The new methods of analysis have been used to characterise the track deflection and find the track system support modulus determined from geophone data for a well-performing sleeper (3.6_{O}) at the Crissmill plain line site on two single days of measurements in May 2015 and May 2016. The results are shown in Figure 8.1. On both occasions, the mean characteristic deflection was 0.36 mm with a coefficient of variation of 4-5%. This is close to the 4% coefficient of variation found for the mean inter-train wheel load for Javelin data in Chapter 3. In 2015 and 2016, the mean track system support moduli were found to be 44 MN/m^2 and 48 MN/m^2 respectively. The coefficients of variation were 7.5% and 5.5%. This type of data is provided for the defect sites studied later in this Chapter. If recorded at a sufficiently regular interval over an extended period of time these data can then be used to show how the performance and properties of the track change over time.

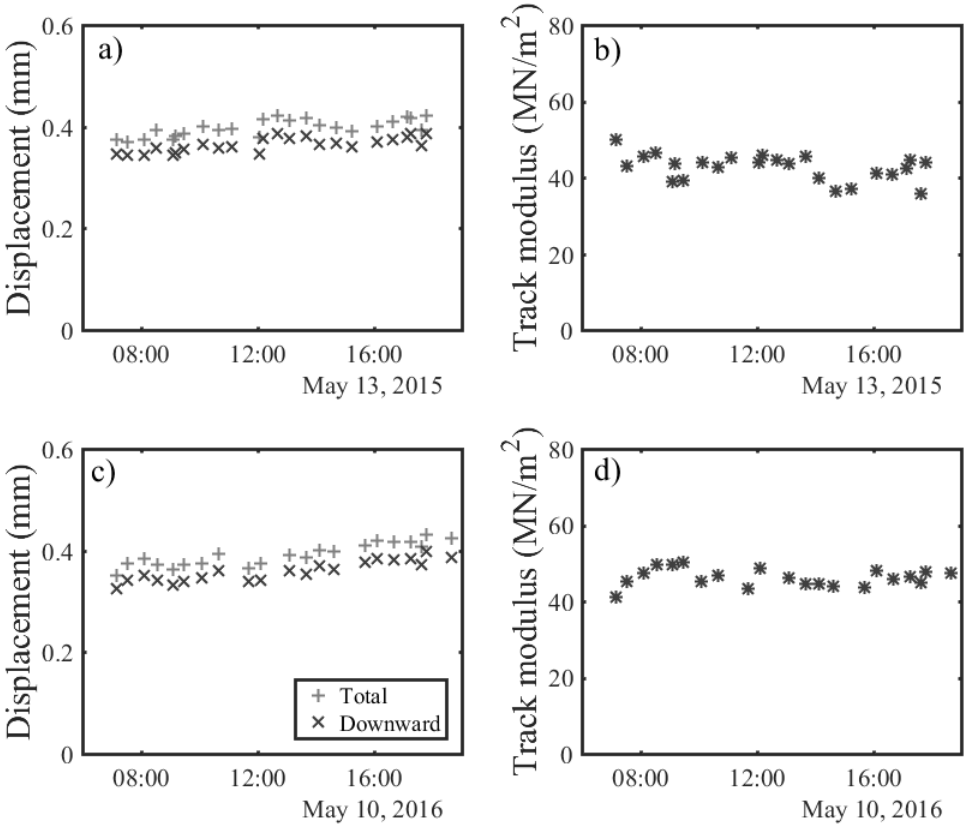

Figure 8.1 12 hours of (a) characteristic total and downwards track displacement and (b) track system support modulus data from May 2015 and (d) characteristic total and downwards track deflection and (d) track system support modulus data from May 2016 for Javelin trains from sleeper 3.6_O at the Crissmill plain line site.

When many transducers are deployed, it can informative to plot profiles for typical data along the length of a site. This can be done for a single train, or using average results for a given train type over a meaningful period of time (e.g. one day). Figure 8.2 shows (a) the mean deflection, and (b) track system support modulus profiles for the cess side of the Crissmill plain line site obtained from one day of geophone measurements in May 2015 and 2016. The error bars show the 99.7% confidence interval. The mean values of the equivalent wheel loads are also given in (c); these are mostly plausible, although there is more spread than in the quasi-static results from weighing-in-motion system seen in Figure 3.4(b).

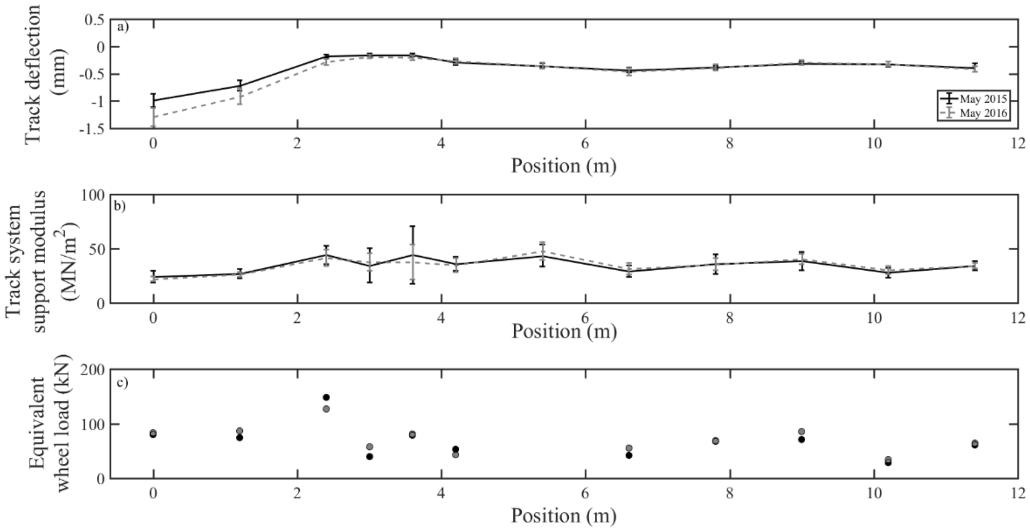

Figure 8.2 (a) Mean and 99.7% confidence intervals of the characteristic downward deflection, (b) mean and 99.7% confidence intervals of the track system support modulus, (c) mean equivalent applied wheel load, for the cess side of the Crissmill plain line site from one day of measurements taken in May 2015 and May 2016 from Javelin passage data.

8.2.2 Variation

Data from lineside measurements contains variation. Understandably, the behaviour of the track will differ for heavier and faster trains, but there will also be variation between results for the same train type. These may be systematic, e.g. directly attributable to variation in occupancy, train speed and environmental conditions, or statistical and thus more difficult to associate with a particular process. This section aims to understand the effect of variations in load, operational speed and air temperature on the results from lineside monitoring. The effect of transducer type is also considered. The impact of these variables is studied with reference to deflection and stiffness data from the Crissmill plain line site for the May 2015 visit. Data from the weighing-in-motion system near Wennington (Figure 3.4(b)) is used to obtain train loads; train speed is obtained from the vibration measurements and air temperature from a nearby weather station at Hollingbourne (Weather Underground, 2015).

A chi-squared test was used to establish that these environmental variables were independent of each other. The characteristic downward deflection and track system support modulus were then plotted against each of these variables. The deflections were obtained using the CDF method and the track system support modulus obtained from the ratio of the magnitudes at the 7th and 3rd dominant frequencies. Results are presented for data from each end of the sleeper positioned 4.2 m from the first sleeper instrumented with a geophone at the site. This sleeper was chosen as deflections were low and the track support conditions were similar at either end. Generally, the trends were the same for other sleepers and for the November 2015 monitoring visit. Figure 8.3 shows the results of the effect of train weight, Figure 8.4 train speed and Figure 8.5 air temperature.

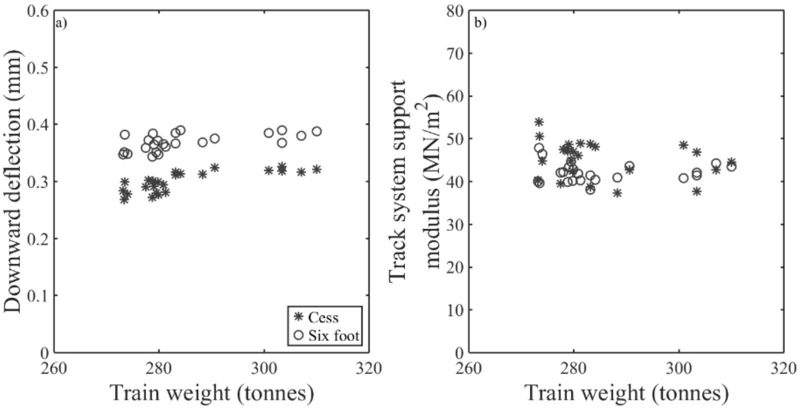

Figure 8.3 (a) Characteristic downward deflection, (b) track system support modulus either end of sleeper 4.2 at Crissmill plain line plotted against train weight from a weighing-in-motion system.

Figure 8.3(a) shows a slight linear increase of deflection with train weight. This is not unexpected, as the relationship between the static wheel load and deflection is normally assumed to be so as seen in the BOEF model. It should be noted that there is an intermediate station stop between the weighing-in-motion system and the study site, meaning that the exact train weights are not known. As would be expected, the stiffness is independent of train weight in Figure 8.3(b). Track deflections in Figure 8.4 and Figure 8.5 have been adjusted for the weight of the train to account for this relationship.

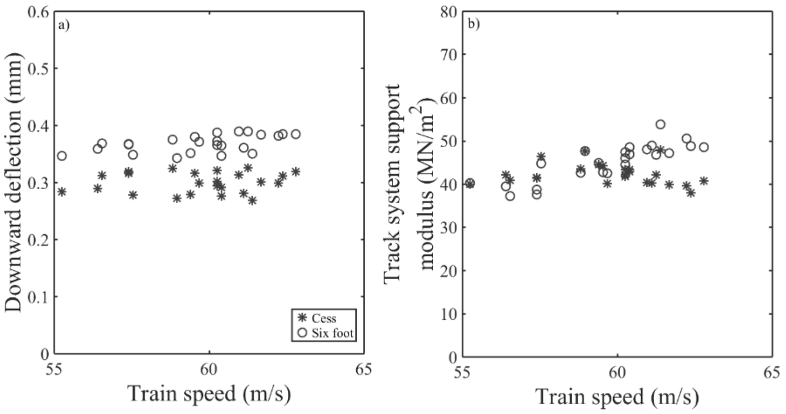

Figure 8.4 (a) Characteristic downward deflection (adjusted for the weight of the train), (b) track system support modulus either end of sleeper 3.6 at Crissmill plain line plotted against train speed.

Figure 8.4 shows no clear trend between train speed and either deflection (adjusted for the weight of the train) or stiffness, although the range of train speeds 55-63 m/s may not be wide enough to discern a relationship.

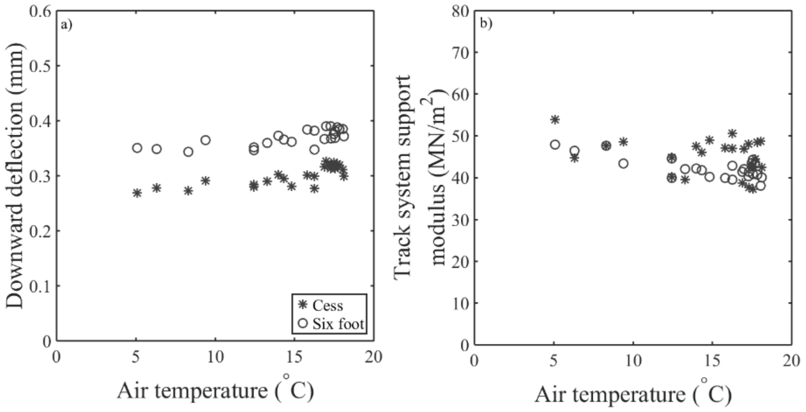

Figure 8.5 (a) Characteristic downward deflection adjusted for train weight, (b) track system support modulus either end of sleeper 3.6 at Crissmill plain line plotted against air temperature from a local weather station.

Figure 8.5 shows that air temperature and deflection (corrected for train weight) increased together. This was accompanied by a corresponding trend of the track system support modulus reducing with increasing air temperature. This suggests that the reduction in stiffness may be from the track. Squicciarini et al. (2016) showed that the rail pad stiffness reduces with increases in temperature, which could explain the observations. Again, the sample size from the field data is small and only covers a narrow temperature range of 4-18° C.

In theory temperature effects should not affect filtered accelerometer data from the monitoring system. Temperature has a negligible for the sensitivity of the transducer (Analog Devices, 2009), and the variable component of the voltage in the cable. As although an increase in temperature would increase resistance of the cable and hence the voltage drop between the sensor and the data acquisition system. As the current in the circuit is constant the voltage drop will reduce the D.C. offset of the signal, which is removed by filtering. The variable part of the voltage signal, which is proportional to the dynamic acceleration, is unaffected (Horowitz and Hill, 2015).

8.2.3 Influence of transducer choice

The transducer type used for monitoring may have an influence on the variability of the results. For example, it was shown in Chapter 4 that the raw output from MEMS accelerometers is much noisier than from geophones. The effect of this will be even more significant for displacement, owing to the double integration of the acceleration signal. Figure 8.6 compares the characteristic downward displacement data and track system support moduli obtained from a geophone and a MEMS accelerometer co-located on a sleeper end. The mean deflections were similar at 0.27 mm for the geophone and 0.28 mm for the MEMS accelerometer, but the accelerometer had a coefficient of variation of 13% compared with 5% found for the geophone. Similarly, the mean track system support modulus was found to be 33 MN/m^2 using both sensors, with coefficients of variation of 10% and 13% for the geophone and MEMS accelerometer respectively. The accelerometers thus give the same mean result as the geophones, but are more variable. This is consistent with the conclusions from Chapter 4.

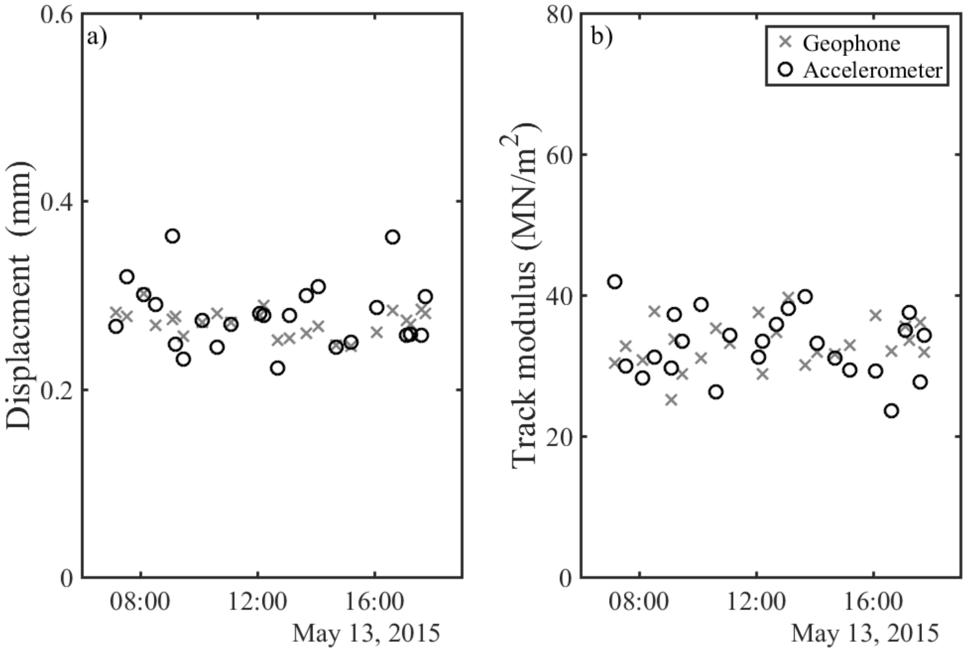

Figure 8.6 (a) Characteristic downward displacement data and (b) track system support modulus obtained from a geophone and a MEMS accelerometer co-located on a sleeper end.

8.2.4 Conclusion

This analysis has shown that there is variability between the displacement and stiffness results obtained from measurements of the same train type. Generally, coefficient of variation found for the stiffness (5.5-7.5%) was greater than that found for deflection (4-5%), which for a single day of measurements was similar to the variation in the inter-train mean wheel load for the Javelin. The magnitude of deflection was shown to increase with the train weight. No other relationships between train speed and displacement or track system support modulus were found, suggesting quasi-static behaviour is dominant. Increasing track deflections and a reducing track system support modulus were associated with increasing air temperature, indicating that the properties of the track may change with temperature. Clearly the environmental variables and transducer used do influence the results from monitoring, although some of the variability could arise from the assumptions that the processes used to characterise and analyse the data are based on (e.g. a linear and uniform track support, the frequency and magnitude of the dominant trainload frequencies and choice of probability values for the downward deflection, at-rest position and uplift, see Chapters 5-7). The new techniques have been used to analyse large volumes of data obtained from near continuous monitoring at the Crissmill, North Downs Tunnel and Rainham Viaduct defect sites. Results for these are presented in the subsequent sections.

8.3 Crissmill defect site

At Crissmill there was a recurring track defect on the down line at the end of a crossing, where the track transitioned from mono-block sleepers used at the end of the crossing back to duo-block sleepers used for plain line. The site is complex owing to the change in sleeper type, a shallow UTX, a rail weld and a comparatively high (0.7 m) and steep (35°) ballast shoulder. This makes it a challenge to discern which feature or combination of features may have influenced the formation of the track defect. Lineside monitoring with MEMS accelerometers was used to assess the performance of the track in response to three different maintenance interventions. Monitoring began in January 2015 prior to any work commencing on site, and continued for an extended period after the last intervention from April 2015 until October 2016 and then resumed in May 2017. This was to investigate whether the improvements were sustained. The three interventions were: shimming between the rail and the sleepers in the defect zone, to reduce size of the voids; tamping, necessary after an unsuccessful attempt to install USPs; and installation of new sleepers with USPs and ballast replacement. The timings of these interventions are given in Table 8.1.

Table 8.1 Timing of maintenance interventions

Intervention	Date
Shimming between sleepers	February 2015
Machine tamping (after an unsuccessful attempt to retrofit USPs)	March 2015
Installation of new sleepers with USPs and ballast replacement	April 2015

Figure 8.7 shows track geometry data from the TRC supplied by NRHS for the track 50 m either side of the Crissmill defect site. The locations of the defect site as well as the points motor and plain line study site, described in Chapter 3, are marked. These results are from three occasions: one run before any intervention (January 2015), two runs after

tamping, (March and April 2015) and two runs after installation of the under-sleeper pads (May and June 2015). This shows how each invention affected the track geometry, which can be compared with the results from lineside monitoring below.

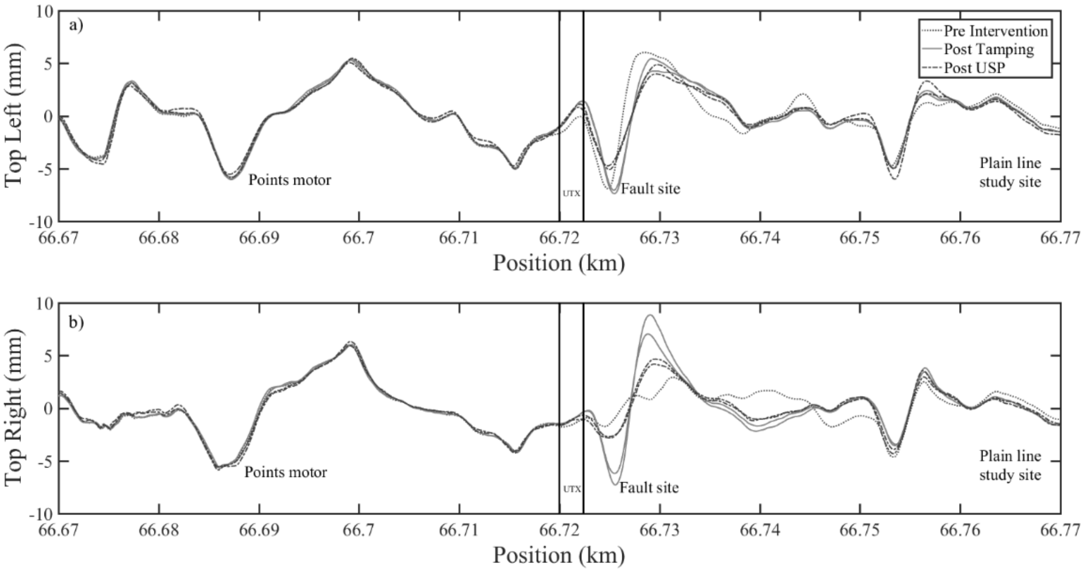

Figure 8.7 Vertical track geometry for 100 m of track (66.67-66.77 km) surrounding the Crissmill defect site. Before any interventions (January 2015), after tamping (March and April 2015) and after instaltion of USPs (May and June 2015). Direction of travel is left to right.

The fault site was instrumented using six MEMS accelerometers. The transducer positions are indicated in Figure 8.8. Transducer 2.4_O was mistakenly replaced one sleeper back up the line at 1.8_O after the installation of the under-sleeper pads in April 2015, it was subsequently returned to the original position in November 2015.

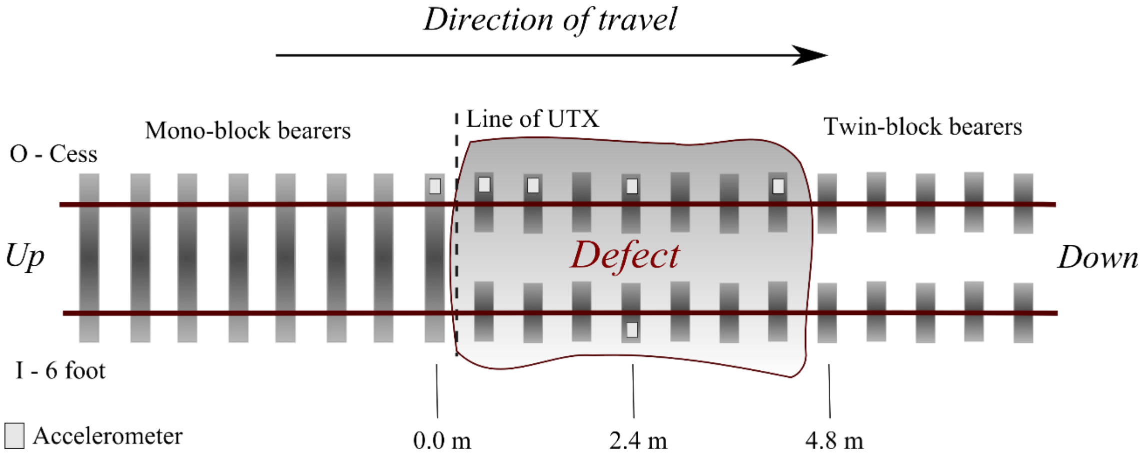

Figure 8.8 Transducer locations used for continuous monitoring as the Crissmill defect site.

Results are presented from when the instrumentation was first deployed in January 2015 until October 2016. Within this period, data were obtained for approximately 14000 trains, almost every train that passed the system. There are gaps due to a fault with the data logger in June 2015, damage to the sensor in position 0.6_O from May 2015 until November 2015 and again from July 2016, and occasional power supply problems.

The characteristic total and downward displacements are presented in Figure 8.9 and Figure 8.10 for the Eurostar and Javelin train types. Results for the Velaro (November 2015 onwards) were similar to those for the Eurostar.

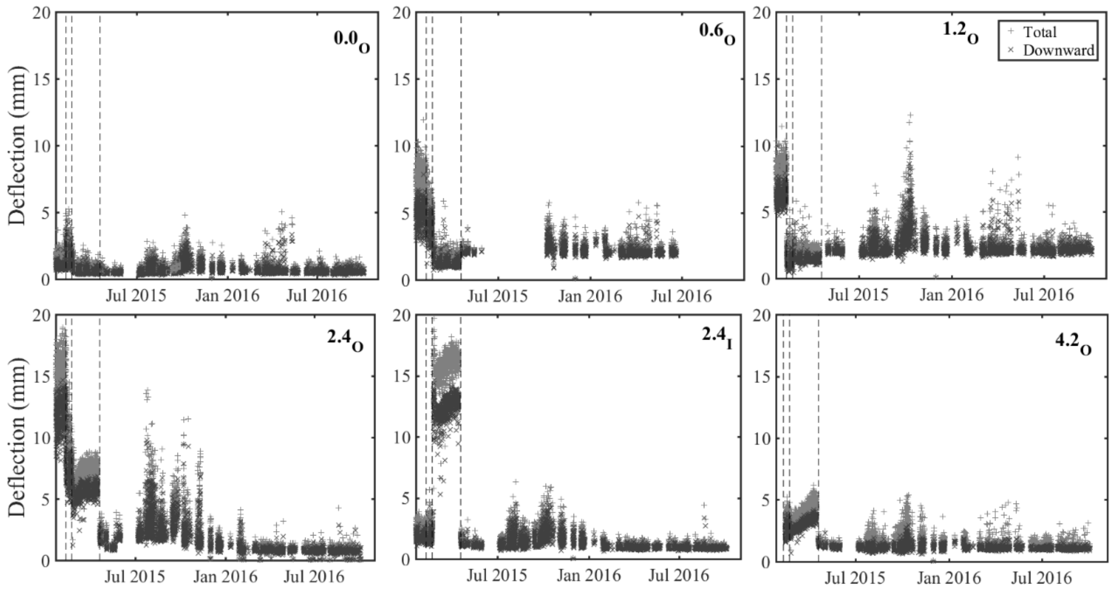

Figure 8.9 Characteristic total (P=0.025-0.975) and downward (P=0.025-0.7) track deflection due to passing Eurostar at the Crissmill defect site.

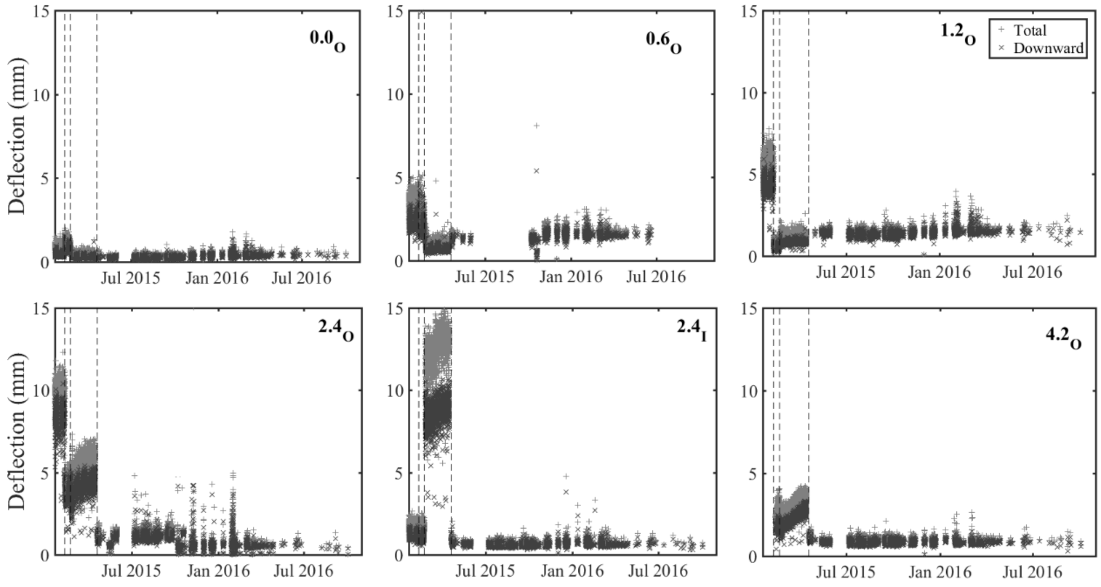

Figure 8.10 Characteristic total (P=0.025-0.975) and downward (P=0.025-0.7) track deflection due to passing Javelin at the Crissmill defect site.

Downward deflection of the mono-block sleeper 0.0_O was generally less than 1 mm for all train types. Deflections of instrumented duo-block sleepers on the cess rail (0.6_O, 1.2_O and 2.4_O) were large before any intervention. Downward movements exceeding 2.5 and 5 mm; 5 and 7 mm; 8 and 12 mm were obtained for the Javelin and Eurostar respectively, indicating poor performance and possible voiding. More acceptable deflections of around 1.3 mm were found on the six-foot side at 2.4_I.

The interventions had different effects. First, 4.5 mm thick shims were installed between the rail and the duo-block sleepers on the cess side to reduce the size of the voids. The deflections at 1.2_O and 2.4_O were reduced by the shim thickness. Following the unsuccessful attempt to install USPs, the track was machine tamped. This reduced the deflection at 0.6_O, 1.2_O and 2.4_O, but led to a significant increase at location 2.4_I. This increase is likely to have been caused by disturbance to the track bed during the intervention. After tamping, deflections at location 4.2_O began to increase steadily. Successful installation of new duo-block sleepers with under-sleeper pads stabilised deflections at all locations to 1.8-2.2 mm at 0.6_O and 1.2_O and 0.7 – 1.1 mm at 2.4_O, 2.4_I and 4.2_O. Addition of the resilient pad is responsible for the increase in sleeper deflections beyond the 0.3-0.6 mm measured at the well-performing site a short distance down the track (Figure 8.1 and Figure 8.2). Results for the track system support modulus are presented; these are obtained in the frequency domain using data for the Javelin and the Velaro, and are shown together in Figure 8.11.

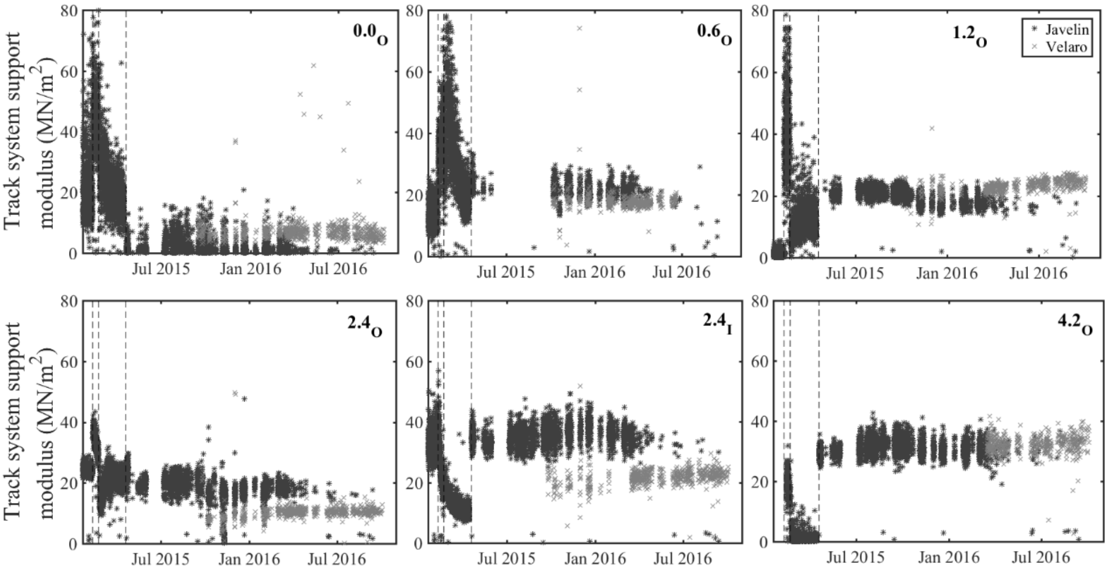

Figure 8.11 Track system support modulus calculated using the ratio of the magnitudes of 7th to the 3rd dominant frequencies in the acceleration spectrum for Javelin and Velaro trains at the Crissmill defect site.

The non-linear support conditions from voiding and the variability of support conditions along the defect zone mean that the results for the track system support modulus are not meaningful for data obtained prior to installation of USPs. At some locations, application of the frequency domain method gives highly variable results. Results from either end of sleeper 2.4 are remarkably consistent, but are not plausible given the amplitude of the deflections. The way in which the presence of a void may affect low frequency track vibration, and hence the value obtained for the track system support modulus when analysed in the frequency domain needs to be understood.

After installation of the under-sleeper pads onto the duo-block sleepers at locations 0.6 – 4.8 in April 2015, the results obtained for the track system support modulus stabilised for the remainder of the monitoring period. Generally, the values obtained from frequency analysis were between 15 and 35 MN/m^2 with a mean of around 20 MN/m^2. This is a plausible reduction from the 30 - 45 MN/m^2 found for well-performing track on the same line (Figure 8.1 and Figure 8.2), considering that an additional resilient element with a static stiffness of 15-20 MN/m per sleeper end has been introduced into the track.

At locations 0.6_O, 1.2_O & 4.2_O the stiffnesses obtained for the Velaro and the Javelin agreed consistently. At locations 2.4_O and 2.4_I, the results for the Velaro were consistently lower than for the Javelin. At location 2.4_O the mean stiffness for the Javelin (20 MN/m^2) was closer in value to that at other locations within the site, whereas the value for the Velaro (15 MN/m^2) was lower than elsewhere. At 2.4_I, the result for the Javelin (40 MN/m^2) was higher than the rest of the results but for the Velaro (20 MN/m^2) was similar. Generally, the displacements at 2.4_I were about 0.1-0.2 mm more than at 2.4_O for the same train. Similar results (not shown) were obtained by fitting a BOEF model to the spectrum for track vibration as were obtained by analysing the ratio of magnitudes of the 7th and 3rd dominant frequencies. This suggests there were consistent differences in how these sleepers were behaving for the two train types, which is indicative of non-linear behaviour.

Estimates of the equivalent wheel load applied by each Javelin and Velaro found from the characteristic downward deflection, corrected for rail deflection and the track system support modulus, are shown in Figure 8.12.

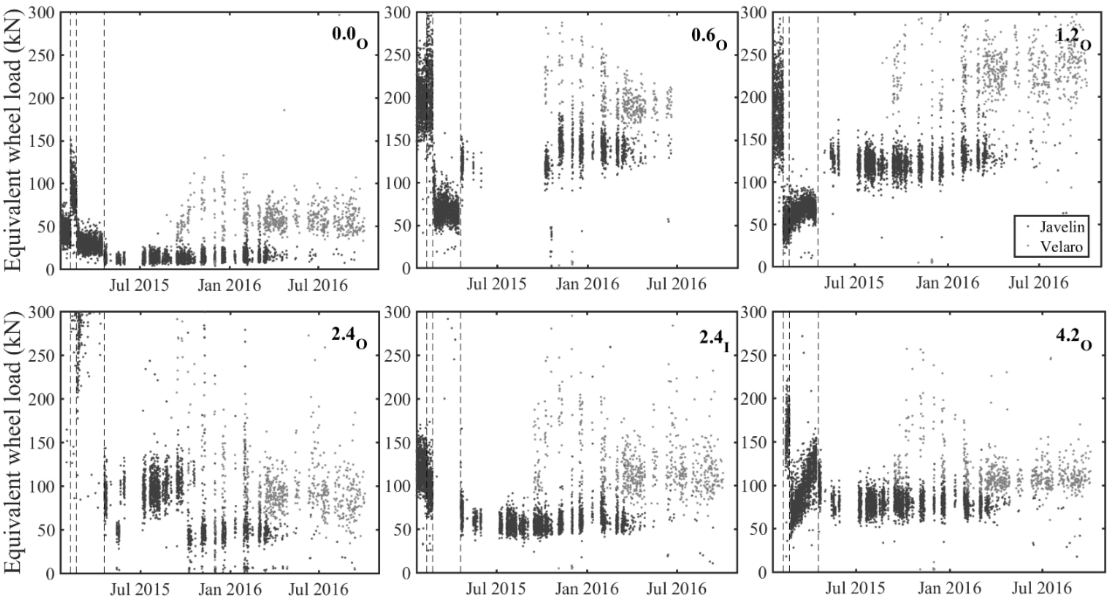

Figure 8.12 Equivalent applied wheel load from the characteristic downward deflection and track system support modulus for Javelin and Velaro at the Crissmill defect site, assuming a rail pad stiffness of 84 MN/m.

The BOEF model has been used to find an equivalent wheel load corresponding to the measured track displacements and track system support moduli. Although there is a lot of scatter in the data and the values should not be taken as precise; these results give an order of magnitude that is appropriate for actual wheel loads and the trends of behaviour are consistent. These results can be used to assess whether a certain location is being overloaded compared with another, and typical static wheel loads can be determined. From Figure 8.12 this analysis suggests that after installation of the USPs the applied loads for the mono-block sleeper (0.0_O) were much lower than for the rest of the site and lower than typical wheel loads. It is possible that first two duo-blocks at 0.6_O and 1.2_O are being overloaded compared with the rest of the site. Locations 2.4_O and 2.4_I, on the sleeper that was near the centre of the defect zone, may be underloaded compared with elsewhere in the site. The calculated equivalent wheel loads at this sleeper are a little lower than typical static wheel loads. Additionally, there seems to be a consistent imbalance in the loads applied to either side of the track; generally, about 10 kN more is being applied to the six-foot side for a Javelin on what should be straight track. The results for location 4.2_O lie between the others at the site.

Lineside monitoring resumed at this site in May 2017. Figure 8.13, which uses data from location 4.2_O shows that performance and system properties had not changed. This demonstrates that the improvements in performance and restoration of support conditions made during the installation of USPs have been sustained for over two years, despite possible variation or enhanced loads being applied across the site, as was seen in Figure 8.12. The impact of the intervention on performance is considered further in Chapter 9.

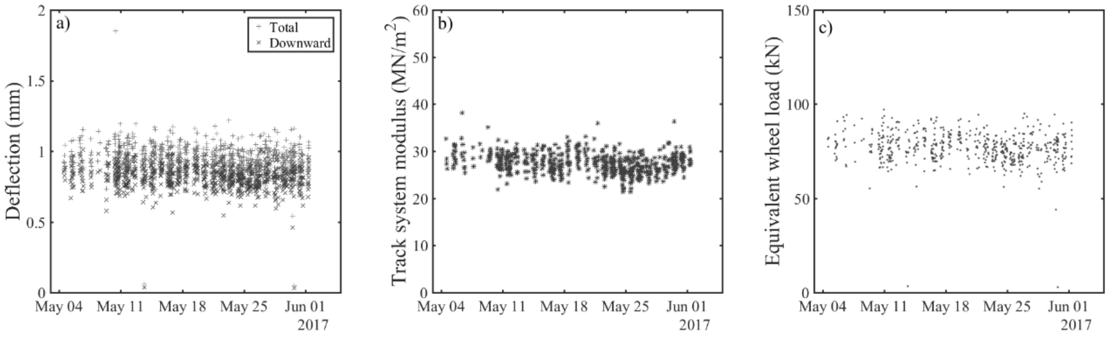

Figure 8.13 (a) Characteristic downward deflection (b)track sytem support modulus (c) equivalent wheel load at location 4.2_O after monitoring was resumed in May 2017 for Javelin trains.

8.4 North Downs Tunnel

This site, located on the down line about 20 m beyond the country end portal of the North Downs Tunnel, around 57.7 km from London, was affected by a severe track defect. Here the track is in a chalk cutting, on a 4900 m radius curve, with 130 mm cant and descending at a gradient of 1% in the direction of travel. Just before the defect there is a pair of shallow UTXs, each of which is about four sleeper bays wide (2.4 m); they are separated at 4.8 m centres. This site was monitored for around five months using MEMS accelerometers.

Data obtained from monitoring was used to inform and evaluate maintenance approaches. Two interventions were carried out. The first, in June 2015, involved raising the track level, breaking up the ballast layer beneath the sleepers and repacking beneath the sleepers just within the defect zone. The second, in September 2015 was required as monitoring data showed that the performance of the sleepers just outside the defect zone had been adversely affected by the first intervention, the intervention involved repacking those sleepers.

Figure 8.14 shows the vertical track geometry of each rail for the defect zone, obtained 3 months prior to the first intervention (March – May 2015), and 3 months after (June – August 2015). Before maintenance, it appears that the pair of UTXs corresponded to local maxima in the track level, just ahead of the defect zone. The data show how the packing resulted in much more level track across what was previously the defect zone. After the intervention, the track geometry above the under-track crossings corresponded to a ‘low’ position, possibly because of the over-lift in the defect zone (Figure 8.14(a) and (c)). Interestingly, this feature would not have been classified or identified as a geometry fault from these data, despite lineside monitoring recording large movements from voided sleepers above the UTX.

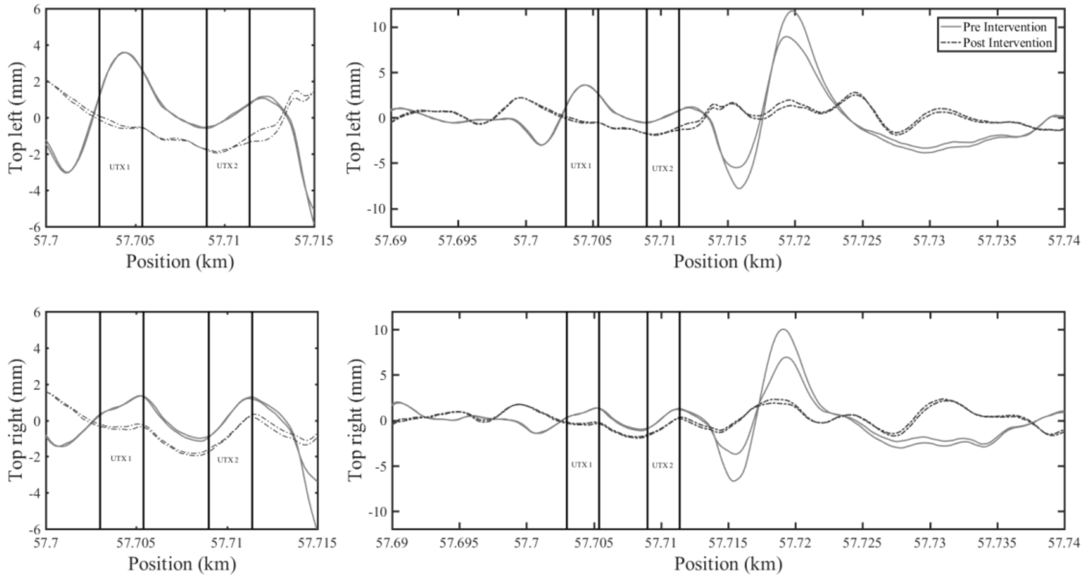

Figure 8.14 Vertical track geometry from the North Downs Tunnel defect site (a) and (c) above the UTX and (b) and (d) along the site, before and after maintenance.

Ten MEMS accelerometers were deployed at this site in the arrangement shown in Figure 8.15.

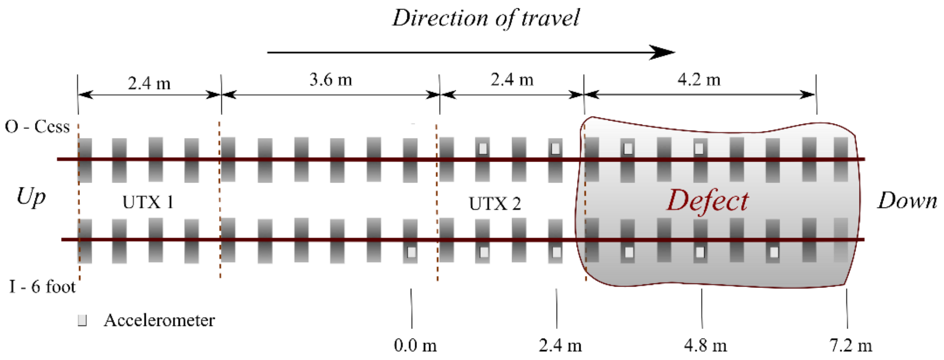

Figure 8.15 Transducer locations and UTX positons for the North Downs Tunnel defect zone.

Results obtained for the characteristic total and downward deflections are presented in Figure 8.16 and Figure 8.17 for the Eurostar and Javelin trains respectively. The Velaro was not in service while this site was being monitored. The two dashed vertical lines indicate the timing of the maintenance interventions in June and September 2015.

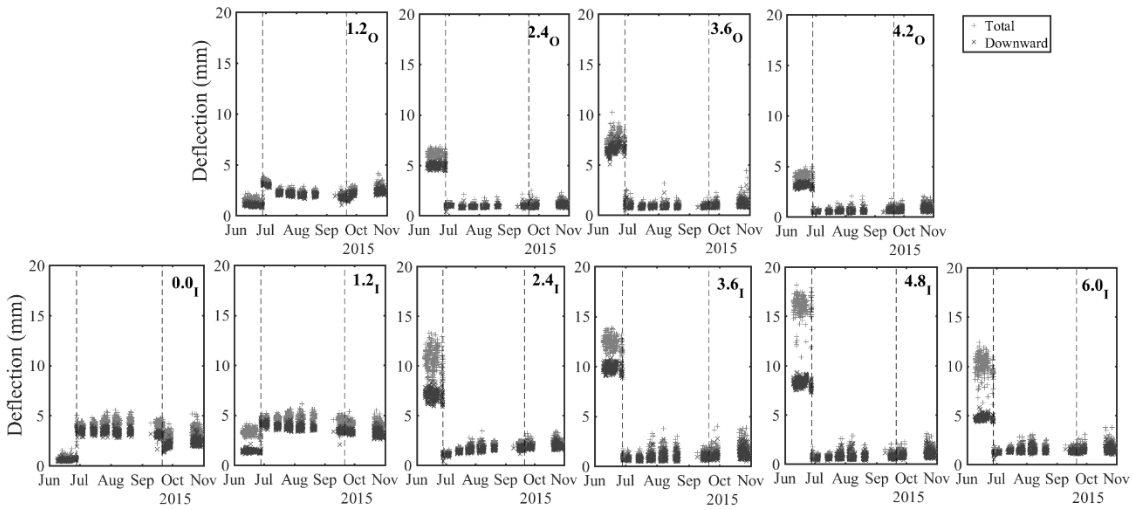

Figure 8.16 Characteristic total (P=0.025-0.975) and downward (P=0.025-0.7) track deflections due to passing Eurostars at the North Downs Tunnel defect site.

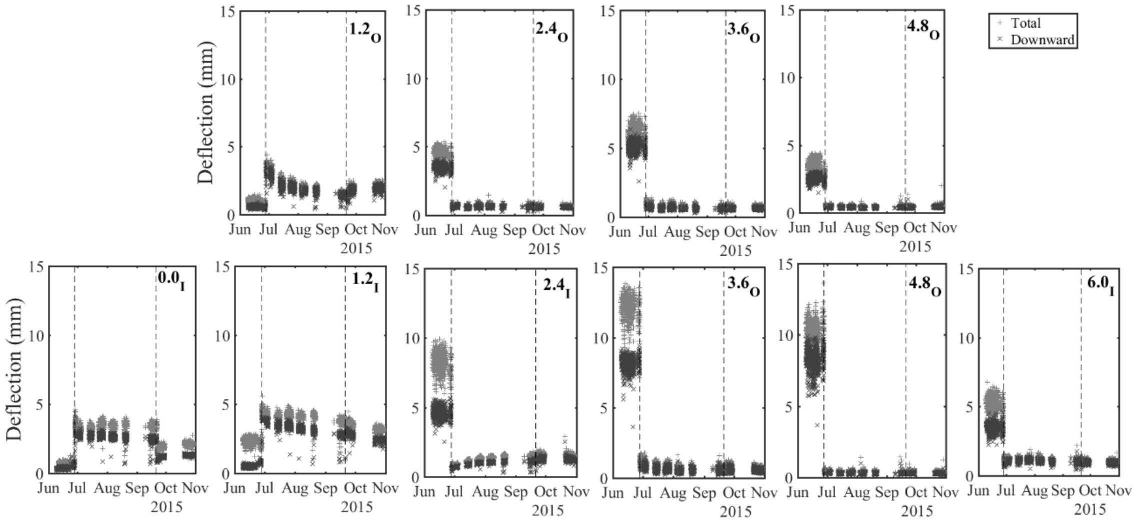

Figure 8.17 Characteristic total (P=0.025-0.975) and downward (P=0.025-0.7) track deflectionds due to passing Javelins at the North Downs Tunnel defect site.

The results show that prior to the first intervention, the magnitude of deflections varied significantly over a few sleeper bays (2-3 m). At location 0.0_I, where the sleeper is thought to be above the second UTX (just outside the defect zone), downward deflections of less than 1 mm were obtained for both train types. Progressing into the defect zone the deflections began to increase. On the six-foot side of the track (the outside of the curve) at location 1.2_I, downward deflections increased to 1-2 mm depending on train type. Downward deflections increased steadily to about 5-10 mm at locations 2.4_I, 3.6_I and 4.8_I before beginning to decrease at 6.0_I. A similar trend was seen on the cess side where the deflections increased from 3-4 mm at 2.4_O to 5-6 mm at 3.6_O and reducing to 2-3 mm at 4.8_O. This means that track deflections were more significant, and the defect was influencing a greater number of sleepers, on the six-foot side than on the cess side, suggesting a twist towards the outside of the curve. Increased downward deflection was associated with a significant increase in the total range of movement, suggesting there were also uplift effects. Generally, the downward displacements for the Eurostar were not significantly greater than those for the Javelin. However, the total range of movement was, suggesting there may be more significant uplift effects for the heavier and faster train.

After the first intervention, track deflections increased to 3-4 mm at locations 0.0_I, 1.2_I and 1.2_O. This is thought have been a consequence of applying an over-lift to the track within the defect zone, but not packing sleepers outside the defect zone that may have been affected by the over-lift. Deflections at 1.2_I and 1.2_O, reduced over the following two months, possibly due to settlement of the track within the defect zone after the lift. These and the surrounding sleepers were repacked after three months. At 0.0_I the deflections were reduced; no change was seen at 1.2_I and there was a slight increase at 1.2_O. After maintenance, those three sleepers were all deflecting by about 2 mm. This suggests there may have been residual performance issues after maintenance despite the track geometry being acceptable.

At the other locations, deflections reduced after maintenance to an acceptable range of 0.5–1 mm, comparable with the well-performing plain line site (Figure 8.2). These amplitudes of movement were seen for the remainder of monitoring; moreover, there was no longer a significant difference between the total and downward movements, indicating little or no uplift.

Figure 8.18 shows the track system support modulus determined for the Javelin using the ratio between magnitudes at the 7th and 3rd dominant frequencies.

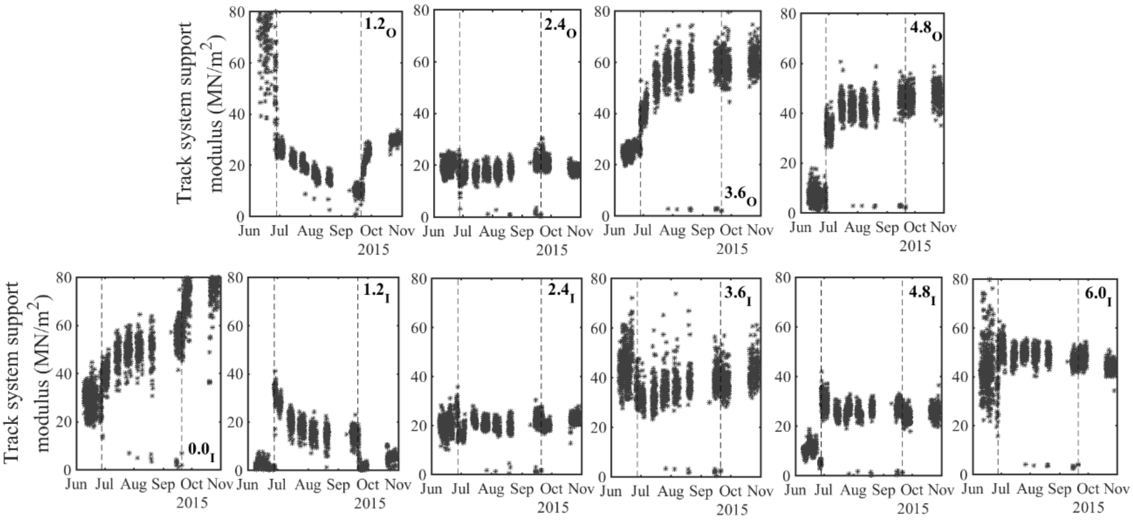

Figure 8.18 Track system support modulus calculated using the ratio of the 7th to the 3rd dominant frequency using the acceleration spectrum for the Javelin at the North Downs Tunnel defect site.

Considering the track system support modulus, the values found before the first intervention, and subsequently at 0.0_I, 1.2_I and 1.2_O, are affected by voids and should therefore be discounted. The way in which the presence of voids affects low frequency track vibration is not understood. After maintenance, the values found for the sleepers between 2.4 m and 6.0 m are plausible for this track (20-50 MN/m^2). These results suggest variation in the support conditions along the track. The BOEF model is based on the assumption of uniform linear support conditions; the effect and significance of this variation in support conditions needs to be better understood. There is variability in the results from one train to another, but the mean values are consistent for the duration of monitoring at each location. Figure 8.19 shows the equivalent wheel load data corresponding to the measured downward deflection (corrected to the rail deflection) and track system support modulus determined for the Javelin trains. Results are variable from one train to another, suggesting dynamic effects, but the trends are consistent with the other results for the duration of monitoring. The results are in the expected order of magnitude for typical wheel loads, and data from either end of a sleeper generally sum to a plausible axle load.

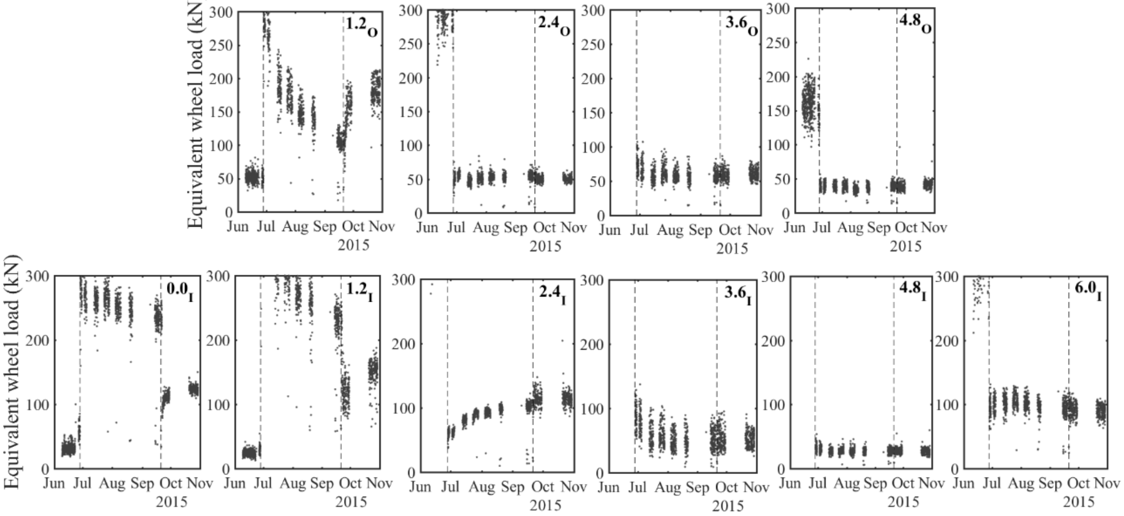

Figure 8.19 Equivalent applied wheel load corresponding to the measured characteristic downward deflection and track system support modulus data for the Javelin, assuming a rail pad stiffness of 84 MN/m, at the North Downs Tunnel defect site.

Sustained small track deflections in combination with stable and plausible values for the track system support modulus shown by monitoring within the former defect zone indicate that the intervention successfully restored performance. However, unintended consequences of the maintenance intervention affected the performance at locations previously outside the defect zone.

8.5 Rainham Viaduct

Rainham Viaduct was studied using both conventional and more continuous approaches to lineside monitoring. This section describes the application of continuous monitoring at the site. The use of conventional instrumentation to investigate bridge-ballast interaction is discussed in Chapter 9.

The purpose of monitoring was to obtain measurements before and after remediation work, to inform and evaluate that work and more actively monitor the condition of the track. Measurements were made on the track and on the bridge using MEMS accelerometers in the positions shown in Figure 8.20. The instrument at location 1.2_O was damaged in August 2016. During the period of monitoring one intervention was carried out. This involved shimming between the rail and seven of the sleepers on the cess side, starting at 0.0_O and ending at 3.6_O, to lower the sleepers down into the voids with the objective of reducing the track deflections. For this, data from lineside monitoring was used to specify the thickness of the shims, which had not been done when this intervention was first used at the Crissmill defect site (Section 8.3).

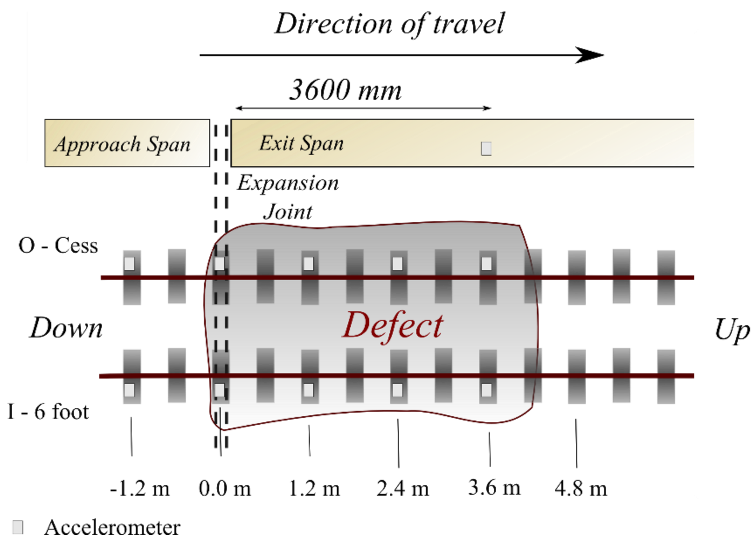

Figure 8.20 Transducer positions on Rainham Viaduct fault site used for continuous monitoring.

Figure 8.21 shows the track geometry supplied by NRHS obtained using the TRC across the entire bridge before (April 2016) and after (May 2016) shimming. The fault site is marked. The locations of all structural expansion joints between bridge decks are shown as dotted lines. The track geometry tends to be more irregular in the vicinity of the joints.

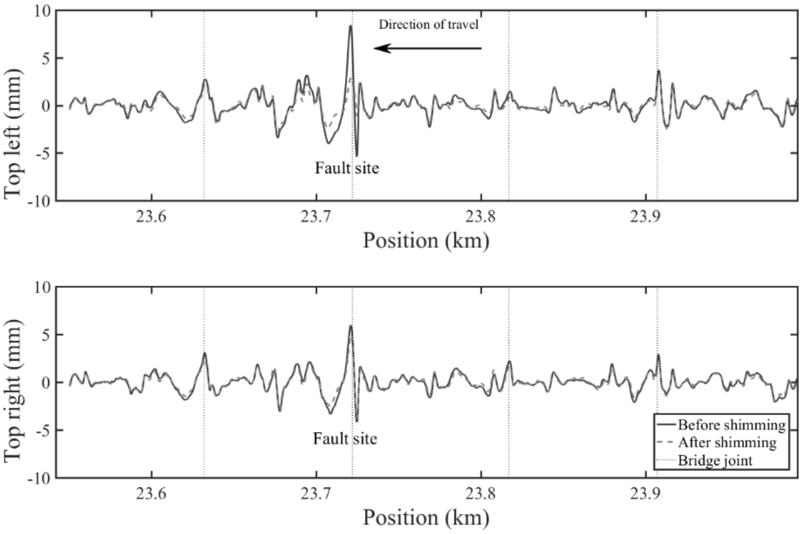

Figure 8.21 Vertical track geometry from the TRC across Rainham Viaduct before and after shimming of the cess side rail.

Deflection measurements of the track made more than 1.2 m away from the expansion joint were corrected for the bridge movement, to give the deflection of the track relative to the bridge. This correction was based on an assumption that the bridge was vibrating with a sinusoidal mode shape (Frýba, 1996), and was applied to account for the difference in transducer position between those on the track and that on the bridge:

$$\frac{A_b}{A_a} = \frac{\sin\left(\frac{\pi a}{L_s}\right)}{\sin\left(\frac{\pi b}{L_s}\right)} \tag{8.1}$$

where A_a and A_b are the amplitudes at locations a and b from the end of a bridge span having a length of L_s. Here b=3.6 m and L_s=30 m and a is a transducer position on the rail. The track system support modulus has not been determined, as the bridge vibration may influence the result obtained in using the frequency domain method. Figure 8.22, Figure 8.23 and Figure 8.24 show the characteristic downward and total displacement for the track within the defect zone caused by the three different passenger train types operating on HS1. The line speed for all trains is 230 km/h. Figure 8.25 shows the range of bridge movement measured 3.6 m from the expansion joint for all train types.

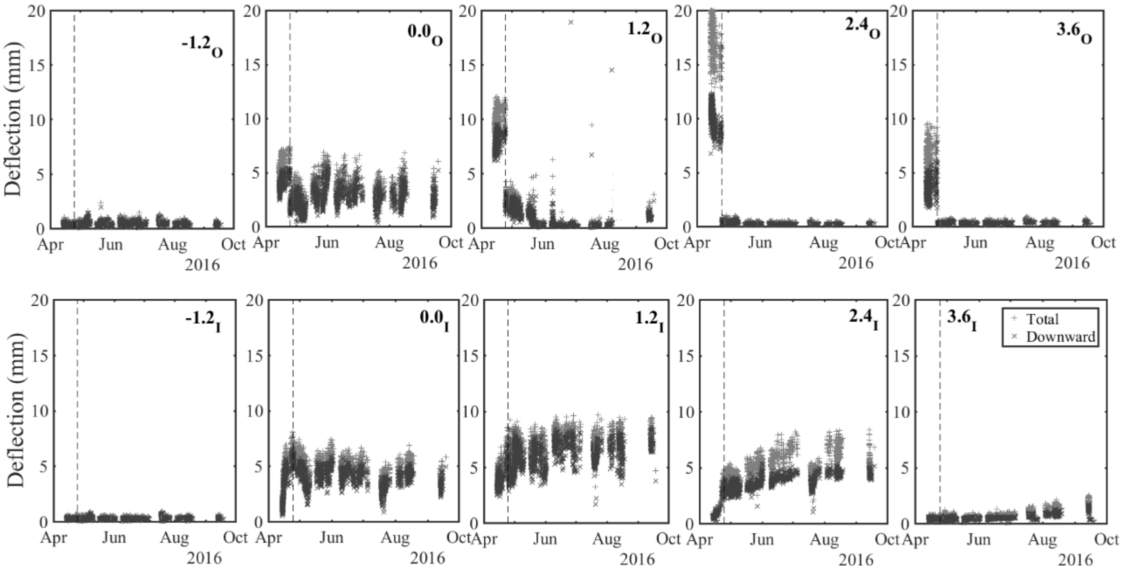

Figure 8.22 Characteristic total and downwards track displacement at Rainham Viaduct due to passing Javelins (Sleepers 2.4 and 3.6 have been corrected for bridge deflection).

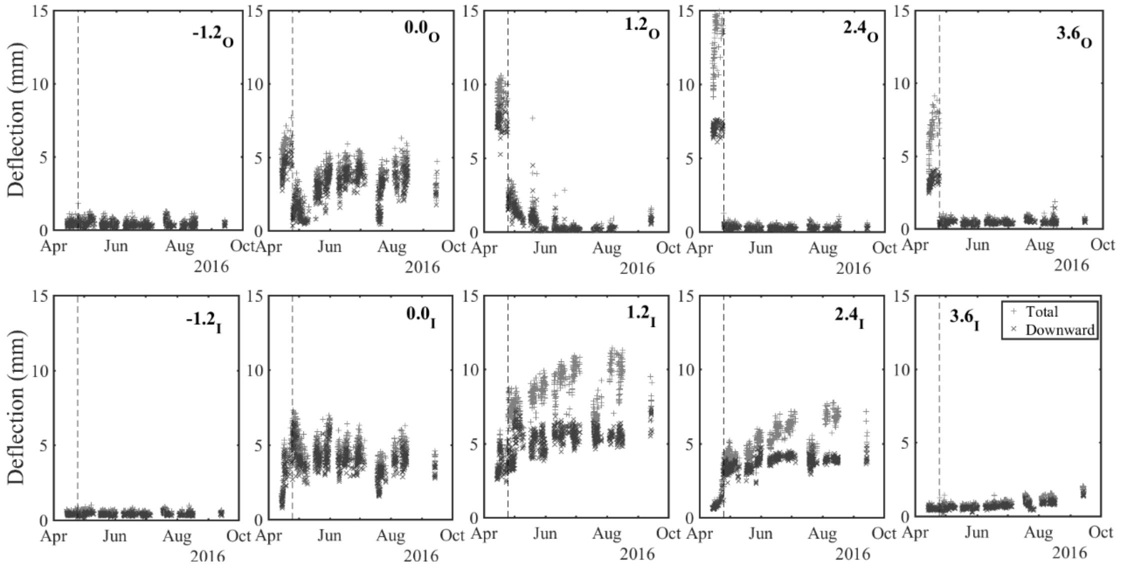

Figure 8.23 Characteristic total and downwards track deflections at Rainham Viaduct due to passing Eurostars (Sleepers 2.4 and 3.6 have been corrected for bridge deflection).

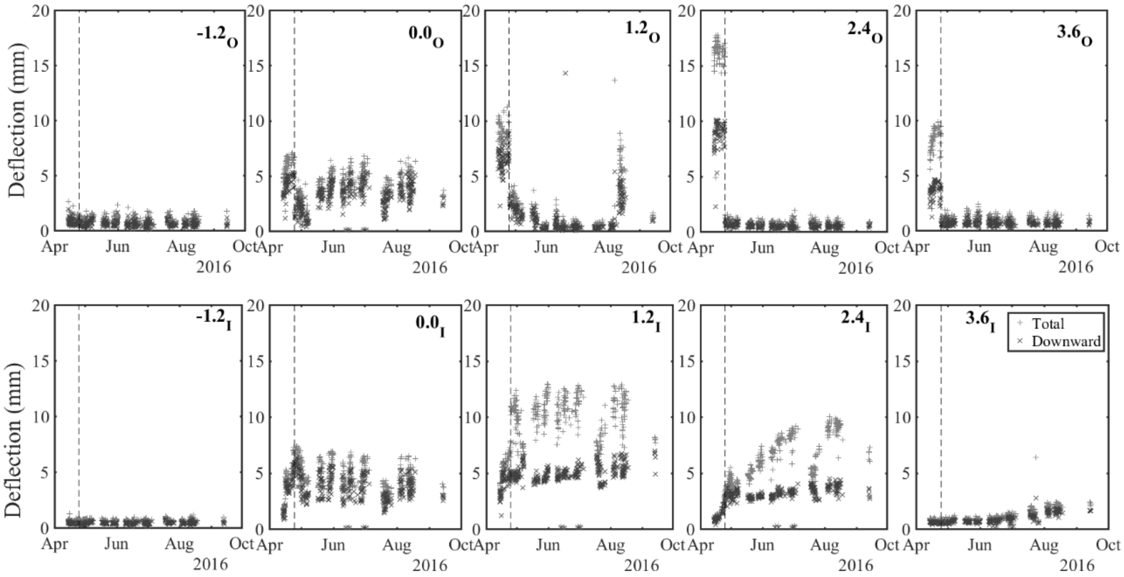

Figure 8.24 Characteristic total and downwards track deflections at Rainham Viaduct due to passing Velaros (Sleepers 2.4 and 3.6 have been corrected for bridge deflection).

Generally, trends in the behaviour were similar for the different trains passing this site, with slight differences in the magnitudes of movement. Results for the first instrumented sleeper at locations -1.2_O and -1.2_I, located on the approach span just ahead of the expansion joint, indicate normal performance. Deflections were typically less than 1 mm. These sleepers were not shimmed, nor were they affected by shimming at other locations. At locations 0.0_O and 0.0_I, which are directly above the structural expansion joint, the deflections were much larger and there was far more variation between trains than at other locations. From the start of monitoring there was initially a decrease in the magnitude of movement, from around 4 mm to 2.5 mm at 0.0_O and 1.8 mm to 0.7 mm at 0.0_I. This was followed by a steady increase to 4-5 mm on both sides over 3-4 days. This level of movement was maintained at 0.0_O until shimming. Shimming initially reduced downward deflections at 0.0_O to around 2 mm, with no change at 0.0_I. Over the course of monitoring, the results indicate cycles of increasing and decreasing deflection of this sleeper, with deflections as low as 0.5 mm on the cess side (0.0_O) and 1.5 mm on the six-foot side (0.0_I) and as high as 6 mm on both sides. Variation between train passages was more significant at this sleeper than at other locations. The implications of this with reference to the thermal expansion of the bridge and ballast are considered further in Chapter 9.

Within the defect zone (locations 1.2–3.6 m), downward deflections were large. Deflections were larger on the cess side: 7-10 mm at 1.2_O, 9-11 mm at 2.4_O and 3-5 mm at 3.6_O, indicating voiding. Deflections on the six-foot side were smaller, initially around 2.5 mm at 1.2_I, and 1 mm at 2.4_I and 3.6_I. The deflections at 1.2_I and 2.4_I increased to around 5 mm and 3 mm; at the same time increases were seen at 0.0_I. Shimming of the cess rail reduced the track deflection at 1.2_O, 2.4_O and 3.6_O to less than 1 mm. Track deflections remained at this level for 5 months with little or no uplift.

During the monitoring period, behaviour of the six-foot rail deteriorated. The general trend over the 5 months at 1.2_I and 2.4_I was for increasing downward track deflections. There is evidence of short cycles of slight decreases and increases in the amount of downward track deflection. Total deflection, and hence uplift, is more significant in this period. The results imply that there is a significant difference in movements between the two ends of these sleepers, suggesting either rotation or bending of the sleeper. The deflections for sleeper 3.6_I were unchanged at around 1 mm for the first 2-3 months after shimming. Subsequently these began to increase, possibly because of the increased track movement at locations 1.2_I and 2.4_I.

Figure 8.25 shows that the bridge movements were unaffected by the changes in track deflection for the duration of monitoring. This range of movement was found using P=0.025 and 0.975 from the CDF for the bridge deflections measured when a train was passing the instrumented span.

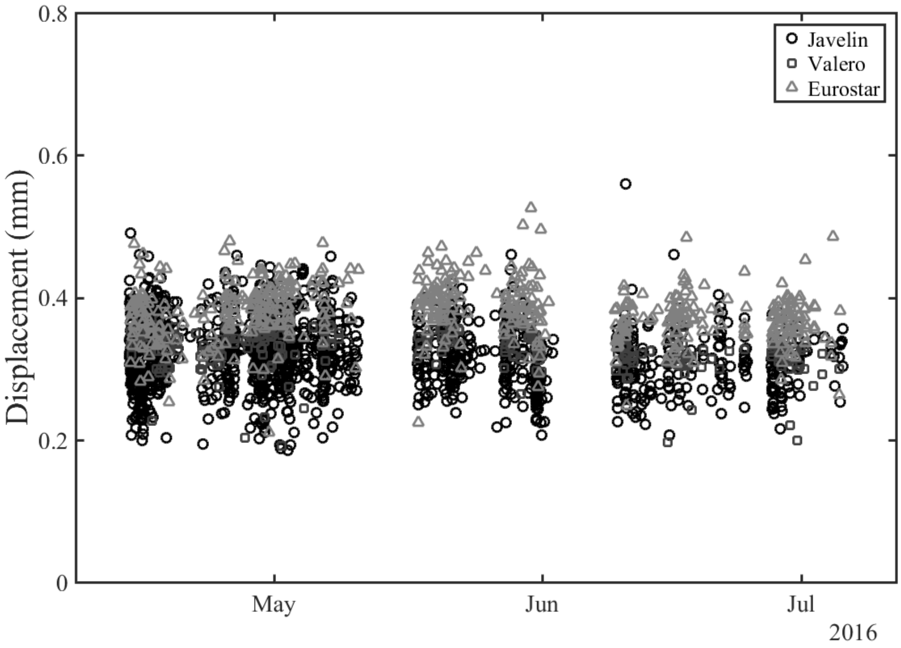

Figure 8.25 Amplitude of bridge movement 3.6 m from expansion joint for all train types.

8.6 Trends and forecasting

Long term monitoring techniques enable changes in track performance beneath each train to be recorded and evaluated as monitoring progresses. The characteristic total and downward deflections, as well as the track system support modulus, can be obtained from track vibration to measure the performance and properties of the track. This approach has been demonstrated in this chapter using three case studies. The results show a variety of different trends and changes in performance and system properties.

Increasing deflection could signify different behaviours, including:

- development of voids beneath the sleepers,
- reduction in the track system support modulus, if the sleeper and ballast is maintained,
- an increase in applied loading associated with changes in nearby track geometry.

Reduced deflection could signify:

- reduced gaps beneath sleepers or re-seating of a sleeper onto the track bed, owing to settlement of the surrounding track,
- reduced dynamic loads as settlement of surrounding sleepers may result in more uniform geometry, or
- stiffening of the track bed.

Combining the results with other methods of analysis to consider whether the elastic stiffness and estimates of the applied loads are plausible for the amount of deflection, the data can be used to provide evidence either for stiffening or softening of the track, and/or over- or under-loading of the track, thus suggesting which of these modes of deterioration (or improvement) may be more likely in a given situation.

Often infrastructure managers want to apply forecasting techniques to extrapolate monitoring data to estimate when the track performance will no longer be acceptable in order to plan maintenance. Clearly caution must be exercised when attempting this, as data from this research shows that the rate at which the track behaviour changes can vary significantly and exhibit non-linear trends. In curve fitting or forecasting from data from long-term lineside monitoring it would be appropriate to:

- use data for the same train type, to reflect changes in system performance rather than variations due to different vehicle types;
- look at trends over time rather than in terms of train passages, as data from continuous monitoring may be incomplete and influenced by the mix of traffic, whereas trends over time can subsequently be related to traffic or stress history.

8.7 Conclusions

The MEMS accelerometers that were validated for use on a high-speed railway in Chapter 4 have been used successfully to monitor the performance at three defect sites. Extended deployments of between 4 months and 2 years in length were made. During these periods, data for thousands of train passages were collected. These data were analysed automatically using the techniques developed in Chapter 5, 6 and 7, which have been tested using data from the Crissmill plain line site.

The CDF for track deflection was used to characterise the range of total and downward deflections for each train passing the sites. The ratios between magnitudes of the 7th and 3rd dominant frequency from the spectrum for track vibration were analysed to determine the track system support modulus using data from the 6-vehicle Javelin and the Velaro trains for the Crissmill and North Downs Tunnel fault sites. This provided direct evidence of how the performance and track system properties were changing as the track deteriorated, and showed the effects of different maintenance interventions.

Long-term track vibration measurements can, and are, being used for condition and performance monitoring; although the techniques are developmental in nature, these data have directly informed industry practice. For future research, this work demonstrates that it is feasible to obtain and analyse the larger, more long-term datasets necessary for quantifying rates of change and understanding the variability in performance and properties both along the line and over time. Moreover, the approach can provide evidence to diagnose the causes of accelerated deterioration, evaluate maintenance on a site-specific basis and understand better the behaviour of isolated defects and their consequences. This is addressed in Chapter 9.

Chapter 9: Lessons from lineside monitoring

9.1 Introduction

The aim of this research was to improve and apply lineside monitoring techniques to investigate, diagnose and evaluate remediation of performance issues on a ballasted high-speed railway. The previous chapters have described the improvements made to lineside monitoring techniques, and applications demonstrating their versatility in investigating and evaluating the performance of railway track. These systems are useful for quantifying and visualising the current state of the track (condition) and providing a record of how that changes, either as a consequence of that state or from maintenance interventions. This chapter makes use of both conventional and continuous monitoring data, obtained for the defect sites described in Chapter 3, to diagnose the causes of track defects, investigate aspects of track behaviour within defect zones and evaluate maintenance, as outlined below.

9.1.1 Diagnosing the cause of track defects

A common aspiration of research employing lineside monitoring is to use the data to explain the causes of accelerated track deterioration and poor track performance. Alone, data from lineside monitoring may not be sufficient for this. For example, it can confirm that the track is voided and that the presence of a void is leading to increased deterioration, but cannot explain why the void formed. Lineside monitoring can be used to identify features, mechanisms and processes that result in performance issues. However, this is challenging as deterioration is progressive and depends on how the track geometry, support conditions and consequently the amplitude and distribution of loading change with the accumulation of differential settlement. Once identified, these need to be tested with appropriate modelling, controlled experiments and perhaps field trials on new or test infrastructure, to understand and explain the mechanics of deterioration.

A variety of distinct features that could affect the track have been encountered in the various field studies carried out in the current work. Section 9.2 describes how shallow

UTXs, where concrete culverts are used to carry services under the line, installed just beneath the ballast may affect the track geometry and stiffness leading to deterioration. Section 9.3 considers the impact from structural movement joints, where bridge movements may affect the ballast. Section 9.4 discusses how track-mounted operational equipment may influence low frequency track vibration. These sections use the track geometry data and results from continuous monitoring presented in Chapter 8, as well as results for more conventional monitoring, to identify the mechanisms and processes that may have led to poor performance observed in the field studies. As discussed in Chapter 3, many of the sites were associated with a combination of features that could influence performance, making it difficult to discern their relative importance.

9.1.2 Behaviour within defect zones

A large volume of data was collected during this research related to track performance within defect zones. Within these areas, track behaviour is likely to be quite variable owing to irregular geometry, variation in support conditions, non-linearity, damaged or worn componentry and possible influence on vehicle dynamics. Section 9.5 discusses the condition of the trackbed within a defect zone as well as observations of uplift phenomena, defect geometry and accelerated deterioration made during site monitoring.

9.1.3 Evaluating maintenance

Lineside monitoring can be used to provide timely feedback on the effect of maintenance. This allows the performance of the track to be determined almost immediately after a return to normal operation, rather than waiting for track geometry data from a TRC to become available. Furthermore, measurements may highlight any unexpected but not yet severe behaviour affecting the track after maintenance. Track geometry measurements would simply show whether the track geometry has been corrected (or not), and whether it is acceptable for the time being.

In this research, different maintenance interventions were carried out by NRHS at the field sites. Lineside monitoring was used both to inform and to assess this work. Section 9.6 uses the results from lineside monitoring to evaluate the effectiveness of machine tamping, targeted packing informed by lineside monitoring, shims between the rail and the sleepers and USPs for the remediation of defect zones, to show whether and suggest why a particular form of maintenance was effective.

9.2 Track geometry and stiffness: stiff spots

Evidence from this research suggests that the type of shallow UTXs used to carry services beneath the railway on HS1 are associated with higher rates of deterioration. Shallow UTXs were found near the defect zones at the Crissmill and the North Downs Tunnel defect sites. Furthermore, results from a section survey looking to identify sites affected by accelerated deterioration presented in Appendix B, showed that the local deviations in track geometry around shallow UTXs were frequently more significant than was typical for the surrounding track.

In the track geometry data from the Crissmill and the North Downs Tunnel defect sites, shown in Figure 8.7 and Figure 8.14 respectively, the locations of the UTXs correspond to relative high points in the longitudinal level profile. This irregularity may indicate that differential settlement has occurred around the UTX, or it is caused by a local variation in stiffness or both. Regardless of the cause, irregular geometry is likely to enhance the dynamic loading in the vicinity of the UTX. Locally-enhanced loads would be expected to increase the rate of settlement, and to initiate the formation of a defect.

Evidence supporting the idea of the irregularity associated with the UTX enhancing the applied load can be seen by comparing the equivalent wheel loads estimated after maintenance at the Crissmill and the North Downs Tunnel fault sites from Figure 8.12 and Figure 8.19 respectively. No comparison could be made before maintenance owing to voiding at both sites. At Crissmill the geometry irregularity associated with the UTX was not removed during maintenance (Figure 9.35), whereas at the North Downs Tunnel it was (Figure 8.14), although the support conditions ahead of the defect zone may not be ideal (Figure 8.18). The equivalent applied loads determined at Crissmill after maintenance were greater than those at the North Downs Tunnel, which were closer to the typical values for a static wheel load.

9.3 Structural movement: bridge and ballast interaction

Both Rainham Viaduct and the A20 bridge were studied using more conventional approaches to lineside monitoring, to investigate bridge and ballast interaction and the impact of bridge dynamics. At Rainham, geophones were used on the track and the structure (complemented by DIC for large track deflections). At the A20 bridge DIC was used to quantify the track displacement and geophones to measure bridge vibration.

9.3.1 Rainham Viaduct: lineside measurements

At Rainham, the track and the bridge were instrumented using geophones in the arrangement shown in Figure 9.1. These were used to record the track and bridge movements due to passing trains, three days after the fault had been manually packed.

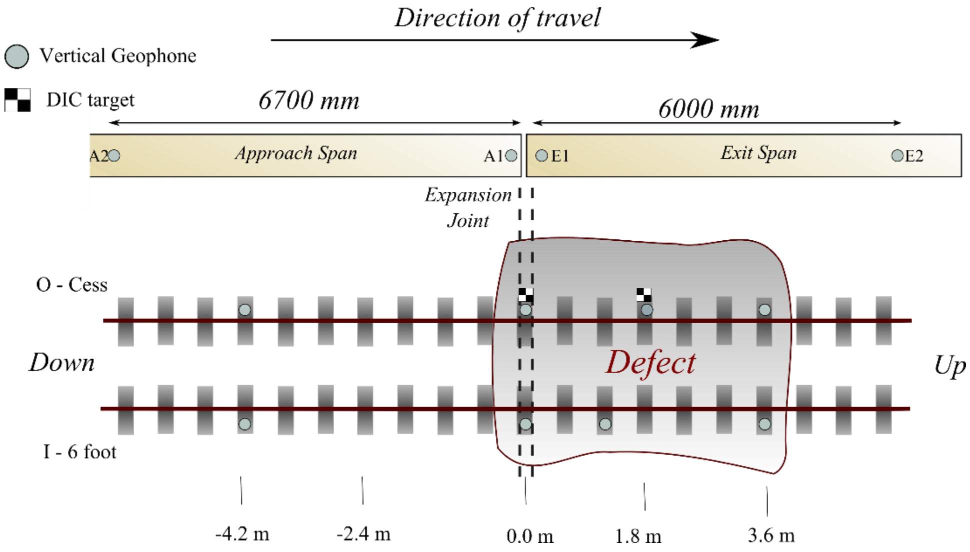

Figure 9.1 Transducer locations used for conventional montioring at Rainham.

Figure 9.2 shows track displacements obtained on the six-foot rail for both train types. These movements have been corrected for the bridge movement using Eq.(8.1). Within the defect zone the deflections were large, approaching 1.5 and 2 mm for the Javelin and Eurostar respectively. The geophones on the cess side at 0.0_O and 1.8_O were going off scale, indicating the possibility of very large track movements. This was confirmed using DIC on a later visit to the site, the results of which are shown in Figure 9.3. Location -4.2_I , which was outside the defect zone was moving around 0.35-0.45 mm.

Deflections (not shown), were similar at -4.2_O, 3.6_O and 3.6_I; these are typical of well-performing track (Figure 8.2).

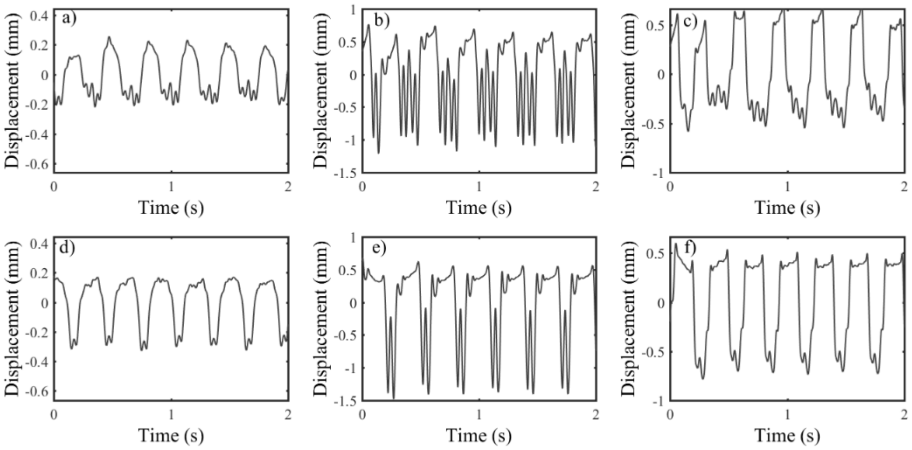

Figure 9.2 Trackbed deflecion found on the six-foot side (a) ahead of the defect zone -4.2_I, (b) directly above the joint 0.0_I, and (c) on the first insturmented sleeper after the joint 1.2_I for a Javelin; and at the sames locations (d), (e) and (f) for a Eurostar. (Obtained using geophones sampled at 1000 Hz with 2 and 40 Hz high- and low-pass filter cut-off frequencies).

High speed video was used to confirm excessive movement on the cess side. The camera was mounted on the bridge parapet directly in line with the sleeper of interest, to give the track bed displacement relative to the bridge. These measurements show that the track was moving in excess of 2 mm above the bridge joint and close to 5 mm in the centre of the defect zone for a Javelin (Figure 9.3). These results confirmed that the track movements were large, suggesting that the sleepers were voided.

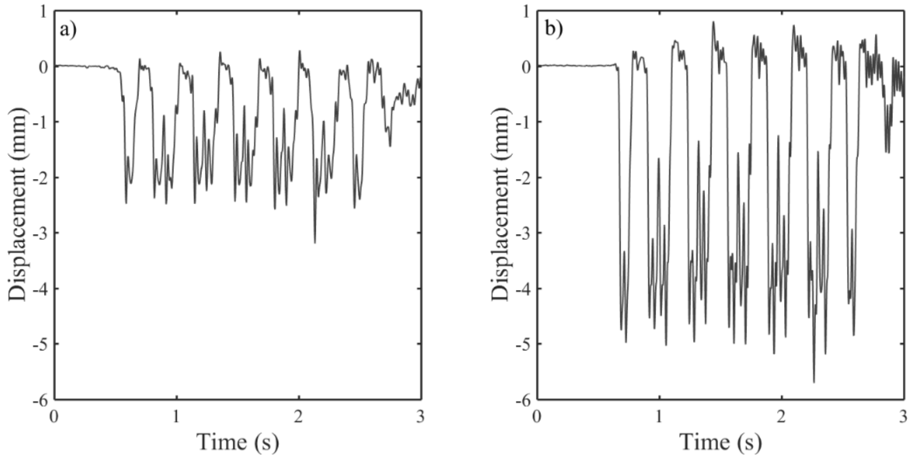

Figure 9.3 Track bed displacements found at Rainham on the cess side (a) directly above the joint 0.0_O and (b) towards the centre of the defect zone 1.8_O. Obtained using high speed video at 200 Hz (fps), low-pass filtered with a 40 Hz cut-off freqeuncy.

In addition to the on-track instrumentation, geophones were placed on the bridge spans and over the supports at the joints at the locations given in Figure 9.1. Figure 9.4 and Figure 9.5 show the span deflections and velocity spectrum for measurements made 6.7 and 6 m either side of the structural expansion joint on the approach and exit span for a Javelin and a Eurostar respectively. These data have been high-pass filtered at 2 Hz so static bridge deflection due to the train load will have been filtered out. The results show that the most significant movements occur when the train is on the bridge span (between 5 s and 7 s for the Javelin in Figure 9.4(a) and (c) and 5 s and 12 s for the Eurostar in Figure 9.5(a) and (c). The bridge begins to vibrate as soon as the train arrives on the first deck (around 2.5 s in both Figure 9.4 and Figure 9.5). Vibration levels increase while the train traverses the other spans in a continuous deck (3.5-5 s in Figure 9.4(a) and Figure 9.5(a) but not (c)). Free vibrations of the deck can be observed after the train has left the bridge (after about 11 s for the Javelin and 16 s for the Eurostar). During the train passage the dominant spectral peaks occur at multiples of the vehicle-passing frequency around 3, 6, 9 Hz… for the Javelin and 3.2, 6.4, 9.6 Hz… for the Eurostar. There is also significant frequency content between 4 and 5.5 Hz.

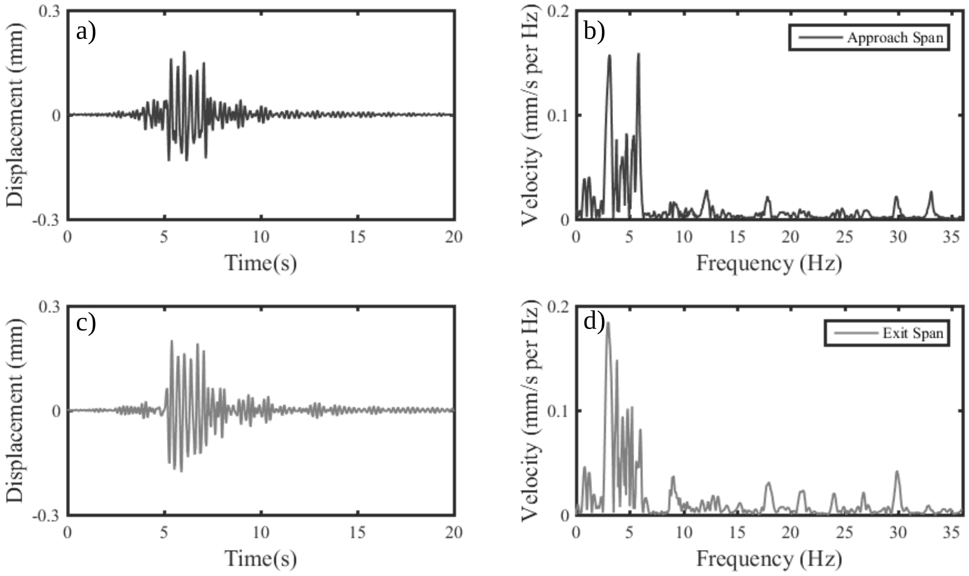

Figure 9.4 Bridge deflections at Rainham, filtered between 2 and 40 Hz and corresponding velocity spectrum for bridge span vibration (a) and (b) on the approach span A2 and (c) and (d) on the exit span E2 for a Javelin.

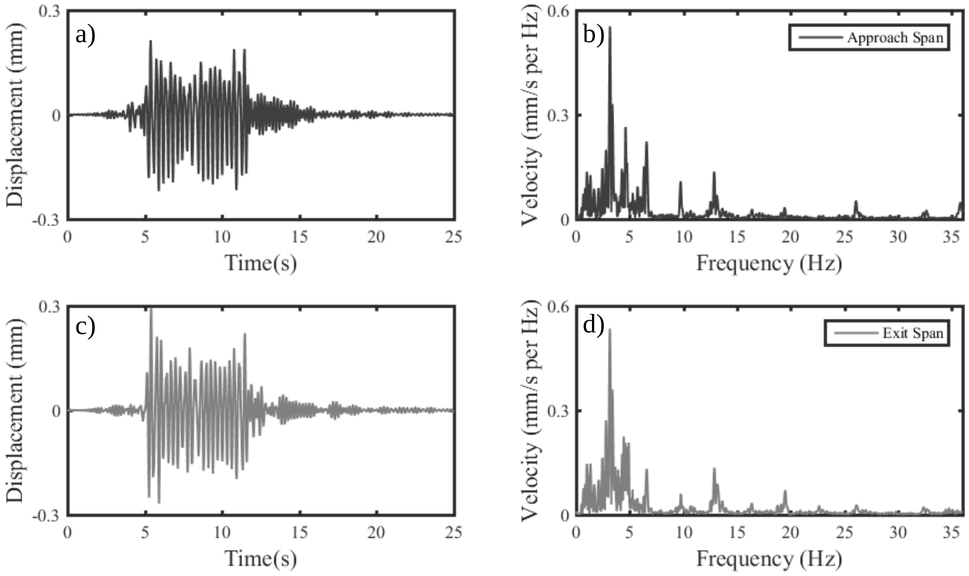

Figure 9.5 Bridge deflections at Rainham, filtered between 2 and 40 Hz and corresponding velocity spectrum for bridge span vibration (a) and (b) at A2 on the approach span and (c) and (d) at E2 on the exit span for a Eurostar.

Figure 9.6 shows a section of the free vibration of both instrumented spans after a Eurostar train had left the bridge and the corresponding velocity spectra. The spectra show a high amplitude region between 3.8 and 5.5 Hz for both spans, with the first peak at 3.9-4.0 Hz. This type of free response is expected for a continuous bridge with constant cross-section and equal spans (Frýba, 1996). For this type of structure, the natural frequencies for the first three bending modes are expected to be close to each other. Here, where the natural frequency of the 1st mode is around 4 Hz, the frequencies for the 2nd and 3rd are expected to be around 4.5 Hz and 5.5 Hz, respectively, covering the region of high amplitude seen in Figure 9.6(c). Although the approach deck has an unequal central span, the difference in length will not have a significant effect on the expected response (Frýba, 1996). The dynamics of the structure are appropriate for vehicle-passing frequencies of around 3 Hz, assuming the structure was designed to avoid exciting resonant type vibration (Yang et al., 1997; Frýba, 2001).

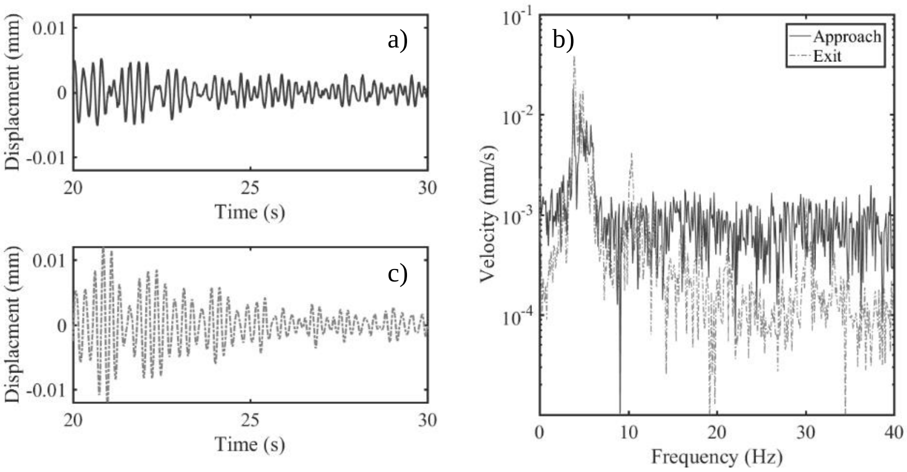

Figure 9.6 Vibration of Rainham Viaduct at the approach (A2) and exit spans (E2) and corresponding velocity spectra after a Eurostar trainset had left the bridge.

Estimates of the mass of the bridge deck per unit length, based on structural cross-sections of the bridge, including the ballast, supplied by NRHS, are between 15000-20000 kg/m. For a 1st natural frequency of 4 Hz the estimates of mass suggest that the bending stiffness of the bridge is between 8×10^{10} and 1×10^{11} Nm^2. These values are plausible for the materials and geometry of the cross sections. The logarithmic decrement of the free vibration suggests the bridge is lightly damped, with a damping ratio of 1.5%.

9.3.1.1 Bridge and ballast interaction, bridge vibration

The design of the structural expansion joint means that the movement of the bridge may affect the ballast. Combined measurements of the bridge and the track allow visualisation of how the bridge vibrates during the passage of a train. Figure 9.7 shows the deflection of each bridge span 6.7 m before structural expansion joint for the approach span and 6.0 m after it for the exit span for (a) a Javelin and (b) a Eurostar. The record of sleeper deflection from the sleeper 0.0_O above the joint has been plotted together with the bridge movements, indicating the time when each wheel crosses from one span onto the other. Results are shown for a Javelin and the first half of a Eurostar.

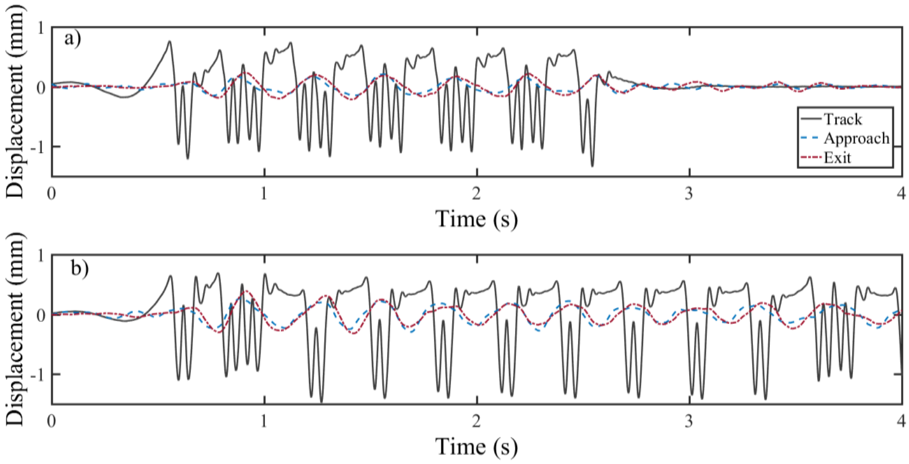

Figure 9.7 Sleeper deflection at 0.0_I over the joint overlain by bridge deflection 6.7 m away from the joint on the approach span A2 and 6 m away from the joint on the exit span E2, for (a) the Javelin and (b) half a Eurostar.

Figure 9.7 suggests that the upward and downward movements of both spans are synchronised with each other and with the passage of the vehicle, regardless of train type. The maximum upward movement occurs when the vehicle ends are over the joint. The amplitudes of motion are similar for both spans. Bending of the bridge spans will cause the bridge to rotate at the deck ends supported at the joint. The synchronised motion means that there will be simultaneous equal and opposite rotations at the joint as shown in Figure 9.8. The design of the structural expansion joint means that movement at the joint can affect the ballast. The depth of the bridge deck including the girders and the ballast above it results in a lever arm of approximately 3 m from the bridge bearings (where the deck is supported) to the ballast surface. This means that the bridge movement from passing trains will cause a volume change above the joint and extension-compression behaviour in the ballast, as indicated in Figure 9.8.

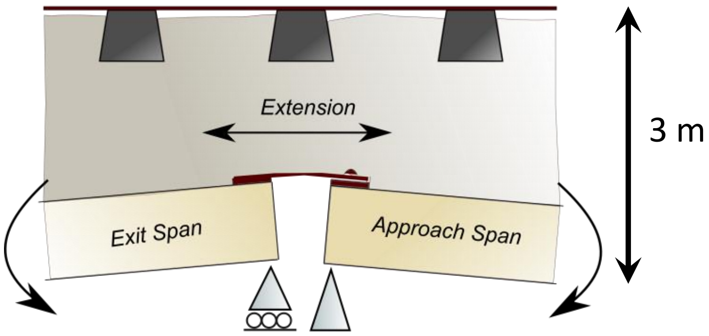

Figure 9.8 Effect of deck end rotations on the ballast above the joint.

A simple mechanism is proposed in Figure 9.9 to assess the significance of the deck end rotations under passing trains on the volume above the expansions joint. Here, θ is the rotation at the deck end, d is the depth of the bridge deck and girders, t is the depth of ballast, and x is the width of the expansion joint.

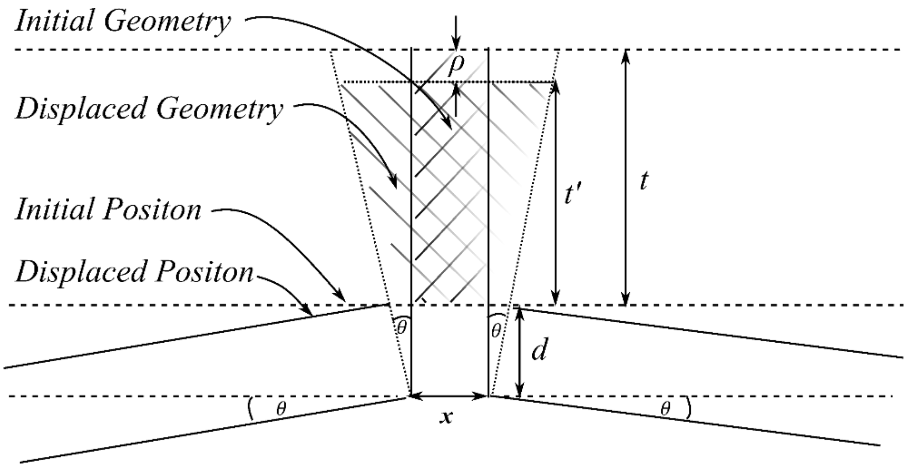

Figure 9.9 Mechanism to identify volume change above the expansion joint due to passing trains.

Assuming the total volume of ballast remains constant, any relative rotation of the deck ends would cause a settlement of the ballast ρ. This can be estimated by equating the volumes associated with the initial and displaced geometries, to obtain:

$$\rho = \frac{\theta t_b(t_b + 2d)}{2\theta(t_b + d) + x_j} \tag{9.1}$$

Figure 9.4 and Figure 9.5 indicate that the range of dynamic bridge deflection measured approximately 6 m away from the bridge supports is close to 0.4 mm for both the Javelin and the Eurostar, resulting in a deck rotation of θ = 6x10^{-5} radians, which neglects the static deflection from the train loads. For a deck depth of 3 m, covered by 0.5 m of ballast and a joint width of 0.2 m, the settlement calculated from Eq.(9.1) is 0.9 mm. If even a small proportion of this settlement is permanent, this would cause a void to develop between the ballast and sleeper above the joint over a number of expansion-contraction cycles.

The deck end rotations have been checked against measurements of expansion above the joint taken by NRHS. Linear Variable Displacement Transducers (LVDT) were fixed to hand railings on each side of the expansion joint approximately 0.3 m above the ballast surface (Figure 9.10(a)). Figure 9.10(b) shows results for a Eurostar passing over the joint. This confirms the expansion behaviour and shows that there was an average expansion for the duration of the passage of around 0.25 mm with a variable component of ±0.1 mm. A dynamic deck end rotation of 6x10^{-5} radians acting at a lever arm of 3.6 m would be expected to cause a range of movement of 0.2 mm, which is of the same order of magnitude. However, the measured expansion was half what was calculated assuming synchronous rotation of the two decks. This could be due to an over-estimation of the deck end rotation, the lever arm or conservatism in the assumption that the rotations were synchronous, equal and opposite. Figure 9.10(b) shows static deflection due to the average load acting on the track from the train. This was not seen in the bridge vibration data owing to the use of a high pass filter. This contribution will affect the ballast in a similar way to the vibration.

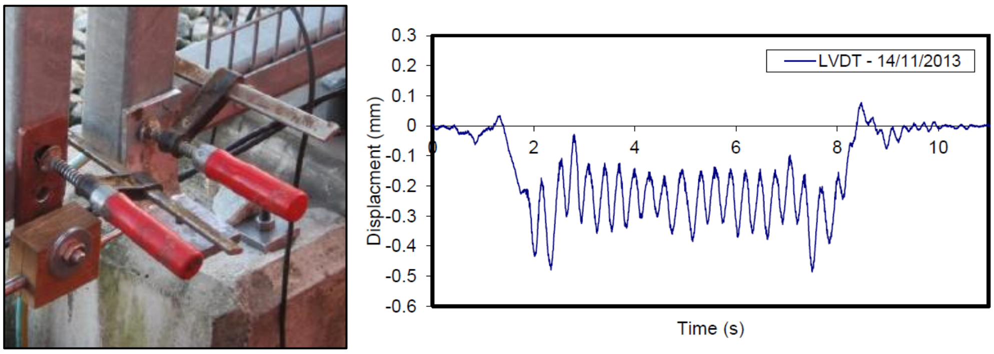

Figure 9.10 (a) Photograph of LVDT used to measured expansion across the bridge joint, (b) results for a Eurostar supplied by NRHS.

Although these measurements show that rotation at the decks ends can cause a volumetric change at the joint, which may result in additional settlement above the joint, the state of the track means that this process is unlikely to be observable. The voiding and possible instability of the ballast in the defect zone control the observable behaviour.

Time lapse cameras were used to obtain qualitative visual evidence for instability of the ballast surface. The relatively poor fixity and optical stability of the camera used mean that digital image correlation was not possible. Photographs were taken every 30 minutes, meaning that there are likely to between 2 and 4 train passages between frames; examples are shown in Figure 9.11. 40 ballast grains were painted white and placed on the ballast surface to identify movement. Often, these grains were seen to move between frames (Figure 9.11). Re-constructing a video from individual frames gave a clear indication that the ballast particles were moving, particularly around the sleeper ends and the cross bar of the duo-block sleepers.

Figure 9.11 Time lapse photos of the track above the bridge joint, used to visualise ballast stability, taken 30 minutes apart.

9.3.1.2 Bridge and ballast interaction, thermal expansion

Results from continuous monitoring at Rainham presented in Chapter 8 show significant variation and cycles of improving and deteriorating performance of track above the structural expansion joint. This has been reproduced in Figure 9.12, alongside daily temperature data from a local weather station. Cycles of increasing and decreasing deflection show significant variation from one train to another, suggesting that the local support and loading conditions at these sleepers were changing throughout the period of monitoring. This possibly occurs as a consequence of instability of the ballast above the joint, and/or volume changes at the joint. Generally, sleeper deflections appear to reduce as the air temperature increases. No other locations in the monitoring site exhibited this behaviour (see Figure 8.22 to Figure 8.24), nor was any correlation between air temperature and deflection found in Chapter 8. This suggests that thermal expansion of the bridge may affect the ballast above the joint.

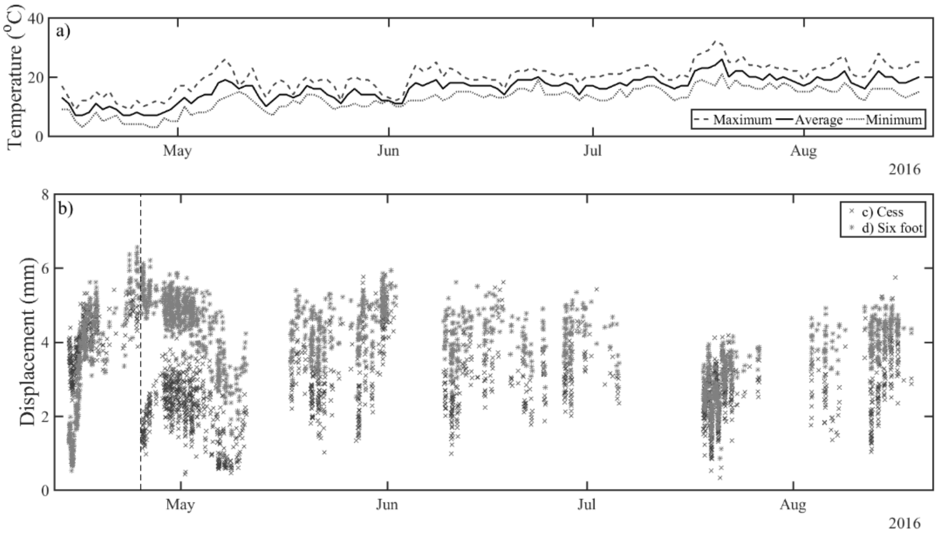

Figure 9.12 (a) Daily temperature record from a weather station near Rainham Viaduct for April to August 2016, (b) record of characteristic downward deflections for either end of the sleeper located above the structural expansion joint for the same period.

Movement from thermal expansion of the bridge deck will manifest itself at the expansion joint. In winter, a witness mark caused by the steel cover plate across the joint scratching the concrete bridge deck indicated around 30 mm of annual bridge movement was visible at the site. If the temperature drops the bridge will contract increasing the volume to be occupied by the ballast above the expansion joint and vice versa.

A linear thermal expansion calculation can be used to estimate the amount of differential movement between the bridge and ballast. The effect this may have on the volume of the ballast above the joint is illustrated in Figure 9.13.

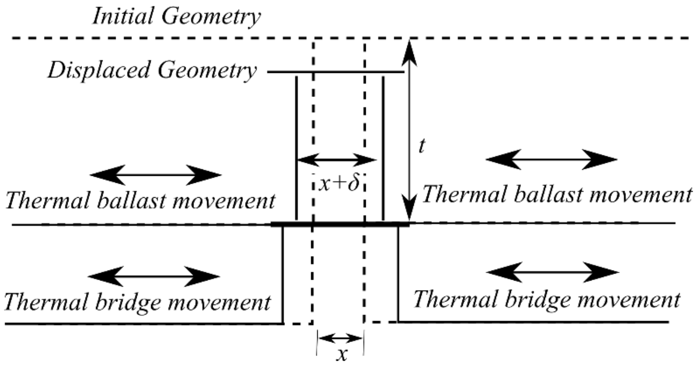

Figure 9.13 Mechanism for volume change in ballast above joint from thermal expansion/contraction.

The bridge and the ballast have different coefficients of thermal expansion α. The coefficient for a composite bridge will be around $10\text{x}10^{-5}$ /°C (British Standards Institution, 2004) and granite aggregates around $8\text{x}10^{-5}$ / °C (Bonnell and Harper, 1950). This will lead to relative expansion or contraction of the ballast above the joint. Assuming the joint moves to accommodate the expansion or contraction of the entire bridge deck of length L_d=90 m, a temperature drop ΔT of 10° C will cause 9 mm of contraction ΔL_d of the bridge but only between 7.2 mm of the ballast, leading to 1.8 mm of differential contraction δ, in the material above the joint.

$$\Delta L_d = \alpha \Delta T L_d \tag{9.2}$$

Assuming an initial joint width x = 0.2 mm and a ballast thickness t = 0.5 m of ballast and no volume change from material behaviour the calculated range of differential movement would cause a drop in the ballast level of 5 mm.

$$\rho = t - \frac{x_j t_b}{x_j + \delta} \tag{9.3}$$

This result is sensitive to the assumed geometry of the joint. However, the result is the same order of magnitude as the changes in sleeper deflection corresponding to an approximately 10° C drop in air temperature seen in Figure 9.12.

Alternatively, if the ballast behaved as an elastic solid with a Poisson's ratio of μ = 0.2-0.3, the change in level from the estimated differential movement would be expected to be around 0.4-0.8 mm.

$$\rho = \mu\delta \tag{9.4}$$

The design of the bridge expansion joints means that both bridge vibration and thermal expansion might affect the volume of the ballast above the joint. Simple calculations suggest both effects may be significant. These are crude models and may not accurately represent how the ballast responds to the different movements at the joint. It might be worthwhile to develop a discrete element model of the ballast above the joint to study how the granular material responds under imposed movements representing bridge vibration and cycles of thermal expansion and contraction, for future research.

9.3.2 A20 Bridge

A similar study was conducted on the A20 overbridge. Isolated track defects were identified at both ends of this single-decked, triple-span bridge. It has a similar joint detail to those used at Rainham, between the bridge deck and the abutments, rather than between adjacent decks. Measurements were made on the down line, but defects were present on both sides of the bridge. High speed video for DIC was used to quantify the track movements at both ends of the bridge in the vicinity of the structural expansion joint. Geophones in the arrangement shown in Figure 9.14 were used to investigate the bridge dynamics. Measurements were made using two separate systems, which were not synchronised, hence that the motion of the bridge relative to the passage of the train could not be considered in the same way as at Rainham in Figure 9.7.

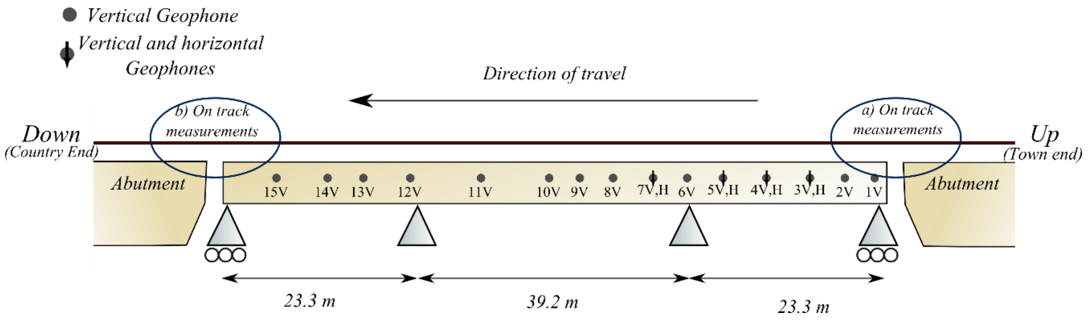

Figure 9.14 Geophone positions on the A20 bridge. V – vertical and H – horizontal sensor.

Figure 9.15 shows the most significant track deflections from sleepers in the defect zones at each end of the bridge directly above the structural expansion joint, for both a

Javelin and a Eurostar. Movements of around 2.7 mm were measured at the defect on the approach to the bridge which were greater than the 1.5 mm found at the defect on the exit from the bridge. The defect zone was also longer on the approach than on the exit. Movements were less than 0.5 mm elsewhere on the bridge and the abutment.

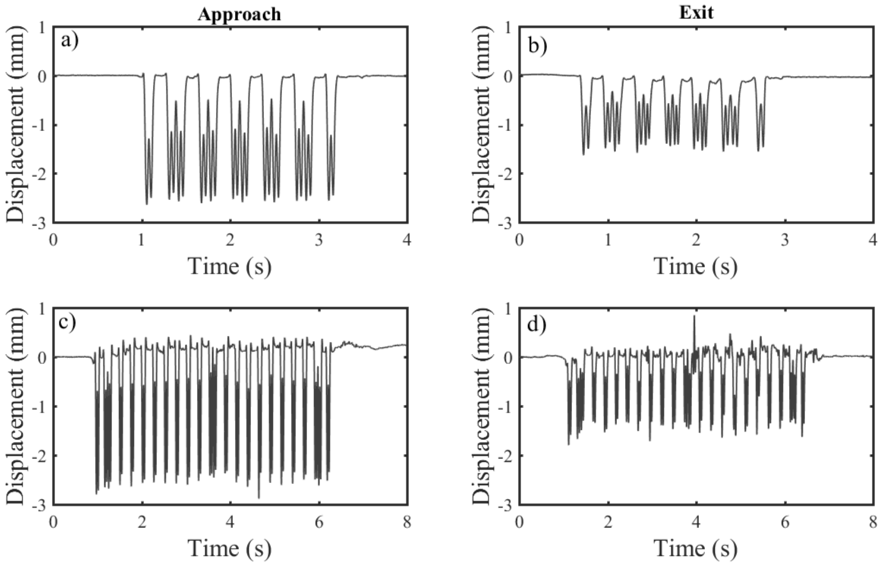

Figure 9.15 Track deflection data obtained using high speed video for DIC for the defects zones above structural expansion joints (a) and (c) on the approach to and (b) and (d) exiting from the A20 bridge for Javelin and Eurostar trains.

Figure 9.16 shows typical results for the bridge movements above an intermediate support and in the middle of the central span. The typical ranges of movement are given in Table 9.1 for all measurement locations and trains. The heavier and faster Eurostar and Velaro trains caused larger bridge movements than the Javelins. Interestingly the bridge movements were much larger for the Eurostar than for the Velaro, i.e. 2 mm rather than 0.75 mm in the centre of the middle span. Each track is supported by a separate bridge deck, with shared abutments. A Eurostar passing on the other bridge deck led to significant vibration of the instrumented one. This was not a significant effect for the other trains.

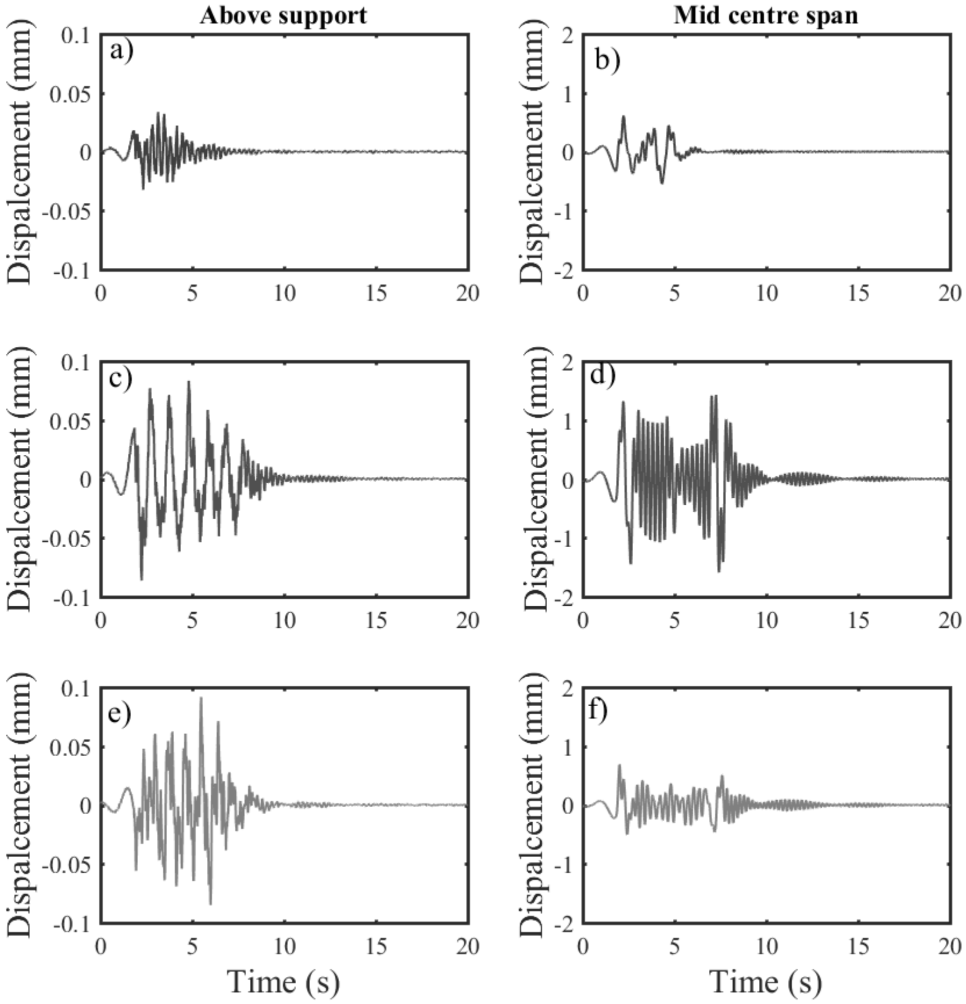

Figure 9.16 Bridge deflections obtained using geophones, filtered between 2-40 Hz (a), (c) and (e) above an intermediate support and (b), (d) and (f) at the middle of the central span for Javelin, Eurostar and Velaro trains passing across the A20 bridge.

Table 9.1 Typical range of total deflection obtained for each train type at each measurement location along the A20 bridge.

Setup	**Transducer Position**	**Distance from town end joint (m)**	**Displacement Range (mm)**		
			Javelin	*Eurostar*	*Velaro*
1	1	0.1	0.07	0.07	0.11
	2	4.5	0.30	0.58	0.48
	3	8.6	0.51	0.92	0.77
	4	13.7	0.56	1.07	0.89
	5	18.8	0.25	0.59	0.45
	6	23.0	0.06	0.13	0.11
	7	26.9	0.17	0.63	0.29
	8	31.7	0.48	1.45	0.43
	9	35.6	0.76	2.02	0.75
2	10	39.2	0.61	2.07	0.62
	11	47.2	0.55	1.34	0.56
	12	55.2	0.04	0.09	0.07
	13	61.0	0.33	0.64	0.68
	14	65.2	0.45	0.97	0.95
	15	71.2	0.46	0.97	0.80

The increased magnitude of bridge vibration suggests the possibility of resonant type behaviour. An analysis of the free vibration measured in the middle of the central span after a Eurostar had passed on either track is given in Figure 9.17. The spectrum in Figure 9.17(c) has a distinct peak around 4.4 Hz. There are also peaks between 6 and 7 Hz and also between 10.5 and 12.5 Hz. According to Frýba (1996), these peaks correspond to the first three modes of vibration, assuming the peak around 4.4 Hz is the first natural frequency of the bridge. Around line speed (approximately 60 m/s for the Javelin and 80 m/s for both the Eurostar and the Velaro), the primary vehicle-passing frequencies will be around 3, 3.2 and 4.2 Hz for the Javelin, Velaro and Eurostar respectively. The shorter primary vehicle length means that the Eurostar's vehicle-passing frequency is higher and much closer to the natural frequency of the first bending mode of the bridge. Excitation of the bridge by the vehicle-passing frequency explains the increased magnitude of vibration when the Eurostar passes and the significant vibration even when that train type passes on the opposite line. Although the natural frequency found for Rainham Viaduct is similar, the line speed is lower so resonant excitation did not occur.

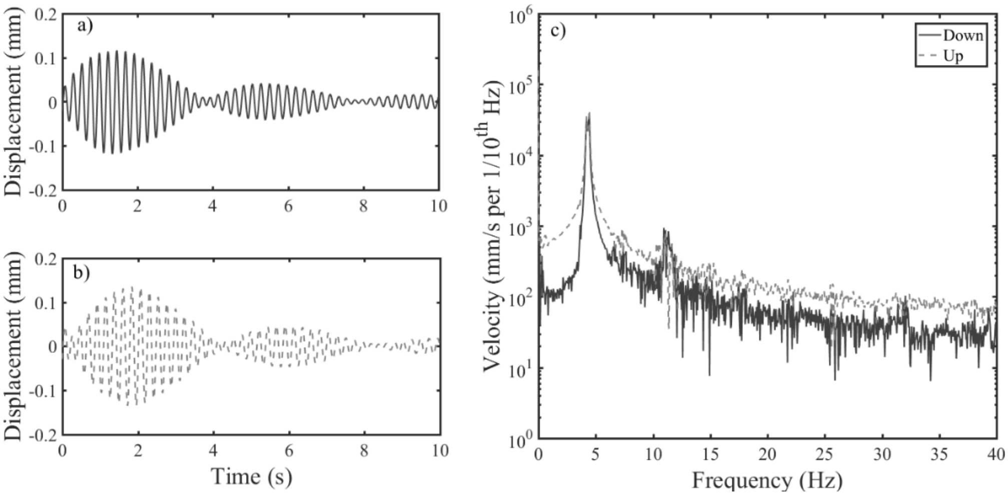

Figure 9.17 Free vibration in the middle of the central span of the A20 bridge, for a Eurostar passing on (a) the instrumented side, (b) the opposite side and (c) the corresponding velocity spectrum for these measurements.

Estimates of the mass of the bridge per unit length, based on structural cross-sections of the bridge supplied by NRHS, are between 8000 and 10000 kg/m per track. For a fundamental natural frequency of 4.4 Hz the estimates of mass suggest that the bending stiffness of the bridge is between 7×10^{10} and 8.5×10^{10} Nm^2. The logarithmic decrement of the free vibrations suggests the bridge is lightly damped, with a damping ratio of 0.9%, less than that found for Rainham Viaduct.

9.3.2.1 A20 Bridge: bridge and ballast interaction

As the ballast is continuous over the joint between the bridge deck and the abutment, the rotation of the deck-end will cause a volume change above the joint similar to that shown in Figure 9.9, but with only a single deck end rotation:

$$\rho = \frac{\theta t(t+2d)}{2x+2\theta(t+d)} \tag{9.5}$$

with the same notation as for Eq.(9.1).

The results in Table 9.1 suggest that the total deck-end rotation will be between 9×10^{-5} and 12×10^{-5} radians. For a bridge deck depth of 2.1 m, 0.5 m of ballast and a 0.2 m wide expansion joint, Eq.(9.5) gives a settlement of 0.5 – 0.7 mm. This, as was suggested for

Rainham, could lead to the voids forming beneath the sleeper above the joint, initiating further deterioration.

No long-term performance data were collected at this site, meaning that thermal effects were not observed. However, Eq.(9.2) can be used to estimate whether they may have a significant effect. Assuming that half the movement from thermal contraction of the bridge acts at each end, a temperature drop of 10° C will cause the bridge to contract by 4.3 mm and the ballast by around 3.4 mm leading to 0.9 mm of differential movement in the material above the joint. Using Eq.(9.3) for the same assumed joint geometry, this suggests 2.2 mm of ballast settlement could occur above the joint, if the volume of ballast is conserved or 0.2 mm if it behaves as an elastic solid, Eq.(9.4). As for Rainham, these simple models suggest that both thermal expansion and bridge vibration could cause additional settlement directly above the bridge movement joint, which may be significant enough to lead to voiding or differential settlement around the joint. A more sophisticated model would be needed to account for the behaviour of the granular material above the joint, to give improved understanding the relative importance of each mechanism.

9.4 Excitation of track-mounted equipment

The point motors for the S&C on HS1 are mounted on brackets cantilevered out from supporting sleepers. These locations are often associated with poor track geometry, excessive track deflection and vibration of the track-mounted equipment. This leads to concerns over further deterioration of the track and failure of the points motor. At Crissmill crossings, on the down line, a motor, the bracketry and the supporting sleepers were instrumented with ten MEMS accelerometers as shown in Figure 9.18. Primarily, this was to provide timely and regular information to understand the condition of this equipment and to assist in managing maintenance. Continuous monitoring was conducted at this site. However, the results are not reported as they showed stable albeit poor performance for the duration of monitoring.

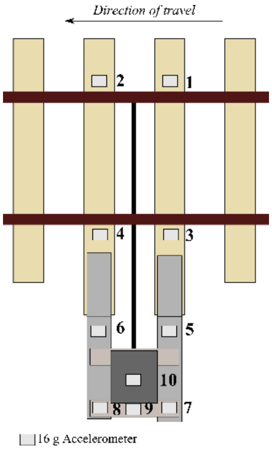

Figure 9.18 transducer locations on the sleepers and points motor.

The data from lineside monitoring can be used to investigate the state of the track and vibration of the points motor. Figure 9.19(a) and (c) shows displacements measured on a supporting sleeper and on the points motor bracket at locations 3 and 9 in Figure 9.18. The range of movement is 4–5 mm, which is similar for the sleeper and the motor. The pattern of the displacement follows the wheel loads from the train. The individual wheel loads appear to have a more significant effect on the vibration of the bracket than on the sleeper.

Figure 9.19(b) and (d) compares the acceleration spectra from 1 s of data when a train is passing, and when the sleeper and bracket are free to vibrate. When the system is being forced by the train, the spectral peaks occur at multiples of the vehicle-passing frequency for both the sleeper and the bracket. Generally, the amplitudes are similar for both the sleeper and the bracket, although the frequency content between 12 and 16 Hz is more significant for the bracket than for the sleeper. After the train had passed, the spectra for both the sleeper and the bracket have a broad peak around 14 Hz. This is probably the natural frequency of the points motor and bracket. This frequency is low enough to be affected by quasi-static deflection of the track. If the points motor were being excited, the increased vibration would affect the amount of movement of the supporting sleepers, possibly leading to an increased rate of settlement compared with the surrounding track. Either modelling of the sleeper and motor bracket system or comparative measurements at a site where the sleepers are adequately supported would be needed to begin to assess the significance of the points motor for increased track vibration.

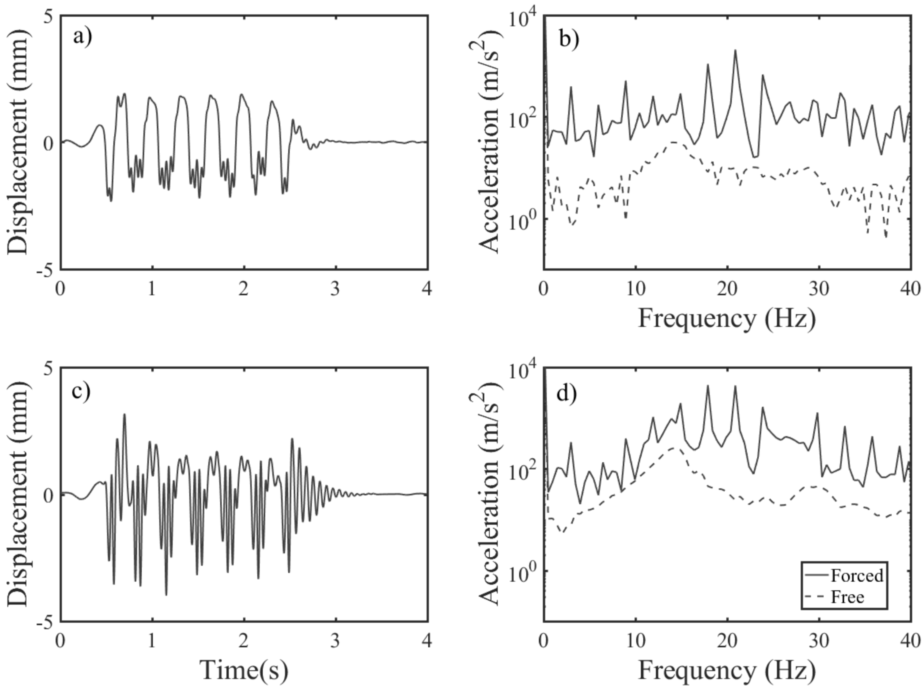

Figure 9.19 Track deflection for (a) cess sleeper end at location 3, (c) points motor bracket at location 9. Acceleration spectrum for forced and free vibration of (b) cess sleeper end at location 3, (d) points motor bracket at location 9 for a Javelin passing at 60 m/s.

9.5 Defect zones

9.5.1 Track bed condition within defect zones

The results from monitoring suggest that the condition or state of the track tends to govern the observed behaviour. Before an intervention, effects that can be associated with voided track and unstable ballast, such as large deflections and uplift, dominate the measured behaviour within defect zones. These zones are often visible from the side of the line, characterised by ‘white spotting’ from abrasion and attrition of the ballast (Figure 9.20(a)) and damage to the sleepers. Figure 9.20(b) and (c) give close-up views of a sleeper end and the surrounding ballast inside and outside a defect zone respectively. The grains in the defect zone are abraded and appear less angular and the surface of the sleeper is more worn. To understand why different types of intervention are effective (or not), it is useful to consider the state of the ballast and possible structures of the track bed within defect zones.

Figure 9.20 (a) A defect zone, (b) ballast and sleeper end outside a defect zone and (c) inside a defect zone.

Figure 9.21 shows photographs from excavations into the track bed, down to the bottom of the sleepers, within the defect zones at Crissmill. There is visible damage to the sleepers; the ballast grains were noticeably smaller than elsewhere on the track and the ballast appears ‘fouled’ with quantities of fine material, suggesting ballast and/or sleeper breakage. The ballast and sleepers were in a similar state at Rainham. NRHS suggest that machine tamping and the equipment used for manual packing may be responsible for some of the damage to the track bed and sleepers. However, the condition of the track might also suggest that there are enhanced forces acting within the defect zones.

NRHS reported that the material beneath the sleepers was very dense and that breaker bars rather than shovels were needed to break through it. This suggests the development of layering in the ballast bed inside defect zones, with dense and compacted material overlain by more loosely packed, possibly larger ballast grains.

Figure 9.21 (a) Excavation into the ballast crib, (b) damage to sleepers, (c) track bed below sleeper level.

9.5.2 Uplift phenomena

A small amount of uplift is likely to be associated with each wheel. From the BOEF model, this is expected to be a little more than 4% of the downward deflection. On well-performing track, this might be imperceptible in deflections obtained from dynamic lineside measurements. However, distinct uplift phenomena have been observed in deflection-time histories for track within defect zones using accelerometers, geophones and high-speed video. Figure 9.22 shows an example obtained using DIC, where the at-rest datum is retained and thus uplift is real. Uplift effects are discernible for both the Javelin and the Eurostar trains. They are more significant for the Eurostar and are more than 4% of the downward deflection, but the sleeper is voided. DIC data for smaller movements typical of a well-performing sleeper from HS1 were not available owing to the influence of air- and ground-borne vibration.

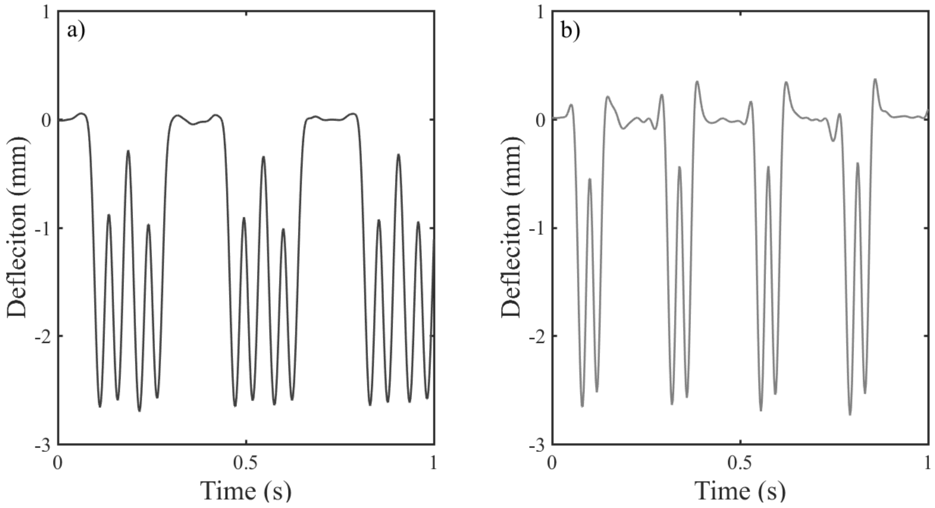

Figure 9.22 Track deflection for a voided sleeper on the A20 overbridge obtained using high speed video and DIC for (a) a Javelin and (b) and Eurostar.

Quantifying uplift from deflections obtained from velocity or acceleration measurements depends on the accuracy with which the at-rest position can be identified in the data. This can be done using the CDF for track deflection, as proposed in Chapter 6. Figure 9.23 shows displacements obtained at either end of a voided sleeper at the Crissmill plain line site. A datum correction for the at-rest position has been applied to all figures, assuming the at-rest position corresponds to *P*=0.7 in the CDF for the measured data. Plausible uplift effects are apparent in all the figures.

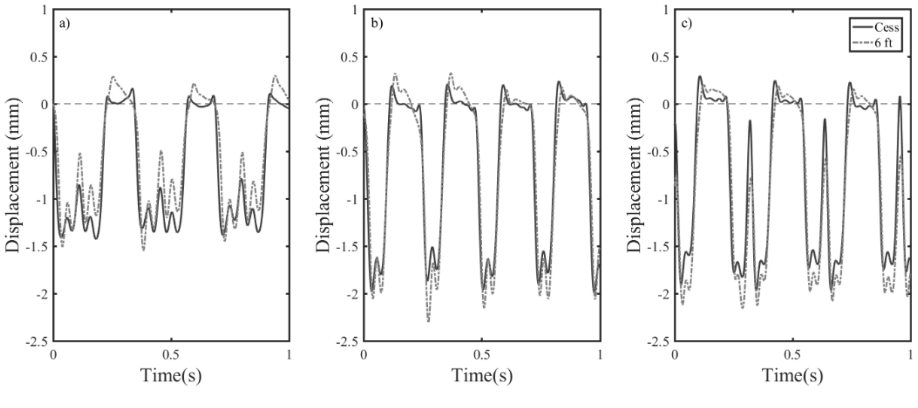

Figure 9.23 Track deflection of a voided sleeper at 1.2 m in the Crissmill plain line site obtained using MEMS accelerometers for (a) Javelin, (b) Eurostar, (c) Velaro.

Referring back to the records of characteristic downward and total track deflection obtained from continuous monitoring for all sites in Chapter 8, there is typically a more significant difference between these two measures of deflection prior to remediation when the track is performing poorly, than after. Figure 9.24 shows the uplift from (a) the North Downs Tunnel following targeting packing at either end of a sleeper at location 3.6 and (b) Crissmill locations 2.4_O and 4.2_O. In both cases a reduction is seen following targeted packing and the installation of USPs. At these sites, the amount of uplift was generally found to be 40-50% of the downward deflection prior to the intervention and 15-25% after. These are larger than would be expected from the BOEF model. However, it is clear that the absolute value of uplift tends to be small after maintenance; and uplift effects were proportionately more significant before the intervention, when performance was poor, than after.

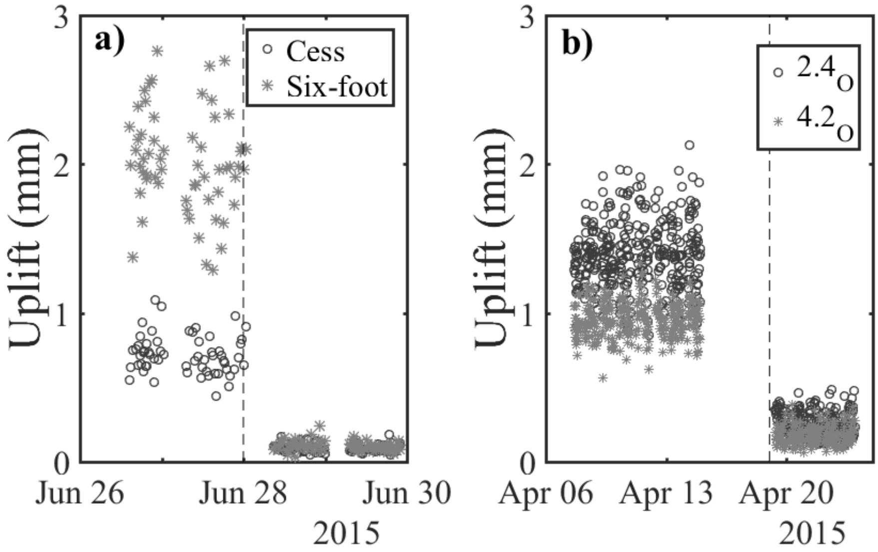

Figure 9.24 Uplift data from (a) either end of sleeper 3.6 from the North Downs Tunnel fault site following targeting packing and (b) cess side data from sleepers 2.4_O and 4.2_O from the Crissmill fault site following installation of USPs. Maintenance interventions are indicated by the vertical dashed line.

9.5.3 Defect geometry

In Chapter 6, a technique was proposed for visualising the deflected shape of the track under load as a train passed through a monitoring site, and the contribution of the track deflection to the loaded track geometry, using data from multiple transducers. Here, this technique has been used to investigate the influence of a defect zone on track deflection along the line. Data from the North Downs Tunnel and the Crissmill plain line site are used. Data were interpolated along the line for each point in time using a ‘cubic spline’ to account for bending of the rail to visualise deflection under load.

The maximum deflection along the line was recorded for a single vehicle passage, to show the deflected track geometry. To compare the behaviour from heavier and faster trains, ratios of the deflection between a Javelin and a Eurostar and a Javelin and a Velaro have been calculated. This ratio is expected to be between 1.1 and 1.4 from typical static loading, for both pairs of trains. These results are presented in Figure 9.25 and Figure 9.26 for the Crissmill plain line site and Figure 9.27 for the North Downs Tunnel site.

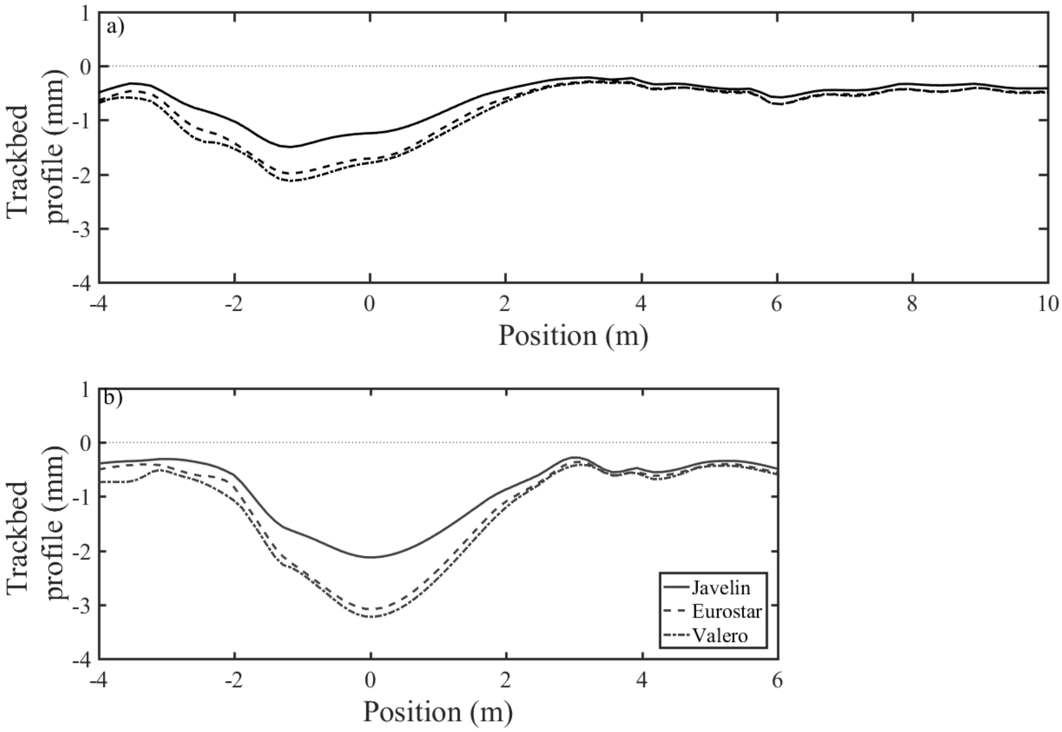

Figure 9.25 Visualisation of deflected track geometry at the Crissmill plain line site, (a) on the cess side, (b) on the six-foot side.

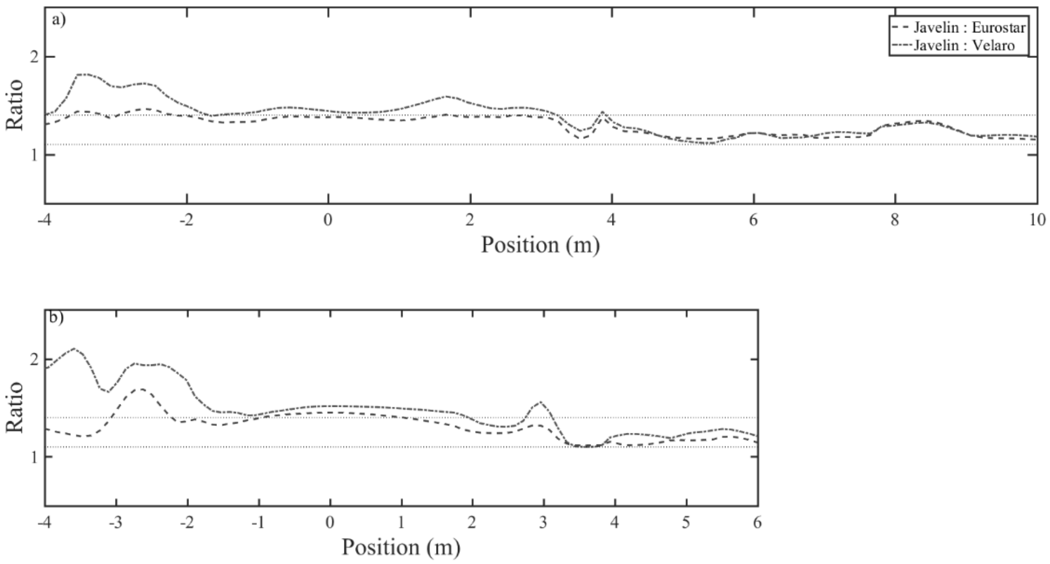

Figure 9.26 Ratio of deflected track geometry at the Crissmill plain line site between a Javelin and a Eurostar and a Javelin and a Velaro, (a) on the cess side, (b) on the six-foot side.

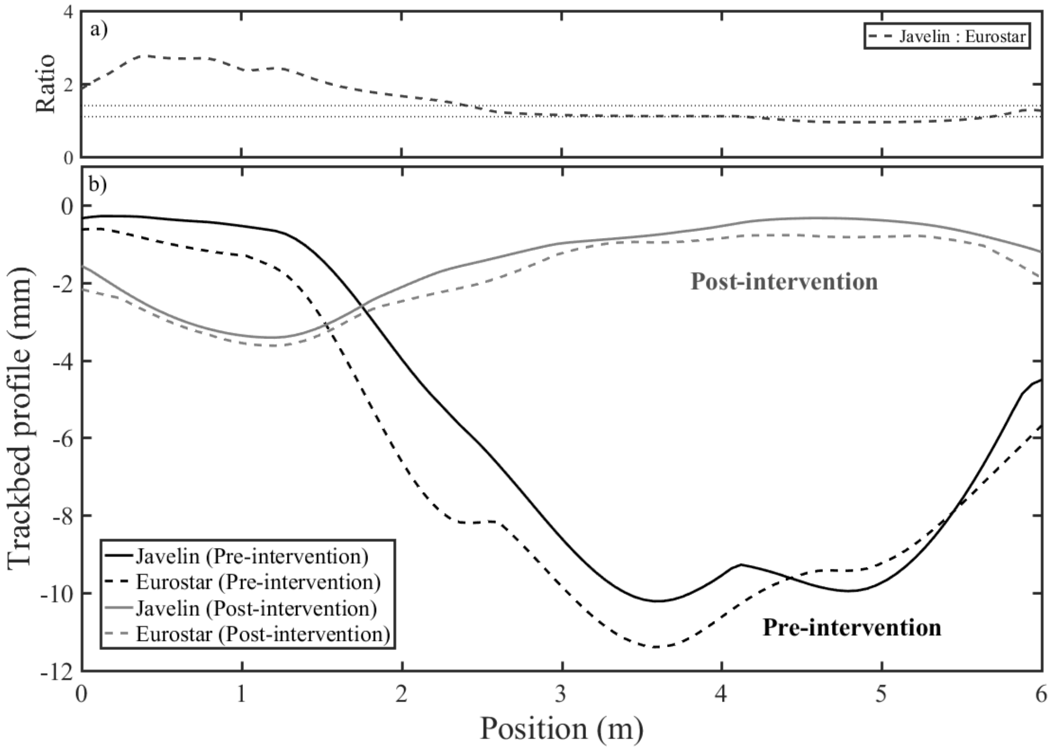

Figure 9.27 (a) Ratio of deflected track geometry, pre-intervention, between a Javelin and a Eurostar, (b) visualisation of deflected track geometry on the six-foot side of the North Downs Tunnel defect site.

Each of the defects studied have different geometries and affect different lengths of track. For the North Downs Tunnel site, the defect probably has an influence beyond the end of the monitoring site.

Interpreting and explaining these observations relies on a conceptual model of how a voided track deflects, how it might interact with a train and effect the surrounding track. A simple model for a void involves a gap, into which the rail and sleeper move down under load, ‘seating’ onto the track bed; followed by elastic deflection (Sussman et al., 2001). This results in increased loads on sleepers adjacent to the voided ones. Thus, the ratio of deflection between the lighter and heavier train should reduce over a void, as the gap would be constant for both train types. This appears to be the case for the North Downs Tunnel in Figure 9.27(a), where track bed deflection is large, exceeding 8 mm, and the ratio of deflection between a Javelin and a Eurostar is less than 1.1. At Crissmill, Figure 9.26, the ratio was found to be greater, around 1.4 - 1.5, in the voided area (around 0 m) than for well-performing track, where it is 1.1-1.2. This suggests that there may be more significant dynamic effects from the heavier and faster trains in that voided region or other non-linearities, beyond those created by a gap between sleeper and the ballast.

The effects of the defect on the ratios of the deformed geometry between a Javelin and a Eurostar or Velaro were not consistent between the two sites around the voided sleeper. The behaviour at the North Downs Tunnel site agrees with a simple conceptual model for a void, but that at the Crissmill does not. However, in both cases, the ratio of deflections was greatest for sleepers adjacent to the voided ones, at the leading edge of the defect.

9.5.4 Accelerated deterioration

Track defects occur as a result of localised accelerated deterioration. Voiding and irregular geometry due to a defect may exacerbate this. Models have been used to show that the presence of a voided sleeper may increase loading on the track and lead to stress concentrations at the edges of the defect, which would be expected to result in increased settlement and growth of the defect zone (Grassie and Cox, 1985; Lundqvist and Dahlberg, 2005; Bezin et al., 2009). Figure 9.28 shows field evidence for this from

Crissmill, from Figure 8.10. These data are for Javelin trains at locations 2.4_O and 4.2_O; obtained between 22nd February 2015 (after tamping), and 16th April 2015 (before installation of USPs). These sleepers were thought to be in the centre and at the edge of the defect zone respectively.

Example track deflections are given for 2nd March and 2nd April 2015 in Figure 9.28(a) and (c) for locations 2.4_O and 4.2_O. Figure 9.28(b) and (d) records the development of the characteristic downward deflection over this period. Figure 9.28(b) records an increase in downward deflection at location 2.4_O, from mean values of around 2.5 mm to 3.5mm in the first week after tamping, levelling off at about 4.5 mm three weeks after tamping. At location 4.2_O track deflections rose at a fairly constant rate (0.2-0.3 mm/week), from around 1.8 mm to around 2.6 mm between 2nd March to 2nd April 2015. Increasing loads acting on the sleeper or the growth of a void beneath it could be responsible for this trend.

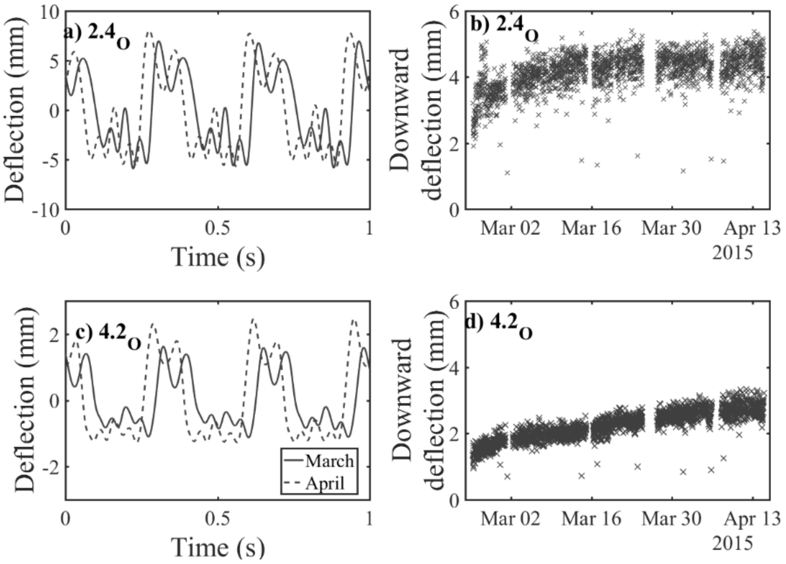

Figure 9.28 Deterioration of performance at sleepers within the Crissmill defect zone.

The data reproduced in Figure 9.28 show that deterioration happens at different rates at these two locations and that the changes in performance at one location appear to be associated with the behaviour at other locations. The trends recorded here suggest progressive growth in the length and severity of the defect zone.

9.6 Evaluating maintenance

9.6.1 Localised Tamping

Machine tamping was used on the defect on Rainham Viaduct, and after an unsuccessful attempt at installing USPs at Crissmill. Neither intervention was successful in restoring performance. This sub-section considers why tamping may have proved ineffective.

Figure 9.29 shows segments of track deflection data obtained using DIC for a voided sleeper within the defect zone studied on Rainham Viaduct. Results are shown for Javelin and Eurostar train types. These are given for the day before and the day after the defect was tamped in May 2014. There is a clear reduction in track deflection after tamping from around 5.5-6 mm before, to a little over 2 mm after. Although this was a significant reduction, the sleeper deflections were still in excess of the 0.5-1 mm of sleeper movement expected for well-performing track. This shows that good performance was not fully restored by the tamping operation.

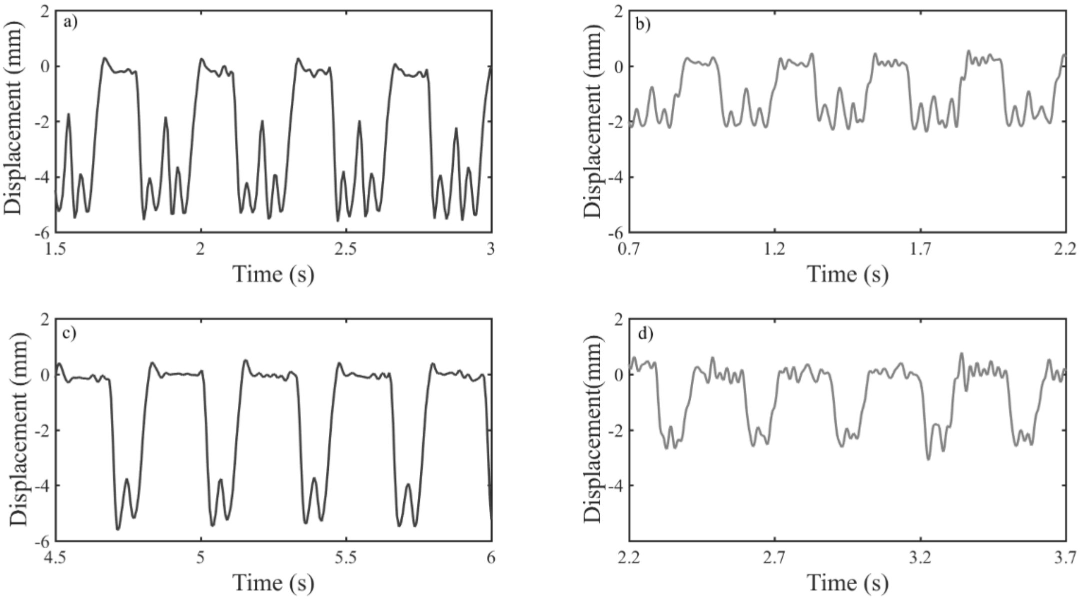

Figure 9.29 Track deflection data for a sleeper within the defect zone on Rainham Viaduct obtained using DIC before (left) and after tamping (right) for a Javelin (a) and (b) and for a Eurostar (c) and (d) train types. Filmed at 300 fps and low-pass filtered at 40 Hz.

The sequence of photographs in Figure 9.30 show deterioration and effects of instability of the ballast at this defect zone after tamping. Immediately after tamping the ballast surface was painted in a regular pattern at the sleeper edges and above the tie bar. Six days after tamping many of the ballast grains had become mobile. After six months paint is only visible at the edges of the defect zone. The 2 mm of residual movement suggest that tamping did not leave the track adequately compacted or free from voids. Thus, it was unable to resist the track forces, leading to large de-stabilising track movements, after maintenance.

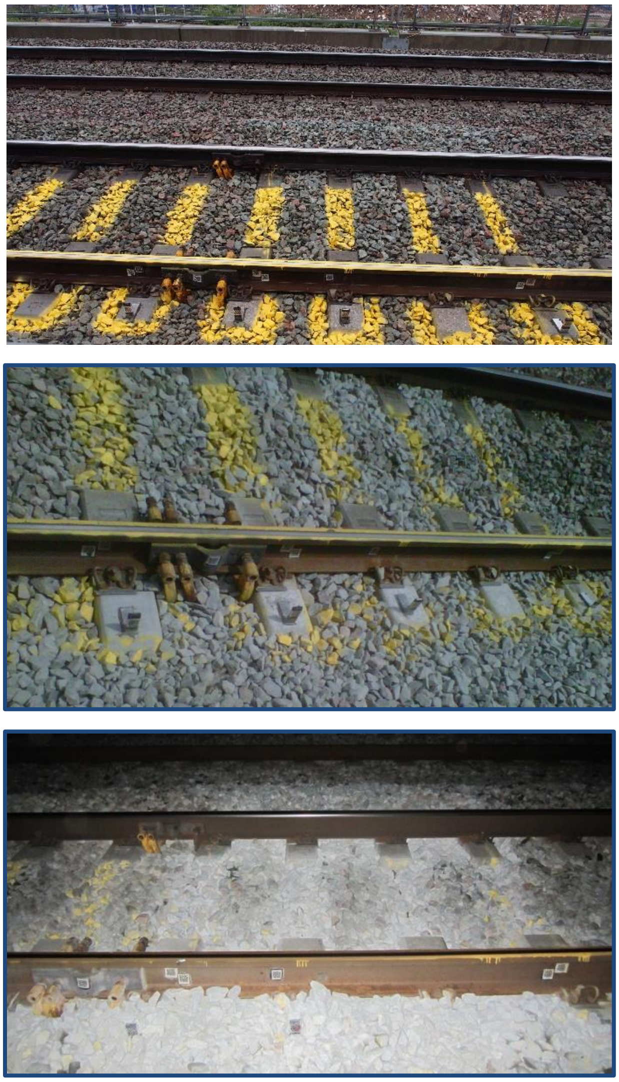

Figure 9.30 Photographs of track on Rainham Viaduct (a) 1-day (b) 6 days (c) 6 months after tamping.

Localised tamping was also used at the Crissmill defect site when acceptable track geometry could not be achieved after an attempt to retrofit USPs. Failure of the logging system meant that no data were available from the first two days after tamping. The results from continuous monitoring (Figure 8.9 and Figure 8.10) show that the deflections of the first two instrumented duo-block sleepers 0.6_O and 1.2_O were small after tamping. However, further into the defect zone deflections at 2.4_O remained large, a previously well-performing sleeper 2.4_I was now voided and deflections found at 4.2_O began to increase at an accelerated rate, as seen in Figure 8.9 and Figure 8.10. Disturbance to the track bed during the attempted installation of the USPs may have been responsible for introducing a new void beneath the previously well-supported sleeper. Regardless of the cause of the void, machine tamping was not effective at-restoring support conditions. Large deflections were prevalent after tamping, and these continued to increase over time.

The tamping tines are designed to penetrate to a depth of 3-4 grain diameters below the sleeper. Excavation into the defect zone suggests that the material at that depth is likely to be dense and compact. It is difficult to say what the effect of tamping would be on this material and whether the squeezing action will be sufficient to raise the level of the ballast to restore contact with the sleeper and provide adequate support. The tamping machine has no feedback process to determine whether the track is adequately supported. It relies solely on a local geometry measurement immediately after the intervention to assess the line and level of the track.

9.6.2 Shimming

Shimming between the rail and the sleepers was trialled at the Crissmill defect site and on Rainham Viaduct. The rail was unfastened for the sleepers which were allowed to drop until they made contact with the ballast bed. A number of 4.5 mm thick Ethylene vinyl acetate (EVA) shims were installed between the sleeper and the existing rail pad. Then the rail was fastened back onto the sleeper.

At Crissmill, a single additional shim was placed between the rail and the sleeper within the defect zone. The objective of this was to reduce the depth of the voids between the sleeper and the trackbed. Lineside measurements were not used to specify the shim thickness in this case. Figure 9.31 shows the effect of this at different ends of the same sleeper (a) at the voided end and (b) at the well-performing end. For the voided end in Figure 9.31(a) sleeper movements were reduced from around 9 mm to 4.5 mm (i.e. by the shim thickness) and uplift effects were also reduced. This suggests that the shim was not thick enough to fully restore contact between the sleeper and the track bed. No change was seen for the well-performing end in Figure 9.31(b). This means that the rail level will have been raised, as that end of the sleeper was already in contact with the track bed.

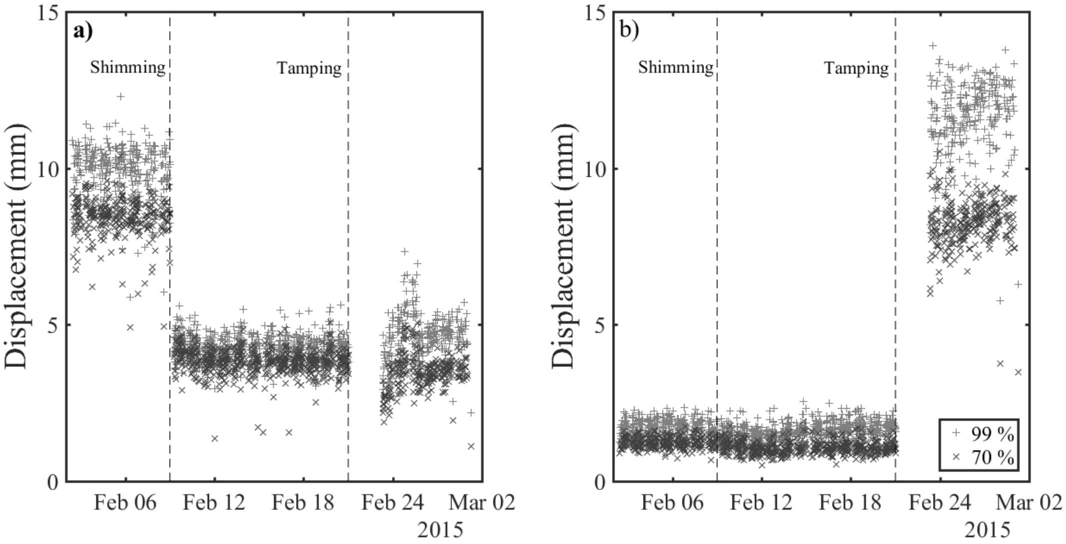

Figure 9.31 data from Figure 8.10 showing the effect of shimming and tamping on the track at Crissmill, (a) at the voided end and (b) at the well-performing end of the sleeper 2.4 using Javelin data.

Shimming was also used at Rainham Viaduct. Here, the results of the lineside monitoring were used to inform the number of shims placed between the rail and the sleepers on the cess side. Where downward deflections were less than 5 mm a single 4.5 mm shim was used. Where deflections were between 5 mm and 10 mm two shims were used for the instrumented and adjacent sleepers. Monitoring results were shown in Figure 8.22 to Figure 8.24. Apart from the sleeper above the joint, the performance of which remained highly variable, matching the shim thickness to the amount of track movement was effective in reducing the amount of track movement, stabilising it at normal levels. This suggests that the sleepers were brought into contact with the track bed by insertion of shims of the correct thickness. The effects of shimming on the cess rail side were sustained for the remainder of the monitoring period. However, it appears that the improvements on the cess rail side had an adverse effect on the six-foot rail, where track deflections increased after the intervention. Owing to the demonstrable and sustained reduction in deflection throughout the majority of the defect zone, NRHS plan to shim the six-foot rail at the joint studied, and both rails at other defect zones on the bridge.

9.6.3 Targeted packing

Manual packing is the other standard method used to remediate isolated defect zones. Much as for localised tamping, the track engineers report that this is rarely effective for the more severe defect zones. Lineside monitoring techniques were used to inform and evaluate a more targeted use of manual packing at the North Downs Tunnel defect site. As shown in Chapter 8 (Figure 8.16 to Figure 8.19), lineside monitoring was used to gain an understanding of how the track was performing within the defect zone, before and after maintenance.

Lineside monitoring showed sleeper movements in excess of 10 mm (see Figure 8.16 and Figure 8.17). From this, the maintainer decided that the ballast below sleeper level was likely to be in a similar condition to that found during excavation at Rainham and Crissmill, where tamping and packing type interventions were not successful. Normally, manual packing involves lifting the affected sleepers and then using Kango or Cobra packers to force ballast underneath the affected sleepers. In the present intervention, the ballast surrounding the affected sleepers was excavated until a dense/fouled layer was identified. This layer was broken up manually. The objective of breaking it up was to encourage returned and replacement material to mix and interlock with the existing ballast during packing, creating a more homogeneous material and preventing discontinuities in the structure of the ballast bed. New and excavated material was then returned to the track bed and the superstructure was packed until the desired track geometry had been achieved.

Monitoring was restarted after the intervention. This showed directly that the track deflections were reduced and support conditions were restored within the defect zone immediately after the intervention. Moreover, performance did not deteriorate over the subsequent 3-4 months. Results from near-continuous lineside monitoring shown in Figure 9.32 demonstrate a sustained reduction in track deflection and the restoration of support conditions after this intervention at location 2.4_I.

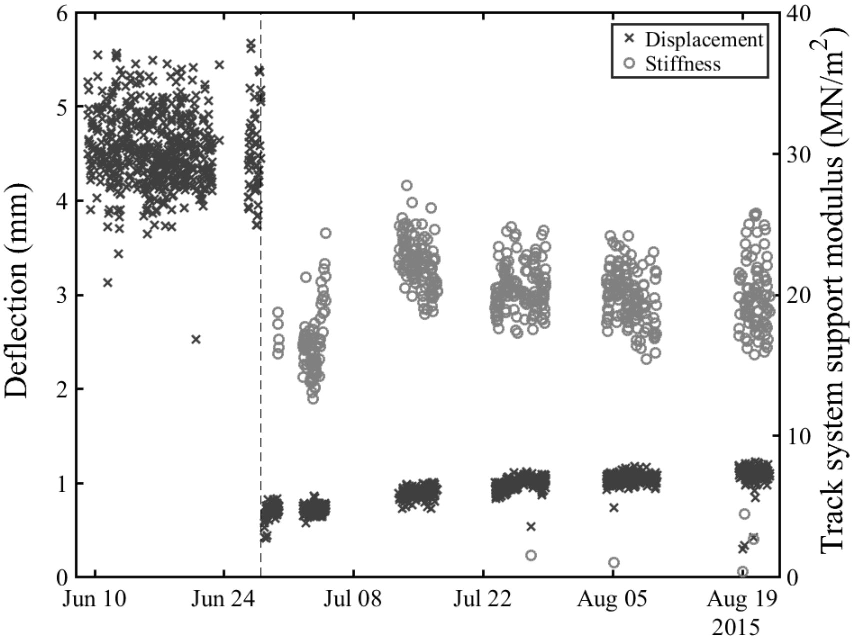

Figure 9.32 Data from the North Downs Tunnel defect site from Figure 8.17 and 8.13 showing improvements in track deflection and restoration of support conditions after targeted packing at sleeper 2.4_I for Javelin train passages.

Data from monitoring also highlighted the increased deflection of sleepers previously considered to be outside the defect zone (0.0_I and 1.2). These were not packed during the intervention. After the intervention, deflection of these sleepers increased to levels typically associated with voiding. It is likely that lifting the track within the defect zone resulted in new gaps forming between the sleepers and the ballast bed at the extremities of the defect zone. A second intervention was therefore carried out to remove these gaps and ensure continuity of support along the section. Although the first intervention introduced new voids into the track, data from the TRC indicated that the geometry was acceptable (Figure 8.14). Without feedback from lineside monitoring these voids might not have been detected and would potentially have had an adverse effect on the track. The packing of sleepers at either end of the defect zone to alleviate potential consequences of a local track lift has now been incorporated into routine practice, based on the outcomes from this study.

In this example, lineside monitoring provided the maintainers with data that helped them to understand the behaviour of the track, relate it to other sites and anticipate the condition of the trackbed. This gave them the confidence to innovate with their maintenance practice, with the reassurance that they had the tools and analysis techniques available to evaluate the intervention. This study showed that by breaking up the dense layer of ballast bed as part of targeted packing, the intervention was more effective, leading to a longer lasting repair and improvements to maintenance practice.

9.6.4 Under-sleeper pads

Two attempts were made at the Crissmill defect site to install USPs. The first involved retro-fitting pads to the existing sleepers (Figure 9.33). However, it was not possible to achieve acceptable track geometry using this method, possibly due to the condition of the sleepers within the defect zone.

Figure 9.33 Photographs of retrofitting USPs to sleepers in situ.

For the subsequent, successful attempt, the pads were glued to new sleepers prior to delivery to the site. The damaged sleepers were dug out and replaced; the dense and compact material found below sleeper level was broken up and the site was repacked with new and returned ballast and then tamped (Figure 9.34(a)). Spent ballast was left at the trackside, and used to re-profile the ballast shoulder (Figure 9.34(b)).

Figure 9.34 Photographs of installing new sleepers with USPs.

Track geometry data supplied in by NRHS in Figure 9.35 shows that the track geometry in the vicinity of the defect zone was still irregular after installation of the USPs. The track above the under-track crossing remains a local high point and the geometry is irregular where the under-sleeper pads were installed. The local reduction in track stiffness associated with the pads will be part responsible for the irregular geometry, as the track will deflect more under load in that area. The relative high spot ahead of the pads may explain the variation in the applied wheel load found along the site using lineside monitoring (Figure 8.12). There was a slight deterioration in geometry between May 2015 and 2016, but no further significant changes in the track geometry up to May 2017. This is consistent with the sustained levels of performance seen from lineside monitoring for the same period (Figure 8.9, Figure 8.10 and Figure 8.13).

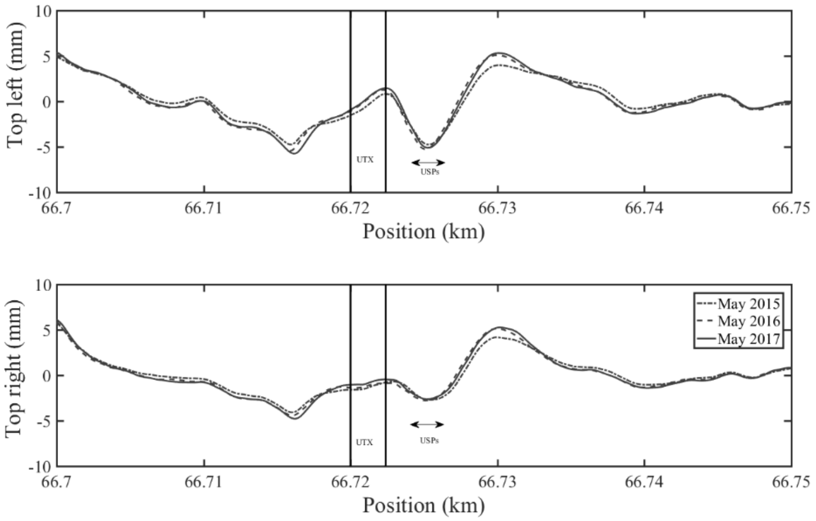

Figure 9.35 Vertical track geometry from the TRC the Crissmill defect site after installation of the USPs.

The results from continuous monitoring (Figure 8.9 and Figure 8.10) showed that this intervention restored performance at the site. Improved performance has been sustained for two years despite the possibility that irregular track geometry may increase the loads applied at the site (Figure 8.12 and Figure 9.35). The combination of interventions made at the site mean that is challenging to assess the significance of individual improvements. For example, this research has shown that targeted re-packing with breaking up of dense and compact material can restore performance; research by Abadi et al. (2015; 2016) has shown that both USPs and reprofiling of the ballast shoulder can improve the performance of railway track. Although lineside monitoring was effective in showing that improvements have been made and sustained, these results cannot be used to explain the mechanisms of how and why the improvements were effective.

9.7 Conclusions

This Chapter has shown that, when taken in context with information about the trackform and track geometry, data from lineside monitoring can be used to identify features that might influence the formation of defect zones. Data provided evidence for the track behaviour in the vicinity of these features. Examples shown include over-loading associated with irregular geometry from a stiff spot caused by a shallow UTX and the potential for additional settlement above structural expansion joints where bridge movement can affect the ballast.

For the sites studied there are often multiple features that may influence the track. This means that field trials, laboratory experiments and appropriate modelling are required to assess the significance or provide a mechanistic description of different processes that have been identified. Monitoring provides a wealth of real scenarios to investigate and highlights behaviours and processes that should be taken into account in future research to model the progressive deterioration of railway track.

Continuous monitoring has been shown to be an effective means of evaluating maintenance. The systems and means of analysis developed in this research can be used to show directly how the performance of the track has changed and whether support conditions have been restored after an intervention. Long-term data indicates whether performance is sustained. This approach also drew attention to adverse effects from maintenance that would not have been identified using track geometry data. This enabled corrective measures to be carried out before performance was significantly affected.

This approach has provided information used to inform maintenance and understand why different techniques were or were not successful. Where interventions were planned using data from lineside monitoring, these were successful, while those that did not use such data, often were not.

Chapter 10: Conclusions

The aim of this research was to *improve lineside measurement systems and apply them to investigate, diagnose and evaluate remediation associated with performance issues on a ballasted high-speed railway line.* This Chapter presents the main conclusions and outcomes from this research and suggests avenues for further study. Conclusions have organised according to the objectives of *improve,* and *investigate, diagnose and evaluate*.

10.1 Improvements to lineside monitoring

This research has resulted in several improvements to lineside monitoring systems and the analysis of the data obtained which can help make long-term condition monitoring a viable proposition.

Laboratory and field trials of low-cost MEMS accelerometers showed that these types of transducer can provide data suitable for obtaining track displacements. Testing showed that these sensors are more effective for faster trains and larger displacements. Data for slower trains or circumstances where deflections are small are more susceptible to low frequency noise. The affordability, small size and robustness of MEMS accelerometers means that they are well suited to extended deployments on a high-speed railway. This is necessary for obtaining regular data for studying changes in performance or for use as a condition monitoring system. Confidence in the data obtained using these sensors enabled their use for the long-term studies.

An improved understanding of low frequency track vibration signals has allowed development of new analysis techniques including methods for characterising the performance (track deflection) and properties of the track system (track system support modulus) from track vibration data from passing trains 7. The downward sleeper deflection and the track system support modulus were combined to estimate the applied wheel load.

A statistical process based on the CDF for track deflections has been developed for characterising the range of total and downward deflection. This process can be used to remove artefacts from signal processing, including the shift in the at-rest position in data obtained from velocity or acceleration measurements. It can be implemented in a way that implicitly averages the data to provide a result representative of typical behaviour, and reduce the sensitivity of the analysis to impacts from wheel flats. The method also works for voided and poorly performing sleepers. This approach is efficient to implement numerically, and hence can be incorporated into algorithms for automatically characterising the range of track movement from large amounts of field data.

The Fourier transform of the response from the BOEF model and the sequence of loads from a train can be used of interpret the spectrum for measured track vibration at low frequencies and obtain a measure of track stiffness. The relative magnitudes of the dominant spectral peaks, which occur at multiples of the vehicle-passing frequency, can be related to the track system support modulus using the known geometry of the train or, in some cases, the vehicle. Theoretically, this method is independent of the applied loads for trains with equal wheel loads and has been shown to be insensitive to plausible variations of unequal loads. This removes a source of uncertainty from the analysis and the need to measure the load. This process can be implemented using an algorithm to determine the track system support modulus automatically from track vibration data.

The ability to implement these methods of analysis automatically to interpret and analyse track vibration data made it feasible to interpret the large volumes of data generated by extended deployment of lineside monitoring systems at the various study sites. Recording the typical track deflection and stiffness obtained for each passage of a train type over time directly shows any changes in the performance and the properties of the track.

10.2 Investigations, diagnosis and evaluation of remediation

Data collected using the techniques developed in this research have been used to *investigate, diagnose and evaluate remediation associated with performance issues* at the study sites. The approaches allowed a record of progressive deterioration and evidence to be obtained for different mechanisms that have the potential to influence the track. Possible mechanisms included overloading due to track geometry irregularities associated with stiff UTXs, and bridge/ballast interaction above structural expansion joints. The complexity of most study sites means that appropriate modelling would be required to assess the significance of possible mechanisms. The data are also valuable for showing how a defect zone might influence the behaviour, geometry and support conditions of the track, insights that would be needed for a more in-depth understanding of poor performance and deterioration.

Monitoring proved to be an effective tool for specifying and evaluating maintenance. Improvements to performance from interventions that used field data to inform thicknesses of new resilient layers (shims and USPs) and addition of new aggregate were shown to be sustained. Records of characteristic downward deflection and track system support modulus for individual train passages from large volumes of track vibration data showed reductions in track deflection and the restoration of support conditions in a clear and intuitive way. NRHS are now more confident in using lineside monitoring to manage the condition of the track, as well as using the data to plan and justify now-proven maintenance techniques such as targeted packing, shimming beneath the rail and use of USPs, to remediate isolated defect zones. The maintainers are now aware of possible consequences of remediation that might not be identified using TRC data. They have now adapted maintenance practice to account for the possibility that an intervention may affect the track outside the defect zone.

10.3 Recommendations for future research

This research provides several avenues for further work. These concern development of instrumentation, understanding the effects of non-linearity and variability on the analysis methods and modelling to assess the significance of different mechanisms and processes identified from monitoring.

The performance of low-cost MEMS sensors is continually improving. The sensors used in this research were validated for high-speed situations. To obtain deflections for lower speed trains, sensors with a lower noise floor at low frequency would be needed. It would be worthwhile to explore options for measurement of sleeper rotation, to determine whether this is significant and to understand any impact on vertical vibration signals obtained using MEMS accelerometers. Continued trials of different sensors would lead to a more versatile system, suitable for a wider range of operational conditions, and provide more axes of measurement for a more complete description of track motion. The use of digital sensors with microprocessors for data acquisition has the potential to reduce significantly the capital cost of a lineside monitoring system and facilitate data transfer back to the end user. Initial trials using this type of sensor and acquisition system have been promising. However, these systems need further development. Further challenges relate to powering to the system, aggregating, transmitting, processing, analysing and storing the data.

Calculations of the track system support modulus are based on the assumption that the track is homogeneous, well-supported and behaving linearly. Lineside monitoring is often used in situations where this is not the case. There is a need for studies that investigate the effect of non-linearity from voiding on the spectrum of low frequency track vibration. It is also necessary to quantify variability of the support conditions over an extended length of track, and to understand the consequences of that variability.

Finally, there is a need for appropriate modelling, to provide a more detailed understanding of the different mechanisms identified from monitoring. This could include a discrete element model of the ballast above a bridge joint to give improved understanding of the significance of movement from thermal contraction and deck end rotation on the ballast volume.

To understand how the presence of a shallow UTX or a void influences track performance and explain progressive deterioration and the formation of track defects, a model or combination of models with an appropriate level of detail would be required. Finite element models (or multibody simulation with a flexible track model) could be used to incorporate vehicle dynamics to investigate effects of stiffness variation or nonlinearity along the length of the track. This could be adapted to account for accumulated differential settlement along the track to study progressive deterioration and to provide a mechanistic explanation for behaviours recorded using lineside monitoring and the formation of track defects. Requirements of a model that would be suitable for this purpose are given in Appendix D.

References

Abadi, T., Le Pen, L., Zervos, A. & Powrie, W. (2015) Measuring the Area and Number of Ballast Particle Contacts at Sleeper/Ballast and Ballast/Subgrade Interfaces. *International Joural of Railway Technology* **4(2)**:45-72.

Abadi, T., Le Pen, L., Zervos, A. & Powrie, W. (2016) Improving the performance of railway tracks through ballast interventions. *Proceedings of the Institution of Mechanical Engineers, Part F: Journal of Rail and Rapid Transit*.

Ah Fat, J. (2017) A Neural Network Implementation of a Train Monitoring System. University of Southampton.

Albarbar, A., Badri, A., Sinha, J. K. & Starr, A. (2009) Performance evaluation of MEMS accelerometers. *Measurement* **42(5)**:790-795.

Alva-Hurtado, J. & Selig, E. (1981) Permanent strain behavior of railroad ballast. In *Proceedings of The International Conference on Soil Mechanics and Foundation Engineering, 10th.*, vol. 1.

Alves Costa, P., Calçada, R. & Silva Cardoso, A. (2012) Track–ground vibrations induced by railway traffic: In-situ measurements and validation of a 2.5D FEM-BEM model. *Soil Dynamics and Earthquake Engineering* **32(1)**:111-128.

Analog Devices (2009) ADXL 326 Datasheet.

Auersch, L. (2005) The excitation of ground vibration by rail traffic: theory of vehicle–track–soil interaction and measurements on high-speed lines. *Journal of Sound and Vibration* **284(1–2)**:103-132.

Auersch, L. (2006) Ground vibration due to railway traffic—The calculation of the effects of moving static loads and their experimental verification. *Journal of Sound and Vibration* **293(3–5)**:599-610.

Aursudkij, B., McDowell, G. R. & Collop, A. C. (2009) Cyclic loading of railway ballast under triaxial conditions and in a railway test facility. *Granular Matter* **11(6)**:391-401.

Baeza, L. & Ouyang, H. (2011) A railway track dynamics model based on modal substructuring and a cyclic boundary condition. *Journal of Sound and Vibration* **330(1)**:75-86.

Banimahd, M., Woodward, P. K., Kennedy, J. & Medero, G. M. (2012) Behaviour of train - track interaction in stiffness transitions. In *Proceedings of the ICE - Transport*. vol. 165, pp. 205-214.

Berggren, E. G., Nissen, A. & Paulsson, B. S. (2014) Track deflection and stiffness measurements from a track recording car. *Proceedings of the Institution of Mechanical Engineers, Part F: Journal of Rail and Rapid Transit* **228(6)**:570-580.

Bezin, Y., Iwnicki, S. D., Cavalletti, M., de Vries, E., Shahzad, F. & Evans, G. (2009) An investigation of sleeper voids using a flexible track model integrated with railway multi-body dynamics. *Proceedings of the Institution of Mechanical Engineers, Part F: Journal of Rail and Rapid Transit* **223(6)**:597-607.

Bezin, Y., Neves, S. G. M., Grossoni, I. & Kaushal, A. (2016) Understanding Track Loading Requirements to achieve Better Track Design In *Proceedings of The Third International Conference on Railway Technology: Research, Development and Maintenance* (Pombo, J. (ed)). Civil Comp Press, Stirlingshire, United Kingdom.

Bian, X., Jiang, H., Chang, C., Hu, J. & Chen, Y. (2015) Track and ground vibrations generated by high-speed train running on ballastless railway with excitation of vertical track irregularities. *Soil Dynamics and Earthquake Engineering* **76**:29-43.

Bonnell, D. G. R. & Harper, F. C. (1950) The thermal expansion of concrete. Engineering research. (Summary of a report to be published by the building research station). *Journal of the Institution of Civil Engineers* **33(4)**:320-330.

Bowness, D., Lock, A. C., Powrie, W., Priest, J. A. & Richards, D. J. (2007) Monitoring the dynamic displacements of railway track. *Proceedings of the Institution of Mechanical Engineers, Part F: Journal of Rail and Rapid Transit* **221(1)**:13-22.

British Standards Institution (2004) BS EN 1991-1-5:2003. Eurocode 1. Actions on structures. General actions. Thermal actions. .

British Standards Institution (2014) BS EN 13848. Railway applications. Track. London.

Brough, M., Stirling, A., Ghataora, G. & Madelin, K. (2003) Evaluation of railway trackbed and formation: a case study. *NDT & E International* **36(3)**:145-156.

Brown, S. F. (1996) Soil mechanics in pavement engineering. In *Géotechnique*. vol. 46, pp. 383-426.

Coelho, B., Hölscher, P., Priest, J., Powrie, W. & Barends, F. (2011) An Assessment of Transition Zone Performance. *Proceedings of the Institution of Mechanical Engineers, Part F: Journal of Rail and Rapid Transit* **225(2)**:129-139.

Dahlberg, T. (2001) Some railroad settlement models—A critical review. *Proceedings of the Institution of Mechanical Engineers, Part F: Journal of Rail and Rapid Transit* **215(4)**:289-300.

Dahlberg, T. (2010) Railway track stiffness variations–consequences and countermeasures. *International Journal of Civil Engineering* **8(1)**:1-11.

Dimitrovová, Z. (2010) A general procedure for the dynamic analysis of finite and infinite beams on piece-wise homogeneous foundation under moving loads. *Journal of Sound and Vibration* **329(13)**:2635-2653.

Dimitrovová, Z. & Varandas, J. N. (2009) Critical velocity of a load moving on a beam with a sudden change of foundation stiffness: Applications to high-speed trains. *Computers & Structures* **87(19–20)**:1224-1232.

Dyson, S. W. & Kirk, M. J. D. (2006) A high-speed railway through marshlands (CTRL). *Proceedings of the ICE - Transport* **159**:75-82.

Ellis, I. (2014) *Ellis' British Railway Engineering Encyclopaedia (3rd Edition).* LULU Press.

Esveld, C. (2001) *Modern railway track.* Second Edition edn. Delft, MRT-Productions.

Ferreira, P. A. & Lopez-Pita, A. (2013) Numerical Modeling of High-Speed Train/Track System to Assess Track Vibrations and Settlement Prediction. *Journal of Transportation Engineering-Asce* **139(3)**:330-337.

Frohling, R. D., Scheffel, H. & EbersÖHn, W. (1996) The Vertical Dynamic Response of a Rail Vehicle caused by Track Stiffness Variations along the Track. *Vehicle System Dynamics* **25(sup1)**:175-187.

Frýba, L. (1972) *Vibration of solids and structures under moving loads.* Groningen, The Netherlands, Noordhoff.

Frýba, L. (1996) *Dynamics of railway bridges.* London, Thomas Teflord.

Frýba, L. (2001) A rough assessment of railway bridges for high speed trains. *Engineering Structures* **23(5)**:548-556.

Gao, Y., Qian, Y., Stoffels, S. M., Huang, H. & Liu, S. (2017) Characterization of railroad crosstie movements by numerical modeling and field investigation. *Construction and Building Materials* **131**:542-551.

Gatti, G., Brennan, M. J., Tehrani, M. G. & Thompson, D. J. (2016) Harvesting energy from the vibration of a passing train using a single-degree-of-freedom oscillator. *Mechanical Systems and Signal Processing* **66–67**:785-792.

Gotcha Montioring Systems (2011) A flexible monitoring platform for advanced asset management of rolling stock and infrastructure: system description. Lloyd’s Register Rail Europe B.V.

Graff, K. F. (2012) *Wave Motion in Elastic Solids.* Dover Publications.

Grassie, S. & Cox, S. (1985) The dynamic response of railway track with unsupported sleepers. *Proceedings of the Institution of Mechanical Engineers, Part D: Journal of Automobile Engineering* **199(2)**:123-136.

Grossoni, I. & Bezin, Y. (2015) The influence of support conditions on short- and long-term track behaviour In *Proceedings of The Stephenson Conference - Research for Railways*.

Guerin, N. (1996) Approche expérimentale et numérique du comportement du ballast des voies ferrées. Ecole Nationale des Ponts et Chaussées.

Harkness, J., Zervos, A., Le Pen, L., Aingaran, S. & Powrie, W. (2016) Discrete element simulation of railway ballast: modelling cell pressure effects in triaxial tests. *Granular Matter* **18(3)**:65.

Hetényi, M. (1946) *Beams on elastic foundations.* Ann Arbor, The University of Michigan Press.

Horowitz, P. & Hill, W. (2015) *The Art of Electronics.* Cambridge, Cambridge University Press.

Hosseingholian, M., Froumentin, M. & Robinet, A. (2011) Dynamic Track Modulus from Measurement of Track Acceleration by Portancemetre In *Proceedings of World Congress on Rail Research*.

HS1 Ltd (2013) *Five year asset management statement*. London.

Hunt, H. E. M. (1997) Settlement of railway track near bridge abutments. *Proceedings of the ICE-Transport* **123(1)**:68-73.

Indraratna, B., Ionescu, D. & Christie, H. (1998) Shear Behavior of Railway Ballast Based on Large-Scale Triaxial Tests. *Journal of Geotechnical and Geoenvironmental Engineering* **124(5)**:439-449.

Indraratna, B., Lackenby, J. & Christie, D. (2005) Effect of confining pressure on the degradation of ballast under cyclic loading. *Géotechnique* **55(4)**:325-328.

International Union of Railways (1994) UIC code 719R. Earthworks for track bed layers for railway lines.

International Union of Railways (2017) *High-speed lines in the world*. Paris.

Iwnicki, S. (2006) *Handbook of Railway Vehicle Dynamics.* CRC Press.

Jenkins, H. H., Stephenson, J. E. & Clayton, G. A. (1974) Effect of track and vehicle parameters on wheel/rail vertical dynamic forces. *Railway engineering journal* **3(2)**:2-16.

Ju, S.-H., Lin, H.-T. & Huang, J.-Y. (2009) Dominant frequencies of train-induced vibrations. *Journal of Sound and Vibration* **319(1–2)**:247-259.

Ju, S. H., Liao, J. R. & Ye, Y. L. (2010) Behavior of ground vibrations induced by trains moving on embankments with rail roughness. *Soil Dynamics and Earthquake Engineering* **30(11)**:1237-1249.

Kaplan, E. L. & Meier, P. (1958) Nonparametric Estimation from Incomplete Observations. *Journal of the American Statistical Association* **53(282)**:457-481.

Kerr, A. D. (1964) Elastic and Viscoelastic Foundation Models. *Journal of applied mechanics* **31(3)**:491-498.

Kerr, A. D. (2000) On the determination of the rail support modulus k. *International Journal of Solids and Structures* **37(32)**:4335-4351.

Kim, H. (2016) Trackside measurement of critical zones in railway tracks. In *School of Engineering*. University of Birmingham, pp. 236.

Knothe, K. L. & Grassie, S. L. (1993) Modelling of Railway Track and Vehicle/Track Interaction at High Frequencies. *Vehicle System Dynamics* **22(3-4)**:209-262.

Koroma, S. (2015) *Static tests on railpads*.

Kouroussis, G., Connolly, D. P., Forde, M. & Verlinden, O. (2013) Train speed calculation using ground vibrations. *Proceedings of the Institution of Mechanical Engineers, Part F: Journal of Rail and Rapid Transit* **229(5)**:466-483.

Kouroussis, G., Connolly, D. P. & Verlinden, O. (2014) Railway-induced ground vibrations – a review of vehicle effects. *International Journal of Rail Transportation* **2(2)**:69-110.

Lackenby, J., Indraratna, B., McDowell, G. R. & Christie, D. (2007) Effect of confining pressure on ballast degredation and deformation under cyclic triaxial loading. *Géotechnique* **57(6)**:527-536.

Lamas-Lopez, F., Alves-Fernandes, V., Cui, Y. J., Costa D'Aguiar, S., Calon, N., Canou, J. C., Tang, A. M. & Roubinet, A. (2014) Assessment of the double Integration method using accelerometers data for conventional railway platforms. In *Proceedings of the second international conference on railway technology: Research, development and maintenance*. (Pombo, J. (ed) Civil-Comp Press, Ajaccio.

Le Pen, L., Bhandari, A. & Powrie, W. (2014a) Sleeper End Resistance of Ballasted Railway Tracks. *Journal of Geotechnical and Geoenvironmental Engineering* **140(4)**:1-14.

Le Pen, L., Milne, D., Thompson, D. & Powrie, W. (2016) Evaluating railway track support stiffness from trackside measurements in the absence of wheel load data. *Canadian Geotechnical Journal* **53(7)**:1156-1166.

Le Pen, L., Watson, G., Powrie, W., Yeo, G., Weston, P. & Roberts, C. (2014b) The behaviour of railway level crossings: Insights through field monitoring. *Transportation Geotechnics* **1(4)**:201-213.

Li, D. & Davis, D. (2005) Transition of Railroad Bridge Approaches. *Journal of Geotechnical and Geoenvironmental Engineering* **131(11)**:1392-1398.

Li, D. & Selig, E. T. (1998a) Method for railroad track foundation design. I: Development. *Journal of Geotechnical and Geoenvironmental Engineering* **124(4)**:316-322.

Li, D. & Selig, E. T. (1998b) Method for railroad track foundation design. II: Applications. *Journal of Geotechnical and Geoenvironmental Engineering*.

Li, D., Thompson, R. & Kalay, S. (2002) Development of continuous lateral and vertical track stiffness measurement techniques In *Proceedings of*

Railway Engineering 2002 - 5th International Conference & Exhibition.

Lombaert, G., Degrande, G., François, S. & Thompson, D. J. (2015) Ground-Borne Vibration due to Railway Traffic: A Review of Excitation Mechanisms, Prediction Methods and Mitigation Measures In *Proceedings of Noise and Vibration Mitigation for Rail Transportation Systems* (Nielsen, J. C. O., Anderson, D., Gautier, P.-E., Iida, M., Nelson, J. T., Thompson, D., Tielkes, T., Towers, D. A., andDe Vos, P. (eds)). Springer Berlin Heidelberg vol. 126, pp. 253-287.

Lombaert, G., Degrande, G., Kogut, J. & François, S. (2006) The experimental validation of a numerical model for the prediction of railway induced vibrations. *Journal of Sound and Vibration* **297(3–5)**:512-535.

Lopez-Caballero, F., Bonilla, F., Costa D'Aguiar, S. & Voivret, C. (2016) Evaluation of the Dynamic Behaviour of Railway Soil Foundations using In-Situ Buried Instrumentation. In *The Third International Conference on Railway Technology: Research, Development and Maintenance*. (Pombo, J. (ed) Civil-Comp Press, Cagliari.

Lu, M. & McDowell, G. (2010) Discrete element modelling of railway ballast under monotonic and cyclic triaxial loading. *Géotechnique* **60(6)**:459-467.

Lundqvist, A. & Dahlberg, T. (2005) Load impact on railway track due to unsupported sleepers. *Proceedings of the Institution of Mechanical Engineers, Part F: Journal of Rail and Rapid Transit* **219(2)**:67-77.

McDowell, G. R. & Li, H. (2016) Discrete element modelling of scaled railway ballast under triaxial conditions. *Granular Matter* **18(3)**:66.

Milne, D., Le Pen, L., Thompson, D. J. & Powrie, W. (2016a) Measurement of ballast grain acceleration at track level. *The Journal of the Permanent Way Instituion* **134(4)**.

Milne, D., Le Pen, L., Watson, G., Thompson, D., Powrie, W., Hayward, M. & Morley, S. (2016b) Proving MEMS Technologies for Smarter Railway Infrastructure. *Procedia Engineering* **143**:1077-1084.

Milne, D. R. M., Le Pen, L. M., Thompson, D. J. & Powrie, W. (2017) Properties of train load frequencies and their applications. *Journal of Sound and Vibration* **397**:123-140.

Mishra, D., Qian, Y., Huang, H. & Tutumluer, E. (2014) An integrated approach to dynamic analysis of railroad track transitions behavior. *Transportation Geotechnics* **1(4)**:188-200.

Muramoto, K., Nakamura, T. & Sakurai, T. (2012) A Study of the Effect of Track Irregularity Prevention Methods for the Transition Zone between Different Track Structures. *Quarterly Report of RTRI* **53(4)**:211-215.

Murray, C. A., Take, W. A. & Hoult, N. A. (2014) Measurement of vertical and longitudinal rail displacements using digital image correlation. *Canadian Geotechnical Journal* **52(2)**:141-155.

Network Rail (2016) Network Rail Standardised Tasks: Lifting and Packing. London.

Network Rail High Speed (2013) Discussion on track defects and maintenance. (Milne, D. (ed).

Ni, S.-H., Huang, Y.-H. & Lo, K.-F. (2011) An automatic procedure for train speed evaluation by the dominant frequency method. *Computers and Geotechnics* **38(4)**:416-422.

Nielsen, J., Berggren, E., Lölgen, T. & Müller, R. (2013) Overview of methods for measurement of track irregularities. *RIVAS Railway Induced Vibration Abatement Solutions Collaborative Project*.

O'Riordan, N. (2003) Channel Tunnel Rail Link section 1: ground engineering. *Proceedings of the ICE-Civil Engineering* **156(6)**:28-31.

O'Riordan, N. & Kirk, M. (2007) Channel Tunnel Rail Link section 2: north Thames marshes. *Proceedings of the ICE-Civil Engineering* **160(6)**:19-23.

O'Riordan, N. & Phear, A. (2001) Design and construction control of ballasted track formation and subgrade for high speed lines In *Proceedings of Procceding of the International Conference Railway Engineering 2001*.

Office of Rail and Road (2017) *UK Rail Industry Financial Information 2015-16*. London.

Oppenheim, A. V. & Schafer, R. W. (1975) *Digital signal processing.* Prentice-Hall.

Ordnance Survey (2015) EDINA Digimap Ordnance Survey Service, .

Paixão, A., Alves Ribeiro, C., Pinto, N., Fortunato, E. & Calçada, R. (2014) On the use of under sleeper pads in transition zones at railway underpasses: experimental field testing. *Structure and Infrastructure Engineering*:1-17.

Permanent Way Institution (2001) *Plain Line Rail Maintenance of Track* 7edn. London, Permanent Way Institution.

Plasser & Theurer (2016) *Faster to higher quality: Levelling, lifting, lining and tamping machines.*, See https://www.plassertheurer.com/en/machines-systems/tamping.html2016).

Priest, J. & Powrie, W. (2009) Determination of Dynamic Track Modulus from Measurement of Track Velocity during Train Passage. *Journal of Geotechnical and Geoenvironmental Engineering* **135(11)**:1732-1740.

Priest, J. A., Powrie, W., Le Pen, L., Mak, P. & Burstow, M. C. (2012) The effect of enhanced curving forces on the behaviour of canted ballasted track. *Proceedings of the Institution of Mechanical Engineers, Part F: Journal of Rail and Rapid Transit* **227(3)**:229-244.

Priest, J. A., Powrie, W., Yang, L. A., Grabe, P. J. & Clayton, C. R. I. (2010) Measurements of transient ground movements below a ballasted railway line. *Géotechnique* **60**:667-677.

Rail Link Engineering (1998) Channel Tunnel Rail Link Systemwide specification: Ballast. Union Railways.

Rail Safety and Standards Board (2011)GC/RT5021 Track System Requirements. London.

Raymond, G. P. (1985) Analysis of track support and determination of track modulus. *Transportation Research Record* **1022**:80-90.

Riley, K. F., Hobson, M. P. & Bence, S. J. (2002) *Mathematical Methods for Physics and Engineering: A Comprehensive Guide.* 2 edn. Cambridge, Cambridge University Press.

Sato, Y. (1995) Japanese Studies on Deterioration of Ballasted Track. *Vehicle System Dynamics* **24(sup1)**:197-208.

Selig, E. T. & Waters, J. M. (1994) *Track geotechnology and substructure management.* London, Telford.

Sharpe, P. (2000) Trackbed Investigation. *PWI Journal* **118(3)**:238-254.

Sheng, X., Jones, C. J. C. & Thompson, D. J. (2003) A comparison of a theoretical model for quasi-statically and dynamically induced environmental vibration from trains with measurements. *Journal of Sound and Vibration* **267(3)**:621-635.

Sheng, X., Jones, C. J. C. & Thompson, D. J. (2004) A theoretical study on the influence of the track on train-induced ground vibration. *Journal of Sound and Vibration* **272(3–5)**:909-936.

Shenton, M. J. (1984) Ballast deformation and track deterioration In *Proceedings of Track Technology*, pp. 253-265.

Shih, J. Y., Thompson, D. J. & Zervos, A. (2017) The influence of soil nonlinear properties on the track/ground vibration induced by trains running on soft ground. *Transportation Geotechnics* **11**:1-16.

Soper, D., Baker, C., Jackson, A., Milne, D. R., Le Pen, L., Watson, G. & Powrie, W. (2017) Full scale measurements of train underbody flows and track forces. *Journal of Wind Engineering and Industrial Aerodynamics* **169**:251-264.

Squicciarini, G., Thompson, D. J., Toward, M. G. & Cottrell, R. A. (2016) The effect of temperature on railway rolling noise. *Proceedings of the Institution of Mechanical Engineers, Part F: Journal of Rail and Rapid Transit* **230(8)**:1777-1789.

Stark, T. D. & Wilk, S. T. (2015) Root cause of differential movement at bridge transition zones. *Proceedings of the Institution of Mechanical Engineers, Part F: Journal of Rail and Rapid Transit*.

Steenbergen, M. J. M. M. (2013) Physics of railroad degradation: The role of a varying dynamic stiffness and transition radiation processes. *Computers & Structures* **124**:102-111.

Sussman, T., Ebersöhn, W. & Selig, E. (2001) Fundamental Nonlinear Track Load-Deflection Behavior for Condition Evaluation. *Transportation Research Record: Journal of the Transportation Research Board* **1742**:61-67.

Talbot, A. N. (1980) *Stresses in Railroad Track: The Talbot Reports : the Reprinted Reports from A.R.E.A. Bulletins of the Special Committee on Stresses in Railroad Track 1918-1940.* American Railway Engineering Association.

Thanagasundram, S. & Schlindwein, F. S. (2006) Comparison of integrated micro-electrical-mechanical system and piezoelectric accelerometers for machine condition monitoring. *Proceedings of the Institution of Mechanical Engineers, Part C: Journal of Mechanical Engineering Science* **220(8)**:1135-1146.

Thompson, D. (2009) Railway noise and vibration mechanisms, modelling and means of control. 1st edn. Elsevier, Oxford, UK, pp. xv, 518 p.

Timoshenko, S. & Langer, B. F. (1932) Stresses in railroad track. *ASME Transactions* **54**:277-293.

Track Stiffness Working Group (2016) *A guide to track stiffness.* Southampton, University of Southampton.

Triepaischajonsak, N., Thompson, D. J., Jones, C. J. C., Ryue, J. & Priest, J. A. (2011) Ground vibration from trains: experimental parameter characterization and validation of a numerical model. *Proceedings of the Institution of Mechanical Engineers, Part F: Journal of Rail and Rapid Transit* **225(2)**:140-153.

Van Dyk, B. J., Edwards, J. R., Dersch, M. S., Ruppert Jr, C. J. & Barkan, C. P. L. (2017) Evaluation of dynamic and impact wheel load factors and their application in design processes. *Proceedings of the Institution of Mechanical Engineers, Part F: Journal of Rail and Rapid Transit* **231(1)**:33-43.

Varandas, J. N., Hölscher, P. & Silva, M. A. (2014) Settlement of ballasted track under traffic loading: Application to transition zones. *Proceedings of the Institution of Mechanical Engineers, Part F: Journal of Rail and Rapid Transit* **228(3)**:242-259.

Watson, G. (2016) Photographs from lineside monitoring on HS1.

Weather Underground (2015) *Weather history for Hollingbourne Kent*, See https://www.wunderground.com/personal-weather-station/dashboard?ID=IKENTHOL2.

Weaver, W., Timoshenko, S. P. & Young, D. H. (1990) *Vibration Problems in Engineering.* John Wiley & Sons.

Weston, P., Roberts, C., Yeo, G. & Stewart, E. (2015) Perspectives on railway track geometry condition monitoring from in-service railway vehicles. *Vehicle System Dynamics* **53(7)**:1063-1091.

Weston, P. F., Ling, C. S., Roberts, C., Goodman, C. J., Li, P. & Goodall, R. M. (2007) Monitoring vertical track irregularity from in-service railway vehicles. *Proceedings of the Institution of Mechanical Engineers, Part F: Journal of Rail and Rapid Transit* **221(1)**:75-88.

Wheeler, L. N., Take, W. A. & Hoult, N. A. (2016a) Measurement of rail deflection on soft subgrades using DIC. *Proceedings of the Institution of Civil Engineers - Geotechnical Engineering* **169(5)**:383-398.

Wheeler, L. N., Take, W. A. & Hoult, N. A. (2016b) Performance assessment of peat rail subgrade before and after mass stabilization. *Canadian Geotechnical Journal* **54(5)**:674-689.

White, D. J., Take, W. A. & Bolton, M. D. (2003) Soil deformation measurement using particle image velocimetry (PIV) and photogrammetry. *Géotechnique* **53(7)**:619-631.

Yang, L. A., Powrie, W. & Priest, J. A. (2009) Dynamic stress analysis of a ballasted railway track bed during train passage. *Journal of Geotechnical and Geoenvironmental Engineering* **135(5)**:680-689.

Yang, Y.-B., Yau, J.-D. & Hsu, L.-C. (1997) Vibration of simple beams due to trains moving at high speeds. *Engineering Structures* **19(11)**:936-944.

Zhang, X., Thompson, D. J. & Squicciarini, G. (2016) Sound radiation from railway sleepers. *Journal of Sound and Vibration* **369**:178-194.

Appendix A Software

This research has involved the collection, processing and development of new techniques for analysing track vibration data obtained using geophones and accelerometers. Signal processing and analysis was carried out in MATLAB. New processing scripts and functions and adaptions of existing ones used in this research are included with the thesis. A brief description of each script and function is supplied here.

Processor.m – Script to batch process and analyse track vibration data from multiple train passages obtained using different sensor types by calling the various functions listed below.

geoPro.m – Function to calibrate, filter and integrate geophone data.

accPro.m - Function to calibrate, then filter and integrate accelerometer data (twice).

TrainPassTime.m - Function to determine the train passing time, and identify the first and last wheels in a train.

NVPF.m - Function to identify the vehicle passing frequency.

Nfreqs.m - Function to find the frequency and magnitude of the first N dominant trainload frequencies.

TrainTypeFinder.m - Function to identify the Train Type in a vibration record.

TrackCDF.m – Function to characterise the range of total and downward movement.

MagRatModTG.m - Function to determine the track system support modulus in the frequency domain using train geometry.

MagRatModVG.m - Function to determine the track system support modulus in the frequency domain using vehicle geometry.

LoadFinder.m – Function to estimate the applied wheel load.

Appendix B Fault finding from track geometry measurement

Track defects are identified by applying tolerance thresholds to measured track geometry. Severe geometry deviations due to poor track quality and from isolated defects will be identified during this process. This is appropriate for operational reasons as faults from both isolated defects and poor track quality may be hazardous. However, this approach does not distinguish between isolated faults and poor track, nor will it identify small geometry deviations on good quality track that might exhibit the characteristics of an isolated defect that may deteriorate until they become a hazard. To identify those from track geometry data, it may be more appropriate to use a variable rather than an absolute threshold and account for track quality.

A spatially varying threshold G_D can be defined using a number N of standard deviations over a length of length of track σ.

$$|G_D| \geq |N\sigma| \qquad (B1)$$

The length of track and number of deviations that define the threshold will affect defect identification. Network Rail use 1/8th mile (200 m) sections to define 'Track Quality', but other lengths may be more appropriate.

Here, results from a track inspection survey have been compared with analysis of track geometry measurements to test the use of a variable threshold for identifying track defects. The down line between the country portal of the North Downs Tunnel and Boxley tunnel (57.63-60.13 km) was surveyed. Within the section there are transition zones, combinations of horizontal and vertical curves, shallow and deep UTXs, changes in the surface geology (grey chalk to gault clay), rail welds and an area of water abstraction (from a deep sandstone aquifer 130 m beneath the clay). 13 locations affected by visible localised ballast attrition were recorded as observed faults. Seven of these faults were in the vicinity of shallow UTXs. Only one of these observable defects was associated with a geometry deviation that would exceed a typical maintenance absolute threshold.

Twist and longitudinal level data for both rails were analysed using the variable threshold. The threshold was defined according to Eq.(B1) with $N = 3$ for a standard deviation σ over 200 m of track centred on the position of interest. This is different from the normal track quality standard, which considers 200 m blocks rather than a running standard deviation, as proposed here. Any geometry deviation that exceeded that threshold was recorded as an identified fault. The TRC data supplied by NRHS, variable thresholds, and locations of the observed or identified features and any major features, such as under-track crossings are presented in Figure B 1.

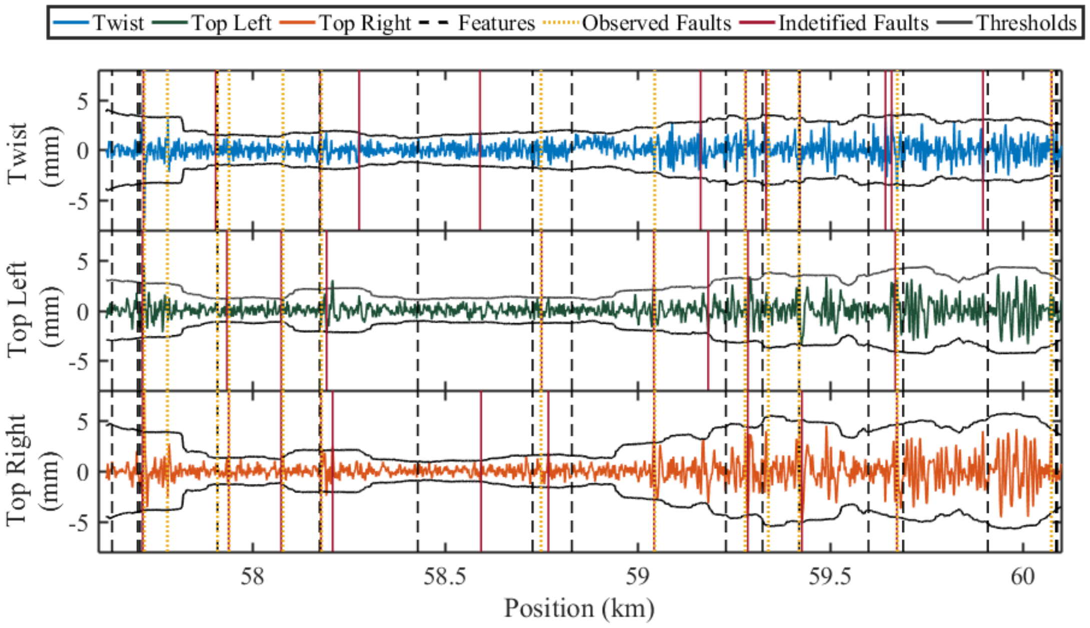

Figure B 1 Twist, top left and top right TRC data between the North Downs and Boxley tunnels, showing the locations of UTXs, adaptive thresholds for isolated defects, locations observed to have characteristics associated with track defects and locations with possible defects identified using the adaptive threshold.

From the twist and top geometry, 12 of 13 observed defects were identified using the variable threshold. The false negative was close to a more severe defect. Proximity to a more severe defect would increase the local standard deviation making it less likely that less severe defects would exceed the local threshold. Six non-observed faults, possible false positives, were also identified from the track geometry using the variable threshold. Using other values of N and different lengths of track may give different results.

Figure B 2 shows how the track geometry data is distributed for each centred 200 m section of track at every 0.2 m measurement point. Symmetry about the origin suggests this data can be assumed to be normally distributed; this was confirmed by analysing quantile-quantile plots and using chi-squared and Kolmogorov-Smirnov tests. This means that *N* is a standard score and for *N*=3 an isolated defect could be defined as any geometry deviation that exceeds 99.7% of the expected range of deviation within a 200 m section of track.

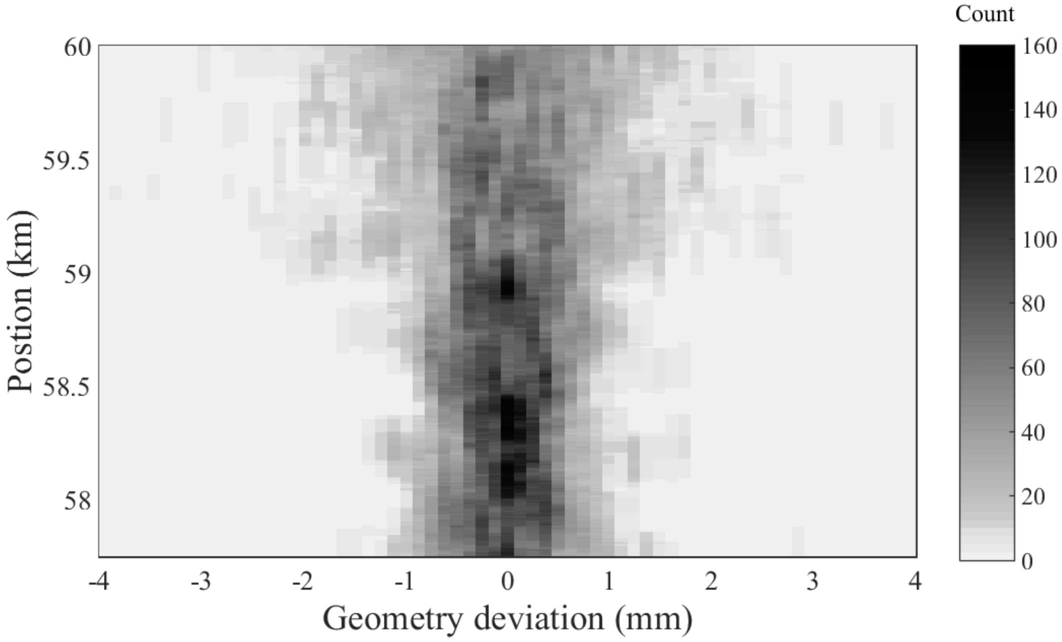

Figure B 2 Histogram for the vertical track geometry within local 200 m sections along the track in between the North Downs and Boxley tunnels.

Although this method was not used to identify the sites used as case studies in this research, which were selected by NRHS, all the geometry defects for the sites studied would have been identified using the variable threshold. NRHS have implemented this method on other parts of the route and confirm that this method has proved very effective for identifying areas where track performance is imperfect, before they are identified using conventional absolute thresholds.

Appendix C Study of ballast vibration

Parts of this appendix have been published in (Milne et al., 2016a).

C.1 Instrumented grains

Four instrumented ballast grains were made for this study. Axivity AX3 sensors Figure C 1(a), were inserted into slots drilled into each ballast stone Figure C 1(b) using a diamond tipped coring bit. Coolant was required to prevent damage to the drill and ballast grain and to facilitate cutting. An AX3 device was sealed into the slots using epoxy resin. The ballast stones were painted white for ease of identification on the track, as shown in Figure C 1(c).

Figure C 1 (a) AXIVITY AX3, (b) Ballast grain with slot for sensor (c) Instrumented grain ready for use.

Each ballast grain (Figure C 2) had to be large enough to accept a slot suitable to receive the MEMS device enclosure without compromising its integrity. The grains selected were at the upper 30% sieve size of a typical UK ballast gradation, with all grains passing through a 50 mm sieve. Embedding the sensor causes a change Δm in the mass of the grain from m_1 to m_2, as the device and resin are of lower density than the parent rock. The changes in mass are recorded in Table C 1, together with the volume of each grain V. The reduction in mass was less than 9% for all grains.

Figure C 2 Four instrumented ballast grains.

Table C 1 Table of grain volumes and masses.

Grain	V (m^3)	m_1 (g)	m_2 (g)	Δm (g)	% change
1	1.12×10^{-4}	298	281	17	-5.7
2	1.26×10^{-4}	334	316	18	-5.4
3	1.14×10^{-4}	301	278	23	-7.6
4	0.57×10^{-4}	198	181	17	-8.6

MEMS accelerometers operate down to 0 Hz and therefore “see” gravity. The calibration of each sensor was checked by aligning each measurement axis with gravity to confirm a reading of 9.81 m/s^2. This baseline reading allowed the three orthogonal axes of measurement to be transformed into one vertical and two horizontal axes from any initial orientation.

C.2 Study sites

These instrumented grains have been deployed in two arrangements at the Crissmill plain line site. In the first arrangement, the four grains were placed onto the surface of the ballast bed, in a line between a pair of sleepers between the running rails, as shown in Figure C 3(a). In the second the instrumented grains were pressed firmly into the surface of the ballast bed closer to the 6-foot side as shown in Figure C 3(b). Placement of the grains controls whether the measurements are for a grain vibrating on top of the ballast bed or are more representative of the surface of the ballast bed. The measurements of ballast grain acceleration presented are useful for understanding ballast vibration and how this may contribute to ballast flight and ballast stability.

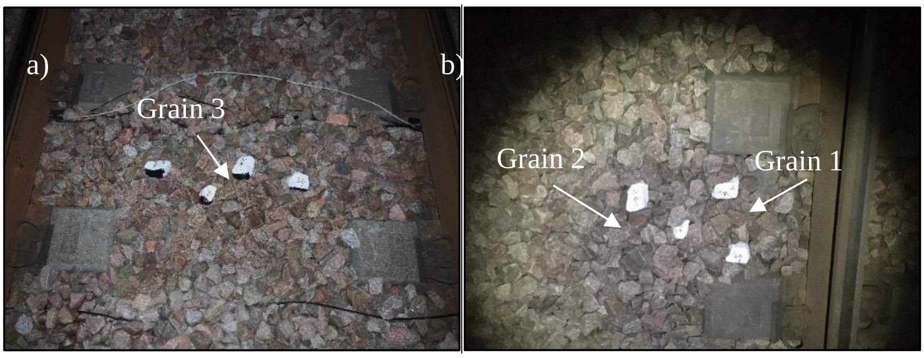

Figure C 3 Photographs of instrumented grains (a) placed on the surface of the ballast bed and (b) pressed into the surface of the ballast bed.

C.2.1 Ballast vibration

The subsequent figures show examples of ballast bed vibration data, sampled at 400 Hz as vertical acceleration time histories and corresponding spectra for acceleration from ballast grains 1 and 2 in the second arrangement (Figure C 3(b)). Grains 1 and 2 were positioned 250 and 500 mm away from the 6-foot rail respectively. Both were 200 mm away from the leading edge of the second sleeper. Typical results are presented for each train type: Figure C 4 and Figure C 5 for the Javelin, Figure C 5 and Figure C 6 for the Eurostar and Figure C 8 and Figure C 9 for the Velaro.

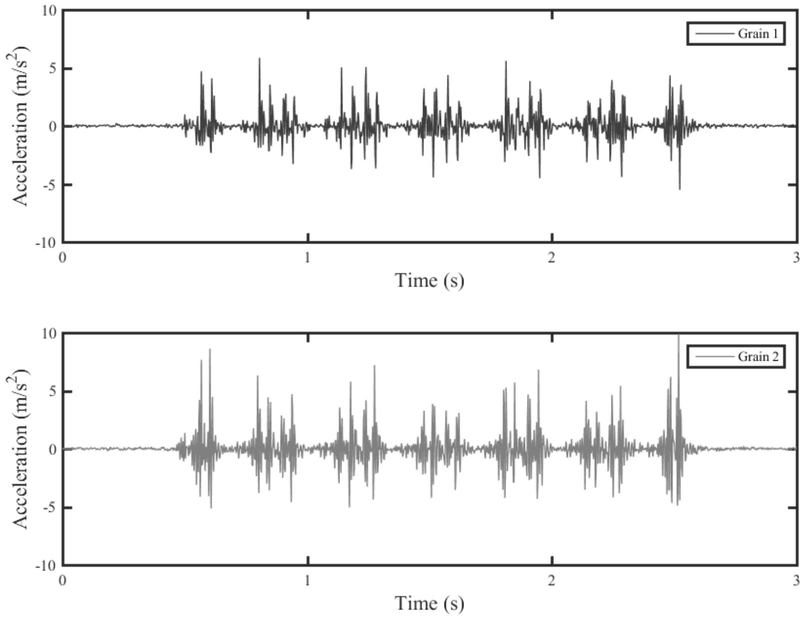

Figure C 4 Ballast grain acceleration due to a Javelin from (a) Grain 1 and (b) Grain 2.

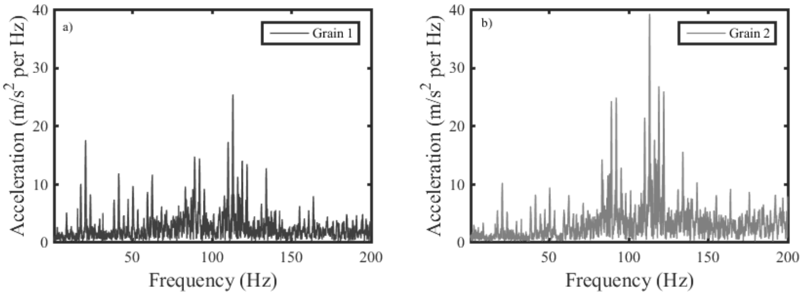

Figure C 5 Ballast grain acceleration spectra for (a) Grain 1 and (b) Grain 2 for a Javelin.

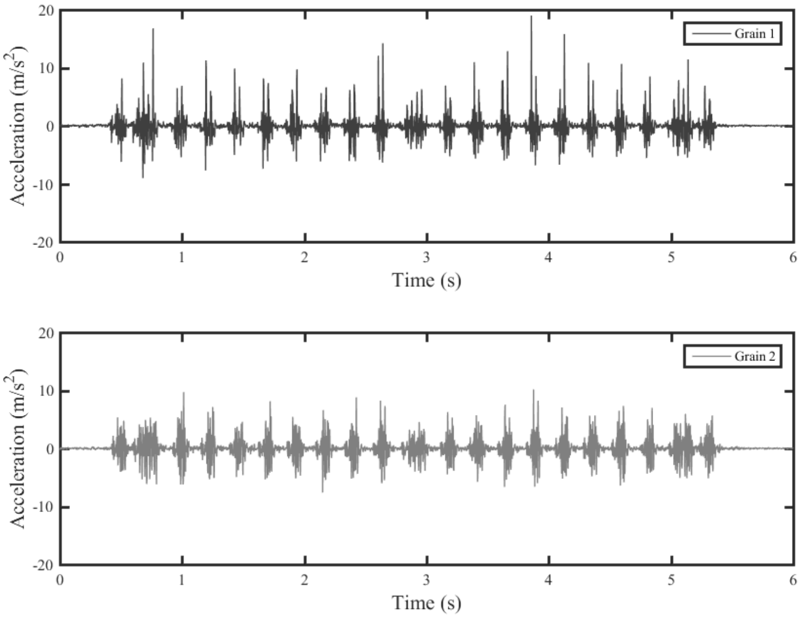

Figure C 6 Ballast grain acceleration due to a Eurostar from (a) Grain 1 and (b) Grain 2.

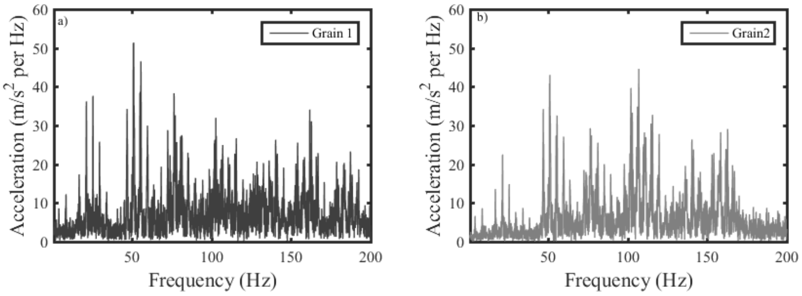

Figure C 7 Ballast grain acceleration spectra for (a) Grain 1 and (b) Grain 2 for a Eurostar.

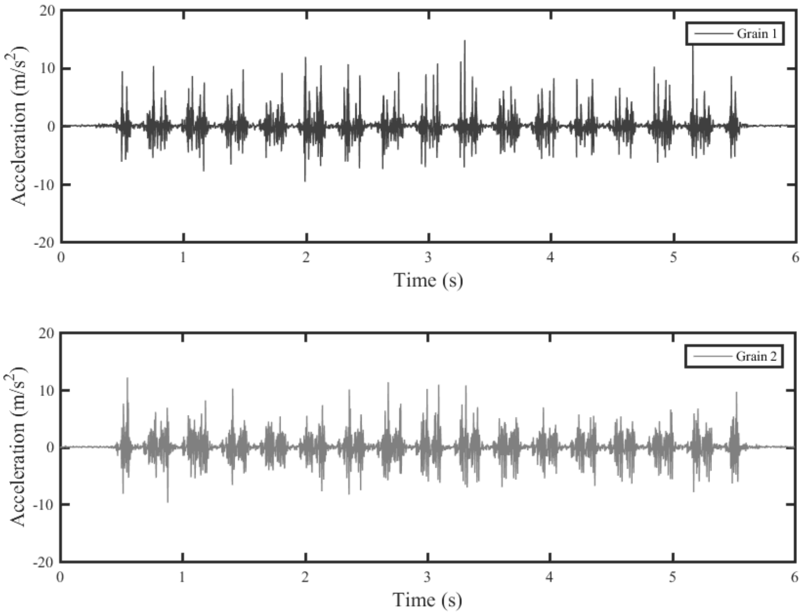

Figure C 8 Ballast grain acceleration due to a Velaro from (a) Grain 1 and (b) Grain 2.

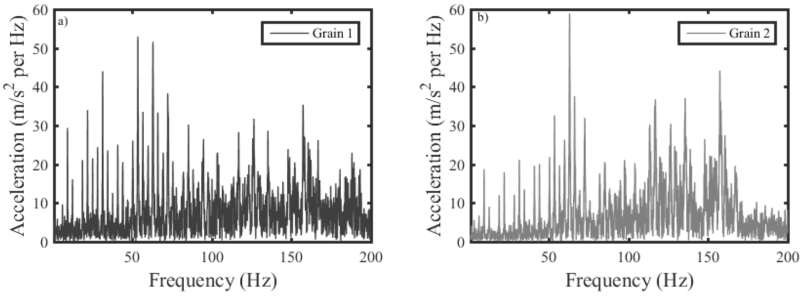

Figure C 9 Ballast grain acceleration spectra for (a) Grain 1 and (b) Grain 2 for a Velaro.

The ballast grain acceleration signals have similarities to measurements made on the sleeper. The signals have periodic characteristics during the passage of train due to the train geometry. This can be seen in the acceleration and velocity spectra where the spectral peaks occur close to the vehicle-passing frequency. Variations in the amplitude of acceleration can be seen along the train. The typical range of acceleration is less than ±5 m/s^2 for Javelin and less than ±10 m/s^2 for the Eurostar and Velaro, although certain peaks for these trains did exceed 10 m/s^2.

Ballast grain acceleration is significant at higher frequencies, up to 180 Hz, for all trains. The greatest amplitudes were between 80 and 120 Hz for the Javelin (~ 60 m/s). The amplitudes at frequencies less than 80 Hz were more significant for Grain 1, which was nearer the rail than for Grain 2. For the faster and heavier Eurostar and Velaro trains (~75 m/s) the amplitudes of frequencies less than 80 Hz were more significant than they were for the slower and lighter Javelin trains. There was another region of high amplitude frequency content between 110 Hz and 180 Hz.

Figure C 10 presents data from when the instrumented grain was placed onto rather than pressed into the ballast surface. This data is for a Javelin train. Here the amplitudes of the frequencies in the 60-80 Hz range are more significant than when the grain was pressed into the ballast surface.

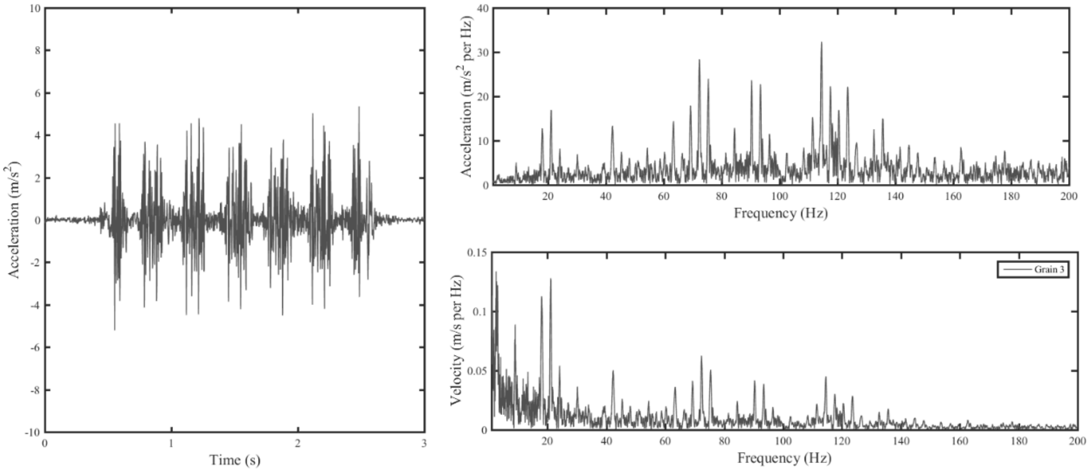

Figure C 10 Ballast grain (a) acceleration, (b) acceleration spectrum and (c) velocity spectrum from a grain placed on top of the ballast bed for a Javelin.

The acceleration data obtained for a Javelin has been integrated to obtain ballast velocity, given in Figure C 11. This shows that the highest amplitudes for velocity are at frequencies of less than 50 Hz, although the amplitudes at frequencies between 80 and 120 Hz are still significant.

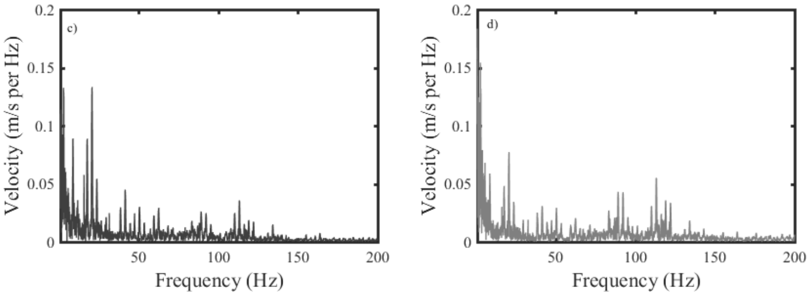

Figure C 11 Ballast grain velocity spectra for (a) Grain 1 and (b) Grain 2 for a Javelin.

C.3 Peak acceleration and velocity

Although ballast vibration beneath a passing train is a transient process, the signal will tend to have periodic characteristics from the repetition of wheel loads within a train. Peak acceleration (and velocity) levels are thought to be significant for ballast flight and stability. This will be discussed later. However, selecting an appropriate value for peak acceleration or velocity needs thought. The ballast grain acceleration measurements have shown that ballast acceleration and velocity are frequency dependent. This means that different mechanisms of vibration are important, and although the peak acceleration could be significant and may exceed gravitational acceleration, the vibration may be of short duration and not cause significant movement.

Despite the periodic characteristics of the acceleration signal, there is variability. Although the peak amplitude in the signal can be identified, it may have influenced by wheel flats or other impacts leading to events with increased accelerations. These events may be important, but it is also important to have data that are representative of the typical vibration levels for the train. A measure of the average peak vibration (for a given frequency range) is needed. This could be obtained by taking an average of the peak values exceeding a threshold or by examining how acceleration level is distributed in the measurements (see Figure C 12) and selecting an appropriate probability value to represent the peak acceleration level (e.g. P=0.025 and 0.975). This is similar to the method prosed for interpreting track deflection signals in proposed in Chapter 6. This method has been used to determine the peak upward and downward ballast acceleration from Grain 1 and Grain 2 for each passage recorded for every train type.

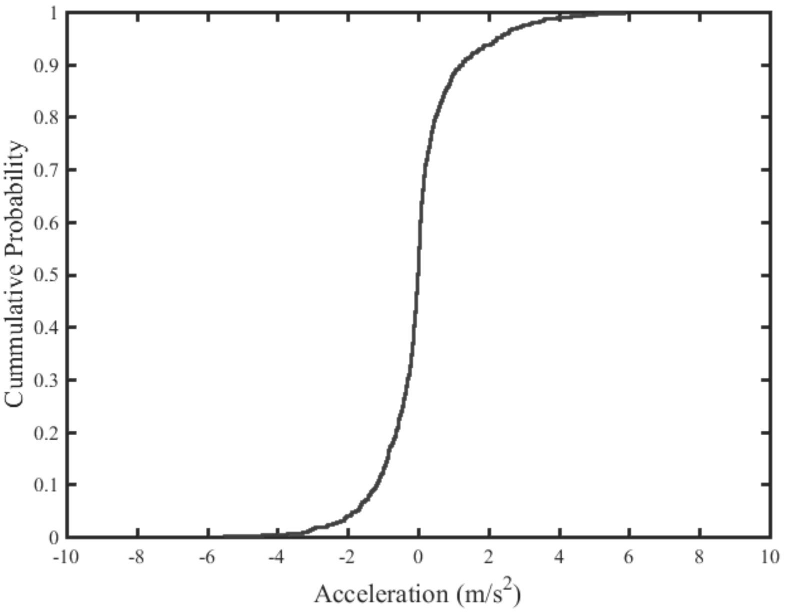

Figure C 12 Cumulative distribution of ballast grain acceleration during passage of a Javelin.

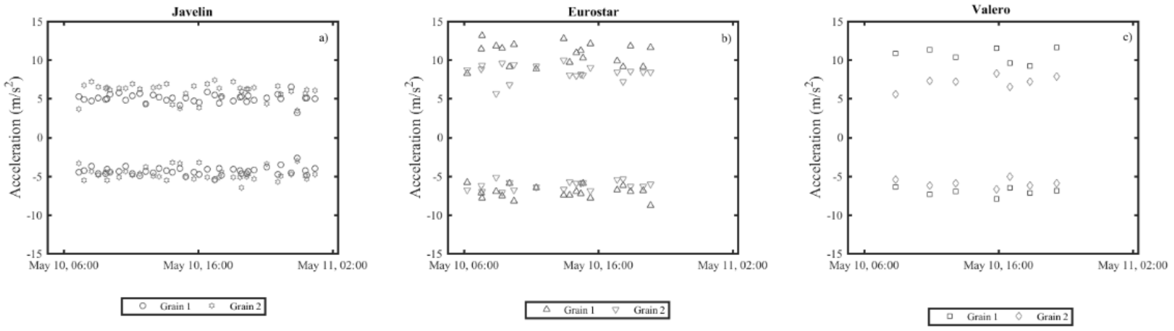

Figure C 13 Typical peak grain acceleration for (a) Javelin, b Eurostar and (c) Velaro. Found from the CDF for ballast grain acceleration using P=0.025 and 0.975 for typical peak upward and downward grain acceleration.

The results in Figure C 13 confirm that the typical peak level of upward acceleration is around 5-6 m/s^2 for Javelin and 8-15 m/s^2 for the Eurostar and Velaro. The downward levels are 4-5 m/s^2 for Javelin and 6-8 m/s^2 for the Eurostar and Velaro. The downward result is important as although the upward results were in excess of gravitation acceleration this result indicates the particles were never in free fall, and thus in all likelihood did not lift.

C.4 Ballast lift

One objective of measuring ballast grain acceleration was to understand whether the mechanical vibration of the track was sufficient to initiate lift and cause ballast flight. This section considers how low frequency track vibration could induce lift of a ballast grain. Soper et al. (2017) state that: *when the imposed mechanical force from track bed vibration exceeds the weight, a ballast grain may lift from the track bed or off a sleeper*.

There are three possible locations on the track where mechanical vibration may influence the flight of a ballast grain

- ballast grain *in* the surface of the ballast bed;
- ballast grain *on* the surface of the ballast bed;
- ballast grain *on* a sleeper.

The first scenario is challenging to analyse as the forces acting on a ballast grain will tend to be resisted by the surrounding grains, making it difficult to distinguish between the behaviour of the ballast bed and individual grains. The second and third are similar to each other as only the self-weight of the ballast grain is resisting lift. The condition of the forces exceeding the weight of the particle is necessary but not sufficient for ballast flight as the particle needs to be moving with sufficient velocity when lifted for the potential for significant flight/lift. This means a particle needs to be accelerated for sufficient duration or experience significant acceleration.

Unless lift is initiated a ballast grain will vibrate as part of the track system. For normal mechanical vibration, the velocity v_b and acceleration a_b of a ballast grain on a sleeper or the surface of the ballast bed are the same as the track system v_t and a_t.

$$v_b = v_t \;\&\; a_b = a_t$$

Lift is possible if the upward acceleration of the track system and the ballast grain exceed gravitational acceleration g, as self-weight of particle has been exceeded

$$a_t \geq g$$

However, a grain will only lift off if the grain velocity is greater than the track system velocity

$$v_b \geq v_t$$

In the absence of aerodynamic lift forces the track system cannot do additional work on a ballast grain, nor can a grain propel itself. This means lift is only possible if the downward acceleration of the track system is greater than downward acceleration of the ballast grain due to gravity.

$$a_t \leq -g \; \& \; a_b = -g$$

Otherwise the particle will move with the sleeper or track bed. If the grain lifts with velocity v_i the grain velocity can be found during flight from:

$$v_b = v_i - gt$$

These conditions are illustrated in Figure C 14 using measurements from an instrumented grain caused to lift by an instrumented launch platform.

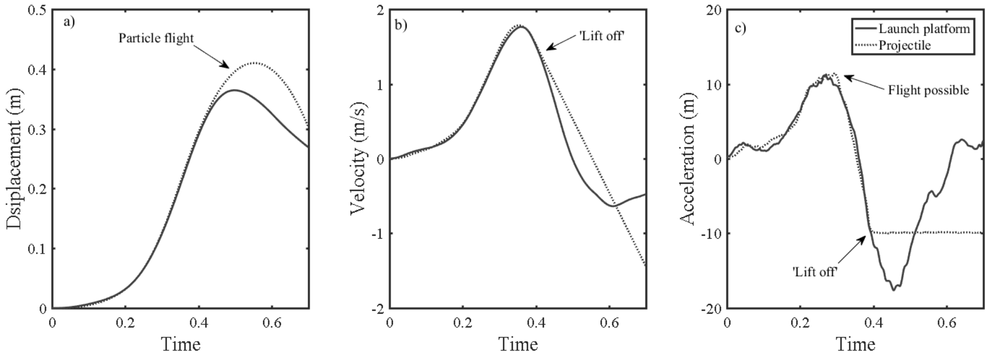

Figure C 14 Particle and platform motion when particle is thrown by an instrumented platform.

The BOEF model for track deflection can be used to study the influence of low frequency track vibration on ballast flight. The beam-on-elastic-foundation is a routinely used model for low frequency track deflection due to moving loads.

$$w(t) = -\frac{P}{2kL} \mathrm{e}^{-\frac{|vt|}{L}} \left(\cos\left(\frac{|vt|}{L}\right) + \sin\left(\frac{|vt|}{L}\right) \right)$$

where $L = \sqrt[4]{\frac{4EI}{k}}$, *k* is the track system support modulus *EI* is the bending stiffness of the rail, *w* is the track deflection, *P* is the applied load, *v* is the train speed and *t* is time.

Differentiating the above allows investigation of sleeper and track bed motion to determine whether the conditions necessary for ballast flight are met, whether lift occurs and determination of the height of flight for a particle on the track bed or on a sleeper.

There are several independent variables in the BOEF model that relate to the speed and amplitude of the applied load (P, v) and the track bed properties (k, EI & L). To simplify the analysis, potential for ballast flight has been investigated different prescribed sleeper deflections δ by setting:

$$\delta = \frac{P}{2kL}$$

and assuming typical system properties for a high-speed railway of k=40 MN/m^2 and EI of 6.42 MNm^2 for a UIC 60 rail such that L=0.89, for current and proposed operating speeds. Figure C 15 shows the particle and track motion when ballast flight conditions are met for 5 mm track deflection due to 80 m/s moving load.

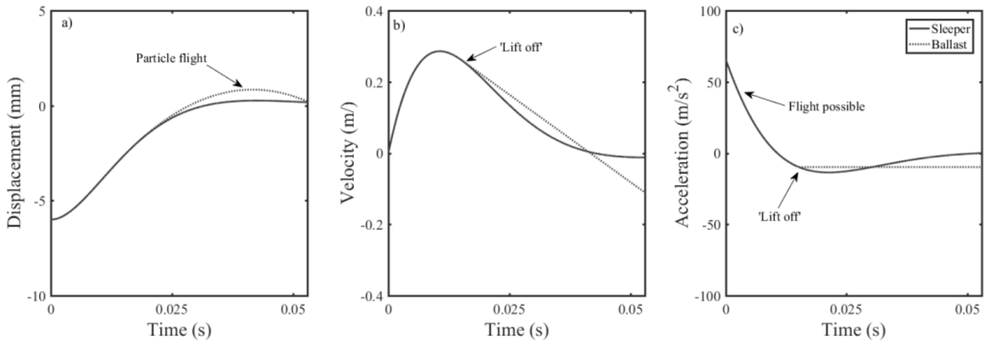

Figure C 15 Ballast grain flight due to 5 mm of track deflection imposed on a track system modelled with a support modulus of 40 MN/m^2 and a UIC 60 rail, representing a wheel moving at 80 m/s.

The potential lift δ_b above sleeper rest level may be calculated from the lift velocity v_i and the sleeper position w_i found for the time when the downward sleeper acceleration exceeds gravity. t_i.

$$w_b = \frac{v_i^2}{2g} + w_i$$

This has been used to determine the grain velocity at lift and the potential lift once the conditions for ballast lift are met using the BOEF model. Results are shown in Figure C 16 for a series of prescribed track deflections for possible speeds representative of high-speed lines on a track with a support modulus of 40 MN/m^2 and a UIC 60 rail. The speeds are 60 and 80 m/s (typical of the Javelin and Eurostar trains that are operated on HS1) and 100 and 111 m/s (close to the proposed operating and design speeds of 360 and 400 km/h of HS2).

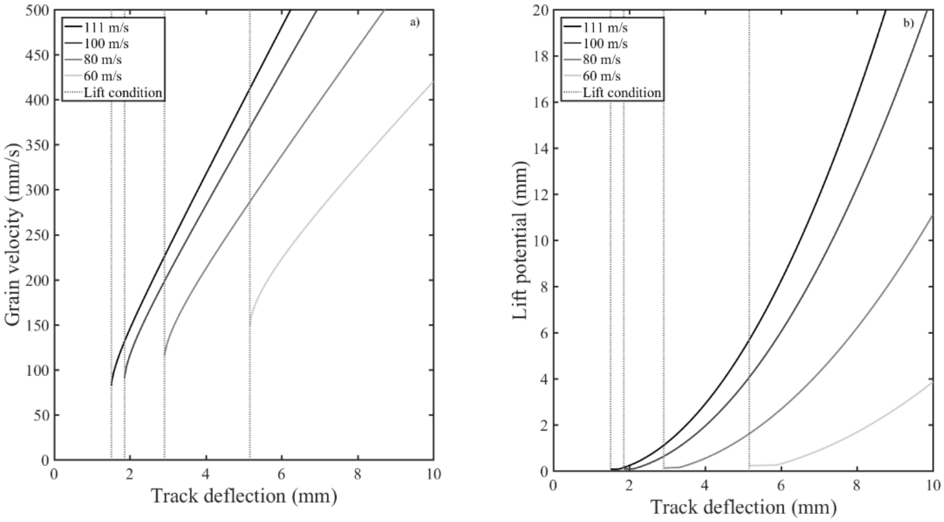

Figure C 16 (a) Grain velocity and (b) lift potential from low frequency track vibration from a wheel for a series of prescribed track deflections for possible speeds representative of high-speed lines on a track with a support modulus of 40 MN/m^2 and a UIC 60 rail. The speeds are 60, 80, 100 and 111 m/s.

Figure C 16 shows that ballast flight from low frequency track vibration is initiated for smaller deflections at higher speeds. The potential lift increases with speed, this is due to higher track velocities associated with increased train speed.

Figure C 16 was based on a fixed track system support modulus of 40 MN/m^2 typical of a high-speed railway. In Figure C 17 the track system support modulus has been varied between 10 and 80 MN/m^2 for a load moving at 80 m/s. This suggests that ballast lift will occur for smaller deflections on stiffer track than on softer track and that lift will be more significant on the former than the latter. Softer track leads to increased load spreading over a wider deflection bowl, which reduces the track velocity.

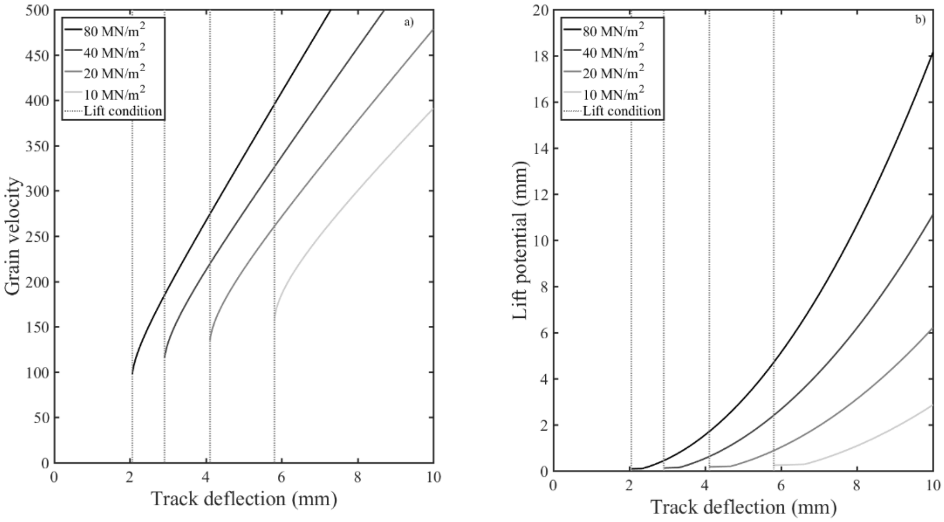

Figure C 17 (a) Grain velocity and (b) lift potential from low frequency track vibration from a wheel moving at 80 m/s for a series of prescribed track deflections on a track with a range of track system support moduli and a UIC 60 rail.

The analysis thus far has considered prescribed deflections. It is reasonable to consider the load at the rail that would be required to cause those sleeper/track bed deflections on well supported track. Assuming a rail pad stiffness of 84 MN/m the loads needed at the rail for the minimum track bed/ sleeper deflection to initiate ballast flight from the results in Figure C 16 and Figure C 17 are tabulated in Table C 2 and Table C 3 respectively. The track bed deflections and corresponding loads needed to initiate lift for various track system support moduli for 111 m/s have also been found. These loads are larger than typical wheel loads from high speed trains (50 – 100 kN), suggesting that it is unlikely that normal loads from a passing high-speed train could cause the amount of track movement needed to initiate ballast flight on well supported track at current and proposed operating speeds., although wheel flats could generate larger peak loads.

Table C 2 Table of wheel loads corresponding to the minimum track deflection needed to intiate lift of a ballast grain for various speeds.

Train Speed (m/s)	Trackbed deflection (mm)	Load at rail (kN)
60	5.2	510
80	2.9	290
100	1.9	185
111	1.5	150

Table C 3 Table of wheel loads corresponding to the minimum track deflection needed to intiate lift of a ballast grain for various track system support moduli at 80 m/s and 111 m/s.

Track system support modulus (MN/m^2)	**80 m/s (300 km/h)**		**111 m/s (400 km/h)**	
	Trackbed deflection (mm)	**Load at Rail (kN)**	**Trackbed deflection (mm)**	**Load at Rail (kN)**
10	5.8	155	3.0	80
20	4.1	200	2.1	105
40	2.9	290	1.5	150
80	2.0	575	1.1	300

However, experience from lineside monitoring indicates that large sleeper deflections are possible where there are voided or partially supported sleepers. This means the conditions necessary for flight may occur in sections of poorly performing track and should be studied further.

Appendix D Requirements for a model to study progressive deterioration of railway track

Chapter 9 showed that lineside monitoring is important for studying but not sufficient for explaining and assessing different mechanisms and processes that might be responsible for the formation of track defects. For this a model or combination of models with an appropriate level of detail would be required. These would need to account for:

- irregular track geometry,
- variation in track stiffness,
- generation of enhanced dynamic loads (including vehicle dynamics),
- presence and growth of voids between the track superstructure and substructure (requiring separate structures with a contact law),
- variable rates of settlement (including an elastic-plastic material model or taking account of variable loading in a settlement equation),
- accumulation of the effect of track settlement and updating of the track geometry and support conditions for many train passages.